9. Non-Newtonian Flows

Rheological constitutive equations of non-Newtonian liquids are discussed in detail in Chap. 1.8. In the present chapter they are used in the discussion of measurement techniques intended to establish an appropriate constitutive equation of a given liquid and attribute values for its material parameters. As is widely done in rheology, shear viscosity (not necessarily constant) is always denoted by η; only for Newtonian liquids, where $\eta =$ constant, is it denoted by μ as elsewhere in this Handbook.

9.1 Viscoelastic Polymeric Fluids

An introduction into the viscoelastic phenomenon of polymeric materials in their fluid state is presented. First, the three principal measurement methods are described: stress relaxation, creep, and dynamic mechanical measurements. This is followed by the description of the Maxwell model, the Voigt–Kelvin model and the Burgers model. Finally, the Boltzmann superposition principle is introduced and applied to various flows.

For the measurement of viscoelastic properties of polymeric fluids in principle three methods are available: stress relaxation, creep, and dynamic mechanical measurements.

Stress Relaxation. In a stress relaxation experiment a constant shear deformation γ_0 is applied; the resulting stress is time dependent and decreases as a function of time. The shear modulus or relaxation modulus is de-

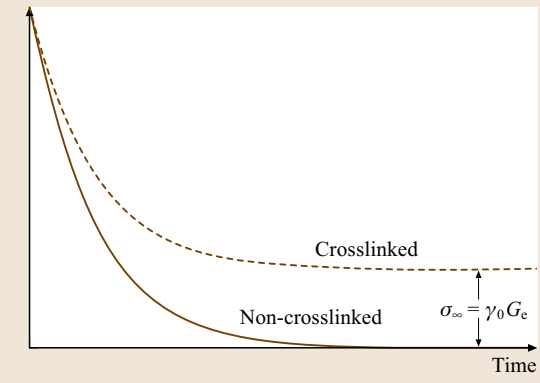

Fig. 9.1 Schematic representation of stress relaxation for viscoelastic and for a rubber-like materials

fined as the proportionality between the time dependent stress, $\sigma(t)$ and the imposed deformation:

$$G(t) = \frac{\sigma(t)}{\gamma_0} \,. \tag{9.1}$$

In Fig. 9.1 the stress relaxation is schematically shown for a viscoelastic material (non-crosslinked) and for a rubber-like (crosslinked) material. For the viscoelastic fluid the stress decreases to zero (fading memory), whereas for the rubber-like material the stress relaxes to a value $\gamma_0 G_e$, where G_e is the rubber shear modulus.

Creep. In a creep experiment a constant shear stress σ_0 is applied; the resulting deformation, i. e., the creep, is time dependent and increases as a function of time. The shear

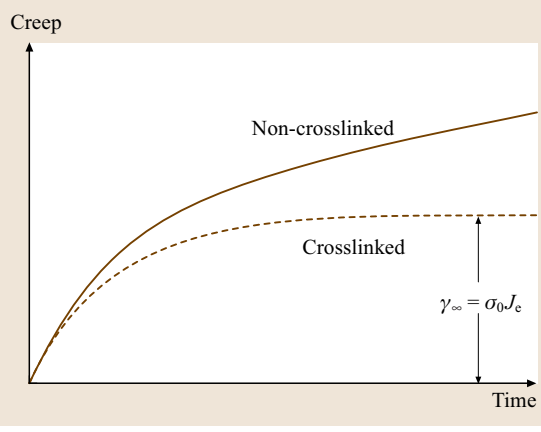

Fig. 9.2 Schematic representation of creep for viscoelastic and for a rubber-like materials

compliance is defined as the proportionality between the time dependent shear deformation $\gamma(t)$ and the imposed stress σ_0:

$$J(t) = \frac{\gamma(t)}{\sigma_0} \,. \tag{9.2}$$

In Fig. 9.2 creep is schematically shown for a viscoelastic and a rubber-like material. For a viscoelastic fluid the long-time creep increases linearly with time, with a slope equal to σ_0/η, whereas for the rubber-like material the creep increases to a constant value $\sigma_0 J_e$, where J_e is the rubber shear compliance, equal to $1/G_e$.

Dynamic Mechanical Measurements. In dynamic mechanical measurements a sinusoidal shear deformation with radian frequency ω is applied (Fig. 9.3). For linear viscoelastic materials the stress response is in the steady state also sinusoidal, but is out of phase with the strain:

$$\gamma(t) = \gamma_0 \sin(\omega t) \,. \tag{9.3}$$

$$\begin{aligned}\sigma(\omega, t) &= \sigma_0 \sin(\omega t + \delta) \\ &= \gamma_0 [G' \sin(\omega t) + G'' \cos(\omega t)] \,,\end{aligned} \tag{9.4}$$

where: δ is the loss angle and

$$G' \equiv \frac{\sigma_0}{\gamma_0} \cos\delta \quad \text{and} \quad G'' \equiv \frac{\sigma_0}{\gamma_0} \sin\delta \,. \tag{9.5}$$

G' is called the storage modulus, representing the elastic properties, whereas G'' is called the loss modulus, representing the viscous properties. For ideal rubbers $G' = G_e$ and $\delta = 0$, whereas for Newtonian liquids $G'' = \eta\omega$ and $\delta = \pi/2$.

The dynamic moduli can also be defined in complex notation:

$$\begin{aligned}&\gamma^* = \gamma_0 \exp(\mathrm{i}\omega t) \quad \sigma^* = \sigma_0 \exp[\mathrm{i}(\omega t + \delta)] \\ &\text{and} \quad G^* \equiv \frac{\sigma^*}{\gamma^*} = \frac{\sigma_0}{\gamma_0} \exp(\mathrm{i}\delta) = \left|G^*\right| \exp(\mathrm{i}\delta)\end{aligned} \tag{9.6}$$

where:

$$G^* = G' + \mathrm{i}G'' \quad \text{and} \quad \mathrm{i} = \sqrt{-1} \,. \tag{9.7}$$

The complex viscosity is defined as:

$$\begin{aligned}\eta^* &\equiv \frac{\sigma^*}{\mathrm{d}\gamma^*/\mathrm{d}t} = \frac{\sigma^*}{-\mathrm{i}\omega\gamma^*} \\ &= -\frac{\mathrm{i}G^*}{\omega} = \frac{G''}{\omega} - \mathrm{i}\frac{G'}{\omega} = \eta' - \mathrm{i}\eta''\end{aligned} \tag{9.8}$$

with:

$$\eta' = \frac{G''}{\omega} \quad \text{and} \quad \eta'' = \frac{G'}{\omega} \,. \tag{9.9}$$

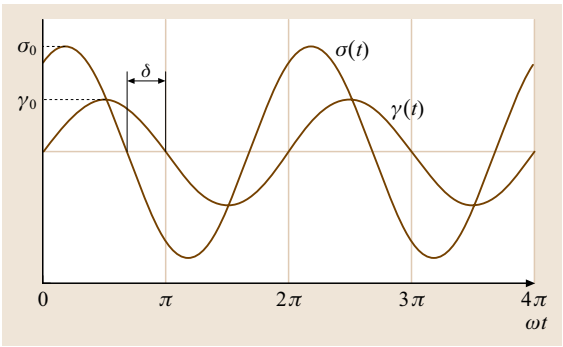

Fig. 9.3 Dynamic experiment: sinusoidal stress and deformation δ (rad) out of phase

The absolute values of the complex modulus and viscosity are:

$$|G^*| = \sqrt{G'^2 + G''^2} \quad \text{and} \quad |\eta^*| = \sqrt{\eta'^2 + \eta''^2} \,. \tag{9.10}$$

In Fig. 9.4 the complex material properties are demonstrated in the complex plane for $\omega = 1/2$ rad.

Mechanical Models. In order to describe the viscoelastic behavior of polymeric fluids use is made of mechanical models consisting of an elastic Hookean spring with spring constant G and a viscous Newtonian dashpot with viscosity η. The relationships between stress and deformation are, for a spring and dashpot,

$$\sigma = G\gamma \quad \text{and} \quad \sigma = \eta \frac{\mathrm{d}\gamma}{\mathrm{d}t} \,, \tag{9.11}$$

respectively.

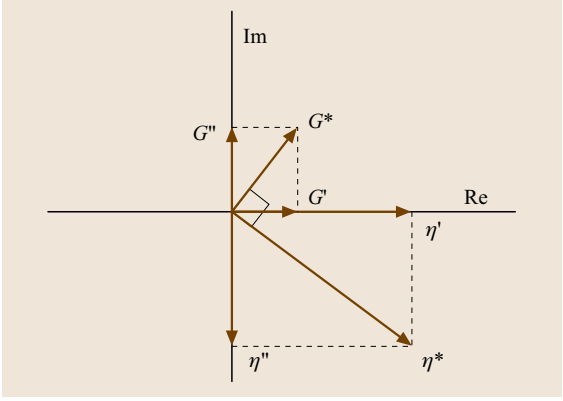

Fig. 9.4 The dynamic moduli and viscosities in the complex plane

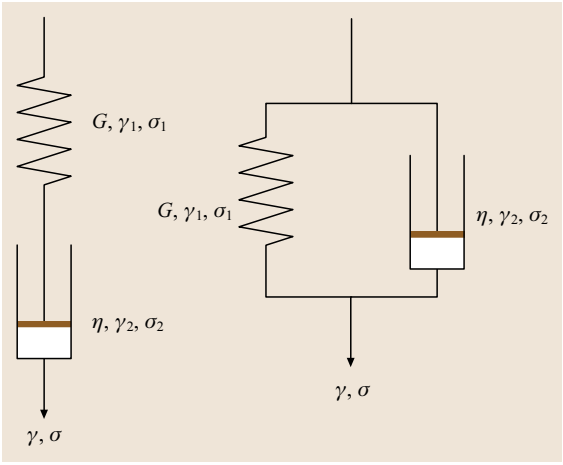

Fig. 9.5 Maxwell (*left*) and Voigt–Kelvin models (*right*)

In the Maxwell model, the spring and dashpot are linked in series while in the Voigt–Kelvin model they are linked parallel (Fig. 9.5). The Maxwell model is appropriate to describe stress relaxation, and the Voigt–Kelvin model to describe creep.

For the Maxwell model the relationships between deformations and between stresses are:

$$\gamma = \gamma_1 + \gamma_2 \quad \text{and} \quad \sigma = \sigma_1 = \sigma_2 \tag{9.12}$$

and for the Voigt–Kelvin model they are

$$\gamma = \gamma_1 = \gamma_2 \quad \text{and} \quad \sigma = \sigma_1 + \sigma_2 \,. \tag{9.13}$$

Stress Relaxation of a Maxwell Model. If at time $t = 0$ a Maxwell model has a constant strain of γ_0 suddenly

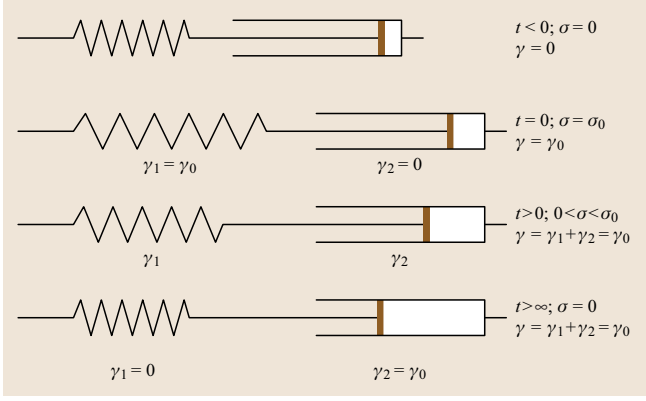

Fig. 9.6 Schematic representation of the stress relaxation of a Maxwell model

imposed, the spring is momentarily stretched to γ_0. The stress needed for this deformation is

$$\sigma_0 = G\gamma_0 \,. \tag{9.14}$$

Due to this stress the plunger of the dashpot starts to move (Fig. 9.6). As a result the stress starts to decrease gradually.

The relationships between the stress and deformation are

$$\sigma_1 = G\gamma_1 \quad \text{and} \quad \sigma_2 = \eta\frac{\mathrm{d}\gamma_2}{\mathrm{d}t} \,, \tag{9.15}$$

$$\sigma_1 = \sigma_2 = \sigma \,, \tag{9.16}$$

and

$$\gamma_1 + \gamma_2 = \gamma_0 \,. \tag{9.17}$$

By differentiation of (9.17) with respect to time:

$$\frac{\mathrm{d}\gamma_1}{\mathrm{d}t} + \frac{\mathrm{d}\gamma_2}{\mathrm{d}t} = \frac{\mathrm{d}\gamma_0}{\mathrm{d}t} = 0 \tag{9.18}$$

and by subsequent combination with (9.15) we obtain

$$\frac{1}{G}\frac{\mathrm{d}\sigma}{\mathrm{d}t} + \frac{\sigma}{\eta} = 0 \,. \tag{9.19}$$

Integration of (9.19) with the boundary value $\sigma(t=0) = \sigma_0$

$$\int_{\sigma_0}^{\sigma(t)} \frac{\mathrm{d}\sigma}{\sigma} = -\frac{G}{\eta}\int_0^t \mathrm{d}t \tag{9.20}$$

yields

$$\sigma(t) = \sigma_0 \exp(-t/\tau) \,, \tag{9.21}$$

where

$$\sigma_0 = G\gamma_0 \quad \text{and} \quad \tau = \frac{\eta}{G} \,, \tag{9.22}$$

where τ is the relaxation time of the Maxwell model, i. e., the time needed for relaxation of the stress from σ_0 to σ_0/e (i. e., approximately $0.37\sigma_0$, Fig. 9.7a). The shear modulus is defined as

$$G(t) \equiv \frac{\sigma(t)}{\gamma_0} = G\exp(-t/\tau) \,. \tag{9.23}$$

Upon plotting $\sigma_{\mathrm{red}} = \sigma(t)/\sigma_0 = \exp(-t/\tau)$ versus $\log t$ a curve is obtained with a strong decrease from 1 to 0 around $t = \tau$, according to the results in Table 9.1.

Hence, the stress $\sigma(t)$ decreases *stepwise* within a few decades from approximately σ_0 to zero, which manifests viscoelastic liquid-like behavior. This is demonstrated in Fig. 9.7a, where the reduced relaxation modulus $G_{\mathrm{red}}(t) = G(t)/G = \sigma(t)/\sigma_0$ is plotted versus log time, for two Maxwell models with relaxation times of $\tau = 1$ s and $\tau = 10\,000$ s, respectively.

In general, the decrease of the stress is not as sharp as shown in Table 9.1 and in Fig. 9.7a. One could imagine that this is the result of the presence of more relaxation times. We can describe this phenomenon by a so-called Maxwell–Wiechert (MW) model, i. e., N Maxwell elements linked in parallel, each with its own spring

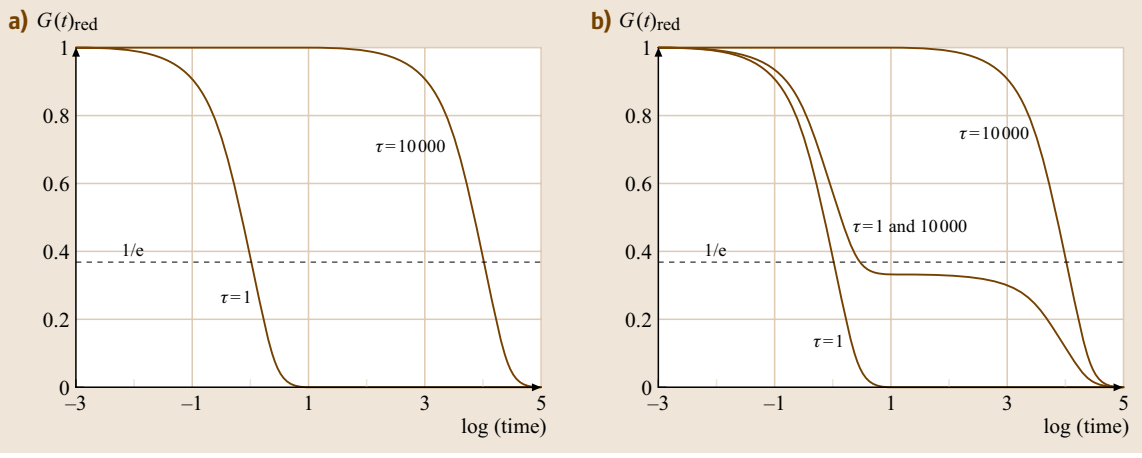

Fig. 9.7 **(a)** Semi-logarithmic plot of the reduced relaxation modulus $G_{\mathrm{red}}(t) = G(t)/G = \sigma(t)/\sigma_0$ for two Maxwell elements, with relaxation times of 1 s and 10 000 s, respectively **(b)** Semi-logarithmic plot of the relaxation of the reduced stress σ/σ_0 for a Maxwell–Wiechert model, with relaxation times of 1 s and 10 000 s and spring constants G_1 and $G_2 = 0.5G_1$; the results of **(a)** are also shown

Table 9.1 Fast decrease of $\exp(-t/\tau)$ in two decades of time around $t/\tau = 1$

t/τ	0.01	0.1	1	10
$\log(t/\tau)$	–2	–1	0	1
$\exp(-t/\tau)$	0.990	0.904	0.365	0.000

constant G_i and relaxation time τ_i, for which the shear modulus can be found to be

$$G(t) = \sum_{i=1}^{N} G_i \exp(-t/\tau_i) \,. \tag{9.24}$$

The number of Maxwell elements needed in the MW model depends on the accuracy desired to describe the viscoelastic behavior.

If there are two distinct relaxation times far away from each other (e.g., 1 s and 10 000 s), then in a plot of $\sigma(t)$ versus $\log t$ the stress decreases in two steps (Fig. 9.7b): first a step from $\sigma_0 = \gamma_0(G_1 + G_2)$ to $\sigma = \gamma_0 G_2$ at around $t = 1$ s and subsequently a step from $\sigma = \gamma_0 G_2$ to $\sigma = 0$ at around $t = 10\,000$ s.

For high-molecular-weight polymers the modulus also decreases in two steps from the glassy state, at approximately 3×10^9 N/m^2, via the pseudo-rubber plateau, at approximately 10^5 N/m^2, to the fluid state. However the decrease is much less sharp than the decreases shown in Fig. 9.7b. The viscoelastic behavior of these polymers can be described by a (large) number of relatively short relaxation times around the glass rubber transition and another (large) number of relatively long relaxation times around the decrease from the pseudo-rubber plateau to the fluid state. The pseudo-rubber plateau is the result of the presence of entanglements in high-molecular-weight polymers.

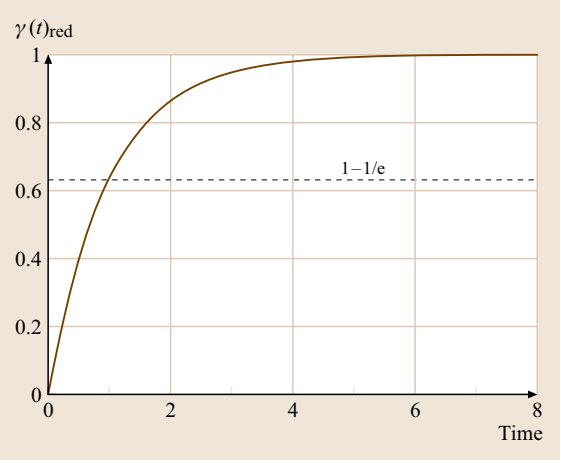

Fig. 9.8 Creep for a Voigt–Kelvin model with a retardation time of 1 s

Creep of a Voigt–Kelvin Model. When a stress σ_0 is suddenly applied to a Voigt–Kelvin model, we have:

$$\frac{d\sigma_0}{dt} = \frac{d\sigma_1}{dt} + \frac{d\sigma_2}{dt} = 0$$
$$= G\frac{d\gamma_1}{dt} + \eta\frac{d^2\gamma_2}{dt^2} = G\frac{d\gamma}{dt} + \eta\frac{d^2\gamma}{dt^2} \,. \tag{9.25}$$

The boundary values are:

$$\gamma(t=0) = 0 \quad \text{and} \quad \gamma(t=\infty) = \sigma_0/G \,. \tag{9.26}$$

Hence, the solution of the differential equation reads

$$\gamma(t) = \frac{\sigma_0}{G}[1 - \exp(-t/\tau)] = \sigma_0 J[1 - \exp(-t/\tau)] \,, \tag{9.27}$$

where the characteristic time, now called the retardation time, is again $\tau = \eta/G$, and $J = 1/G$ is the compliance of the spring.

In Fig. 9.8 the reduced creep, i. e., $\gamma_{red} = \gamma(t)/\gamma_\infty = \gamma(t)G/\sigma_0$, is shown for a viscoelastic system with a retardation time of 1 s. The retardation time is equal to the time needed to reach a value of $1 - 1/e \approx 0.63$, as illustrated in Fig. 9.8. Upon comparing this figure with Fig. 9.2 it becomes clear, that it illustrates the creep of a crosslinked polymer, a rubber-like material. Hence, the Voigt–Kelvin model describes a viscoelastic solid and is not able to describe the creep behavior of viscoelastic fluids.

Creep of a Burgers Model. The creep behavior of viscoelastic fluids can be described in a better way with the Burgers model, i. e., a Maxwell model linked in series with a Voigt–Kelvin model (Fig. 9.9). The following equations are available:

$$\gamma = \gamma_1 + \gamma_2 + \gamma_3 \quad \text{and} \quad \sigma = \sigma_1 + \sigma_2 \,, \tag{9.28}$$

$$\gamma_1 = \sigma/G \,, \quad \gamma_2 = \frac{\sigma}{G_1}[1 - \exp(-t/\tau_1)] \quad \text{and}$$
$$\frac{d\gamma_3}{dt} = \frac{\sigma}{\eta} \quad \text{where} \quad \tau_1 = \eta_1/G_1 \,. \tag{9.29}$$

The solution of these equations yields, for a Burgers model subjected to a constant stress σ_0, the following

expression for creep

$$\gamma(t) = \sigma_0 \left\{ \frac{1}{G} + \frac{1}{G_1}[1 - \exp(-t/\tau_1)] + \frac{t}{\eta} \right\}$$
$$= \sigma_0 \left\{ J + J_1[1 - \exp(-t/\tau_1)] + \frac{t}{\eta} \right\} = \sigma_0 J(t) \,, \tag{9.30}$$

where the time-dependent compliance is given by

$$J(t) = J + J_1[1 - \exp(-t/\tau_1)] + \frac{t}{\eta} \tag{9.31}$$

and where $J = 1/G$ and $J_1 = 1/G_1$, i. e., the compliances of the two springs, and the retardation time is $\tau_1 = \eta_1/G_1$.

It is clear that creep of a Burgers model is the sum of the creep of a Maxwell model and of a Voigt–Kelvin model. As demonstrated in Fig. 9.10, the values of J and J_1 can be obtained by extrapolation of the linear part that is obtained after long times, well after the retardation time, where the slope is equal to $1/\eta$.

For polymer melts, J and J_1 are of the order of $3 \times 10^{-10}\,\mathrm{m^2/N}$ and $10^{-5}\,\mathrm{m^2/N}$, both nearly independent of temperature and molecular weight, whereas the viscosity η is strongly dependent on both the temperature and molecular weight.

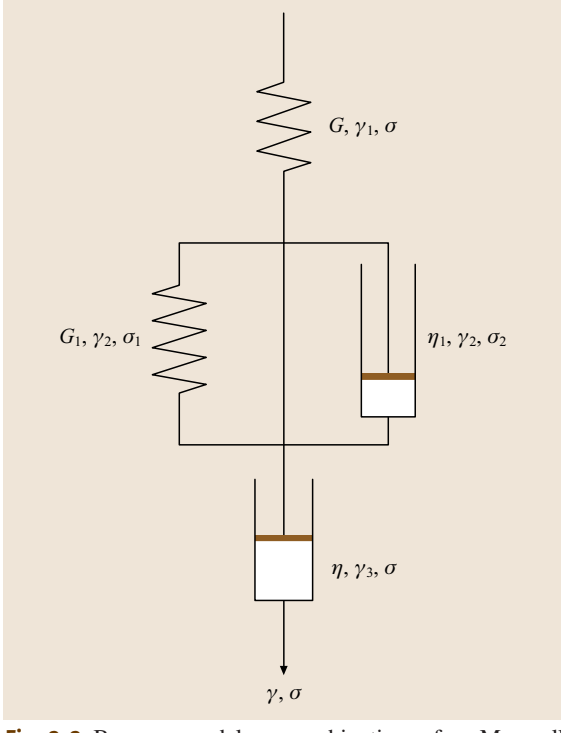

Fig. 9.9 Burgers model, a combination of a Maxwell model and a Voigt–Kelvin model in series

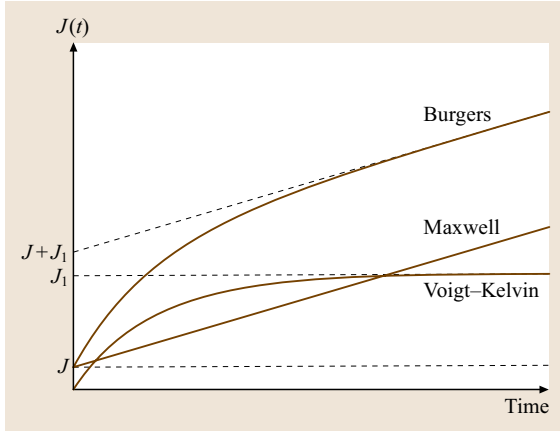

Fig. 9.10 Creep of a Burgers model

Boltzmann Superposition Principle. If at time $t = 0$ a viscoelastic system is suddenly subjected to a deformation γ_0 and at time $t = t_1$ suddenly to an extra deformation γ_1 then for $t \geq t_1$ the stress will be given by

$$\sigma(t \geq t_1) = \gamma_0 G\,(t) + \gamma_1 G\left(\overline{t - t_1}\right) \,, \tag{9.32}$$

where the bar above $t - t_1$ means that G is a function of $t - t_1$. This principle is called the Boltzmann superposition principle, which is only appropriate to describe linear behavior. In general the stress after stepwise deformations $\Delta\gamma_i$ at times t_i is given by

$$\sigma(t) = \sum_i \Delta\gamma_i G\left(\overline{t - t_i}\right) \,. \tag{9.33}$$

If the deformation changes continuously then the sum changes into an integral

$$\sigma(t) = \int_{-\infty}^{t} G\left(\overline{t - t'}\right) \frac{\partial\gamma(t')}{\partial t'}\,\mathrm{d}t' \tag{9.34}$$

where t' is the running time or time in the prehistory, and t is the actual time.

Examples of the Application of the Boltzmann Superposition Principle.

Steady Shear Flow. Steady shear flow means that the shear flow was started at $t' = -\infty$ and is still going on at time $t' = t$. The constant shear rate is then given by

$\dot\gamma_0$, hence, $\partial\gamma/\partial t' = \dot\gamma_0$. Equation (9.34) yields:

$$\sigma(t) = \dot\gamma_0 \int_{-\infty}^{t} G\left(\overline{t-t'}\right) \mathrm{d}t' \tag{9.35}$$

Upon substitution of $s = t - t'$ we obtain

$$\sigma(t) = \dot\gamma_0 \int_{0}^{\infty} G(s)\,\mathrm{d}s = \sigma_\infty \,, \tag{9.36}$$

which appears to be independent of t.

If the viscoelastic behavior is given by a sum of Maxwell models, i. e., by an MW model, then we obtain

$$\begin{aligned}\sigma(t) &= \dot\gamma_0 \int_{0}^{\infty} \sum_i G_i \exp\left(-s/\tau_i\right)\,\mathrm{d}s \\ &= \dot\gamma_0 \sum_i G_i \int_{0}^{\infty} \exp\left(-s/\tau_i\right)\,\mathrm{d}s = \dot\gamma_0 \sum_i G_i \tau_i \,.\end{aligned} \tag{9.37}$$

Hence, the viscosity is equal to

$$\eta = \frac{\sigma_\infty}{\dot\gamma_0} = \int_{0}^{\infty} G(s)\,\mathrm{d}s = \sum_i G_i \tau_i = \sum_i \eta_i \,. \tag{9.38}$$

Starting Steady Shear Flow at Time $t = 0$. Upon starting steady shear flow at time $t = 0$ the stress at time t can be calculated as follows

$$\sigma(t) = \dot\gamma_0 \int_{0}^{t} G\left(\overline{t-t'}\right)\,\mathrm{d}t' = \dot\gamma_0 \int_{0}^{t} G(s)\,\mathrm{d}s \tag{9.39}$$

so that the time-dependent viscosity $\eta^+(t)$ is equal to

$$\eta^+(t) = \frac{\sigma(t)}{\dot\gamma_0} = \int_{0}^{t} G(s)\,\mathrm{d}s \,. \tag{9.40}$$

Upon substitution (9.24) we obtain

$$\eta^+(t) = \sum_{i=1}^{N} G_i \tau_i [1 - \exp(-t/\tau_i)] \,. \tag{9.41}$$

For $t \to \infty$ we have

$$\eta = \lim_{t\to\infty} \eta^+(t) = \sum_{i=1}^{N} G_i \tau_i \,. \tag{9.42}$$

From (9.40) and (9.41) it becomes clear that the stress increases gradually to $\dot\gamma_0\eta$, as demonstrated schematically in Fig. 9.11a. It is also clear that the stress is proportional to the shear rate $\dot\gamma_0$. Hence, if the shear stress is divided by the shear rate then the various curves are identical, while at $t \to \infty$ the viscosity has a constant value. This is only in agreement with practice if the shear rate is small. For higher shear rates the stresses are not proportional anymore with the shear rate and for polymeric fluids $\sigma(t)/\dot\gamma_0$ becomes smaller or can even show a maximum value, the so-called stress overshoot (Fig. 9.11b). As a result the corresponding steady-state value after long times has a smaller value so that the viscosity decreases with increasing shear rate.

Sinusoidal Deformation. Upon substitution (9.3) into (9.34) we obtain

$$\sigma(t) = \gamma_0\omega \int_{-\infty}^{t} G\left(\overline{t-t'}\right) \cos\left(\omega t'\right)\,\mathrm{d}t' \tag{9.43}$$

which, upon substitution of $s = t - t'$, is transformed into

$$\sigma(t) = \gamma_0\omega \int_{-\infty}^{t} G(s) \cos\left[\omega\,(t-s)\right]\,\mathrm{d}s \tag{9.44}$$

or

$$\begin{aligned}\sigma(t) = \gamma_0\omega \sin(\omega t) &\int_{0}^{\infty} G(s) \sin(\omega s)\,\mathrm{d}s \\ &+ \gamma_0\omega \cos(\omega t) \int_{0}^{\infty} G(s) \cos(\omega s)\,\mathrm{d}s \,.\end{aligned} \tag{9.45}$$

Comparing this result with that of (9.4), we can conclude:

$$G'(\omega) = \omega \int_{0}^{\infty} G(s) \sin(\omega s)\,\mathrm{d}s \,, \tag{9.46}$$

$$G''(\omega) = \omega \int_{0}^{\infty} G(s) \cos(\omega s)\,\mathrm{d}s \,. \tag{9.47}$$

Upon substituting a sum of Maxwell models, i. e., (9.24), we obtain

$$G'(\omega) = \sum_i G_i \frac{\omega^2\tau_i^2}{1+\omega^2\tau_i^2} \,, \tag{9.48}$$

$$G''(\omega) = \sum_i G_i \frac{\omega\tau_i}{1+\omega^2\tau_i^2} \,. \tag{9.49}$$

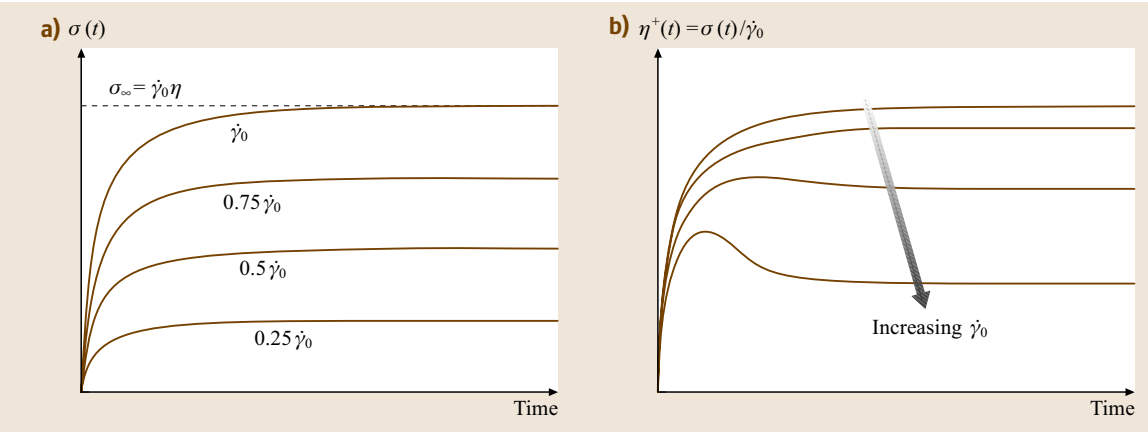

Fig. 9.11 **(a)** Increase of stress after starting steady shear flow at zero time $\dot{\gamma} = \dot{\gamma}_0 =$constant. **(b)** Non-Newtonian shear flow schematically shown

From (9.48) and (9.49) it follows, for very low angular frequencies, that

$$\lim_{\omega\to 0} \frac{G'}{\omega^2} = \sum_i G_i \tau_i^2 = \Psi_1 \,, \tag{9.50}$$

$$\lim_{\omega\to 0} \frac{G''}{\omega} = \sum_i G_i \tau_i = \eta \,. \tag{9.51}$$

Ψ_1 (i. e., the first normal stress coefficient) and η are material functions that are defined in steady shear rheology (Sect. 9.1.1). From (9.48) and (9.49) it follows that, upon plotting $\log G'$ and $\log G'$ versus $\log\omega$ at low frequencies, straight lines are obtained with slopes of 2 and 1, respectively. From these regions Ψ_1 and η can be determined. Another important conclusion is that there is a correspondence between steady shear flow behavior and oscillatory flow behavior.

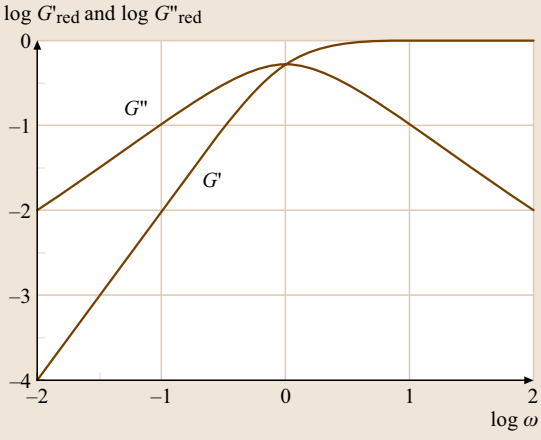

Fig. 9.12 Double logarithmic plot of the reduced dynamic moduli of a Maxwell model with one relaxation time of 1 s, versus the angular frequency

For a Maxwell model with a relaxation time of 1 s the reduced dynamic moduli, i. e., $G'_{red} = G'/G$ and $G''_{red} = G''/G$, are plotted versus angular frequency in Fig. 9.12 on double logarithmic scales. A maximum in G'' arises where the G' and G'' curves cross each other. At low frequencies straight lines are obtained with slopes of 2 and 1, respectively. At high frequencies G' becomes constant, equal to G, whereas G'' decreases with a slope of -1. Both curves cross at $\omega\tau = 1$.

In Fig. 9.13 analogous results are shown for a Maxwell–Wiechert model with one relaxation time $\tau_1 = 10\,000$ s and a corresponding spring constant G and one relaxation time $\tau_2 = 1$ s with a corresponding spring constant of $100G$, hence $G'_{red} = G'/(101G)$ and $G''_{red} = G'/(101G)$. In this case two plateaus in the storage modulus and two maxima in the loss modulus are present.

This result is qualitatively in agreement with the dynamic moduli of high-molecular-weight polymers, where in general two transitions are present: the high-frequency transition is the glass–rubber transition (from approximately 3×10^9 to $10^5\,\mathrm{N/m^2}$) while the low-frequency transition is the rubber-flow transition. Both transitions are attended with maxima in the loss modulus. Of course the transitions are much less sharp.

Creep of a Burgers Model. The Boltzmann superposition principle holds not only for stress relaxation but also for creep experiments. It reads, for discrete changes in

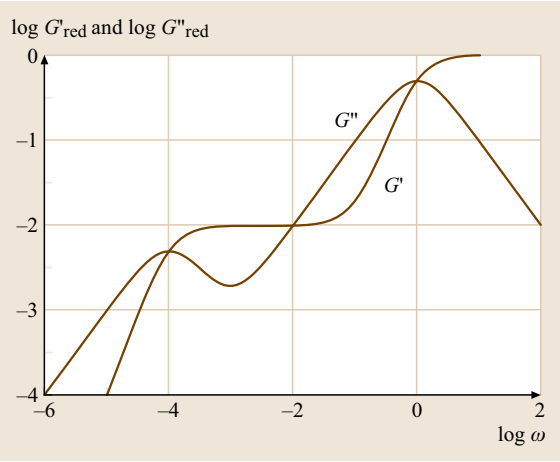

Fig. 9.13 Double logarithmic plot of the reduced dynamic moduli of a Maxwell–Wiechert model with two relaxation times of 10 000 s and 1 s, versus the angular frequency. The corresponding spring constants are G and 100 G

the stress,

$$\gamma(t) = \sum_i \Delta\sigma_i J\left(\overline{t - t_i}\right) \tag{9.52}$$

and for a continuously changing stress

$$\gamma(t) = \int_{-\infty}^{t} J\left(\overline{t - t'}\right) \frac{\partial\sigma(t')}{\partial t'} \mathrm{d}t' \,. \tag{9.53}$$

If a Burgers model is subjected to a constant stress at time $t = 0$, which is removed at time t_1, then the Boltzmann superposition can be used in the following way: removing a stress at time t_1 is equivalent to continuing the stress σ_0 and adding a stress $-\sigma_0$ at time t_1. Hence, for the deformation, the creep recovery, results:

$$\gamma(t > t_1) = \sigma_0 J(t) - \sigma_0 J(\overline{t - t_1}) \tag{9.54}$$

or

$$\gamma(t > t_1) = \sigma_0 \left(J_1 \{\exp[-(t - t_1)/\tau_1] - \exp(-t/\tau_1)\} + \frac{t_1}{\eta} \right) . \tag{9.55}$$

For $t \gg \tau_1$ this reduces to:

$$\gamma(t > t_1) = \sigma_0 \left(J_1 \left\{\exp\left[-(t - t_1)/\tau_1\right]\right\} + \frac{t_1}{\eta} \right) \tag{9.56}$$

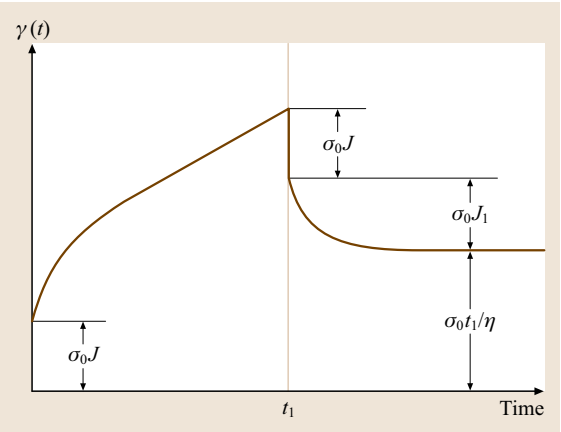

Fig. 9.14 Creep and recovery for a Burgers model

and for $t - t_1 \gg \tau_1$ the final or remaining deformation is

$$\gamma(\infty) = \frac{\sigma_0 t_1}{\eta} \,, \tag{9.57}$$

thus providing an alternative method to determine the viscosity η (see Fig. 9.14).

Conclusions. This introduction covers the subjects stress relaxation, creep, and dynamic mechanical measurements of polymer melts and solutions. In order to describe the viscoelastic behavior of those materials the well-known mechanical models were introduced: (a) the Maxwell model, which is able to describe the stress relaxation of polymer melts qualitatively, (b) the Voigt–Kelvin model, which is able to describe the creep behavior of rubber-like polymers qualitatively, and (c) the Burgers model, which is able to describe qualitatively the creep of polymer melts and rubber-like polymers. The Boltzmann superposition principle was introduced to describe the application of experiments with time-dependent deformation or with time-dependent stress. Examples of this principle were given for various experiments.

9.1.1 Measurements in Shear Flow

In this Section measurements in shear flow will be discussed. It will start with a short introduction to the mechanics of the measurement of the viscoelastic properties of polymeric fluids. This will be followed by a description of the methods to determine the time-dependent compliance with the aid of creep measurements. Most of the discussion concerns the determination of the frequency-dependent dynamic moduli with the aid of

dynamic mechanical measurements. Both compliance and dynamic moduli are illustrated with presentations from literature.

We will first discuss creep, whereas most of the discussion will deal with dynamic mechanical measurements. In shear flow measurements the sample is in general confined to the instrument, e.g., between two cylinders or between a cone and a plate. Accordingly, the translation into viscoelastic properties of the force/linear displacement ratio or of moment-of-force/angular displacement ratio will depend on the shape of the sample via a so-called shape factor. If a force F or a moment of force T_M (or torque T) is applied to a system the resulting strain/stress ratio is equal to

$$\frac{\gamma}{\sigma} = b_F \cdot \frac{x}{F} \quad \text{or} \quad \frac{\gamma}{\sigma} = b_T \cdot \frac{\phi}{T_M} , \tag{9.58}$$

where b is a geometric shape factor (b_F in m, b_T in m^3), x is the linear displacement (in m), and ϕ is the angular displacement (in radians).

Examples of shape factors for various geometries, as shown in Fig. 9.15, are given in Table 9.2 [9.1, 2], where lines e and f are of course not appropriate for polymeric liquids, but for solid polymers.

Creep Tests

In tests to determine the compliance a specimen is subjected to a sudden, constant stress σ_0 and the resulting deformation, $\gamma(t)$, is measured as a function of time. The time-dependent compliance $J(t)$ then follows from

$$J(t) = \frac{\gamma(t)}{\sigma_0} . \tag{9.59}$$

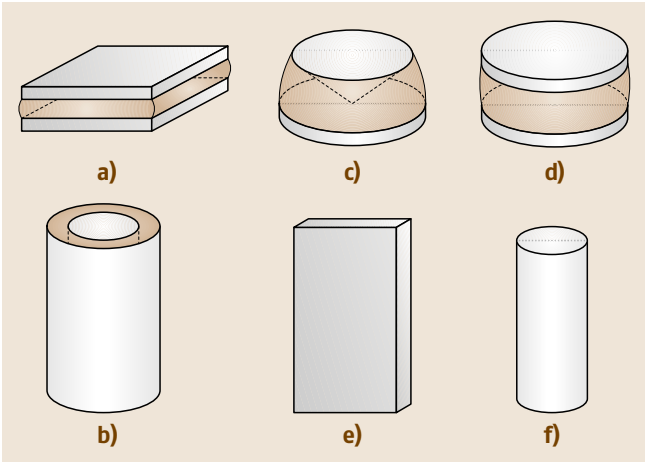

Fig. 9.15a–f Various geometric shapes for the measurement of viscoelasticity (see text) (After [9.1])

If after some time t_0, the stress is removed, the creep will be partly recovered, as was shown in Sect. 9.1:

$$\gamma(t \geq t_0) = \sigma_0 \left[J(t) - J(t - t_0) \right] . \tag{9.60}$$

In Fig. 9.16 two arrangements for creep measurements are schematically shown: a sandwich construction and a cone-and-plate construction. In the sandwich construction the force is applied to the sample by a weight that is connected via a pulley to the surface A of the upper plate. This results in a shear stress F/A. The upper plate moves over a distance $x(t)$ and this causes a shear of the sample equal to $\gamma(t) = x(t)/d$. Accordingly, the compliance is equal to

$$J(t) = \frac{\gamma(t)}{\sigma} = \frac{Ax(t)}{Fd} . \tag{9.61}$$

In the cone-and-plate construction the force F is transferred into a moment of force $T_M = F\,r$, where r is the radius of the cylinder the string is wrapped round. Due to the moment the cone will rotate over an angle $\phi(t)$, resulting in a time-dependent shear of the sample. The constant shear stress in the sample is equal to

$$\sigma = \frac{3T_M}{2\pi R^3} \tag{9.62}$$

and the time-dependent shear in the sample is

$$\gamma(t) = \frac{\phi(t)}{\Delta\Theta} . \tag{9.63}$$

Accordingly, the compliance can be calculated as

$$J(t) = \frac{\gamma(t)}{\sigma} = \frac{2\pi R^3 \phi(t)}{3T_M \Delta\Theta} . \tag{9.64}$$

Dynamic Mechanical Tests

If a viscoelastic material is deformed sinusoidally (Sect. 9.1) according to

$$\gamma = \gamma_0 \sin(\omega t) \tag{9.65}$$

the shear stress is given by

$$\begin{aligned} \sigma(t) &= \sigma_0 \sin(\omega t + \delta) \\ &= \sigma_0 \left[\sin(\omega t) \cos\delta + \cos(\omega t) \sin\delta \right] \\ &= \gamma_0 [G' \sin(\omega t) + G'' \cos(\omega t)] \\ &= G'\gamma + \frac{G''}{\omega} \frac{\mathrm{d}\gamma}{\mathrm{d}t} , \end{aligned} \tag{9.66}$$

where

$$G' \equiv \frac{\sigma_0}{\gamma_0} \cos\delta \quad \text{and} \quad G'' \equiv \frac{\sigma_0}{\gamma_0} \sin\delta . \tag{9.67}$$

Accordingly, the storage and loss moduli, G' and G'', can be calculated easily by determining the amplitudes of strain γ_0 and stress σ_0 and the phase angle δ.

Table 9.2 Various geometric shape factors

Geometry	Geometric shape factor	Units
a) sandwich construction	A/d	m
b) rotation between concentric cylinders	$4\pi L r_i^2 r_0^2/(r_0^2 - r_i^2)$	m^3
c) cone and plate	$2\pi R^3/(3\Delta\Theta)$	m^3
d) parallel plates	$\pi R^4/d$	m^3
e) torsion of a bar with rectangular cross section	$cd^3 f(c/d)/(16L) \quad c/d > 1$	m^3
f) torsion of a bar with circular cross section	$\pi R^4/(2L)$	m^3

where
A = area of the sample in contact with the plates (m^2),
d = thickness of the sample or torsion bar (m); in Sect. 9.3 this notation is changed by h to distinguish from particle diameter,
c = width of the torsion bar (m),
$f(c/d)$ = function of c/d, with numerical values varying between 2.25 and 5.33,
L =height of cylinder or bar (m),
R = radius of bar or plate (m),
r_i = radius of inner cylinder (m),
r_0 = radius of outer cylinder (m),
$\Delta\Theta$ = angle between cone and plate (rad), assumed to be small.

Classification of Techniques. There are various methods to determine the dynamic moduli, as shown in Table 9.3.

Dynamic Techniques. In general, when a shearing force F is applied, for example, to the upper side of the sliding plate of mass m in the sandwich construction in Fig. 9.15a, the equation motion of the plate is given by

$$F - A\sigma_{sh} = m\frac{d^2x}{dt^2} , \tag{9.68}$$

where A is the area that is in contact with the fluid in the gap.

If the force is an oscillating shearing force with amplitude F_0, the equation of motion becomes:

$$F_0 \sin(\omega t) - A\sigma_{sh} = m\frac{d^2x}{dt^2} . \tag{9.69}$$

With $b = A/d$ and $\gamma = x/d$, and using (9.66) we obtain for oscillatory flow

$$F_0 \sin(\omega t) = m\frac{d^2x}{dt^2} + b\frac{G''}{\omega}\frac{dx}{dt} + \left(bG' + c\right)x . \tag{9.70}$$

In (9.70) we additionally introduced an elastic constant for the instrument c. A similar equation can be derived for a rotational device, where x and m have to be replaced

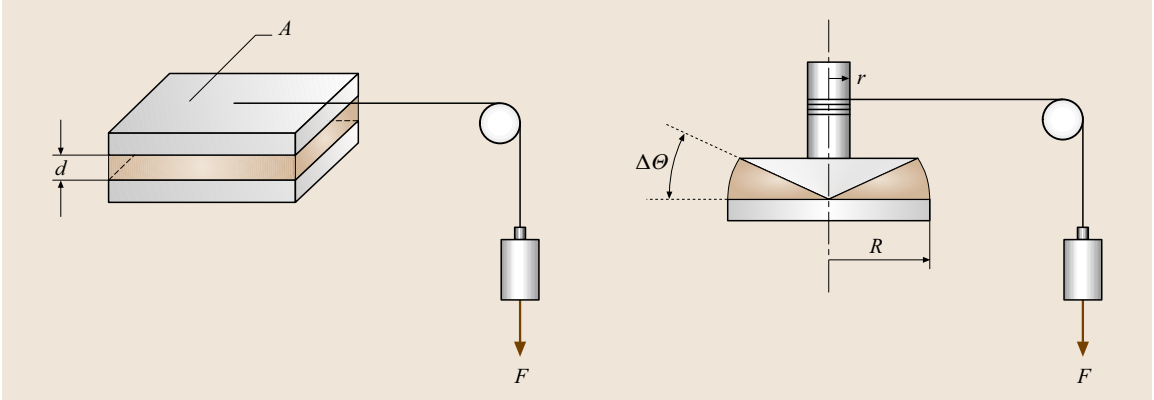

Fig. 9.16 Two set-ups for creep measurements; *left*: sandwich construction; *right* cone-and-plate construction

Table 9.3 Classification of experimental dynamic techniques

Experimental technique	Frequency (Hz)
Free damped vibrations	$10^{-2}-10$
Forced vibrations: resonance	$10^{-2}-10^{4}$
Forced vibrations: nonresonance	$10^{-5}-10^{2}$
Wave propagation	$1-3\times10^{9}$

by θ, i. e., the angle of torsion, and I, i. e., the moment of inertia of the rotor, respectively. In some cases an extra viscous term has to be added to (9.70).

For the solution of (9.70) we distinguish three cases:

1. $F_0 = 0$: free vibrations,
2. $F_0 \neq 0$ and $m\omega^2 \ll bG' + c$: forced vibrations (nonresonance),
3. $F_0 \neq 0$ and $m\omega^2 \approx bG' + c$: forced vibrations (resonance),

where (2) and (3) are written for a sliding device. For a rotational device $m\omega^2$ should be replaced by $I\omega^2$.

Free Vibrations. The solution of (9.70) for $F_0 = 0$ for a rotational instrument is:

$$\theta = \theta_0 \exp\left[-bG''t/(2I\omega_e)\right]\cos(\omega_e t) \tag{9.71}$$

provided

$$bG' + c > \frac{b^2 G''^2}{4I\omega_e^2}\,,$$

$$\text{with} \quad \omega_e^2 = \frac{4I\left(bG' + c\right) - b\eta'^2}{4I^2}\,, \tag{9.72}$$

and where θ_0 is the initial value of θ.

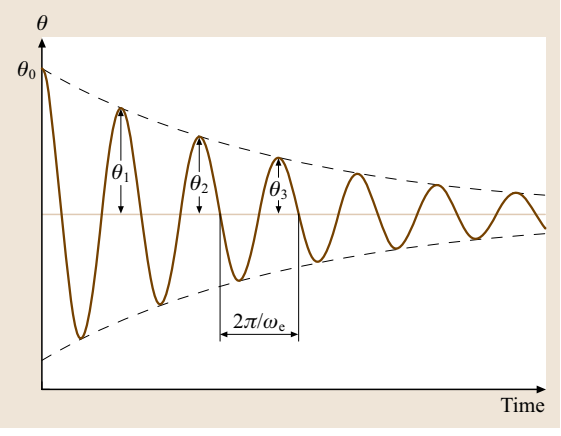

Fig. 9.17 Free damped vibrations

Equation 9.71 is the equation for free vibrations with decreasing amplitude (Fig. 9.17). The ratio of two successive maxima is

$$\frac{\theta_n}{\theta_{n+1}} = \exp\left[\pi bG''/\left(I\omega_e^2\right)\right]\,, \tag{9.73}$$

whereas the so-called logarithmic decrement is given by

$$\Lambda = \ln\left(\theta_n/\theta_{n+1}\right) = \pi bG''/\left(I\omega_e^2\right) \tag{9.74}$$

which is independent of n. Hence, a plot of log θ_n versus n (several successive θ_n are shown in Fig. 9.17) should yield a straight line with slope -0.4343Λ(log e = 0.4343). The dynamic moduli now follow from

$$G' = \frac{I\omega_e^2}{b}\left(1 + \frac{\Lambda^2}{4\pi^2}\right) - \frac{c}{b}\,, \tag{9.75}$$

$$G'' = \frac{I\omega_e^2}{b}\cdot\frac{\Lambda}{\pi}\,. \tag{9.76}$$

If the damping of the test piece is small, then the damping of the instrument itself (air damping, friction in the bearings, the suspension etc.) has to be taken into account. In that case (9.75) has to be replaced by

$$G'' = \frac{I\omega_e^2}{b}\frac{\Lambda}{\pi} - E\omega_e\,, \tag{9.77}$$

where E is the friction coefficient.

For the determination of the dynamic moduli two kinds of torsion pendulums are available (Fig. 9.18): the normal torsion pendulum, used for hard viscoelastic

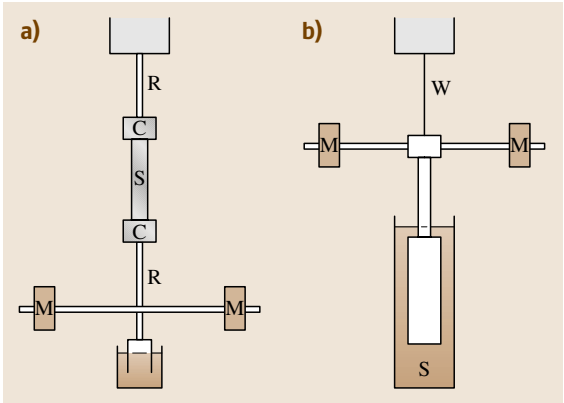

Fig. 9.18a,b Two types of torsion pendulums: **(a)** the normal torsion pendulum and **(b)** the inverted torsion pendulum. S: sample; C: clamps; W: torsion wire; M: extra adjustable masses; R: supporting rods. (After [9.3])

solids and the inverted one, appropriate for elastic liquids. The frequency range, about 0.1–100 rad/s, can be controlled by varying the moment of inertia I. This is possible by varying the masses M and their distance to the axis.

Forced Vibrations. In free vibrations experiment a defined system has a preference for only one frequency ω_e. On the other hand, if the system is driven by a sinusoidal force, then after a starting period the amplitude of the deformation remains constant. The vibration is a forced harmonic vibration. In this case the stationary solution of (9.70) is [9.2]

$$x(t) = F_0 f(\omega) \sin(\omega t - \phi) \ , \tag{9.78}$$

where ϕ is a phase angle, not to be confused with the loss angle δ, and

$$f(\omega) = \left[\left(bG' + c - m\omega^2 \right)^2 + \left(bG'' \right)^2 \right]^{-1/2} \ . \tag{9.79}$$

The result is a harmonic oscillation with a constant amplitude $F_0 f(\omega)$. At low frequencies the term $m\omega^2$ can be neglected. Moreover, if $c \ll bG'$, the solution reduces at low frequencies to

$$x(t) = x_0 \sin(\omega t - \delta) = \frac{F_0}{b\,|G^*|} \sin(\omega t - \delta) \ , \tag{9.80}$$

where $|G^*| = \left(G'^2 + G''^2 \right)^{1/2}$.

Resonance Vibrations. With increasing frequency, $f(\omega)$ increases to a maximum value ω_0 when

$$m\omega_0^2 = bG' + c \ , \tag{9.81}$$

where the amplitude of the oscillation is

$$x_0^{\text{res}} = \frac{F_0}{bG''} \ . \tag{9.82}$$

The system is then said to be in resonance. If c is known and the values of m, ω_0 and x_0^{res} are measured, both dynamic moduli can be determined from (9.81) and (9.82) without measurement of the phase angle. Nevertheless, the value of the loss tangent can also be determined from the resonance curve, shown in Fig. 9.19. The width $\Delta\omega = \omega_2 - \omega_1$ is determined from $\tan\delta$ in the following way:

$$\text{for} \quad f(\omega)/f(\omega_0) = 0.5 \ , \quad \Delta\omega/\omega_0 = \sqrt{3}\tan\delta \ , \tag{9.83}$$

$$\text{for} \quad f(\omega)/f(\omega_0) = \frac{1}{2}\sqrt{2} \ , \quad \Delta\omega'/\omega_0 = \tan\delta \ . \tag{9.84}$$

If the frequency remains far below the resonance frequency, the term $m\omega^2$ (or, in a rotational instrument, $I\omega^2$) can be neglected compared with bG', and the result is:

$$f(\omega) = \frac{1}{b\,|G^*|} \quad \text{and} \quad \tan\phi = \frac{G''}{G'} = \tan\delta \ . \tag{9.85}$$

It has to be mentioned, however, that for large values of the loss modulus the maximum of $f(\omega)$ is hardly perceptible. Moreover, if G' and G'' are strongly frequency dependent, a maximum will not appear at all.

Non-Resonance Vibrations. If the frequency remains far below the resonance frequency, the result for the dynamic moduli is

$$G' = \frac{F_0 \cos\phi}{bx_0} + \frac{m\omega^2}{b} - \frac{c}{b} \ , \tag{9.86}$$

$$G'' = \frac{F_0 \sin\phi}{bx_0} \ . \tag{9.87}$$

In order to determine the values of the dynamic moduli as a function of the frequency, apart from the instrument constants b, c and m (or I), determination of F_0/x_0 and the phase angle ϕ as a function of frequency is required. Note that ϕ is the measured phase angle, which is now not equal to the loss angle δ.

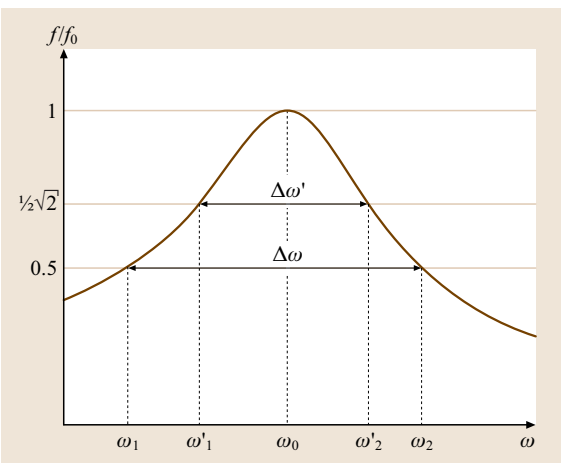

Fig. 9.19 Resonance curve of a forced vibration experiment

For hard materials dynamic measurements are in general taken on rods, bars or tubes in sinusoidal torsion or flexure. Liquids and soft viscoelastic solids are usually confined between two concentric cylinders, two cones, two plates or between a cone and a plate. In Fig. 9.20 two principles of measuring arrangements are shown on the basis of coaxial cylinders. In most types of equipment one of the two boundary surfaces is oscillated over an angle ε_1^0. The oscillation of the other boundary, over an angle ε_2^0, as well as the phase angle ϕ between the two oscillations, is measured.

For the left-hand side instrument the torque T is equal to

$$T = b\left|G^*\right|(\varepsilon_1 - \varepsilon_2)\ . \tag{9.88}$$

If the torsion bar is very stiff, ε_2^O is very small. In that case the dynamic moduli follow from

$$G' = \frac{T_0}{b\varepsilon_1^o}\cos\phi\ , \tag{9.89}$$

$$G'' = \frac{T_0}{b\varepsilon_1^o}\sin\phi\ , \tag{9.90}$$

where ε_1^o, ε_2^o and T_0 are the amplitudes of the respective oscillations. Accordingly the phase angle ϕ is equal to the loss angle δ.

In the right-hand side instrument a driving shaft is brought into oscillation ε_1. Via a torsion wire, with torsion constant c, this oscillation is transferred to the inner cylinder, which then performs an oscillation ε_2. The dynamic moduli follow from

$$G' = \frac{c}{b}\left(\frac{\varepsilon_1^o}{\varepsilon_2^o}\cos\phi - 1\right) + \frac{I\omega^2 - c}{b}\ , \tag{9.91}$$

$$G'' = \frac{c}{b}\frac{\varepsilon_1^o}{\varepsilon_2^o}\sin\phi\ . \tag{9.92}$$

Wave Propagation. In the wave propagation technique the frequency range is enormous: from 1 Hz to 3×10^9 Hz and the technique is appropriate in the range from low-viscosity liquids to solid metals.

Two types of waves can be distinguished in the wave propagation technique, viz. shear waves and longitudinal waves.

Shear Waves. A flat plate with a large area is in contact with an isotropic viscoelastic medium of density ρ. The plate is vibrating, with an angular frequency ω, in the x-direction in its own plane, with an amplitude x_0 (Fig. 9.21). It follows for the shear wave propagating into the medium occupying the semi-space $z > 0$ that:

$$x(z,t) = x_0 \exp\left[\mathrm{i}\,(\omega t - 2\pi z/\lambda) - z/z_0\right] \tag{9.93}$$

where $\mathrm{i} = \sqrt{-1}$, and λ is the wavelength of the attenuated propagating wave, whose amplitude decreases with a factor e over a distance z_0 (Fig. 9.21). The attenuation α is equal to $1/z_0$. The dynamic moduli follow

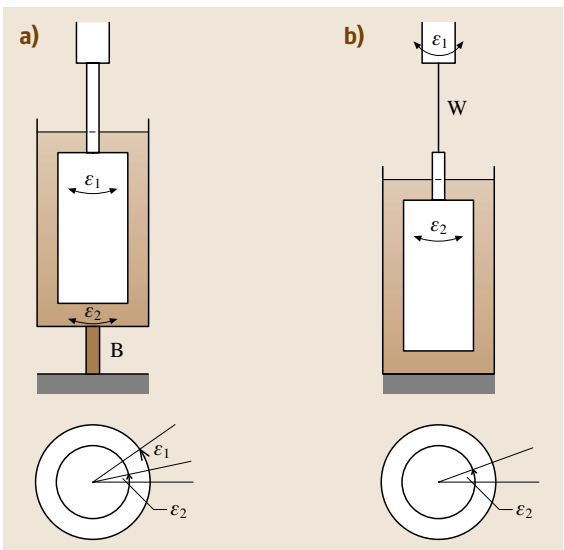

Fig. 9.20a,b Two types of nonresonant forced vibration experiments. B: torsion bar; W: torsion wire; ε_1 and ε_2: angles of rotation. (After [9.4])

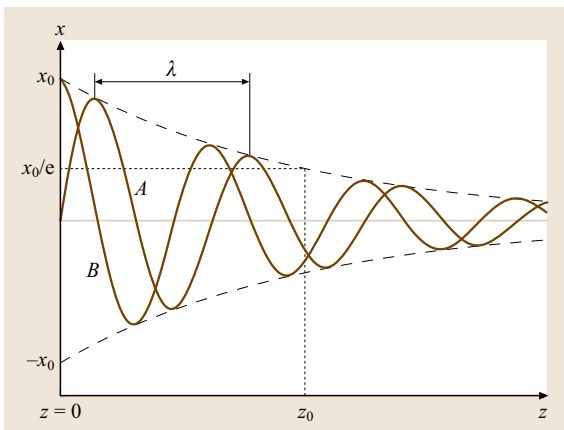

Fig. 9.21 Propagation of a shear wave of wavelength λ and attenuation $1/z_0$ in the positive, semi-infinite direction z, drawn for time $t = 2\pi n/\omega$ (*curve A*) and $t = (2n + 1/2)\pi/\omega$ (*curve B*)

from

$$G'(\omega) = \frac{\rho\omega^2(4\pi^2/\lambda^2 - 1/z_0^2)}{(4\pi^2/\lambda^2 + 1/z_0^2)^2} , \tag{9.94}$$

$$G''(\omega) = \frac{\rho\omega^2 4\pi/(\lambda z_0)}{(4\pi^2/\lambda^2 + 1/z_0^2)^2} , \tag{9.95}$$

$$\tan\delta = \frac{4\pi\lambda z_0}{4\pi^2 z_0^2 - \lambda^2} . \tag{9.96}$$

From these equations it follows that the dynamic moduli are determined by measuring the attenuation α and the wavelength λ (Fig. 9.21). If the damping is small, i. e., if λ/z_0 is small, the shear wave is propagated over a long distance. If, on the other hand, λ/z_0 is large, the wave will be attenuated so fast, that even the determination of the wavelength becomes difficult. According to *Ferry* [9.1] the upper limit would be $\lambda/z_0 = 3$. For this kind of experiments the frequency can be varied from 4 Hz to 5000 Hz.

In particular for very high frequencies (3000–3×10^9 Hz) use is made of reflection of propagating waves in a quartz crystal against an interface between the quartz and a thin film of a viscoelastic liquid [9.1].

Longitudinal Waves. If the flat plate similar to that of Fig. 9.21 is vibrating along the direction of its normal, i. e., in the z-direction, the medium will be compressed and extended in an oscillatory way. In this case G' and G'' have to be replaced by M' and M'', where

$$M' = K' + \frac{4}{3}G' , \tag{9.97}$$

$$M'' = K'' + \frac{4}{3}G'' , \tag{9.98}$$

$$M^* = K^* + \frac{4}{3}G^* , \tag{9.99}$$

where K' and K'' are the components of the complex dynamic bulk modulus K^*, whereas M' and M'' are the components of the complex dynamic longitudinal bulk modulus M^*.

Examples of Measurements on Polymer Melts

We will complete this discussion on methods for shear measurements with some results presented in the literature.

Compliance. Compliance measurements by *Plazek* and *O'Rourke* (tabulated results on page 605 in [9.1]) on polystyrene with a narrow molecular-weight distribution and a molecular weight of 600 000 are shown in Fig. 9.22. With the aid of the so-called time–temperature superposition principle [the William, Landal and Ferry (WLF) equation, see Chap. 11 in [9.1], by which measurements at a number of different temperatures are reduced to one reference temperature, in this case 100 °C, thereby increasing the frequency or time window]. Accordingly, the time window was increased to approximately 18 decades. The compliance $J(t)$, as well as $J(t) - t/\eta_0$ (where η_0 is the zero-shear viscosity) are plotted versus time. Note that at long times the slope of the compliance curve, $J(t)$, is equal to 1. In these regions the viscosity can be calculated to be approximately 2.75×10^{14} Ns/m^2 (i. e., just above the glass-transition temperature). The value of $J(t)$ at very short times is equal to the glass compliance $J_g = 10^{-9}$ m^2/N. The value of the equilibrium shear compliance J_e follows from the curve for $J(t) - t/\eta_0$ at long times, $J_e = 1.6\times10^{-5}$ m^2/N. Both values are in agreement with those mentioned in Sect. 9.1.

Dynamic Moduli. The dynamic moduli, G' and G'', of polystyrene Hostyrene N4000V were measured at temperatures of 140–206 °C in a Couette-type dynamic rheometer [9.5]. With the aid of the time–temperature superposition principle they were reduced to a temperature of 170 °C. In this way the frequency window was increased to approximately seven decades. Results are shown in Fig. 9.23, as $\log G'$ and $\log G''$ versus $\log\omega$ [9.6]. From a comparison of these results with

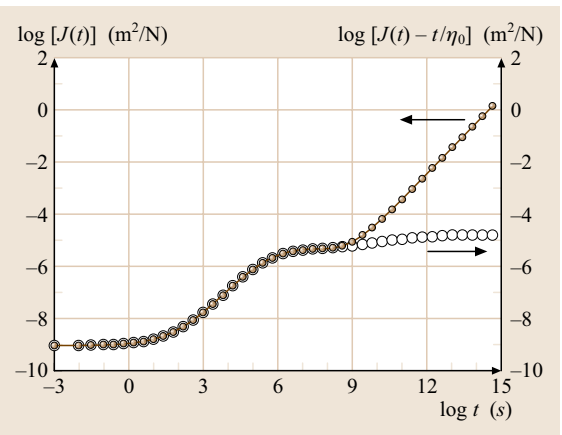

Fig. 9.22 Compliance (m^2/N) of polystyrene with a narrow molecular-weight distribution with $M = 600\,000$ versus time on double logarithmic scales, according to *Plazek* and *O'Rourke* [9.1]

Fig. 9.12, it becomes clear that only a small part of the dynamic moduli was measured: the low-frequency flow behavior of the polymer and the transition to the rubber-like entanglement plateau. A much larger frequency window is needed to describe the viscoelastic behavior up to the glassy region with an instrument that is able to measure much higher moduli, up to $3\times10^9\,\mathrm{N/m^2}$. The dashed straight lines at low frequencies have slopes of 1 (for G'') and 2 (for G'), as was mentioned in Sect. 9.1.

In Sect. 9.1, (9.51), it was shown that the zero-shear viscosity can be determined from the loss modulus by dividing G'' by ω in the limit $\omega\to0$. From Fig. 9.23 it follows for the zero-shear viscosity $\eta_0=10^5\,\mathrm{Ns/m^2}$ (the notation η_0 is introduced here instead of the η of (9.51) in Sect. 9.1). In general the loss modulus divided by the angular frequency is equal to the so-called dynamic viscosity $\eta\prime$ (Sect. 9.1):

$$\eta' \equiv \frac{G''}{\omega} \quad \text{so that} \quad \eta_0 = \lim_{\omega\to0}\frac{G''}{\omega} = \lim_{\omega\to0}\eta' \,. \tag{9.100}$$

Because G' decreases much faster than G'' with decreasing frequency, we can also conclude that

$$\eta_0 = \lim_{\omega\to0}\frac{|G^*|}{\omega} = \lim_{\omega\to0}\left|\eta^*\right| \,. \tag{9.101}$$

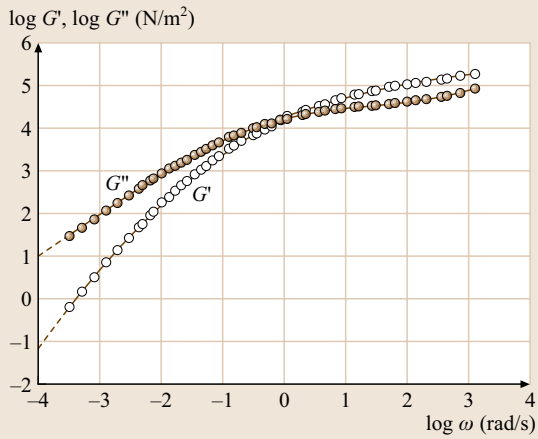

Fig. 9.23 Double logarithmic plot of the dynamic shear moduli G' and G'' versus angular frequency ω for polystyrene Hostyren N4000V, measured at temperatures varying from 140 °C to 206 °C and reduced to the reference temperature of 170 °C (see text), according to [9.6]. The measurements were taken in a Couette-type dynamic rheometer [9.5]

It has to be mentioned that the viscosity in (9.100) and (9.101) is only equal to the zero-shear viscosity η_0, if the amplitude of the sinusoidal deformation is small enough (i. e., only for linear behavior).

In Fig. 9.24 the dynamic viscosity, η', and the absolute value of the complex viscosity, $|\eta^*|$, as calculated from Fig. 9.23, are plotted versus angular frequency on double logarithmic scales, as a dashed and full line, respectively. At low frequencies both viscosities are equal and independent of frequency: they are equal to the zero-shear viscosity of $10^5\,\mathrm{Ns/m^2}$. At higher frequencies they decrease, with the dynamic viscosity decreasing faster than the complex viscosity. In Fig. 9.24 results of measurements of the viscosity in a cone-and-plate rheometer and in a capillary rheometer (Sect. 9.1) are also shown, both plotted as functions of the shear rate $\dot\gamma_0$. The curve $\eta=\eta(\dot\gamma_0)$ is decreasing as $\dot\gamma_0$ is increasing, which is referred to as shear thinning. It appears that in a cone-and-plate rheometer measurements were possible for shear rates of $0.001-0.1\,\mathrm{s^{-1}}$, whereas in the capillary rheometer measurements were possible for $3-3000\,\mathrm{s^{-1}}$. Most striking is the phenomenon that the transient viscosities (the symbols) follow the line of the complex viscosity versus angular frequency. Accordingly, it is experimentally shown that, over a large range of shear

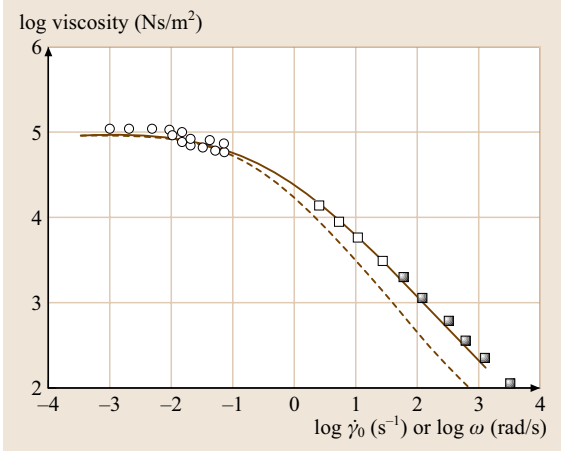

Fig. 9.24 Non-Newtonian shear viscosity $\eta(\dot\gamma_0)$ at 170 °C as a function of shear rate, $\dot\gamma_0$, for the polystyrene mentioned in Fig. 9.23, measured in a (*circles*) cone-and-plate rheometer and in a (*squares*) capillary rheometer, where the *filled squares* show the results at such high shear rates that melt fracture occurs [9.6] and the dynamic and complex viscosities, $\eta'(\omega)$ (*dashed line*) and $|\eta^*(\omega)|$ (*full line*), respectively, as functions of angular frequency, as calculated from Fig. 9.23 [9.6]

rates and angular frequencies,

$$\eta(\dot{\gamma}_0) = \left|\eta^*(\omega)\right| \quad \text{with} \quad \dot{\gamma}_0 = \omega\,. \tag{9.102}$$

This is called the empirical *Cox–Merz relation*.

From the transient measurements it follows first that in general it is impossible to measure the zero-shear viscosity with the aid of a capillary rheometer, because the shear rates are not low enough in this instrument. For that purpose a cone-and-plate rheometer is much more convenient, or in general a rotating rheometer. However, the best method to determine the zero-shear viscosity is measurement of the loss modulus G'', or better the dynamic viscosity η' at low frequencies. The reason for the preference for dynamic mechanical measurements is the fact that the moduli can be measured down to very low frequencies. A second point that follows from Fig. 9.24, is the high-shear-rate behavior, where it follows that $\log\eta$ is a linear function of $\log\dot{\gamma}_0$; this is called power-law behavior, which will be discussed in more detail in the next section.

Conclusion. In this Section it has been shown that there are several techniques to measure the compliance $J(t)$ of polymer melts and solutions. Many more techniques are available to determine the dynamic moduli G' and G'', however, varying in angular frequency from 0.01 to 3×10^9 Hz. Literature data for the compliance of a polymer melt are presented. Results of the dynamic moduli of polymer melts are also shown and the dynamic viscosities calculated from these measurements. It has been shown that there is a close relationship between the absolute value of the complex viscosity, $|\eta^*|$, as a function of the angular frequency, ω, and the steady shear viscosity, η, as a function of shear rate, $\dot{\gamma}_0$, known as the Cox–Merz relation.

9.1.2 Rheogoniometers and Rheometers

This Section starts with an introduction, where equations of motion are introduced in various coordinate systems, local coordinates and shearing planes are defined, and the shear rate is calculated. Subsequently three drag flow rheogoniometers are discussed, followed by pressure-driven rheometers. Shear-rate-dependent viscosity, and first and second normal stress differences and coefficients can be determined as functions of shear rate. It will be shown that measurement of the normal stress differences is possible due to the curvature of the streamlines.

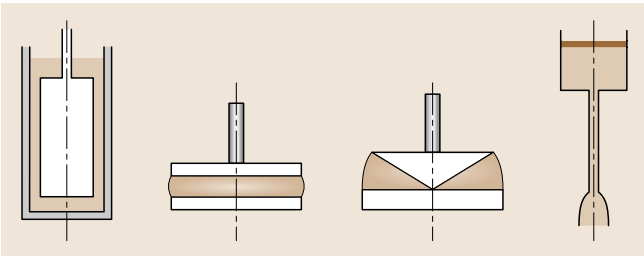

Fig. 9.25 Four commonly used rheo(gonio)meters; from *left to right*: coaxial cylinders in Couette flow, coaxial parallel plates, coaxial cone and plate and cylindrical capillary

Definition and Classification of Rheometers. A *rheometer* is an instrument that measures both *stress* and *deformation history* on a material for which the rheological constitutive equation is not known. A special case of a rheometer is a *viscometer*, which can measure only the steady shear viscosity function, $\eta(\dot{\gamma})$. According to "The British Standard Glossary of Rheological Terms" *rheogoniometers* are rheometers designed for the measurement of normal components as well as shear components of the stress tensor. Accordingly, a rheogoniometer can be used to determine material functions.

The rheological behavior of incompressible, isotropic elastic liquids can be described by σ_{21}, $N_1 = \sigma_{11} - \sigma_{22}$ and $N_2 = \sigma_{22} - \sigma_{33}$, where σ_{ij} denotes the components of the stress tensor, and N_1 and N_2 are the first and second normal stress difference, respectively. The other deviatoric components of the stress tensor are often equal to zero, due to the symmetry of the shear flow on the one hand and material isotropy on the other hand. Stationary simple shear flow is extremely important for the description of engineering processes, because this kind of flow is easily realized in laboratory and frequently occurs in (polymer) engineering. However, the measurement of elongation flow is also of great importance, because in polymer engineering these flows also play an important role Sect. 9.1.3. In practice flows are often complicated mixtures of simple shear and elongation flows.

For the measurement of shear flow many methods have been developed.

Shearing experiments have to take place in principle by moving two infinitely extended parallel plates, with the liquid of consideration in between, with a constant velocity difference with respect to each other. In practice this is of course problematic. Moreover, in this way it is only possible to determine σ_{21} and σ_{22}. For that reason we have to resort to instruments with another geometry: the streamlines do not need to be rectilinear, but they may

be curved and in many cases are circular. It will become clear that, as a result of the curvature of the streamlines, normal stress differences can be determined from measurements of the normal stress σ_{22}, as a function of the position in the flowing material. An example of an approximation of infinitely extended, parallel plates is the Couette geometry, consisting of two coaxial cylinders, where the liquid under consideration is confined in the narrow gap between the two cylinders. The cylinders rotate with respect to each other with different angular velocities, and in general one is fixed. If the diameters of the cylinders are large with respect to the gap width and small with respect to their lengths, then in the gap a shear flow is obtained, which to a good approximation is comparable with the shear flow between two infinitely extended parallel plates.

In principle we distinguish two kinds of rheometers: drag flow rheometers (e.g., Couette, plate–plate, and cone–plate) and pressure-driven flow rheometers (e.g., capillary and slit rheometers). They are shown schematically in Fig. 9.25, with the exception of the slit rheometer, which will be shown later. In the three drag flow rheometers one of the two parts rotates or oscillates: the fluid in the direct vicinity of the rotating part rotates with the same angular velocity Ω, whereas the velocity of the fluid in the direct neighborhood of the fixed part will be zero (the no-slip conditions for non-Newtonian fluids are assumed to hold in these instruments; possible slip effects are discussed in Chap. 19). The fluid in between will rotate with an angular velocity decreasing from Ω to zero, which is the origin of shear and of rate of shear. In pressure-driven rheometers the flow results from a pressure above the capillary or slit and in this case it is assumed that the velocity decreases from its maximum value at the center of the capillary or slit to zero at the walls.

To be able to determine the viscoelastic properties of the liquids, we have to be familiar with local stresses and with local shear rates in the flowing liquids. For the determination of the local stresses we make use of equations of motion and for the calculation of the shear rate we first have to define shearing planes.

Equations of Motion. In order to describe the stresses in rheogoniometers we need equations that are able to express the local stresses induced by flow. For that purpose we make use of the momentum equation:

$$\rho\dot{\boldsymbol{v}} = \nabla\cdot\boldsymbol{\sigma} + \rho\boldsymbol{b}\,, \tag{9.103}$$

where ρ is the fluid density, $\boldsymbol{v}$ is the velocity of the fluid, ∇ is the nabla operator, $\boldsymbol{\sigma}$ is the stress tensor, amd $\boldsymbol{b}$ is the body force (i. e., the force per unit of mass), e.g., the gravitational acceleration. The dot over $\boldsymbol{v}$ denotes material time differentiation.

For constant viscosity (i. e., Newtonian liquids) this equation reduces to the well-known Navier–Stokes equation.

We will neglect inertial forces, i. e., $\rho\dot{\boldsymbol{v}} = 0$, so that the equation is simplified to

$$\nabla\cdot\boldsymbol{\sigma} + \rho\boldsymbol{b} = 0\,. \tag{9.104}$$

In Cartesian coordinates the three projections read

$$\frac{\partial\sigma_{11}}{\partial x_1} + \frac{\partial\sigma_{21}}{\partial x_2} + \frac{\partial\sigma_{31}}{\partial x_3} = -\rho b_1\,, \tag{9.105}$$

$$\frac{\partial\sigma_{12}}{\partial x_1} + \frac{\partial\sigma_{22}}{\partial x_2} + \frac{\partial\sigma_{32}}{\partial x_3} = -\rho b_2\,, \tag{9.106}$$

$$\frac{\partial\sigma_{13}}{\partial x_1} + \frac{\partial\sigma_{23}}{\partial x_2} + \frac{\partial\sigma_{33}}{\partial x_3} = -\rho b_3\,, \tag{9.107}$$

in cylindrical coordinates (r, ϕ, z)

$$\frac{\partial\sigma_{rr}}{\partial r} + \frac{1}{r}\frac{\partial\sigma_{r\phi}}{\partial\phi} + \frac{\partial\sigma_{rz}}{\partial z} + \frac{\sigma_{rr}-\sigma_{\phi\phi}}{r} = -\rho b_r\,, \tag{9.108}$$

$$\frac{\partial\sigma_{r\phi}}{\partial r} + \frac{1}{r}\frac{\partial\sigma_{\phi\phi}}{\partial\varphi} + \frac{\partial\sigma_{\phi z}}{\partial z} + \frac{2\sigma_{r\phi}}{r} = -\rho b_\phi\,, \tag{9.109}$$

$$\frac{\partial\sigma_{rz}}{\partial r} + \frac{1}{r}\frac{\partial\sigma_{z\phi}}{\partial\phi} + \frac{\partial\sigma_{zz}}{\partial z} + \frac{\sigma_{rz}}{r} = -\rho b_z\,, \tag{9.110}$$

and in spherical coordinates (r, ϕ, θ):

$$\frac{\partial\sigma_{rr}}{\partial r} + \frac{1}{r}\frac{\partial\sigma_{r\theta}}{\partial\theta} + \frac{1}{r\sin\theta}\frac{\partial\sigma_{r\phi}}{\partial\phi} + \frac{2\sigma_{rr}-\sigma_{\theta\theta}-\sigma_{\phi\phi}+\sigma_{\theta r}\cot\theta}{r} = -\rho b_r\,, \tag{9.111}$$

$$\frac{\partial\sigma_{r\phi}}{\partial r} + \frac{1}{r}\frac{\partial\sigma_{\theta\phi}}{\partial\theta} + \frac{1}{r\sin\theta}\frac{\partial\sigma_{\phi\phi}}{\partial\phi} + \frac{2\sigma_{r\phi}+\sigma_{\phi r}+\left(\sigma_{\theta\phi}+\sigma_{\phi\theta}\right)\cot\theta}{r} = -\rho b_\phi\,, \tag{9.112}$$

$$\frac{\partial\sigma_{r\theta}}{\partial r} + \frac{1}{r}\frac{\partial\sigma_{\theta\theta}}{\partial\theta} + \frac{1}{r\sin\theta}\frac{\partial\sigma_{\theta\phi}}{\partial\phi} + \frac{(\sigma_{\theta\theta}-\sigma_{\phi\phi})\cot\theta+2\sigma_{r\theta}+\sigma_{\theta r}}{r} = -\rho b_\theta\,. \tag{9.113}$$

In slit rheometers use is made of the Cartesian coordinate system; for coaxial cylinders, parallel-plate, and capillary rheometers the cylindrical coordinate system

is necessary, whereas for cone-and-plate rheometers the use of the spherical coordinate system is convenient.

In the description of the rheometric methods we will make use of the assumption that N_1, N_2, and σ_{21} only depend on the local value of the shear rate, independent of the curvature of the streamlines, provided the shear rate is constant in the gap. However, the local values of σ_{11}, σ_{22}, and σ_{33}, do depend on the curvature. We will come back to this point later in the description of the Couette system.

Local Coordinate System. In the common rheogoniometers the equations of motion can be greatly simplified, because in general: (a) $\partial/\partial\phi = 0$, and (b) $\sigma_{13} = \sigma_{31} = \sigma_{23} = \sigma_{32} = 0$. Here we will consider: (1) Couette flow between two coaxial cylinders, (2) flow between coaxial, parallel plates, (3) flow between coaxial cone and plate, and (4) flow in a cylindrical or rectangular capillary. It is not clear a priori what the three directions are, e.g., in some cases the 1-direction is the ϕ-direction, but it may also be the r-direction or the z-direction, depending on the geometry of the instrument of consideration. Hence, we have to define the *local coordinate system* in the following way (Fig. 9.26)

- The 1-direction is the direction of flow, i. e., the direction of the tangent of the local streamline (steady state is discussed);
- The 2-direction is the direction perpendicular to the local shearing plane (Sect. 9.1.2) and in general (but not always) positive in the direction of increasing flow rate;
- The 3-direction completes a right-handed coordinate system.

Rate of Shear. As we move on from rectilinear to consider curvilinear shear flow, we have to define *shearing planes* as planes that move stiffly during shear flow, i.e., planes where all particles maintain their mutual distance and accordingly have the same velocity. Different planes have different velocities and this is the origin of shear and rate of shear. In rectilinear shear flow between two infinitely extended parallel plates the shear planes are fluid planes parallel to the plates: different planes move with different velocities. In Couette flow the planes of shear are coaxial cylinders: different cylinders rotate with different angular velocities. In parallel-plate (or disks) rheometers they are circular disks perpendicular to the axis: different disks rotate with different angular velocities. In cone-and-plate rheometers they are coaxial cones: different cones rotate with different angular velocities. In capillary rheometers they are coaxial cylinders: different cylinders move axially with different velocities (also called telescopic flow).

The difference in (angular) velocity between the various planes of shear is a measure of the rate of shear. In rectilinear shear flow the rate of shear is easy to calculate as the velocity gradient, as will be shown. In rotating rheometers, however, the rate of shear is not as easy to calculate as in rectilinear flow, because there is a snake in the grass. If in a Couette instrument both the cylinders and the fluid rotate with the same angular velocity there will be no shear. Notwithstanding the lack of shear there is a difference in velocity between the rotating cylinders ($v = \Omega r$), thus there is a velocity gradient. Hence, we have to be careful when calculating the rate of shear.

In rectilinear shear flow the velocity and the velocity gradient are equal to (Fig. 9.27):

$$v_1 = \frac{v_w}{d} x_2 \quad \text{and} \quad \frac{dv_1}{dx_2} = \frac{v_w}{d} \,. \tag{9.114}$$

The shear rate is equal to

$$\dot{\gamma} \equiv \frac{d\gamma}{dt} = \frac{d\tan\alpha}{dt} = \frac{d}{dt}\left(\frac{dx_1}{dx_2}\right) = \frac{d}{dx_2}\left(\frac{dx_1}{dt}\right) = \frac{dv_1}{dx_2} \,, \tag{9.115}$$

where α is the angle shown in Fig. 9.27 and d/dt denotes material time differentiation.

Accordingly, in rectilinear shear flow the velocity gradient is equal to the shear rate. If the shear rate is

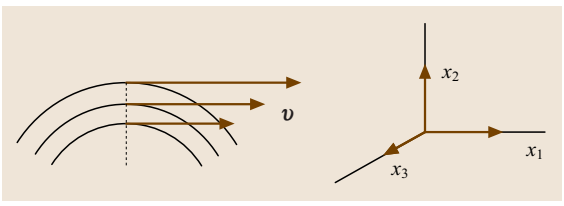

Fig. 9.26 Definition of a local coordinate system in Couette flow

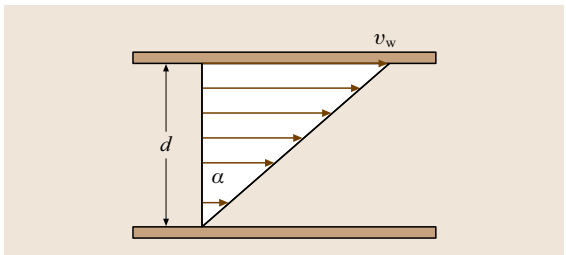

Fig. 9.27 Rectilinear shear flow

independent of time, the flow is called *stationary*, and $\dot{\gamma} = \dot{\gamma}_0 = \text{constant}$.

In Couette geometry the velocity gradient is equal to

$$\frac{dv}{dr} = \frac{d(\Omega r)}{dr} = \Omega + r\frac{d\Omega}{dr} . \tag{9.116}$$

If the inner and outer cylinder rotate together with the fluid as a rigid system, then $\Omega = \text{constant}$ and thus $d\Omega/dr = 0$. In this case the velocity gradient is equal to Ω, whereas the shear rate is equal to zero. Hence, in the determination of the shear rate, we have to take into consideration the fact that the velocities of neighboring shearing planes contain a rigid-body rotation component, $\Omega\Delta r$, which we have to subtract from the difference in velocities (see also Fig. 9.28), in order to calculate the shear rate

$$\begin{aligned} v(r) &= \Omega r \quad \text{and} \\ v(r+\Delta r) &= (\Omega + \Delta\Omega)(r+\Delta r) = \Omega r + \Omega\Delta r \\ &\quad + r\Delta\Omega + \text{higher-order terms} \end{aligned} \tag{9.117}$$

so that

$$\begin{aligned} \dot{\gamma} &= \lim_{\Delta r \to 0} \frac{v(r+\Delta r) - \Omega\Delta r - v(r)}{\Delta r} \\ &= \lim_{\Delta r \to 0} r\frac{\Delta\Omega}{\Delta r} = r\frac{d\Omega}{dr} . \end{aligned} \tag{9.118}$$

Similar considerations lead to expressions of shear rates in other geometries.

Drag Flow Rheometers

In this section we will discuss instruments with coaxial cylinders, coaxial plates, and coaxial cone and plate.

Coaxial Cylinders in Couette Flow: Rate of Shear. It was found before that the shear rate in a Couette instrument (Fig. 9.29) is equal to $\dot{\gamma} = r\,d\Omega/dr$. Because the gap is narrow, i. e., $(r_0 - r_i)/r \ll 1$, use can be made of the following approximation:

$$d\Omega/dr \approx \Delta\Omega/\Delta r = \Omega_0/(r_0 - r_i) ,$$

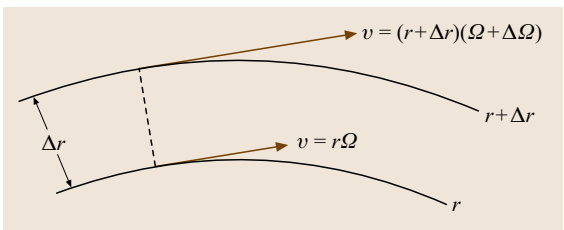

Fig. 9.28 Couette flow in a liquid shell

where $\Delta r = r_0 - r_i$ and $\Delta\Omega = \Omega(r_0) - \Omega(r_i) = \Omega_0$ so that we find for the shear rate

$$\dot{\gamma}_0 \approx r\frac{\Omega_0}{\Delta r} \approx \frac{r_0 + r_i}{2} \cdot \frac{\Omega_0}{\Delta r} = \frac{r_{av}}{\Delta r} \cdot \Omega_0 \tag{9.119}$$

with $r_{av} = (r_0 + r_i)/2$.

Hereafter it is assumed that Ω_0 is constant and thus $\dot{\gamma}$ does not depend on time.

It has to be mentioned that a still better approximation is

$$\dot{\gamma}(r) = \frac{\Omega_0}{r^2} \cdot \frac{r_0^2 r_i^2}{r_{av}\Delta r} . \tag{9.120}$$

It appears from these equations that the shear rate is practically constant in the gap.

Equations of Motion. For this instrument it follows from Fig. 9.29 that the 1-direction corresponds with the ϕ-direction, the 2-direction with the r-direction, and the 3-direction with the z-direction. We will make use of cylindrical coordinates. Many terms will vanish, because, as mentioned above: (a) in the stationary axisymmetric state there will be no ϕ dependence, so that $\partial/\partial\phi = 0$, and (b) $\sigma_{13} = \sigma_{31} = \sigma_{23} = \sigma_{32} = 0$, which in the present system means $\sigma_{\phi z} = \sigma_{z\phi} = \sigma_{rz} = \sigma_{zr} = 0$. Accordingly, from the equations of motion (9.108–9.110) with b_z being the acceleration due to gravity g, only the following terms remain:

$$\frac{\partial\sigma_{22}}{\partial r} - \frac{\sigma_{11} - \sigma_{22}}{r} = 0 \quad \text{or} \quad \frac{\partial\sigma_{22}}{\partial r} - \frac{N_1}{r} = 0 , \tag{9.121}$$

$$\frac{\partial\sigma_{21}}{\partial r} + \frac{2\sigma_{21}}{r} = 0 , \tag{9.122}$$

$$\frac{\partial\sigma_{33}}{\partial z} = -\rho g . \tag{9.123}$$

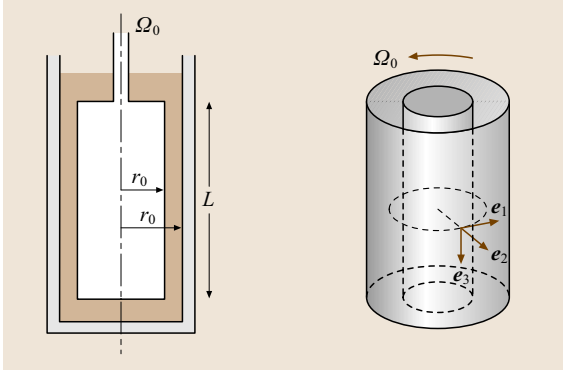

Fig. 9.29 Couette flow expressed in cylindrical coordinates, where $\boldsymbol{e}_1 = \boldsymbol{e}_\phi$, $\boldsymbol{e}_2 = \boldsymbol{e}_r$ and $\boldsymbol{e}_3 = \boldsymbol{e}_z$

Measurement of the First Normal Stress Difference. From (9.122) it follows that

$$r\frac{\partial\sigma_{22}}{\partial r} = \sigma_{11} - \sigma_{22} = N_1 \,. \tag{9.124}$$

In the narrow gap of the Couette instrument

$$\frac{\partial\sigma_{22}}{\partial r} \approx \frac{\Delta\sigma_{22}}{\Delta r} = \frac{\sigma_{22}(r_0) - \sigma_{22}(r_i)}{r_0 - r_i} \tag{9.125}$$

As a result we find

$$N_1 \approx \frac{\Delta\sigma_{22}}{\Delta r} r_{av} \,, \tag{9.126}$$

so that N_1 is practically constant and can be determined *easily* by measuring σ_{22} both on the outer and inner cylinder. Experimentally it has been found that: (a) $\sigma_{22}(r_0)$ and $\sigma_{22}(r_i)$ are negative (Fig. 9.30), and (b) $\Delta\sigma_{22}$ is positive. The important conclusion is that the first normal stress difference N_1 is positive.

For the first normal stress coefficient (Sect. 9.1) we obtain:

$$\Psi_1 \equiv \frac{\sigma_{11} - \sigma_{22}}{\dot\gamma_0^2} = \frac{N_1}{\dot\gamma_0^2} = \frac{\Delta\sigma_{22}}{\Omega_0^2} \cdot \frac{\Delta r}{r_{av}} \,, \tag{9.127}$$

where (9.119) has been used.

Local Stresses in Couette Flow. In the description of the measuring methods we have made use of the assumption that N_1, N_2, and σ_{21} are only dependent on the local value of the shear rate. This means that during the flow their values are independent of the curvature of the shearing planes and the streamlines, provided that the shear rate is constant in the gap. However, the values of σ_{11}, σ_{22}, and σ_{33} do depend on the curvature and even at constant shear rate they depend on their location in the flowing liquid. Such a situation is shown in Fig. 9.30 for Couette flow.

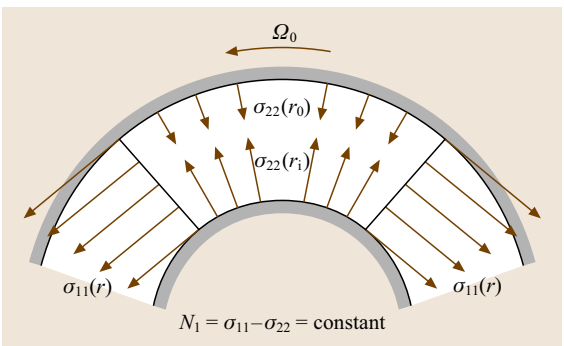

Fig. 9.30 Local stresses dependent on the position in the gap between two coaxial cylinders. Note that $\sigma_{22}(r_0)$ and $\sigma_{22}(r_i)$ are both pointing into the fluid, which means that both are negative normal stresses, and that $\sigma_{22}(r_i)$ is more negative than $\sigma_{22}(r_0)$, hence it follows that $\sigma_{22}(r_0) - \sigma_{22}(r_i) > 0$

The normal stresses σ_{11} and σ_{22} are not constant in the gap between the inner and outer cylinders, but it appears that at every point their difference $\sigma_{11} - \sigma_{22} = N_1$ is constant, independent of the location in the gap. In fact, in some cases we make use of the change of the stress components with the streamlines in order to determine N_1 and/or N_2 (Fig. 9.30). For example in a cone-and-plate instrument σ_{22} on the plate is a function of the distance to the cone axis and thus a function of the curvature of the streamlines, whereas in the present case the shear stress and the first normal stress differences are independent of this curvature.

Measurement of the Viscosity. Integration of (9.122) yields

$$r^2\sigma_{21} = \beta = \text{constant} \,. \tag{9.128}$$

The moment of the shear force acting on a fluid cylinder in the gap ($r_i \le r \le r_0$), with respect to the cylinder axis reads

$$T_M(r) = Fr = \sigma_{21} 2\pi r L r = 2\pi\beta L \,. \tag{9.129}$$

The important conclusion is that T_M is independent of position in the liquid and thus T_M is also equal to the moment on the inner cylinder, which can be measured. The general result is

$$\frac{T_M}{2\pi L} = \beta = r^2\sigma_{21} = r^2\eta\dot\gamma \tag{9.130}$$

so that

$$\eta(\dot\gamma) \equiv \frac{\sigma_{21}}{\dot\gamma} = \frac{T_M}{4\pi\Omega_0 L}\frac{r_0^2 - r_i^2}{r_0^2 r_i^2} \,, \tag{9.131}$$

where use has been made of (9.120).

Hence, by control of the angular velocity of the outer cylinder and by measuring the momentum on the inner cylinder the viscosity can be determined as a function of the shear rate.

The Parallel-Plate Instrument in Torsional Flow

In this instrument the gap, of thickness z_0, between two circular, parallel plates is filled with the liquid under investigation (Fig. 9.31). The lower plate is fixed and the upper plate rotates with an angular velocity Ω_0 around the vertical axis CC' through both mid points.

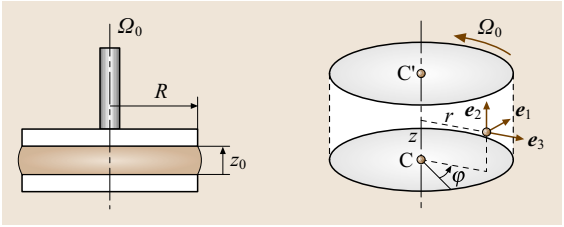

Fig. 9.31 Parallel plates with cylindrical coordinate system ϕ, z, r, with $\boldsymbol{e}_1 = \boldsymbol{e}_\phi$, $\boldsymbol{e}_2 = \boldsymbol{e}_z$ and $\boldsymbol{e}_3 = \boldsymbol{e}_r$

We consider the rotation as anticlockwise if observed from above.

The velocity is directed along the tangents on the circular streamlines, hence the ϕ-direction is the 1-direction; the 2-direction is the direction in which the velocity of the shearing planes increases, i. e., the z-direction ($z = 0$ on the bottom plate and $z = z_0$ on the upper plate). The 3-direction, i. e., the r-direction, completes a right-handed coordinate system ($r = 0$ at the axis and $r = R$ at the outer edge of the boundary). The effect of the outer boundary is neglected, which is possible if $z_0 \ll R$.

Rate of Shear. The shear rate is found to be

$$\dot{\gamma} = \lim_{\Delta z \to 0} \frac{r\Omega(z+\Delta z) - r\Omega(z)}{\Delta z} = r\frac{\mathrm{d}\Omega}{\mathrm{d}z} \,. \qquad (9.132)$$

The shear rate is not constant in the gap: it increases from $\dot{\gamma} = 0$ on the axis to $\dot{\gamma}(R) = \Omega_0/z_0$ at the outer boundary. This is a big disadvantage of the parallel-plate instrument: it can be used properly only in the range where the viscoelastic properties are not shear rate dependent. In general the instrument is used only for oscillatory measurements with small amplitudes. It will be shown however, how to overcome these disadvantages.

Equations of Motion. The equations of motion in cylindrical coordinates are

$$\frac{\partial \sigma_{33}}{\partial r} = \frac{N_1 + N_2}{r} \,, \qquad (9.133)$$

$$\frac{\partial \sigma_{12}}{\partial z} = 0 \,, \qquad (9.134)$$

$$\frac{\partial \sigma_{22}}{\partial z} = -\rho b_z = \rho g \,. \qquad (9.135)$$

It can be proven, with the aid of (9.134), that the shear rate only depends on r and not on z. The result is

$$\dot{\gamma}(r) = r\frac{\mathrm{d}\Omega}{\mathrm{d}z} = r\frac{\Omega_0}{z_0} \qquad (9.136)$$

so that the shear rate appears to increase linearly with distance from the axis.

Determination of the Viscosity η and $\Psi_1 - \Psi_2$ as Functions of the Rate of Shear. If the viscosity is shear rate dependent, it seems impossible to determine the *real* viscosity. The same holds for the difference of the first and second normal stress coefficients $\Psi_1 - \Psi_2$, where

$$\Psi_1 = (\sigma_{11} - \sigma_{22})/\dot{\gamma}^2 \,, \quad \Psi_2 = (\sigma_{22} - \sigma_{33})/\dot{\gamma}^2 \,.$$

However it can be proven that the viscosity and the difference of the first and second normal stress coefficients can be determined as functions of shear rate in a proper way, by measuring the moment T_M exerted by the flowing liquid on the upper plate, and the normal force F_n exerted by the flowing liquid on the upper plate, both as functions of the angular velocity Ω_0. This yields a method to determine σ_{21} and $N_1 - N_2$, both as functions of the shear rate $\dot{\gamma}_\mathrm{R} = \dot{\gamma}$ at $r = R$:

$$\sigma_{21}(\dot{\gamma}_\mathrm{R}) = \frac{T_\mathrm{M}}{2\pi R^3}\left(3 + \frac{\mathrm{d}\log T_\mathrm{M}}{\mathrm{d}\log \Omega_0}\right) \qquad (9.137)$$

and

$$N_1(\dot{\gamma}_\mathrm{R}) - N_2(\dot{\gamma}_\mathrm{R}) = \frac{F_\mathrm{n}}{\pi R^2}\left(2 + \frac{\mathrm{d}\log F_\mathrm{n}}{\mathrm{d}\log \Omega_0}\right) \,. \qquad (9.138)$$

Hence, upon plotting T_M and F_n as functions of Ω_0 on double logarithmic scales, the $\dot{\gamma}_\mathrm{R}$ dependent slopes $d\log T_\mathrm{M}/d\log \Omega_0$ and $d\log F_\mathrm{M}/d\log \Omega_0$ can be determined and thus σ_{21} and $N_1 - N_2$ can be determined as functions of $\dot{\gamma}_\mathrm{R}$, and accordingly also the viscosity $\eta = \sigma_{21}/\dot{\gamma}$ and the difference between the first and second normal stress coefficients $\Psi_1 - \Psi_2 = (N_1 - N_2)/\dot{\gamma}^2$.

The Cone-and-Plate Instrument

In a cone-and-plate instrument the liquid under investigation is present in the gap between a cone with a large top angle (at least 170°) and a circular plate. The top of the cone, whose axis is perpendicular to the plate, is in principle positioned in the central point of the plate. In order to prevent friction between cone and plate during rotation of the cone, the top of the cone is truncated with the virtual, fictitious top corresponding to the plate center. The angle between the cone and plate, $\Delta\Theta$, is small (less than 5°). The cone rotates at an angular velocity of Ω_0, and counterclockwise when seen from above (Fig. 9.32). The shearing planes, the planes that rotate stiffly with a rate increasing from the plate to the cone itself, are coaxial cones with top angles between π and $\pi - 2\Delta\Theta$ rad. The 1-direction is the indifferent

ϕ-direction, in the 2-direction the rotational velocity of the shearing planes increases, i. e., the θ-direction, and the 3-direction is the r-direction.

Rate of Shear. The shear rate can be calculated, in a quite complicated way. The result is

$$\dot{\gamma}_0 = \sin\theta \frac{\mathrm{d}\Omega}{\mathrm{d}\theta} \approx \frac{\Omega_0}{\Delta\Theta} \,. \tag{9.139}$$

This means that the shear rate is almost constant in the sample under investigation ($\sin\theta$ varies approximately from 1 to 0.996). This makes the cone-and-plate instrument highly suitable for the determination of the viscosity and the normal stress coefficients as functions of shear rate.

Equations of Motion. The equations of motion in spherical coordinates can also be simplified in this case. The result, following (9.111–9.113), is:

$$\frac{\partial\sigma_{33}}{\partial r} - \frac{N_1 + 2N_2}{r} = -\rho g \cos\theta \,, \tag{9.140}$$

$$\frac{1}{r}\frac{\partial\sigma_{22}}{\partial\theta} - \frac{N_1}{r}\cot\theta = \rho g \sin\theta \,, \tag{9.141}$$

$$\frac{1}{r}\frac{\partial\sigma_{21}}{\partial\theta} + \frac{2\sigma_{21}}{r}\cot\theta = 0 \,. \tag{9.142}$$

Viscosity Measurement. Integration of (9.142) yields $\sigma_{21}(\theta) = \text{constant} = \sigma_{21}(1/2\,\pi) = C$, i. e., the shear stress on the plate. As a result, the moment T_M on the plate is

$$T_\mathrm{M} = \int_0^R r\sigma_{21}\left(\frac{\pi}{2}\right) 2\pi r \mathrm{d}r = \frac{2\pi}{3} C R^3 \quad \text{so that}$$

$$\sigma_{21} = \frac{3T_\mathrm{M}}{2\pi R^3} \,. \tag{9.143}$$

For the viscosity we now find with the aid of (9.139)

$$\eta \equiv \frac{\sigma_{21}}{\dot{\gamma}_0} = \frac{3T_\mathrm{M}}{2\pi\dot{\gamma}_0 R^3} \approx \frac{3T_\mathrm{M}\Delta\Theta}{2\pi R^3 \Omega_0} \,. \tag{9.144}$$

Hence by measuring T_M as a function of Ω_0, the viscosity can be determined as a function of shear rate.

One remark has to be made, however. Equation (9.142) follows from (9.112) with the assumption that $\sigma_{\phi\theta}$ (i. e., σ_{12}) $= \sigma_{\theta\phi}$ (i. e., σ_{21}), which in general holds for polymeric systems, but not for systems such as low-molecular-weight liquid crystals. Hence, one has to be careful in the determination of the viscosity of low-molecular-weight liquid crystals in the cone-and-plate instrument. For liquid-crystal polymers, however, the polymeric nature overrules the liquid-crystalline behavior, so that the cone-and-plate instrument can also be used to determine their viscosity.

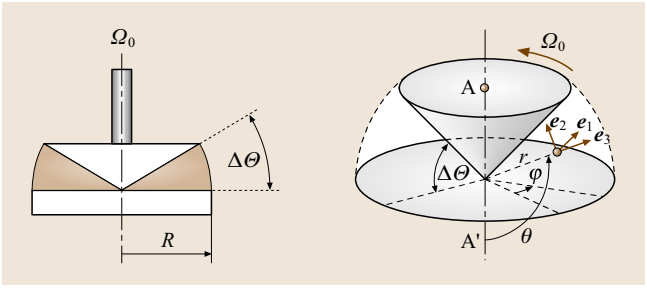

Fig. 9.32 Cone-and-plate instrument with spherical coordinates ϕ, θ, r, with $\boldsymbol{e}_1 = \boldsymbol{e}_\phi$, $\boldsymbol{e}_2 = \boldsymbol{e}_\theta$ and $\boldsymbol{e}_3 = \boldsymbol{e}_r$

Measurement of Normal Stress Differences: $N_1 + 2N_2$. Because $\cos\theta$ is approximately equal to 0, (9.140) may be approximated by

$$r\frac{\partial\sigma_{33}}{\partial r} = N_1 + 2N_2 \,. \tag{9.145}$$

The equation is only correct on the plate ($\theta = \pi/2$). Because $\sigma_{22} - \sigma_{33}$ is a function of $\dot{\gamma}$ and $\dot{\gamma}$ is not a function of r, in (9.145) $\partial\sigma_{33}/\partial r$ may be replaced by $\partial\sigma_{22}/\partial r$. Integration then eventually yields

$$\sigma_{22}(r) = \sigma_{22}(R) + (N_1 + 2N_2)\ln(r/R) \,. \tag{9.146}$$

(N.B. the fact that $\sigma_{11} - \sigma_{22}$ is a function of $\dot{\gamma}$ and thus not a function of on r, has also been used).

From this equation it follows that, upon plotting $\sigma_{22}(r)$ versus $\ln(r/R)$, a straight line will be obtained

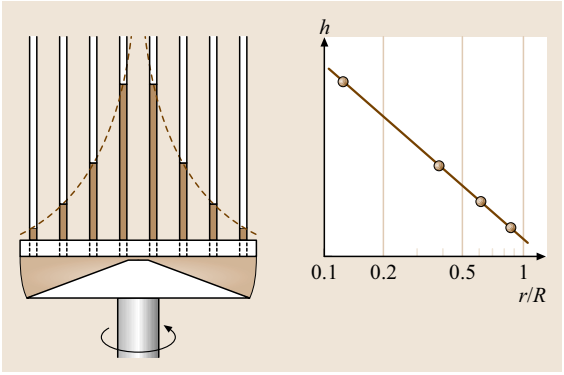

Fig. 9.33 *Left*: cone-and-plate instrument supplied with tubes for the measurement of the normal stress $\sigma_{22}(r)$ as a function of the distance to the axis. Note that the normal stress σ_{22} is negative and equal to $-\rho g h$. *Right*: height of the liquid in the tubes plotted versus $\ln(r/R)$

with a slope equal to $N_1 + 2N_2$. This normal stress $\sigma_{22}(r)$ can be measured as a function of r with pressure gauges positioned at various places on the plate (Fig. 9.33). The method with tubes mounted on the plate is only appropriate for liquids with a low viscosity, which can ascend the tubes within a reasonable time. For more-viscous liquids real pressure gauges are needed. In the figure shown the normal stresses σ_{22} are negative, because a stress is positive if the surroundings pull on the material. In this case the liquid columns push on the liquid in the gap, so that the normal stresses are negative. The slope is negative, in agreement with the observation that N_1 is positive for polymer fluids in general, whereas N_2 is in general negative and absolutely only a small fraction of N_1. In Fig. 9.34 results are shown for a 2% solution of polyisobutylene. This demonstrates that $N_1 + 2N_2$ increases with increasing shear rate. Division by $\dot{\gamma}_0^2$ yields the sum $\Psi_1 + 2\Psi_2$, which appears to be constant, independent of the shear rate.

It has to be mentioned that the device shown in Fig. 9.32, which is inverted with respect to Fig. 9.31, would result in a term $+g\cos\theta$ instead of $-\rho g\cos\theta$ in (9.140). However, because $\cos\theta$ is approximately equal to 0, we can make use of (9.140), which leads to (9.145).

The First Normal Stress Difference. The total force exerted by the flowing fluid on the plate is equal to

$$F_n = -\int_0^R \sigma_{22}(r) 2\pi r \, dr \, . \qquad (9.147)$$

Integration eventually yields

$$N_1 = \frac{2F_n}{\pi R^2} \, . \qquad (9.148)$$

In the derivation of (9.148) it is assumed that the free surface of the sample is spherical. In that case there are no surface stress components present, so that the term $\sigma_{33}(R)$ that arises in the integration of (9.147), is equal to 0.

Hence, by measuring the total normal force exerted by the flowing liquid on the plate as a function of shear rate the first normal stress difference N_1 and thus the first normal stress coefficient $\Psi_1 = N_1/\dot{\gamma}^2$ can be determined as a function of the shear rate.

The method presented before yields the value of $N_1 + 2N_2$, so that it is now also possible to determine the second normal stress difference N_2 and thus the second normal stress coefficient $\Psi_2 = N_2/\dot{\gamma}^2$.

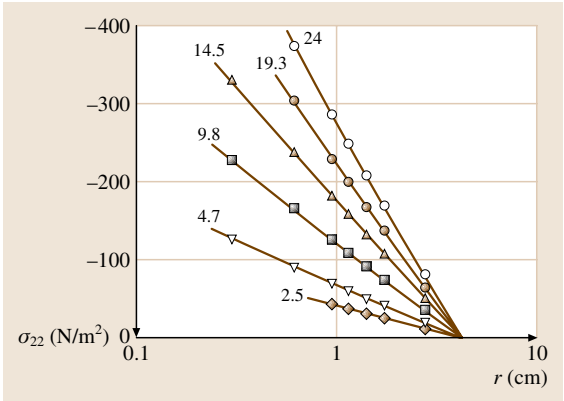

Fig. 9.34 Normal stresses $\sigma_{22}(r)$ on the plate in a cone and plate instrument ($R = 4.4$ cm), versus distance to the axis, during shear flow of a 2% solution of polyisobutylene (B200) in oppanol B1 (a Newtonian liquid with $\eta = 23.6$ mPas at 25 °C), measured at various shear rates, as indicated in s^{-1} accoreding to [9.7]

Hole Effect in the Measurement of Normal Stresses

It is worthwhile mentioning here the so-called *hole effect*. For the measurement of normal stresses use is made of pressure gauges. In general they are mounted in the walls of the instrument. The disadvantage of this is that holes are needed for these, and in the neighborhood of a hole the streamlines will be curved in the direction of the hole. This causes an extra force due to the tension in the streamlines caused by the elasticity of the fluid. The hole pressure is the difference between the pressure that would exist at the wall if the flow were undisturbed and the measured pressure at the bottom of the hole (Fig. 9.35). Theoretically it can be shown that for a circular opening this error is:

$$\Delta P = P - P_{hole} = C_1 N_1 + C_2 N_2 \quad \text{where}$$
$$C_1 \approx 0.25 \quad \text{and} \quad C_2 \ll C_1 \, . \qquad (9.149)$$

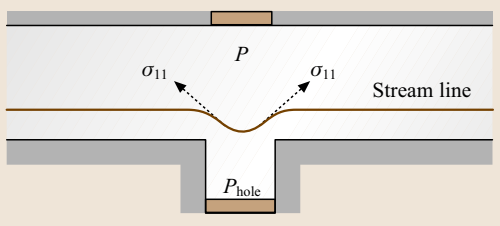

Fig. 9.35 The hole effect in viscoelastic fluids

Pressure-Driven Rheometers

In a pressure-driven rheometer the fluid is pressed from a reservoir into a capillary tube of circular cross section or into a gap of rectangular cross section (Fig. 9.36) and Fig. 9.42, respectively. The pressure drop and flow rate through this tube or gap are used to determine the viscosity. In contrast to drag flows there is an entrance region where the fluid is accelerated and an exit region where a viscoelastic fluid is liable to die swell. For such rheometers the important assumptions in the derivation of the relation between shear stress and shear rate are fully developed steady and laminar flow with no slip at the walls (i. e., $v_w = 0$).

The Capillary Rheometer. In a capillary rheometer the liquid under investigation flows through a straight tube with a circular cross section with radius R. The shear planes are coaxial cylinders with radius r. The velocity is constant in a cylindrical shear plane and decreases from the axis to the wall (for this reason this kind of flow is sometimes called telescopic flow). The streamlines are parallel with the axis and the flow is rectilinear (Fig. 9.37). The z-direction is the 1-direction, the r-direction is the 2-direction (in this case the direction where the rate of the shear planes decreases), and the ϕ-direction is the 3-direction.

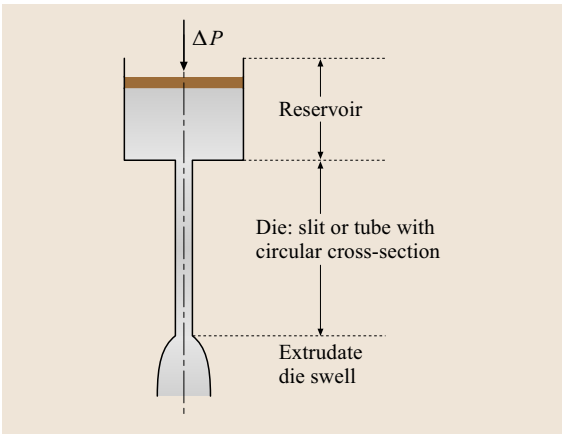

Fig. 9.36 Pressure-driven rheometer

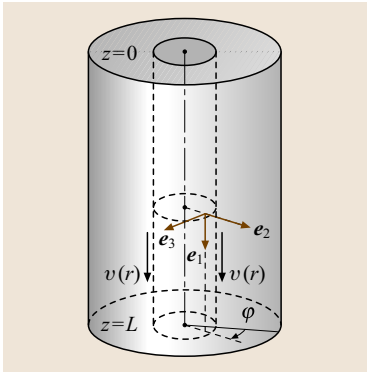

Fig. 9.37 Cylindrical coordinate system z, r, ϕ in a capillary rheometer with $\boldsymbol{e}_1 = \boldsymbol{e}_z$, $\boldsymbol{e}_2 = \boldsymbol{e}_r$ and $\boldsymbol{e}_3 = \boldsymbol{e}_\phi$

Rate of Shear. The flow is rectilinear, so that the shear rate is given by

$$\dot{\gamma} = \dot{\gamma}(r) = \lim_{\Delta r \to 0} \frac{v(r+\Delta r) - v(r)}{\Delta r} = \frac{\mathrm{d}v}{\mathrm{d}r} \leq 0 \,. \tag{9.150}$$

Equations of Motion. The equations of motion in cylindrical coordinates obtained from (9.108–9.110) are

$$\frac{\partial \sigma_{22}}{\partial r} + \frac{\partial \sigma_{21}}{\partial z} + \frac{N_2}{r} = 0 \,, \tag{9.151}$$

$$\frac{\partial \sigma_{21}}{\partial r} + \frac{\partial \sigma_{11}}{\partial z} + \frac{\sigma_{21}}{r} = -\rho b_z \,, \tag{9.152}$$

(the third equation of motion yields the identity $0 = 0$).

Because σ_{21} is a function of $\dot{\gamma}$ and $\dot{\gamma}$ is not a function of z, it follows that $\partial \sigma_{21}/\partial z = 0$. However, this is only true far enough from the entrance of the capillary. If we neglect the entrance effect, both equations can be simplified to

$$\frac{\partial \sigma_{22}}{\partial r} + \frac{N_2}{r} = 0 \,, \tag{9.153}$$

$$\frac{\partial \sigma_{11}}{\partial z} + \frac{1}{r}\frac{\mathrm{d}\,(r\sigma_{21})}{\mathrm{d}r} = -\rho b_z \,. \tag{9.154}$$

Integration of (9.154), and bearing in mind that $\partial \sigma_{11}/\partial z = \text{constant}$, yields

$$\sigma_{21}(r) = -\frac{1}{2} r \left(\rho b_z + \frac{\partial \sigma_{11}}{\partial z} \right) \,. \tag{9.155}$$

Two cases can be distinguished:

a) $\partial \sigma_{11}/\partial z$ is determined by gravitational forces and is comparable to ρg: the vertical viscometer for dilute solutions, e.g., the Ubbelohde viscometer, which is a subject of discussion in the Chapter on viscosity measurements in Newtonian liquids Sect. 3.4.4.

b) $|\partial \sigma_{11}/\partial z| \gg \rho g$: the rheometer for polymer melts, where $\partial \sigma_{11}/\partial z$ is significant and determined by an imposed pressure ΔP, which is the subject of the present discussion.

The Capillary Rheometer for Polymer Melts. In this case a high pressure ΔP is applied, so that the gravitational

forces can be neglected. This means that $\sigma_{11}(0) = -\Delta P$ and $\sigma_{11}(L) = 0$, so that:

$$\frac{\partial \sigma_{11}}{\partial z} = \frac{\sigma_{11}(z=L) - \sigma_{11}(z=0)}{L} = \frac{\Delta P}{L} \,. \quad (9.156)$$

Because $\Delta P/L \gg \rho b_z$, it follows from (9.155)

$$\sigma \equiv \sigma(r) = -\frac{r\Delta P}{2L} < 0 \,. \quad (9.157)$$

Again the shear stress is a linear function of r (independent of the viscosity), and maximal at the wall

$$\sigma_w \equiv \sigma_{21}(R) = -\frac{R\Delta P}{2L} \quad (9.158)$$

and zero on the axis, so that

$$\frac{\sigma}{\sigma_w} = \frac{\sigma_{21}(r)}{\sigma_{21}(R)} = \frac{r}{R} \,. \quad (9.159)$$

Velocity Profile. For *Newtonian liquids* we have

$$\eta = \frac{\sigma_{21}}{\dot\gamma} = -\frac{r\Delta P}{2L\,(\mathrm{d}v/\mathrm{d}r)} \,. \quad (9.160)$$

Integrating yields the velocity profile

$$v(r) = \frac{\Delta P}{4\eta L}\left(R^2 - r^2\right) \,. \quad (9.161)$$

Hence, for Newtonian liquids this velocity profile is parabolic and the flow is called Poiseuille flow. In Fig. 9.38 the velocity and the shear stress profiles are shown for Poiseuille flow. Note that the shear stress is negative: the wall pulls on the flowing liquid and liquid cylinders pull on the neighboring cylinders closer to the axis.

For a *power-law fluid*, the Ostwald–de Waele power-law constitutive equation holds:

$$\sigma = K\dot\gamma^n \quad \text{and} \quad \eta = K\dot\gamma^{n-1} \,, \quad (9.162)$$

where n is the so-called power-law index and K is the consistency index. Then

$$\eta(\dot\gamma) = \frac{\sigma_{21}}{\dot\gamma} = -\frac{r\Delta P}{2L\,(\mathrm{d}v/\mathrm{d}r)} = K\left(\frac{\mathrm{d}v}{\mathrm{d}r}\right)^{n-1} \,. \quad (9.163)$$

Integrating the latter, we obtain the velocity profile

$$v(r) = \left(\frac{\Delta P}{2KL}\right)^{1/n} \frac{n}{n+1}\left(R^{1+1/n} - r^{1+1/n}\right) \,. \quad (9.164)$$

The average velocity is

$$\langle v\rangle \equiv \frac{\int_0^R 2\pi r v(r)\,\mathrm{d}r}{\int_0^R 2\pi r\,\mathrm{d}r} = \left(\frac{\Delta P}{2KL}\right)^{1/n} \frac{n}{3n+1} R^{1+1/n} \quad (9.165)$$

and the normalized velocity profile is

$$v_{rel}(r) \equiv \frac{v(r)}{\langle v\rangle} = \frac{3n+1}{n+1}\left[1 - \left(\frac{r}{R}\right)^{1+1/n}\right] \,. \quad (9.166)$$

Note that for $n = 1$ the Poiseuille profile for Newtonian liquids is recovered.

In Fig. 9.39 the relative velocity profiles are shown for a Newtonian liquid ($n = 1$), for a power-law liquid with $n = 1/3$, and for plug flow ($n = 0.001$). The maximum velocities on the axis are 2, 3/2, and 1, respectively.

Shear Rate at the Wall, the Rabinowitch Equation. Because the shear rate is a function of r, it seems impossible to determine the viscosity as a function of shear rate for non-Newtonian fluids. This problem can be overcome, however, in the following way. The volume flow rate Q (in m^3/s) of a liquid flowing through the tube in unit

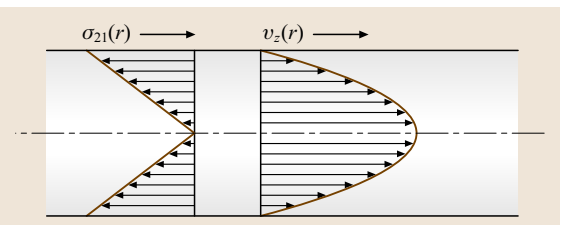

Fig. 9.38 Velocity and stress profiles for Poiseuille flow (i. e., for a liquid of constant viscosity) in straight tubes with circular cross-section: the velocity profile is parabolic and the shear stress profile is linear

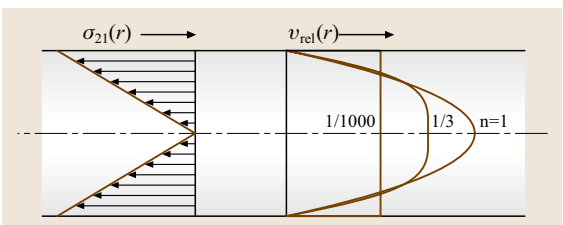

Fig. 9.39 Velocity profile in a straight tube with circular cross section, for power-law fluids with $n = 1$ (Newtonian liquid, Poiseuille flow), $n = 1/3$ and for $n = 0.001$ (plug flow)

time is

$$Q = \int_0^R v(r) \cdot 2\pi r \, dr \, . \tag{9.167}$$

If there is no slip at the wall, integration by parts yields

$$Q = -\int_0^R \pi r^2 \dot{\gamma}(r) \, dr \, . \tag{9.168}$$

It is quite easy to derive that for Newtonian liquids the relationship between the shear rate at the wall and Q is

$$\Gamma \equiv \dot{\gamma}_w = -\frac{4Q}{\pi R^3} \, . \tag{9.169}$$

If for non-Newtonian fluids we define the apparent shear rate at the wall as

$$\Gamma_a \equiv -\frac{4Q}{\pi R^3} \tag{9.170}$$

then the relationship between the shear rate at the wall and the volume flow rate can be derived as

$$\begin{aligned} \dot{\gamma}_w &= \frac{1}{4}\Gamma_a \left(3 + \frac{d \log |\Gamma_a|}{d \log |\sigma_w|}\right) \\ &= -\frac{Q}{\pi R^3}\left(3 + \frac{d \log Q}{d \log \Delta P}\right) \, . \end{aligned} \tag{9.171}$$

Equation (9.171) is called the *Rabinowitch equation* already derived in 1929 (see Tadmor and Gogos in Furthter Reading) for flow of a liquid through a straight tube with a circular cross section. This shows that the shear rate at the wall follows from the volume flow rate and from the slope of the volume flow rate Q versus the imposed pressure ΔP. Upon plotting $\log Q$ versus $\log \Delta P$, the slope can be found for every value of ΔP and/or Q. For Newtonian liquids the line obtained is a straight line with a slope of 1. On the other hand, for shear thinning pseudoplastic fluids with $n < 1$ a line is obtained with an increasing slope larger than 1. For dilatant shear thickening fluids with $n > 1$ a straight line with slope less than 1 is obtained (Fig. 9.40). In general, as it is easy to see from (9.171), since a simple derivation for the power-law liquids yields

$$\dot{\gamma}_w = -\frac{Q}{\pi R^3}\left(3 + \frac{1}{n}\right) \, . \tag{9.172}$$

For a slit rheometer of rectangular cross section, with length L and sides W and H, where $L \gg W \gg H$ (Fig. 9.41) the shear rate at the wall is found to be:

$$\begin{aligned} \dot{\gamma}_w &= \frac{1}{3}\Gamma_a \left(2 + \frac{d \log |\Gamma_a|}{d \log |\sigma_w|}\right) \\ &= -\frac{2Q}{WH^2}\left(2 + \frac{d \log Q}{d \log \Delta P}\right) \quad \text{where} \\ \Gamma_a &\equiv -\frac{6Q}{WH^2} \, . \end{aligned} \tag{9.173}$$

Measurement of the sum $2N_1 + N_2$ and of N_1. The measurements of the volume flow (or of the volumetric flow rate) may be completed with measurements of the total force F at the exit of the capillary, exerted by the fluid on the tube in the direction parallel to the axis. This force is equal to the difference in momentum of the fluid thread just before and after the exit. For molten polymers this difference is almost equal to zero. This yields an expression for $2N_1 + N_2$ at the wall of the capillary.

The mentioned force F is given by the integral of the normal stress $\sigma_{11}(r)$ over the surface:

$$F = -\int_0^R 2\pi r \sigma_{11}(r) \, dr \, . \tag{9.174}$$

This integral can be evaluated, yielding an expression for $2N_{1,w} + N_{2,w}$:

$$\begin{aligned} 2N_{1,w} + N_{2,w} = &-\frac{F + \pi R^2 \sigma_{22}(R, L)}{\pi R^2} \\ &\times \left(2 + \frac{d \log \left|F + \pi R^2 \sigma_{22}(R, L)\right|}{d \log |\sigma_w|}\right) \, , \end{aligned} \tag{9.175}$$

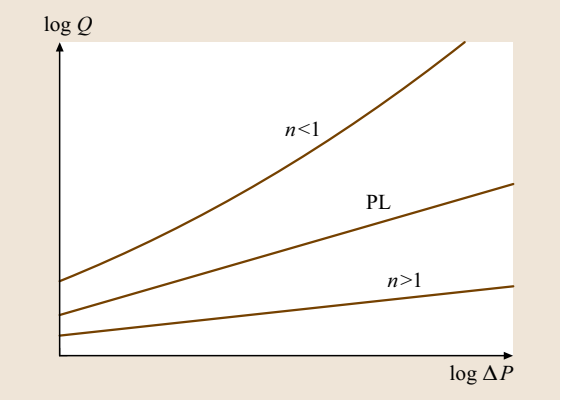

Fig. 9.40 Plot for the determination of $\dot{\gamma}_w$ for a Newtonian fluid (slope 1; denoted PL, Poiseuille); pseudoplastic shear thinning fluid (slope increasing and > 1), and dilatant shear thickening fluid (slope decreasing and < 1)

Table 9.4 Survey of possible outcomes of measurement techniques. [a] means that these measurements are not easy and in general not possible in commercially available instruments

Instrument	Shear rate	Viscosity	Normal stress differences/coefficients		
Couette	$\dot{\gamma} \approx$ const.	$\eta(\dot{\gamma})$	$N_1(\dot{\gamma})$	$\Psi_1(\dot{\gamma})$	[a]
Parallel plates	$\dot{\gamma} = \dot{\gamma}(r)$	$\eta(\dot{\gamma}_R)$	$N_1(\dot{\gamma}_R) - N_2(\dot{\gamma}_R)$	$\Psi_1(\dot{\gamma}_R) - \Psi_2(\dot{\gamma}_R)$	
Cone and plate	$\dot{\gamma} =$ const.	$\eta(\dot{\gamma})$	$N_1(\dot{\gamma})$	$\Psi_1(\dot{\gamma})$	
			$N_1(\dot{\gamma}) + N_2(\dot{\gamma})$	$\Psi_1(\dot{\gamma}) + \Psi_2(\dot{\gamma})$	[a]
Capillary rheometer	$\dot{\gamma} = \dot{\gamma}(r)$	$\eta(\dot{\gamma}_w)$	$2N_1(\dot{\gamma}_w) + N_2(\dot{\gamma}_w)$	$2\Psi_1(\dot{\gamma}_w) + \Psi_2(\dot{\gamma}_w)$	[a]
Slit rheometer	$\dot{\gamma} = \dot{\gamma}(h)$	$\eta(\dot{\gamma}_w)$	$N_1(\dot{\gamma}_w)$	$\Psi_1(\dot{\gamma}_w)$	

where $\sigma_{22}(R, L)$ is the normal pressure at the wall just before the exit, which can be measured. The force F can be calculated as the difference in momentum flux of the flowing fluid just before and after the exit:

$$F = \rho \int_0^R 2\pi r v_r^2(r)\,\mathrm{d}r - \pi R_s^2 \rho v_s^2 \,, \tag{9.176}$$

where v_s and R_s are the velocity and radius of the fluid thread after the exit, respectively ($R_s > R$ due to die swell, which causes the change in the momentum flux). From (9.175) it follows that, upon plotting $\log\left|F + \pi R^2 \sigma_{22}(R)\right|$ versus $\log|\sigma_w|$, the sum $2N_{1,w} + N_{2,w}$ can be determined and thus $2\Psi_{1,w} + \Psi_{2,w}$ as a function of $\dot{\gamma}_w$.

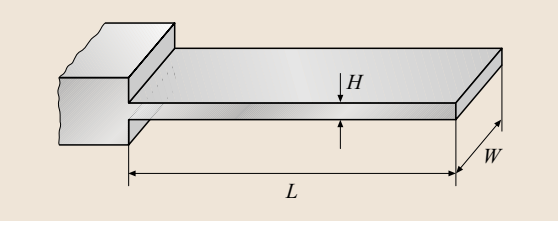

Fig. 9.41 Slit flow geometry, with $L \gg W \gg H$

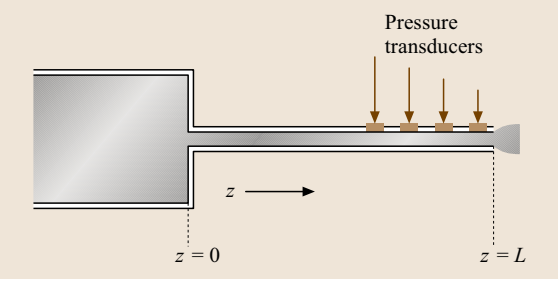

Fig. 9.42 Schematic representation of the extrapolation procedure to determine the exit wall pressure in a slit rheometer

If it is assumed that $F \ll \pi R^2 \sigma_{22}(R)$ (9.175) can be reduced to:

$$\begin{aligned} 2N_{1,w} + N_{2,w} &= P_e \left(2 + \frac{\mathrm{d}\log P_e}{\mathrm{d}\log|\sigma_w|}\right) \\ &= P_e \left(2 + \frac{\mathrm{d}\log P_e}{\mathrm{d}\log \Delta P}\right) \,, \end{aligned} \tag{9.177}$$

where $P_e = P(R, L) = -\sigma_{22}(R, L)$ is the exit pressure exerted by the flowing fluid on the wall of the capillary.

For *slit rheometers* the corresponding equation reads:

$$\begin{aligned} N_{1,w} &= P_e \left(1 + \frac{\mathrm{d}\log P_e}{\mathrm{d}\log|\sigma_w|}\right) \\ &= P_e \left(1 + \frac{\mathrm{d}\log P_e}{\mathrm{d}\log \Delta P}\right) \,. \end{aligned} \tag{9.178}$$

Of course it is difficult to really measure the wall pressure at the exit. For this reason wall pressures at different distances z are measured and the results are extrapolated to the exit $z = L$ (Fig. 9.42). It will be clear that measuring the wall pressure $P(z, R)$ is easier in slit rheometers than in capillary rheometers.

Conclusions Concerning the Discussed Rheogoniometers

In Table 9.1 a survey is shown of the possible results of the discussed measuring techniques. The italics in the Table mean that these properties can be measured in principle, but more-sophisticated instruments are needed than are available from manufacturers.

9.1.3 Elongational Flows

Most industrial processing of polymeric materials involves a combination of shear and extensional flow. The larger strains experienced in extensional flow fields can result in highly non-Newtonian dependencies on both strain and strain rate. As these dependencies are usually inadequately described by shear characterization alone,

extensive research has been conducted in the past several decades in an attempt to understand the extensional flow behavior of polymers. This research has involved a parallel effort in developing the theory of extensional flow behavior in order to determine the critical parameters and desired flow kinematics, and the experimental design of extensional rheometers that will successfully impose these kinematics.

In this Section, we discuss the current state of understanding of extensional rheology for highly viscous polymeric materials, such as polymer melts, and for low to moderately viscous materials. The state of the art in extensional rheometer design is discussed, and examples of commercially available instrumentation are presented.

List of Symbols

η: shear viscosity
η_E^+: extensional viscosity
η_E: steady-state extensional viscosity
η_{app}: apparent extensional viscosity
ε: Hencky strain
$\dot{\varepsilon}$: uniaxial strain rate
$\dot{\varepsilon}_{eff}$: effective strain rate, computed from diameter measurement
$\dot{\varepsilon}_0$: idealized strain rate
R_m: midpoint filament radius
D_m: midpoint filament diameter
D_0: initial midpoint filament diameter
L: filament length
F: tensile force
λ: longest relaxation time (Zimm)
σ: surface tension
g: gravitational constant
t: time
Tr: Trouton ratio $= \eta_E/\eta$
De: Deborah number $= \lambda\dot{\varepsilon}$
Ca: Capillary number $= \eta\dot{\varepsilon}_0 D_0/2\sigma$
Bo: Bond number $= \rho g D_0^2/4\sigma$
Ec: Elastocapillary number $=$ De/Ca

Industrial processing of polymer solutions and melts is usually a combination of shearing and extensional kinematics. Consequently, rheological characterization of materials in both a shear and an extensional flow field is necessary to accurately mathematically model these materials, detect subtle dissimilarities in composition, and to predict the processing conditions that will optimize the properties of the final product.

In most industrial processes, manufacturers desire to maximize line or web speed without compromising material properties. The shear rheological response of a complex fluid such as a polymer solution or melt that is going to be fiber-spun, blow-molded, calendared, foamed, deposited from a gun, or injected into a die or mold, will not correctly predict the processing behavior of these materials in these flow fields, which are dominated by a significant component of extensional strain. The nonlinear behavior of polymeric materials makes inference of their extensional properties from shear properties challenging, if not impossible. It is necessary to perform extensional rheology tests in addition to shear rheology to achieve a reliable characterization of the material.

Despite the recognized need for extensional measurements of polymeric fluids and melts, the development of instrumentation has proceeded slowly due to several challenges. The principal challenge is to generate a homogeneous extensional flow. To impose a deformation on a fluid, it is typically necessary to place the material in contact with a solid surface. Flow over a surface, however, will result in a shear stress, which will corrupt the extensional flow field and the resultant interpretation of the data. Thus, the flow cannot be confined, and must involve deformation in air or a sufficiently low-viscosity outer fluid.

The second challenge is that the strain history must also be known for all the fluid elements in the flow field. Strain rates must be high enough to stretch the chains (see Deborah number) and the strain high enough to stretch the chains beyond their normal radius of gyration. The high levels of strain required to achieve significant polymer chain extension and the increase in stress that ensues necessitates motion control systems with a large dynamic velocity range, a large achievable travel distance, and sensitive position control.

The large range of viscosities exhibited by polymeric materials has segregated individual extensional rheometer designs into distinct designs that are suited to a particular viscosity range, as shown in Table 9.5. High-viscosity materials (with zero-shear viscosity $\eta_0 > 1000$ Pa s) are best characterized by constant-length devices, or by constant-volume devices employing an outer fluid neutral buoyancy. Materials in the medium viscosity range of 1–1000 Pas are best characterized by filament stretching extensional rheometers. Materials in the low-viscosity range, which include dilute polymer solutions 0.01–1 Pas, are best characterized by capillary break-up rheometers, contraction flows, or opposed jet devices. More details on these devices will be provided in the next sections.

Table 9.5 Summary of extensional rheometer designs and application ranges

Instrument type	Geometry	Flow	Shear viscosity range [Pa s]	Limitations	Example ref.
Filament stretching, constant volume, medium viscosity	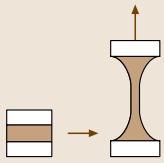	Uniaxial extension, constant strain rate	1–1000	Sample gripping, limited to medium with high viscosity, elastic instability	[9.16–18]
Filament stretching, constant volume, high viscosity	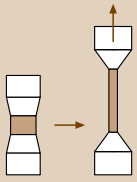	Uniaxial extension, constant strain rate	> 1000	Limited to low strain rates, temperature control	[9.10, 13, 14]
Filament stretching, constant length, high viscosity		Uniaxial extension, constant strain rate	> 1000	Limited to low strain rates, temperature control	[9.15, 19, 20]
Fiber spinning	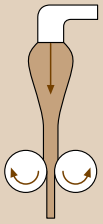	Uniaxial extension	> 1	Low strain, non-uniform strain rates, pre-shear history	[9.21–24]
Capillary breakup rheometry	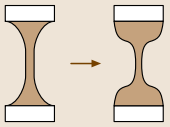	Uniaxial extension	0.01 – 1	Inertial and surface tension dominate at low end of viscosity, variable strain rates	[9.25–27]
Four-roll mill	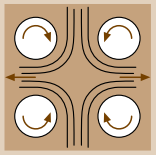	Uniaxial extension	1–1000	Variable strain rates and strain histories	[9.28, 29]

As early as 1906, *Fred Trouton* verified the relationship between the uniaxial extensional viscosity and shear viscosity in Newtonian fluids by performing low-extension-rate experiments on pitch [9.8]. He

Table 9.5 (cont.)

Instrument type	Geometry	Flow	Shear viscosity range [Pa s]	Limitations	Example ref.
Entrance flows	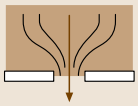	Uniaxial extension	> 1	Variable strain rate, mixed with shear	[9.30,31]
Sheet stretching	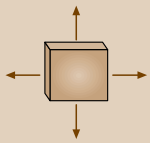	Biaxial planar extension	> 1000	Sample gripping, flow uniformity	[9.15]
Opposed jet		Uniaxial extension	0.01–1	Variable strain rates and strain histories, some shear	[9.32]
Planar elongation	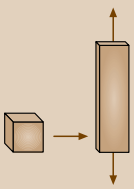	Planar extension, constant strain rate	> 1000	Sample preparation, Planar Elongation, limited to low extension	[9.33]
Tubeless siphon	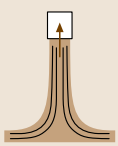	Uniaxial extension	1–1000	Pre-shear history, variable strain rate, low achievable strain rates	[9.34]

also derived theoretically the relationship between the extensional viscosity and shear viscosity of a Newtonian fluid; $\eta_E = 3\eta_0$, where η_E is the steady-state extensional viscosity. This result is a kinematic consequence of the differences in deformation between a shear flow and an extensional flow and is analogous to the relationship between the Young's modulus and the shear modulus in an incompressible isotropic elastic solid. The ratio between the extensional viscosity and shear viscosity is commonly referred to as the Trouton ratio, $\mathrm{Tr} = \eta_E/\eta_0$. Most early work was concerned with characterizing more-qualitative flow behaviors such as *spinnability* (or *Spinnbarkeit* in German) and *stickiness*. This early work is comprehensively reviewed in the only monograph on the topic by *Petrie* [9.9]. As a result of technological difficulties and theoretical misunderstandings, little definitive work in extensional rheology was performed until the 1970s, when force transducer and motion control technology was adequately refined. The initial work in the 1970s and 1980s for extensional viscosity characterization focused on instrument designs for polymeric melts [9.10–15]. The high viscosities of these materials facilitated the imposition of extensional deformations and resulted in relatively high extensional forces that were readily measured with off-the-shelf force transducers. Gripping methods employed in tensile testing of

solids can often be employed on polymeric melts without compromising the flow field [9.10, 11]. The high viscosity of these materials allows the use of a surrounding stabilizing medium, such as an oil that is immiscible with the polymer, to both heat the material as well as provide neutral buoyancy, without imparting a measurable shearing stress at the oil-polymer interface [9.14]. Most testing of polymeric melts occurs at relatively low strain rates $\dot{\varepsilon}_0 \leq 1\, s^{-1}$ and moderate strain levels.

Development of instrumentation for moderate- to low viscosity materials has proceeded more slowly. The low viscosity range presents challenges in designing instrumentation that reliably impose the required kinematics and to measure the force levels that can range from milligrams and span several orders of magnitude. Very low viscosity materials, such as those used in spraying applications, present even greater challenges, where surface tension and gravitational effects are of the same order of magnitude as viscoelastic effects [9.35]. These fluids can also be influenced by inertial effects, which can result in filament break-up before deformation is complete.

The pronounced impact of polymeric additives to Newtonian fluids on jet break-up, drag reduction, and droplet formation has increased the need to characterize these materials in an extensional flow field. An example of an as-yet unresolved need in the industry is a reliable method of measuring the extensional behavior of inkjet ink. The diagram shown in Fig. 9.43 shows a schematic makeup of a printing head of an inkjet printer. Ink flowing through the head and ejected onto the surface of the printed substrate will experience three different types of extensional processes. The quest to maximize print speed while minimizing droplet trailing is facilitated by characterization of the rheological properties of the ink in the flow field dominated in this process, namely uniaxial extension. The low-shear viscosity of these materials, close to that of water, makes this class of materials extremely challenging to characterize in an extensional flow [9.36].

Through the years, a variety of instrument and test methods have been developed that achieve a certain approximation to extensional flow. In addition to uniaxial extensional flows, processes such as blow molding, squeezing flows, and drop impact involve planar and biaxial extensional flows. While these flow fields are important, this chapter is limited to uniaxial flows where the technology to characterize uniaxial extensional flow is more mature and commercially available solutions exist.

Extensional rheometer types are summarized in Table 9.5. Appropriate citations are also included for each instrument type. The accuracy of the data obtained from the types of instruments shown in Table 9.5 depends on the ability of the operator to know both the extensional strain rate and the amount of extensional strain imposed on the sample precisely. In some of the instrumentation, for example filament stretching rheometers, the strain rate and strain is uniform in the sample and constant throughout the test, allowing the calculation of a true transient extensional viscosity. In other instrumentation, for example, the fiber spinning and opposed jet geometries, a representative fluid element experiences a range of strain rates as it is elongated in the flow. To interpret the data from the latter types of instruments, operators will report an average strain rate and strain, thus yielding an *apparent* extensional viscosity. These latter instruments find utility in indexing materials and ranking formulations according to their response to an extensional flow field [9.37].

In this section, we discuss the kinematics of extensional flows from both a theoretical and an experimental viewpoint. The current state of understanding of extensional rheology is presented for highly viscous polymeric materials (i. e., polymer melts) and for low to moderately viscous materials. Currently available commercial instrumentation for extensional rheometry experiments are summarized at the end of the chapter.

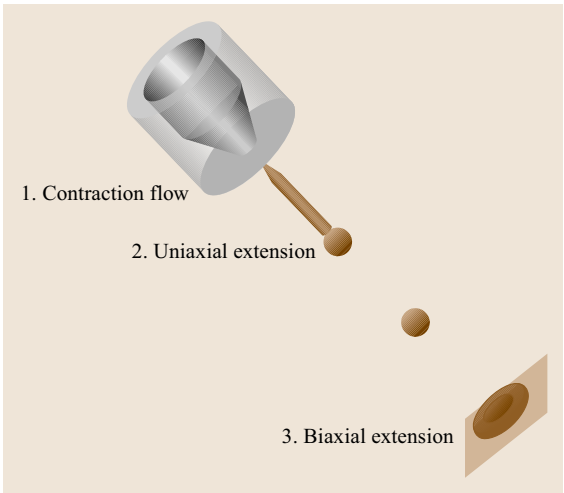

Fig. 9.43 Schematic diagram of an inkjet head, showing: (1) a contraction flow as the diameter of the channel narrows; (2) uniaxial extension followed by droplet breakup as the ink stream accelerates out of the head; and (3) biaxial extension as the ink drop impacts on the solid substrate

Kinematics of Elongational Flows

Homogeneous Versus Nonhomogeneous. A pure extensional flow is an irrotational motion in which there is no vorticity or shearing of material elements [9.38]. Such a deformation provides an extremely efficient way of orienting and elongating the underlying molecular structure of a complex fluid such as a polymer solution, fiber suspension or micellar fluid. If an extensional flow can be realized, it is thus a sensitive probe of material microstructure.

The simplest class of extensional flows is a spatially homogeneous flow, in which the velocity field is given by

$$v_x = -\frac{1}{2}(1+b)\dot{\varepsilon}x\,, \quad v_y = -\frac{1}{2}(1-b)\dot{\varepsilon}y\,, \quad v_z = b\dot{\varepsilon}z\,, \tag{9.179}$$

where $\dot{\varepsilon}$ is the deformation rate, and b is a flow-type parameter; the Cartesian coordinate z is rendered along the stretching direction, and x and y are normal to it. Simple differentiation of these expressions shows that there are no off-diagonal or shearing contributions to the velocity gradient tensor $\partial v_j/\partial x_i$ for $i \neq j$. Uniaxial elongation corresponds to $b = 0, \dot{\varepsilon} > 0$, biaxial extension (or uniaxial compression) corresponds to $b = 0, \dot{\varepsilon} > 0$, and planar elongation corresponds to $b = 1$.

If the flow is temporally homogeneous or steady then $\dot{\varepsilon} \neq \dot{\varepsilon}(t)$ but unsteady formulations (such as the start up of steady elongational flow $\dot{\varepsilon}(t) = \dot{\varepsilon}_0 H(t)$ where $H(t)$ is the Heaviside step function) can also be represented in this formalism.

In particular, it must be recognized, that because there is a natural time scale (the *relaxation time*) in non-Newtonian fluids, the dynamical response to an imposed extensional deformation is not instantaneous but a function of time and the deformation rate. The extensional viscosity functions can then be defined as

$$\bar{\eta}_1^+(\dot{\varepsilon}_0, t) = (\tau_{zz} - \tau_{xx})/\dot{\varepsilon}_0\,, \quad \bar{\eta}_2^+(\dot{\varepsilon}_0, t) = \left(\tau_{xx} - \tau_{yy}\right)/\dot{\varepsilon}_0\,, \tag{9.180}$$

where t is time.

In an uniaxial deformation ($b = 0, \tau_{xx} = \tau_{yy}$), there is only a single material function, the uniaxial extensional viscosity, which is often denoted by $\eta_E^+ \equiv \bar{\eta}_1^+$. Most of the discussion in this chapter focuses on uniaxial flows.

The total material strain accumulated by a material element can be obtained from direct integration of (9.179). For a uniaxial elongation ($b = 0$) at constant extension rate ($\dot{\varepsilon}(t) = \dot{\varepsilon}_0$), the position of a material element (identified by a label $[i]$) at time t is $Z^{[i]}(t) = Z_0^{[i]} \exp(\dot{\varepsilon}_0 t)$ and the strain between two neighboring elements is given by the natural or Hencky strain [9.38]

$$\varepsilon_H = \dot{\varepsilon}_0 t = \ln\left(\Delta Z(t)/\Delta Z_0\right)\,, \tag{9.181}$$

where $\dot{\varepsilon}_0$ is the idealized strain rate.

For a linear viscoelastic material described by a spectrum of discrete relaxation times λ_k and modal viscosity contributions η_k, the extensional response of a material can be solved analytically to give

$$\bar{\eta}_{\mathrm{LVE}}^+(t) = \sum_{k=1}^{N} 3\eta_k \left[1 - \exp(-t/\lambda_k)\right]\,. \tag{9.182}$$

At long times $t \gg \lambda_k$ the material thus approaches a steady-state elongational viscosity $\eta_E \to \sum 3\eta_k = 3\eta_0$.

This *linear viscoelastic envelope* is an important material limit that can be used to validate the performance of a specific instrument as we show below. This material function also quantifies two important adjectives that are commonly used in describing the elongational response of materials.

Strain hardening refers to the progressive deviation of the material response function above the linear viscoelastic envelope as the Hencky strain increases such that $\eta_E^+(\dot{\varepsilon}_0, t)/\bar{\eta}_{E,\mathrm{LVE}}^+(t) > 1$.

Extensional thickening refers to an increase in the steady-state extensional viscosity (measured at long times) above the value of the steady shear viscosity such that $\eta_E(\dot{\varepsilon}_0) > \eta(\dot{\gamma})$. Because most complex fluids also exhibit shear thinning, care must be taken to compare data at equivalent deformation rates. Consideration of the second invariant of the deformation rate tensor suggests that a suitable comparison is under conditions for which $\dot{\gamma} = \sqrt{3}\dot{\varepsilon}_0$.

It is important to recognize that the majority of industrial flows do not lead to spatially homogeneous deformation fields. The material response is then a function of both time and spatial position. This dependency makes it difficult to use such a flow to measure a true material function [9.39]. A representative situation is shown in Fig. 9.44, which compares a filament stretching deformation with a fiber-spinning operation. In a filament stretching operation the displacement of a material element of fixed identity (labeled 'A' here) is controlled to be exponential in time. The resulting Eulerian velocity field at any location (denoted '1' or '2') also changes (approximately exponentially) in time. The material element thus experiences *motion with constant stretch history* $\dot{\varepsilon}(t) = \dot{\varepsilon}_0$ and we can define the transient extensional viscosity in terms of the measured evolution

in the (time-varying) tensile force and the midplane radius of the filament. By comparison, in a fiber-spinning operation, such as the Rheotens test discussed below, the flow is steady in an Eulerian sense (so that the velocity is constant at any axial location) and the tensile force is constant at any specified take-up rate. However material elements now experience a time-varying deformation history including an upstream shear, followed by a die swell at the nozzle exit and finally a spatially varying uniaxial elongation flow. As a result, it is only possible to define an apparent material function such as a *spinning viscosity* or a critical stress to break. For further details see [9.40].

Dimensionless Parameters. It is common to report fluid-dynamical measurements and material functions in terms of dimensionless parameters. For extensional rheology experiments the natural formulation is to express the *transient Trouton ratio* $\mathrm{Tr}(\varepsilon_\mathrm{H}, \mathrm{De}) = \bar{\eta}^+(\dot{\varepsilon}_0, t)/\eta_0$ (i. e., a dimensionless extensional viscosity scaled with the zero-shear-rate viscosity) as a function of the dimensionless time or *Hencky strain* $\varepsilon_\mathrm{H} = \dot{\varepsilon}_0 t$, and a dimensionless ratio of the material and flow time scales *Deborah number* $\mathrm{De} = \lambda\dot{\varepsilon}_0$, where λ is an appropriate measure of the relaxation spectrum λ_k of the non-Newtonian material being tested (typically either the longest time constant or an appropriately weighted *mean* value of the relaxation time). Note that the dimensionless deformation rate may also be referred to as a *Weissenberg number* for elongational flow, since the characteristic deformation rate and flow timescale are inherently related in an extensional flow; $t_\mathrm{flow} \sim 1/\dot{\varepsilon}_0$.

Many extensional flows and elongational rheometers involve free-surface deformations and additional material functions characterizing the relative importance of interfacial tension forces arise. Because of the relative ease of measuring shear flow properties, these are invariably referenced to viscometric properties of a fluid, such as the steady-state shear viscosity, rather than the elongational viscosity. Relevant parameters include the capillary number; a ratio of the viscous stress to capillary

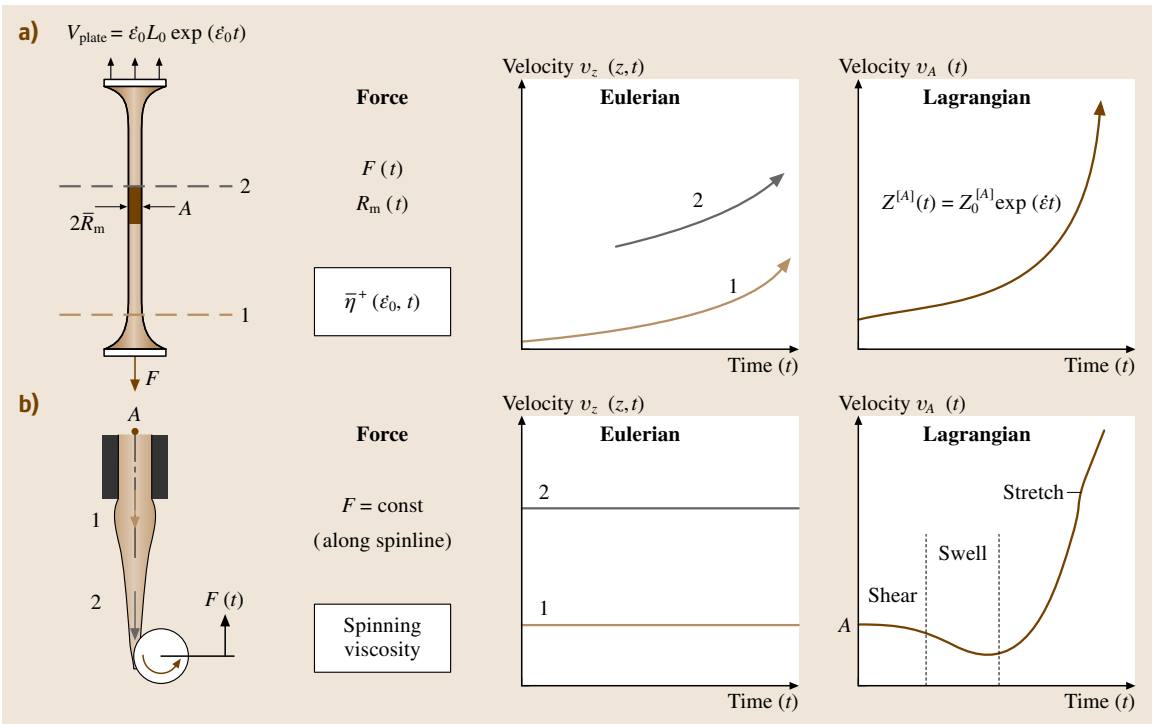

Fig. 9.44a,b Schematic of two different classes of uniaxial elongational flow; **(a)** filament stretching of a sample can be controlled to provide a constant deformation rate; **(b)** fiber spinning or the Rheotens experiment is steady in an Eulerian sense but unsteady from the point of view of a material deformation history. Z is the longitudinal axial coordinate along the filament or spin line. $\bar{\eta}^+(\dot{\varepsilon}_0, t)$ is the extensional viscosity, v_z the longitudinal velocity, and F the tensile force

pressure, $\mathrm{Ca} = \eta_0 \dot{\varepsilon}_0 R/\sigma$ (where σ is the surface tension and R is a characteristic length scale such as a thread or jet radius) and the elastocapillary number (or surface elastic parameter), $\mathrm{Ec} = \mathrm{De}/\mathrm{Ca} = \lambda\sigma/\eta_0 R$. The latter parameter plays an important role in jet break-up [9.41] and adhesive instabilities [9.42]. In deformations in which gravity plays a role it is common to report the Bond number $\mathrm{Bo} = \rho g R^2/\sigma$ as a ratio of the two dominant forces (gravity and surface tension) under static (no-flow) conditions with g being the gravitational constant. Of course any combinations and ratios of these common dimensionless parameters are also valid and have been used in the past.

Highly Viscous Materials ($\eta_0 > 1000$ Pa s). For very viscous materials such as tar or pitch (first studied by Trouton in 1906), the roles of gravity and capillarity can be safely neglected (i. e., $\mathrm{Ca} \gg 1 > \mathrm{Bo}$) and the material does not sag or neck during testing. A number of different Instron-like mechanical testing machines can then be constructed for testing such materials. These devices can be classified as *constant-sample-length* or *constant-sample-volume* instruments and they have been comprehensively reviewed by *Meissner* [9.43] and *Gupta* and *Sridhar* [9.44]; we provide additional details later.

A representative example of the measurement of the transient extensional viscosity function $\bar{\eta}^+(\dot{\varepsilon}_0, t)$ for a highly branched low-density polyethylene (LDPE) melt using the sentmanat extension rheometer (SER) universal test fixture (a constant-length device) is shown in Fig. 9.46 (taken from [9.45]). Equivalent measurements can also be performed with a constant-sample-volume device such as the filament stretching rheometer [9.46]. The linear viscoelastic response is also shown by the dark line (LVE) and provides a bounding envelope for the data at low Deborah numbers, $\mathrm{De} \ll 1$. As the imposed extension rate (and the corresponding Deborah number, $\mathrm{De} = \lambda\dot{\varepsilon}_0$) is increased, the material shows a progressively increased *strain-hardening* response and the viscosity climbs above the value expected from linear viscoelastic characterization. This strain hardening stabilizes the material against necking failure and accounts for the importance of using branched polymeric materials in film-blowing and spinline operations. The transient extensional stress growth of materials such as linear low-density polyethylene (LLDPE) that do not exhibit such pronounced strain hardening can also be measured using the SER fixture and closely follow the LVE envelope for all times and strains [9.45].

A large fraction of early research in the extensional viscosity area was focused on determining the steady extensional viscosity; however it is now recognized that in many commercial processes and flows this is not a relevant parameter as it requires prolonged extension and very large strains to be achieved; such conditions are not commonly attained in industrial operations. Determining the transient material response function and fitting the results to an appropriate constitutive model (such as those covered by *Petrie* [9.9]; *Bird* et al. [9.38] and in more-recent work such as that of *McLeish* and *Larson* [9.47]) is a preferred approach. However, if the long-time limit of the data at each deformation rate shown in Fig. 9.45 is taken as the steady-state value, then a curve of $\eta_\mathrm{E}(\dot{\varepsilon}_0)$ can be constructed, as shown in Fig. 9.46. At very low deformation rates the extensional viscosity approaches a constant Trouton ratio corresponding to $\mathrm{Tr} = \eta_\mathrm{E}(\dot{\varepsilon}_0)/\eta_0 \to 3$. An extensional thickening is then observed at intermediate rates as a result of molecular stretching before rate thinning leads to a power-law-like decrease in the extensional viscosity rate $\eta_\mathrm{E} \sim \dot{\varepsilon}_0^{-0.5}$ at very high deformation rates. The molecular origin of this extensional thinning is still under debate but it may involve either: (i) the anisotropic drag experienced by the polymer molecules as they disentangle and approach full extension, or (ii) the external *pressure* resulting from the surrounding chains [9.48].

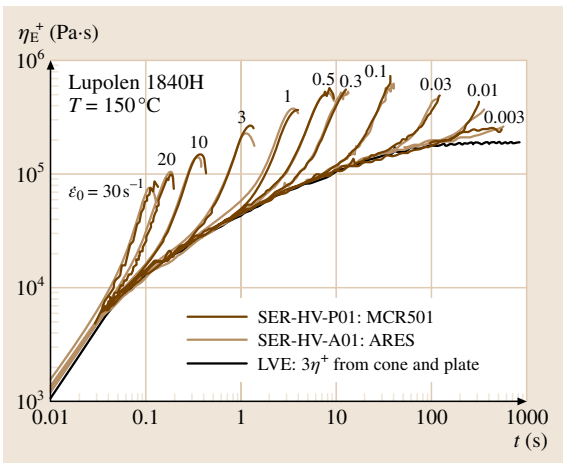

Fig. 9.45 Tensile stress growth curves at a melt temperature of 150 °C for a branched low-density polyethylene (Lupolen 1840H) over a range of Hencky strain rates $\dot{\varepsilon}_0$ of $0.003-30\,\mathrm{s}^{-1}$ generated with the SER on two different host platforms, an MCR501, and an ARES, and a plot of the linear viscoelastic envelope (LVE) taken from cone and plate measurements in start-up of steady shear flow at a shear rate of $0.005\,\mathrm{s}^{-1}$

A final area of recent interest in which the form of the extensional viscosity function for polymer melts and other viscous materials (such as hot melt adhesives) is important is the stability of polymeric threads against rupture and failure. In low-viscosity materials (discussed further below) the degree of strain hardening and its interplay with surface tension controls the formation of beads-on-a-string. In a polymer melt, surface tension is negligible (Ec $\ll 1$) and filament failure is governed purely by the viscoelastic response of the material in extension. In the limit of high De $\gg 1$, the filament stability can be characterized by the Considère criterion [9.49]. The principal result is typically written in terms of the tensile force in the filament; however it can also be re-expressed in terms of the transient Trouton ratio and the requirement for homogeneous extension becomes $\mathrm{d}\ln \mathrm{Tr}^{+}/\mathrm{d}\varepsilon_{\mathrm{H}} \geq 1$ ([9.50]); i. e., the Trouton ratio must increase at least exponentially fast with strain for homogeneous filament elongation. Examination of the data at the highest rates in Fig. 9.46 shows that, soon after the samples cease to strain harden exponentially with strain, the sample fails. The role of viscous stresses at moderate strain rates makes the analysis more complicated than that for a purely elastic material, but rupture events are still to be expected [9.51].

Low to Moderately Viscous Materials (0.01–1000 Pa s). Homogeneous versus Nonhomogeneous Instruments. In the past two decades, the development of extensional rheometers for low to moderately viscous materials has moved along two design paths. On the first path, the deformation kinematics are imposed on the material via the instrument, and the response of the material is monitored. On the second path, the material is deformed into an unstable configuration, but any further response is driven by the material alone. In both types of instrumentation, however, the operator must know the strain rate history of the material as well as the accumulated extensional strain on the fluid element being observed.

The round robin study in the framework of the project M1 compiled by *James* et al. [9.39] demonstrated a key fact in extensional rheometry: for non-Newtonian fluids, the extensional viscosity cannot be characterized by a single value. In this round robin, researchers reported the extensional viscosity of a dilute solution of polyisobutylene in polybutene [9.52] as a function of strain rate, but without consideration of the accumulated strain in the samples. Without the inclusion of this strain, the compiled results showed no correlation between η_{E} and $\dot{\varepsilon}$, and disappointing comparison

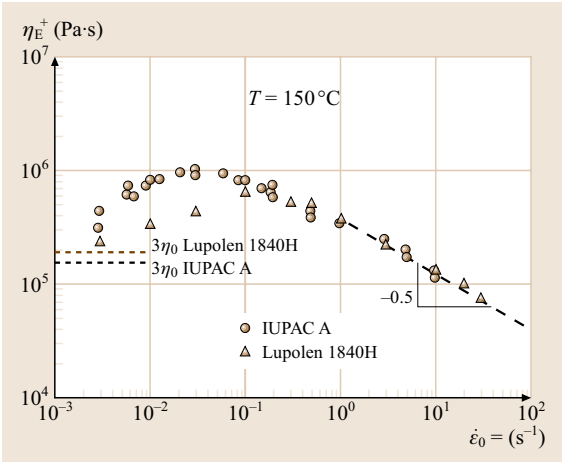

Fig. 9.46 Comparison of the steady-state extensional viscosity behavior as a function of Hencky strain rate at a melt temperature of 150 °C for two LDPE samples taken from the literature; Lupolen 1840H generated with the SER (*triangles*) and IUPAC A (*circles* from *Munstedt* and *Laun* [9.14])

between extensional rheometers. This study pushed researchers to recognize the need to accurately know and report the transient extensional viscosity as a function of both strain rate and strain. This need resulted in the design of the first generation of filament stretching rheometers.

Matta and *Tytus* [9.53] first proposed the use of a falling-plate rheometer, whereby a small volume of test fluid pinned between two circular plates is stretched as the bottom plate falls under the influence of gravity. The lack of active machine control on the movement of the bottom plate resulted in a time-varying extensional strain rate, which complicated the analysis of the data. *Sridhar* and coworkers resolved this issue by driving the two plates apart with a motion control system at user-specified velocity profiles, which allowed them to impose a deformation at a constant axial strain rate [9.17, 54]. By coupling a force transducer on one plate and stationing a laser micrometer at the midpoint of the deforming filament to monitor the filament diameter, these researchers were able to extract the transient extensional viscosity as a function of strain and strain rate for moderate to highly viscous fluids. The success of this design has led to further instrument development from a variety of groups [9.16, 17, 55–58]. The basic design for this class of instruments, termed *filament stretching extensional rheometers*, is shown in Fig. 9.47. These instruments fall under the classification of homogeneous

instrumentation, given that the strain rate is spatially uniform in the fluid sample, for the most part.

Newtonian fluids were used to validate these first-generation extensional rheometers, given that the extensional viscosity is well known ($\bar{\eta} = 3\eta_0$) and is independent of both $\dot{\varepsilon}_0$ and ε_H. The early results by *Sridhar* [9.17] and *Spiegelberg* et al. [9.16] showed that for the first several units of Hencky strain, the Trouton ratio for the Newtonian test fluids exceeded the known value of $\mathrm{Tr} = 3$; after being stretched to approximate $\varepsilon = 2$, the Trouton ratio approached the theoretical value of $\mathrm{Tr} = 3$. Theoretical analysis in Fig. 9.59 showed that the initial flow field is dominated by shear flows resulting from the pinning condition of the fluid at the endplates [9.16]. Numerical simulation studies by *Yao* et al. [9.59] showed that the initial shear flow could be minimized by increasing the initial length of the fluid sample L relative to the initial filament diameter D. It was determined that the effects of the initial endplate shear could be minimized by utilizing an initial ratio $L/D \approx 1$. A further consequence of the fluid pinning conditions at the endplates is that a reduced amount of fluid is participating in the extensional deformation. This phenomenon, coupled with the strain-hardening behavior of most non-Newtonian fluids, usually produced a temporally-varying strain rate as determined from the midpoint diameter. *Kolte* et al. [9.60] suggested three types of experimental strategies to address the nonuniform flow exhibited with these devices:

Type 1. The endplates are separated at an exponentially increasing rate $L(t) = L_0 \mathrm{e}^{\dot{\varepsilon}_0 t}$. The extensional viscosity is based on this imposed strain rate $\dot{\varepsilon}$ and is calculated as

$$\eta_E(t, \dot{\varepsilon}_0) = F(t)/\dot{\varepsilon}_0 A_0 \mathrm{e}^{-\dot{\varepsilon}_0 t} \tag{9.183}$$

where A_0 is the initial fluid area and F is the tensile force. The Hencky strain is calculated as per (9.181).

Type 2. The deformation profile is the same as in the type 1 experiment, but the data are processed differently. In the type 2 experiment, the midpoint radius R_m is measured, in addition to the force on the endplates. The varying midpoint strain rate, or *effective strain rate*, $\dot{\varepsilon}_{\mathrm{eff}}$ is calculated as a function of time as

$$\dot{\varepsilon}_{\mathrm{eff}}(t) = -\frac{2}{R_m}\frac{\mathrm{d}R_m}{\mathrm{d}t} . \tag{9.184}$$

The extensional viscosity is calculated as

$$\eta_E(\dot{\varepsilon}_{\mathrm{eff}}, \varepsilon) = \frac{F(t)}{\dot{\varepsilon}_{\mathrm{eff}} \pi R_m^2(t)} . \tag{9.185}$$

Because the strain rate varies with time due to the nonuniform flow generated by the endplates, the Hencky strain is calculated from the time integral over the strain rate based on the midpoint radius:

$$\varepsilon_{\mathrm{eff}}(t) = \int_0^t \dot{\varepsilon}_{\mathrm{eff}}(t)\,\mathrm{d}t = -2\ln\left(\frac{R_m}{R_0}\right) . \tag{9.186}$$

Type 3. In the type 3 experiment, the endplate velocity is controlled, so that the midpoint filament radius decreases as it would in an ideal flow, namely with a constant effective strain rate strain rate ($\dot{\varepsilon}_{\mathrm{eff}} = \dot{\varepsilon}_0$), or

$$R_m(t) = R_0 \mathrm{e}^{-\frac{1}{2}\dot{\varepsilon}_{\mathrm{eff}} t} . \tag{9.187}$$

The extensional viscosity and Hencky strain are calculated as in the type 1 experiment.

Researchers initially employed trial-and-error approaches to manipulate the velocity profiles to ensure a constant strain rate [9.16, 17]. *Anna* and coworkers developed a feedback system based on real-time measurements of the midpoint radius that adjusted the endplate velocity on the fly to ensure a constant strain rate [9.61], while others have developed endplate velocity profiles for type 3 experiments based on master curves developed from type 2 experiments [9.62].

These refinements, along with higher-resolution force transducers and laser micrometers, and motion control systems capable of resolving several orders of magnitude in velocity while maintaining position control on the micrometer scale, have greatly advanced

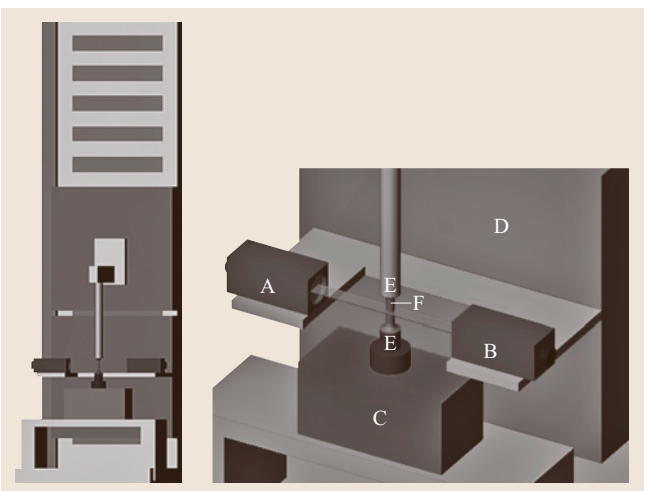

Fig. 9.47 Schematic diagram of a filament stretching extensional rheometer for moderately viscous materials. A: laser emitter; B: laser detector; C: force transducer; D: motor; E: endplates; F: fluid filament

the accuracy and repeatability of extensional viscosity measurements in fluids, as shown in the next section. The improved instrumentation has allowed researchers to conduct more-refined extensional flow experiments, such as probing individual polymer chain conformation with concurrent birefringence measurements [9.63, 64], examining step strain responses of materials [9.62, 65], and characterizing elastic instabilities in extensionally deforming fluids [9.66].

Filament stretching rheometers are typically limited to fluids exhibiting shear viscosities of approximately 1 Pa s or greater. At lower viscosities, surface tension and gravity begin to dominate the flow behavior of the fluid. It is this recognition that led *Rozhkov* and coworkers to the development of capillary break-up rheometers, which are in the class of nonhomogeneous extensional rheometers, given that the strain rate is not spatially homogeneous in the sample [9.26, 67]. Rather than trying to minimize the influence of these forces, surface tension is allowed to drive the deformation of the fluid filament, which resists the deformation through viscous and elastic forces, and gravitational forces are rendered inconsequential through small sample dimensions. In this experiment, a cylindrical fluid filament is placed between two circular endplates, similar to a filament stretching experiment. As opposed to separating the endplates at a constant strain rate while measuring force and radius, in this test a rapid axial step strain is imposed, resulting in a stretched fluid filament. The plate separation occurs at a rate faster than the longest relaxation time in the test fluid. The capillary break-up rheometer monitors the filament radius as a function of time as it thins under capillary pressure. The extensional stress is derived from the surface tension of the fluid σ, reducing the calculation of extensional viscosity to

$$\eta_{\text{app}} = \frac{\sigma/R_{\text{m}}}{\dot{\varepsilon}_{\text{eff}}} = \frac{\sigma/R_{\text{m}}}{-\frac{2}{R_{\text{m}}}\frac{\mathrm{d}R_{\text{m}}}{\mathrm{d}t}} = -\frac{\sigma}{2\,\mathrm{d}R_{\text{m}}/\mathrm{d}t} \,. \tag{9.188}$$

The behavior of Newtonian fluids in a capillary break-up rheometer is well predicted, and these experiments are useful for easily determining their shear viscosity if the surface tension is independently known. As discovered by *Papageorgiou* [9.68], the midpoint radius of a Newtonian filament is expected to evolve according to

$$R_{\text{m}}(t) = 0.0709\frac{\sigma}{\eta_{\text{s}}}(t_{\text{c}} - t) \,, \tag{9.189}$$

where t_{c} is the critical break-up time of the filament. *McKinley* and *Tripathi* [9.25] showed very good correlation between the shear viscosity measured with a torsional shear rheometer and results obtained on a capillary break-up rheometer using this expression. Capillary break-up rheometry has been used to evaluate the time-dependent change in extensional viscosity of adhesives containing a volatile solvent [9.69], the extensional rheology of ink and paint [9.70], the relaxation times of non-Newtonian fluids [9.71, 72], and to probe time scales in low-viscosity fluids [9.73].

Results from Filament Stretching Rheometer Experiments. The considerable improvements made in filament stretching rheometer designs have allowed researchers to attempt another round robin comparison of results to compare and validate the basic approach. As opposed to the original M1 round robin study, this round robin proved to be much more successful. Three universities [9.74] constructed filament stretching rheometers based on the original concept by *Sridhar* [9.17] that were capable of type 3 experiments. Although the basic design was the same in all three instruments, different motion control systems, diameter sensors, and force transducers were used in the three systems. The limitations of the mechanical systems were discussed in detail in this work, and standard error propagation analysis was performed to determine the errors in the results corresponding to various stretching regimes.

In this round robin study, the researchers tested three solutions of high-molecular-weight polystyrenes dissolved in oligomeric styrene oil. The polymer concentration of all three solutions was 0.05 wt %, and the polystyrenes all had very narrow molecular-weight distributions. The material and viscometric properties, including weight-averaged molecular weight of the polystyrene (M_{w}), zero-shear viscosity (η_0), and Zimm relaxation time (λ), are shown in Table 9.6.

The three institutions generated master curves to determine the stretching history that would yield the optimal diameter profile required for a type 3 test [9.61,62]. The resultant diameter profiles of the idealized stretching history showed both excellent agreement within the institutions, as well as good agreement with the ideal curve, given that the experimental diameter at each point was within 10% of the ideal curve.

One set of computed extensional viscosities is shown in Fig. 9.48. The Deborah numbers in these tests were $\text{De} = 12.0 - 17.0$, due to temperature variations and slight variations in motion control between the three institutions. However, these differences did not impact on the results, given the extremely good comparison of the three sets of results shown. The error bars at the four locations were determined from the error propagation

Table 9.6 Viscometric properties of polystyrene-based test fluids dissolved in styrene oil. The solution concentration was 0.05 wt % for all samples

Fluid	M_w [g/mol]	η_0 [Pa s]	λ [s]
SM-1	2×10^6	39.2	3.7
SM-2	6.5×10^6	46.1	31.1
SM-3	2.0×10^7	55.5	155

analysis. The results show that the refinements in instrumentation and testing technique have resulted in a very reproducible and reliable extensional rheometry test.

In addition to examining the interlaboratory reproducibility of this testing technique, Anna and co-workers thoroughly examined the ideal operating range of these rheometers. Achievable strain and strain rate regimes are limited by motor length and motor velocity. The final measurable extensional viscosity is limited by both the resolution of the force transducer and the diameter-sensing device. Highly elastic fluids can exhibit an instability at the endplates, causing partial decohesion of the material at higher levels of strain, which influences the measured extensional viscosity [9.75]. Lower-viscosity fluids are susceptible to gravitational sagging at lower strain rates, which is characterized by the Bond number (Bo) and the ratio of the Bond number to the capillary number Ca. *Anna* et al. provide critical test conditions where these conditions can occur based on fluid properties and test geometry [9.74].

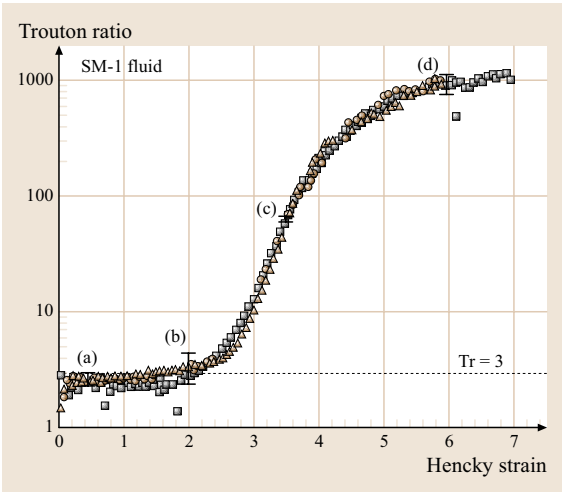

Fig. 9.48 Comparison of transient extensional viscosity results for the round robin study on fluid SM-1 from three institutions MIT (*circles*), Monash (*squares*) and Toronto (*triangles*). The error bars at strains a to d indicate the estimated error at low, moderate, and high Hencky strains (reproduced with permission after [9.74])

Results from Capillary Break-up Extensional Rheometry.

Two representative studies are presented that employ capillary break-up rheometry to indicate the utility of this technique. In the first, *Stelter* and coworkers used a capillary break-up rheometer to quantify the relaxation times and extensional viscosities of a series of ionic and nonionic polymers as a function of concentration [9.76]. This work exploited the influence of ionically charged polymer molecules on their chain flexibility to explore the effects of polymer chain flexibility on the extensional flow behavior.

When a non-Newtonian fluid is stretched in a capillary break-up rheometer, the evolution of the fluid thread diameter $D(t)$ is expected to thin in two distinct regimes, with the first regime decreasing exponentially with time t according to the expression

$$D(t) = D_0\, e^{-t/3\lambda}\,, \tag{9.190}$$

where D_0 is the filament diameter after the initial stretch at time $t = 0$. In the second regime, the filament thins linearly according to

$$D(t) = D_0 - \frac{\sigma}{\mu_{el,t}}t\,, \tag{9.191}$$

where σ is the surface tension of the solution, and $\mu_{el,t}$is the terminal extensional viscosity.

These authors prepared nonionic solutions from Praestol 2500, a linear polyacrylamide (degree of hydrolysis 3–4%, $8-10\times10^6$ g/mol), polyethylene oxide (PEO, $8-10\times10^6$ g/mol), and a branched graft copolymer composed of a carboxymethyl cellulose backbone and polyacrylamide branches (CMC-g-PAM). Two ionic solutions were prepared from a linear polyacrylamide Praestol 2540 (degree of hydrolysis 40%, 14×10^6 g/mol), and a xanthan gum solution (2×10^6 g/mol). All solutions were prepared with concentrations in water at 62–4000 ppm, resulting in values of $c[\eta]$ between 1-2, which indicates that the solutions are in the semi-dilute range; c is the polymer concentration and $[\eta]$ the intrinsic viscosity. The terminal extensional viscosity $\mu_{el,t}$ is plotted as a function of relaxation time in Fig. 9.49.

During extensional testing, each polymer system showed a dependence of the measured relaxation time and terminal elongational viscosity on solution concentration, resulting in the multiple data points shown in Fig. 9.49. The data arrange on two distinct lines. The Praestol 2500, lacking substantial hydrolysis and therefore ionic behavior, will act as a flexible polymer chain,

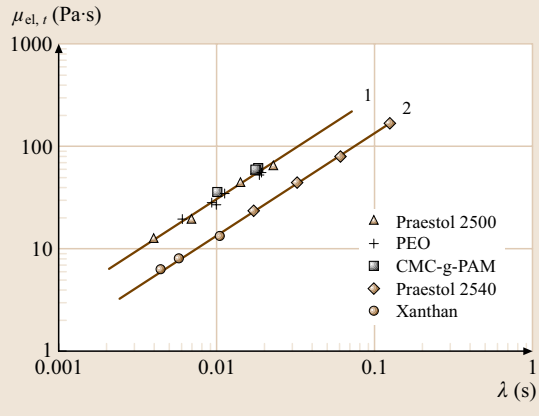

Fig. 9.49 Terminal elongational viscosity plotted as a function of relaxation time for three nonionic and two ionic semidilute aqueous solutions. Line 1 corresponds to flexible polymer chain behavior, while line 2 corresponds to rigid-like behavior. (After [9.76] with permission)

as will the polyethylene oxide. The CMC backbone of the graft copolymer is only weakly ionic, so that this copolymer will also act as a flexible chain. The repulsive behavior of the charges on the ionic polyacrylamides will prevent flexible chain motion, so that these chains will act in a rigid-like manner. The testing allowed these researchers to clearly differentiate materials exhibiting rigid-rod-like behavior and flexible chain behavior. Chain behavior will influence the spraying properties of polymer solutions.

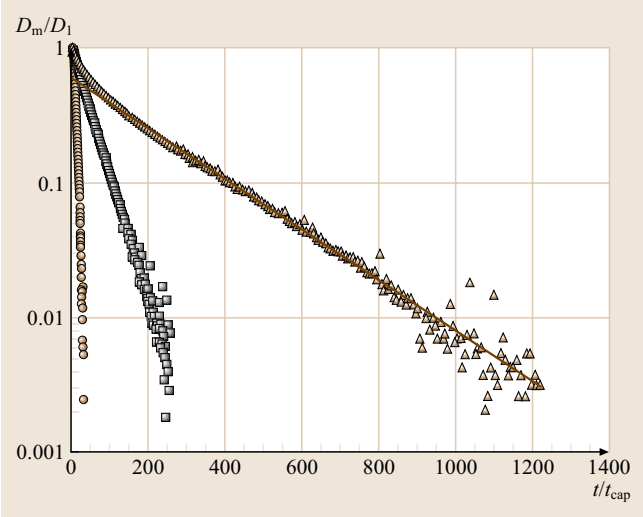

Fig. 9.50 Transient midpoint diameter profile for polystyrene-based [SM-1 (○), SM-2 (□) and SM-3 (△)]. D_1 is the initial diameter, and t_{cap} is trhe capillary time calculated as $t_c ap = \eta_0 D_t/2\sigma$. (After [9.65] with permission)

In another study, *Anna* et al. investigated the dependence of the extensional flow properties on molecular weight with a series of dilute polystyrene solutions [9.65] . In this work, the results from capillary break-up rheometry tests conducted on the three test fluids were compared with results measured on a filament stretching rheometer. The three test fluids had the viscometric properties already shown in Table 9.6.

The evolving midpoint diameters of the three test fluids tested in the capillary break-up rheometer are shown in Fig. 9.50. Regression on the linear portion of the plot yielded relaxation times that compared well with the relaxation times determined from shear rheology and reported in Table 9.6, according to (9.190).

Conversion of the diameter versus time data to the apparent extensional viscosity versus Hencky strain with (9.187) and (9.185), respectively, allows a direct comparison between the capillary break-up rheometric data and the filament stretching data, as shown in Fig. 9.51. The differences between the two sets of curves are consequences of the different kinematics in the two devices. The best comparison between the tests occurred with SM-2, where the two types of extensional tests approached the same final steady-state Trouton ratio of Tr $\approx$ 5000. It is not surprising that the transient extensional viscosities leading up to $\bar{\eta}$ in the SM-2 fluid tested in the two instruments were not similar, given that the filament stretching test was conducted at a constant strain rate, while the capillary break-up rheometer test imposes a variable strain rate set by the fluid itself. It is expected, however, that the final steady-state viscosity will be independent of the prior strain-rate history, however, which the results from SM-2 confirm. The final steady-state plateau can usually not be reached for highly elastic fluids due to endplate instabilities [9.66], which was observed in SM-3. Additionally, gravitational sagging can also limit the operating range of filament stretching rheometry. As Anna and McKinley suggest, capillary break-up rheometry provides a means of increasing the available operating range of extensional rheometry tests in highly elastic fluids [9.65].

Commercially Available Instruments. Several extensional rheometer designs have been commercialized in the past. A list of previously and currently available instruments is summarized in Table 9.7. Rheometrics commercialized an opposed jet device in the 1980s under the model name RFX. Now discontinued, the

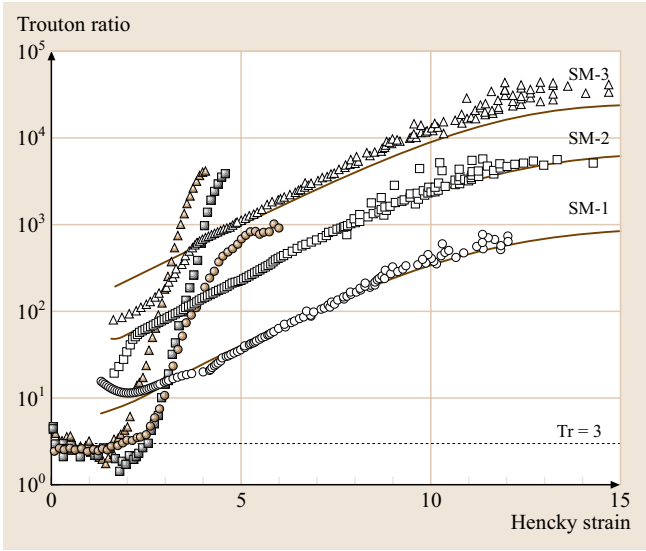

Fig. 9.51 Comparison of transient extensional viscosity measured in a filament stretching rheometer (*solid symbols*) and apparent extensional viscosity measured with a capillary breakup rheometer (*open symbols*). The *lines* show the predictions from multimode FENE (finite extensible nonlinear elastic) calculations. [SM-1, $De = 17.0$ (●), $De \approx 2/3$ (○); SM-2, $De = 15.2$ (■), $De \approx 2/3$ (□); and SM-3 $De = 21.2$ (▲), $De \approx 2/3$ (△)]. Values below a $Tr = 3$ are usually the results of gravitation sagging. (After [9.65] with permission)

instrument suffered from the underlying problems of opposed jet devices, namely a nonhomogeneous deformation and a significant pre-shear history, both of which complicate the data interpretation [9.77]. The instrument is also limited to strains of approximately $\varepsilon = 1$, and can suffer from inertial effects [9.78]. Despite these limitations, the RFX was the only commercially available rheometer for examining low-viscosity fluids, and provided useful information for indexing materials. *Ng* and coworkers [9.79] performed opposed jet measurements on dilute solutions containing carboxymethyl cellulose, polyacrylamide, and polyisobutylene to examine their impact on drag reduction, and were able to observe differences in the solutions in extensional flows, while shear flows led to no measurable differences.

Two extensional rheometers for melts were previously available that both used the constant-length geometry previously discussed. The MXR2, developed by the National Physical Laboratory's Center for Materials Measurement and Technology and commercialized by Magna Projects, stretched polymer melt filaments by winding them onto a rotating wheel. The filaments were both heated and buoyed by an oil bath. The RME, developed by *Meissner* and coworkers and commercialized by Rheometrics [9.19], employed stationary tread-like grips that stretched a polymer melt filament at controlled rates. The filament was both heated and buoyed by gas passed through a hot porous frit. The RME could reach Hencky strains of $\varepsilon_H = 7$ and strain rates of $\dot{\varepsilon}_0 = 1\,s^{-1}$. Neither the MXR2 nor the RME are currently being manufactured.

A currently available melt extensional rheometer is the Sentmanat Extension Rheometer (SER) (Xpansion Instruments, Tallmadge, OH), shown in Fig. 9.52. The SER is designed to be field-installed on commercially available shear rheometers, thus allowing them to

Table 9.7 Previously and currently available extensional rheometers

Instrument name	Company	Viscosity range [Pa s]	Flow type	Data type
Currently available				
Rheotens	Göttfert (Rock Hill, SC)	> 100	Fiber spinning	Indexer
CaBER®	Thermo (Karlsruhe, Germany)	0.01 – 10	Capillary breakup	$\eta(\dot{\varepsilon}_0, \varepsilon)$
Sentmanat extension rheometer (SER)	Xpansion Instruments (Tallmadge, OH)	> 10000	Constant-length filament stretching	$\eta(\dot{\varepsilon}_0, \varepsilon)$
Previously available				
RFX	Rheometrics Scientific	0.01-1	Opposed jet	Indexer
RME	Rheometrics Scientific	> 10000	Constant-length filament stretching	$\eta(\dot{\varepsilon}_0, \varepsilon)$
MXR2	Magna Projects & Instruments	> 10000	Constant-length filament stretching	$\eta(\dot{\varepsilon}_0, \varepsilon)$

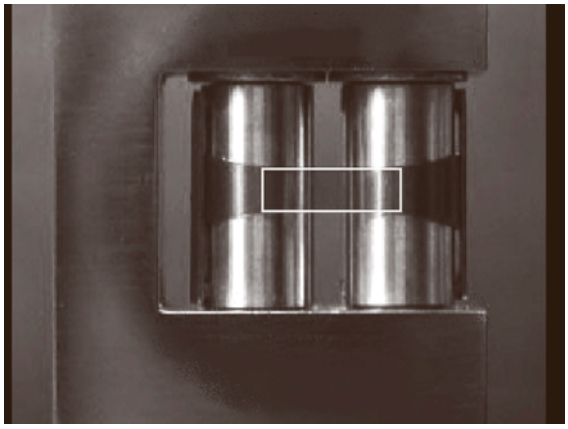

Fig. 9.52 Rheotens filament windup rheometer for characterizing melts

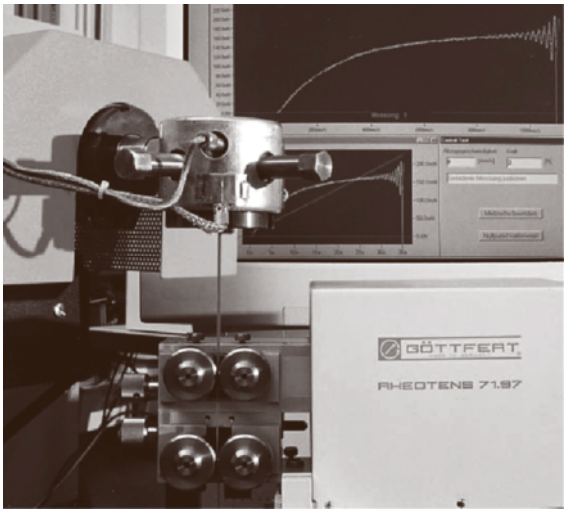

Fig. 9.53 Rotating cylinders of SER melt rheometer. The *rectangle* shows the uniform texting area

perform extensional rheometric experiments. The SER employs two rotating drums that wind up the polymer melt filament, imposing constant, step, or variable strain rates, depending on user choice. The torque exerted on one of the drums provides a measure of the stress in the sample.

A variant of the controlled-rate rheometer discussed above is a controlled-velocity device, embodied in the the Rheotens (Göttfert, Rock Hill, SC). The Rheotens is a fiber spinning apparatus, whereby polymer melt is pumped from an upstream tube. A set of wind-up wheels elongates the fluid, while a force transducer mounted on one of the take-up wheels monitors the resulting force

Fig. 9.54 CaBER® capillary breakup rheometer. *Inset* shows a closeup of a thinning fluid filament stretched in the instrument

exerted by stretching the sample. The Rheotens has significant pre-shear induced while the polymer melt is pumped through the upstream tube, and its extensional flow field has variations in strain rate [9.80]. As a result of these complications, the data obtained from the Rheotens is usually used to index polymer melts, rather than interpreting the data as absolute extensional rheometric data. An example of a Rheotens is shown in Fig. 9.52.

The only currently commercially available extensional rheometer for fluids is the CaBER (ThermoFisher HAAKE, Karlsruhe, Germany). An example is shown in Fig. 9.54. The CaBER is a capillary break-up rheometer, and is based on the work of *Rozhkov*, *Entov*, and coworkers [9.26, 67, 81]. In this instrument, a fluid filament is stretched rapidly between two circular endplates to a fixed level of extensional strain. After the cessation of flow, a laser micrometer monitors the axial midpoint diameter of the fluid filament as a function of time as the

filament thins and breaks up under the influence of surface tension, elasticity, and viscosity. In contrast to the previous devices, the CaBER does not impose a specific deformation rate on the sample; rather, the deformation rate is set by the material. The extensional viscosity as a function of strain rate and strain can be determined from the profile of diameter versus time and knowledge of the surface tension of the test fluid. The CaBER is useful for moderate- to low-viscosity fluids, including Newtonian fluids. Once a researcher has determined that the CaBER data departs from the break-up kinematics of a Newtonian fluid using the models provided in the software, they can compare the data to other non-Newtonian models. The quality of the fit of the non-Newtonian rheological model provides insight to the type of viscoelastic behavior exhibited by the test fluid. Similar to the model fitting used in shear rheology, the optimal choice of the fluid model is up to the researcher.

9.2 Thixotropy, Rheopexy, Yield Stress

Thixotropy is a decrease of the apparent viscosity under constant shear stress or shear rate, followed by a gradual recovery when the stress or shear rate is removed. It comes about first because of the finite time taken for any shear-induced change in the microstructure – that confers the viscosity – to take place. The microstructure is brought to a new equilibrium microstructure by competition between the processes of tearing apart by stress and flow-induced collision, in a time that can be minutes. Then, when the flow ceases, Brownian motion is able to move the elements of the microstructure around slowly to more-favorable positions and rebuild the structure. This can take many hours to complete. The whole process is completely reversible.

In this Section, the history of thixotropy is reviewed. The effects of the microstructural changes on the flow properties, which result in the various manifestations of thixotropy, are described. The various mathematical descriptions of the phenomenon are summarized.

In their *Glossary of Rheological Terms*, *Barnes*, *Hutton* and *Walters* [9.82] (following the 1975 British Standards Institution definition) defined thixotropy as 'A decrease of the apparent viscosity under constant shear stress or shear rate, followed by a gradual recovery when the stress or shear rate is removed. The effect is time-dependent.'

They also defined anti-thixotropy as the precise opposite of thixotropy and said that rheopexy is a synonym of anti-thixotropy. These terms are now generally accepted in the rheological world as definitive descriptions.

Thixotropy comes about because of the finite time required for any shear- or stress-induced changes in the microstructure of structured liquids – suspensions, emulsions, polymer solutions, etc. – to take place. The microstructure of the liquid involved is brought to a new equilibrium by competition between the processes of reordering or tearing apart by stress and flow-induced collision, in a time that can typically be minutes. Then, when the applied flow or stress ceases or is removed, Brownian motion is able to move the elements of the microstructure around slowly to more-favorable positions and hence rebuild the structure. This manifests itself as an increased viscosity and can take many hours to complete. The whole process of breakdown and rebuilding is completely reversible if the basic elements are not destroyed during flow.

Non-experts have deliberately built such thixotropic behavior into some commercial products to make them usable, with the best-known examples being thixotropic paints. However, as will be shown, what is usually wanted in these cases is extreme shear thinning. However the way it is brought about usually introduces thixotropy as well, which is then almost always an irritation.

9.2.1 A History of Thixotropy

In the Beginning

Previous reviews of thixotropy have been produced by *Bauer* and *Collins* [9.83], *Mewis*, 1979 [9.84], *Cheng* [9.85] and *Godfrey* [9.86] and by the present author in 1997. *Barnes* [9.87] noted that the origins of thixotropy as a recognized physical phenomenon go back to 1923 when Schalek and Szegvari found that aqueous iron oxide gels 'have the property of becoming completely liquid through gentle shaking alone, to such an extent that the liquified gel is hardly distinguishable from the original sol. These sols were liquified but become solidified again after a period of time ... the change of state process could be repeated many times without any visible change in the system' [9.88,89]. The word *thixotropy* was used by *Peterfi* in 1927 [9.90,91] in the first paper that properly described the phenomenon,

combining the Greek words *thixis* (stirring or shaking) and *trepo* (turning or changing).

By 1935 *Freundlich* had published a book called *Thixotropie* [9.92] which dealt with the subject: this was the first time that the term was introduced into the title of a publication. Freundlich and coworkers soon found thixotropic effects manifested by a whole variety of systems including vanadium pentoxide sols, starch pastes, and pectin gels.

It is clear that thixotropy originally referred to the reversible changes from a flowable liquid to a solid-like gel. Previously these kinds of physical changes had only been known by changing the temperature, when such gels would melt on heating and then recooling. It was believed at the time that a new kind of phase change had been found albeit a similar behavior of various yoghurts and kefirs was long known but had not attracted the attention of rheologists.

Progress

Early work in this area in the USA is exemplified by three papers published by *McKillen* [9.93] in 1932, who reported the results of his doctoral investigations into the thixotropy of a large number of flocculated paints. He showed that the fluidity (the inverse of viscosity) as a function of time decreased in some cases by four orders of magnitude, showing an almost quadratic dependence on the rest time.

Writing in the UK in 1942, *Scott-Blair* [9.94] could still state that 'the whole subject [of thixotropy] is very new', but in the update of his textbook published in 1949, nearly 120 papers on thixotropy were cited, so things had moved on quickly. Among the examples of thixotropic materials that he cites are clays and soil suspensions, creams, drilling muds, flour doughs and suspensions, fibre greases, jellies, paints, carbon-black suspensions, and starch pastes. He also lists a number of papers on so-called *thixotrometers*, instruments specially devised to characterize the phenomenon. In this respect he raised some interesting points, among them whether thixotropy ought to be studied at constant shear rate or at constant stress, which is still a controversial question.

Scott-Blair quotes Hamaker's explanation of thixotropy as being due to the fact that 'particles can form a loose association which is easily destroyed by shaking but restores itself on standing': this explanation still stands. With our present knowledge of microstructural changes, it is probably safe to say that all materials that are shear thinning are also thixotropic, in that they will always take a finite time to bring about the rearrangements needed in the structural elements that are responsible for shear thinning. However, the number of times that these effects come within the measurable range (say > 1 s) is limited. As Scott-Blair concludes, 'If this recovery is very rapid, the phenomenon is observed as structural viscosity [shear thinning]; if slow, it is observed as thixotropy'.

In the 1930s and 1940s *Pryce-Jones* [9.95, 96] studied around 250 paints, using a so-called *thixotrometer* that he made himself [9.97]. He noted that 'It is a well-established fact that thixotropy is more pronounced in systems containing non-spherical particles', this is because they have to find themselves in the best three-dimensional (3-D) structure by rotation as well as movement, and progress from a solid gel to a freely flowing liquid due to complete microstructural breakdown (Fig. 9.55).

The full extent of thixotropy was maintained by *Bauer* and *Collins* in their 1967 review [9.83]: 'When a reduction in magnitude of rheological properties of a system, such as elastic modulus, yield stress, and viscosity, for example, occurs reversibly and isothermally with a distinct time dependence on application of shear strain, the system is described as thixotropic'. They went on to say that thixotropy was 'usually conceived as an unusual property of very special systems such as aqueous iron oxide dispersions, thixotropy in the sense described above, has been found to be exhibited by a great many and a large variety of systems. Along with the breakdown in structure, other non-rheological features change, such as conductivity and dielectric constant'.

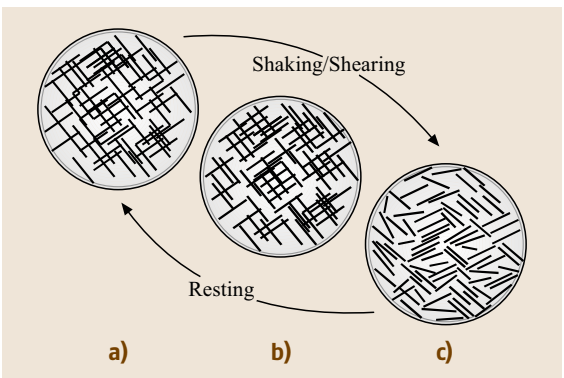

Fig. 9.55a–c Breakdown of an idealized two-dimensional (2-D) thixotropic system: **(a)** completely structured giving elastic, solid-like behavior; **(b)** partly structured giving a viscoelastic response and **(c)** completely unstructured giving a viscous, shear-thinning response

How is Thixotropy Generally Understood Today?

To guide a researcher or an engineer in deciding whether the material with which he or she is dealing is thixotropic or not, the following are various definitions offered in the current general scientific literature, scientific dictionaries, and encyclopaedias that reflect these two points of view. Some are misleading, while even the best are often incomplete. The following are a selection that illustrate the situation.

Oxford Encyclopaedic Dictionary of Physics [9.98]. 'Thixotropy: certain materials behave as solids under very small applied stresses but under greater stresses become liquids. When the stresses are removed the material settles back into its original consistency. This property is associated with certain colloids which form gels when left to stand but which become sols when stirred or shaken, due to a redistribution of the solid phase.'

Chambers Dictionary of Science and Technology [9.99]. 'Rheological property of fluids and plastic solids characterized by a high viscosity at low stress, but a decreased viscosity when an increase in stress is applied. A useful property of paints, because it makes for a thick film which is nevertheless easily worked.'

McGraw–Hill Dictionary of Scientific and Technical Terms [9.100]. 'Property of certain gels which liquefy when subjected to vibratory forces, such as ultrasonic waves or even shaking and then solidify again when left standing. Thixotropic clay: a clay which weakens when disturbed and increases in strength upon standing.'

Van Nostrand's Scientific Encyclopaedia [9.101]. 'A thixotropic fluid is a fluid whose viscosity is a function not only of the shearing stress, but also of the previous history of motion within the fluid. The viscosity usually decreases with the length of time the fluid has been in motion. Such systems commonly are concentrated solutions of substances of high molecular weight colloidal suspensions.'

Oxford Concise Science Dictionary [9.102]. 'More common, however, is the opposite effect in which the viscosity depends not only on the viscosity gradient but also on the time for which it has been applied. These liquids are said to exhibit thixotropy. The faster a thixotropic liquid moves the less viscous it becomes. This property is used in non-drip paints (which are more viscous on the brush than on the wall) and lubricating oils (which become thinner when the parts they are lubricating start to move).'

Chambers 20th Century Dictionary [9.103]. 'Thixotropy: the property of gels of showing a temporary reduction in viscosity when shaken or stirred.'

Definitions given in more-specialized dictionaries emphasize the time aspect of thixotropy.

Polymer Technology Dictionary [9.104]. 'A term used in rheology which means that the viscosity of a material decreases significantly with the time of shearing and then increases significantly when the force inducing the flow is removed.'

Polymer Science Dictionary [9.105]. 'Time-dependent fluid behavior in which the apparent viscosity decreases with the time of shearing and in which the viscosity recovers to, or close to, its original value when shearing ceases. The recovery may take place over a considerable time. This may sometimes occur with polymer systems, when molecular disentanglement increases with time of shearing.'

The definition of thixotropy in the rheological literature has changed over the years. The (American) Society of Rheology was quoted by *Reiner* and Scott-Blair in 1949 [9.106] as defined thixotropy as 'that property of a body by virtue of which the ratio of shear stress to rate of deformation (viscosity) is temporarily reduced by previous deformation'.

Some time later thixotropy was defined as 'a comparatively slow recovery, on standing, of the consistency lost through shearing'.

Gellants like Carbopol, polyacrylates and polysaccharides are used to make fuels and oxidizers (and their simulants) for rocket engines gel. The gelled products become thixotropic (see, e.g., [9.107]).

Internet Use. In general on the Internet, the word thixotropy is often very loosely defined and certainly not according to rheological orthodoxy. At best such definitions are confusing, but often they are incorrect in that no reference is made to time as a variable, the indispensable part of the proper rheological definition of thixotropy. To illustrate this point, the following (anonymous, but easily found) selection of typical definitions currently given on the Internet is cited. These appear in discussions covering a wide range of non-Newtonian liquid products. In most cases, the term thixotropy is either partly or completely confused with what we would properly define as shear thinning (Fig. 9.24 in Sect. 9.1.1).

Typical definitions:

- 'Thixotropy – the property of some gels of becoming fluid when stirred or shaken, and setting to gel again when allowed to stand.'
- 'Reversible behavior of certain gels that liquefy when they are shaken, stirred, or otherwise disturbed and reset after being allowed to stand. Thixotropy occurs in paint ... which flows freely when stirred and reverts to a gel-like state on standing.'
- 'High thixotropy materials become thinner when they are sheared.'
- 'The property of certain gels to become liquid upon being shaken or agitated and to coagulate again when left in an undisturbed condition.'
- 'Thixotropy is the property of [clay] slips becoming thicker when they are at rest, i. e., *thixotropy too high* means that the slip thickens up very quickly.'

Definitions referring to specific systems:

- 'Characteristic of a *lubricant* to become momentarily ... thinner due to mechanical action such as stirring.'
- 'The property of some *printing inks* of becoming fluid when worked and setting to a semi-solid state when at rest; the cause of some inks tending to back away from the ink fountain roller.'
- 'The thixotropic index (*of adhesives*) – a ratio of the low-shear viscosity to high-shear viscosity. For our purposes, the thixotropic index is the Brookfield viscosity at 5 rpm divided by the viscosity at 50 rpm.'
- 'The ability of wet *clay* to maintain a given shape.'
- 'The property possessed by certain *gels* of liquefying when shaken. This is the ability to resist draining off vertical surfaces while retaining spreadability under the applied stress of a brush, roller, or squeegee. Thixotropy should not be confused with viscosity ... a thixotropic liquid's viscosity is high when at rest and diminishes when stressed.'
- 'In *slip-casting*, bad drainage, brittleness, casting spots, cracking, blabbiness, pin holing are all due to too-low thixotropy, i. e., too fluid.'
- 'Property of certain materials to ... liquefy upon agitation ([*paint*] viscosity decreases upon application of shear during brushing or roller), and to stiffen to its original state when allowed to rest (viscosity increases). A product that possesses thixotropy can resist the pull of gravity.'
- 'The *ink* with good thixotropy is not good in leveling, while it is excellent in reproducibility and thick-coating.'
- 'Thixotropy... the viscosity of a substance decreases as the substance is set in motion by some mechanical action such as stirring or shaking. Thixotropy can be observed in *non-drip paints* – as the paint is being applied the viscosity drops and when the paint is on the wall the viscosity increases to its stationary value.'

Even the celebrated Encyclopaedia Britannica has a very strange definition of synovial fluid 'it is a markedly thixotropic fluid; that is, one which is both viscous and elastic'. Of course the proper definition of its rheological properties is 'viscoelastic'.

Helpful Internet Definitions

On the other hand, there are very helpful definitions. A good example is that found on the Thermo-Haake website [www.thermohaake.com/],

Definition of thixotropic flow behavior:

- Decrease of viscosity as a function of time upon shearing, 100% recovery (= regaining the original structures) as a function of time without shearing.

Determination

- Time curves – at *constant shear rate* to observe the destruction of the structures within the material, *dynamic (oscillation)* experiment or time curves after different waiting times to observe/determine the regeneration of the sample.
- Flow curves – *upwards and downwards (loop test)* at constant temperature. The hysteresis is a measure for the thixotropy.

Then the definition given in the IUPAC Compendium of Chemical Terminology 2nd Edition (1979, 51, 1217) (available online) is also very helpful:

- Thixotropy: see *work softening.*
- Work softening: the application of a finite shear to a system after a long rest may result in a decrease of the *viscosity* or the consistency. If the decrease persists when the shear is discontinued, this behavior is called work softening (or shear breakdown), whereas if the original viscosity or consistency is recovered this behavior is called thixotropy.
- Work hardening: opposite of *work softening*, in which shear results in a permanent increase of *viscosity* or consistency with time.

It is obvious then that, while most rheologists take a general view of thixotropy which covers all time effects

resulting from microstructure changes, in the popular image, the older idea of a transition on shearing–resting is still often held. Strictly speaking, what is usually meant by thixotropy in that case would now be termed *extremely shear thinning*, to give near solid-like properties at rest but flow under stress, as for instance in thixo-forming using metals or the addition of so-called thixotropes to paints.

A better and extended definition of thixotropy is clearly needed, and it should contain the ideas of both considerable shear thinning (i. e., gel–fluid transition) and also time changes over and above those encountered when in its structured state the thixotropic material might be viscoelastic with its attendant time effects.

9.2.2 Description of Thixotropic Phenomenon

General Considerations

As stated above, all liquids with microstructure can show thixotropy, because thixotropy only reflects the finite time taken to move from any one state of microstructure to another and back again, whether from different states of flow or to or from rest. The driving force for microstructural change is the result of the competition between breakdown due to flow stresses, build-up due to in-flow collisions, and Brownian motion. Brownian motion is the random thermal agitation of atoms and molecules that results in elements of the microstructure being constantly bombarded, which causes them to move to a favorable position where they can – given the necessary force – attach themselves to other parts of the microstructure. Very occasionally situations arise where existing weakly attached microstructural elements – brought together by collision during shear – are slowly torn apart by the constant action of the random Brownian motion. In that case, the opposite of thixotropy is seen, i. e., anti-thixotropy (rheopexy), where flow and rest destructures the material.

The general term microstructure, as used here, while usually associated in thixotropic systems with particles, can also mean alignment of fibres, favorable spatial distribution of particles in suspensions or drops in emulsions (Sect. 9.3), or entanglement density or molecular associations in polymer solutions. All these determine the level of viscosity and elasticity (Sect. 9.1), and they all take a finite time to change from one state to another under the action of shear and/or Brownian forces. In these cases, the *maximum microstructure* is seen when the alignment and spatial distribution are random (in three dimensions) and entanglement density is at a maximum. Both these conditions result in the greatest viscous (and usually elastic) response. On the other hand, *minimum microstructure* is when there is maximum alignment with the flow of fibres; the drop or particle spatial distribution is asymmetrical in the flow direction, or there are a minimum number of entanglements or associations – all these leading to minimum viscous and elastic response.

When the time scales involved in these changes become long compared with either the response of a viscometer (or rheometer, Sect. 9.1.1), or the flow time in a particular flow geometry, we can sensibly talk about thixotropy. These time scales often range from seconds to hours, with rebuilding usually taking much longer than breakdown.

Typical Behavior

If we place a thixotropic material into a viscometer/rheometer (Fig. 9.56) and apply a constant shear rate, the measured viscosity will decrease with time, but it will eventually tend to a steady, constant value. If we then switch off the shear and allow the material to rest for a some time (without drying or any other artefacts such as sedimentation or separation occurring) and switch the shear on again, the measured viscosity will initially be higher, but will decrease and end up at the same value as that seen after the original shearing. However, the level for the original value will not necessarily be the same, because that will depend on how carefully or vigorously the material was initially loaded and how long it was left to rest before shearing.

If on the other hand, a third experiment is performed where the material is allowed to come to equilibrium and then allowed to rest for the same length of time as before, the results will be identical. If now, after equi-

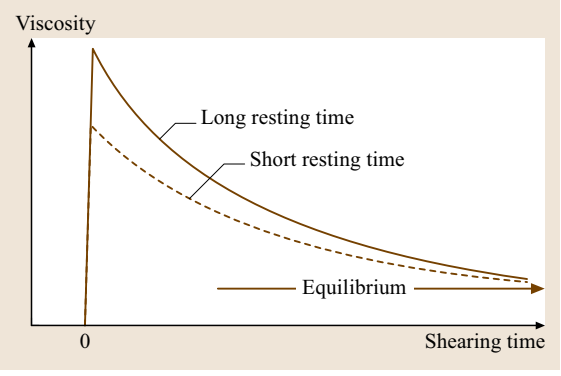

Fig. 9.56 Shearing a thixotropic liquid after short and long rest times

librium is achieved, the shear rate is instantaneously decreased to a lower value, the measured shear stress drops instantly, but thereafter it will slowly increase towards a new equilibrium. If instead of applying a given shear rate we applied a particular shear stress, then the inverse applies – the shear rate would increase as the structure breaks down and the change to another (lower) shear stress will result in a sudden decrease in shear rate followed by a further drop, Fig. 9.57.

If we now enquire what is happening on a microscale, we can imagine the picture in Fig. 9.58, where the viscosity/shear-rate behavior of a typical thixotropic material (which for the sake of argument could be a flocculated suspension) is presented. We start from a point where the microstructure at rest is a series of large flocs. Then, if the applied shear rate is increased progressively and sufficient time allowed, the floc size decreases until at a high enough shear rate, the floc has disintegrated completely into its constituent primary particles. Because large flocs *trap* more continuous-phase liquid than smaller flocs of the same particles, the viscosity is higher. The minimum viscosity is seen with individual particles.

We now imagine another experiment where the shear rate is increased stepwise from point a to end up at point b in Fig. 9.58. Instantaneously, the floc size will be that appropriate to the shear stress condition at point a, but as it experiences the higher shear rate at position a, it begins to erode, until it reaches an equilibrium size appropriate to the higher rate. This process can take some time. If now the opposite happens – the shear rate is instantaneously decreased – the individual particles (which gave the low viscosity) begin to collide and flocculate until the size of the flocs formed is appropriate to the new, lower shear rate. This process also takes time, with the build-up proceeding at a different rate to the breakdown.

Any concentrated suspension of particles is shear thinning, thus when we consider flocs, they show the phenomena as illustrated in Fig. 9.58. If we imagine that the particles in a floc are permanently glued together and thus the floc size is fixed, the flow curve of such a suspension of fixed-size flocs would follow the lines shown in the figure according to the floc size. If the floc size is now decreased (and the overall concentration maintained) but again the floc size remains unchanged when sheared, the flow curve will be lower and (for a given concentration) the degree of shear thinning decreases.

However because we are interested in systems flocculated in a secondary minimum, the size of the floc is not constant but decreases with increasing shear rate (or shear stress). Because viscosity decreases with floc size (see above), we now have a double shear-thinning effect. This means that flocculated systems are very shear thinning, see the equilibrium curve in Fig. 9.58. The extreme shear thinning also results in such flocculated, thixotropic systems appearing to have a yield stress, since the stress only decreases very slowly as the shear rate is decreased.

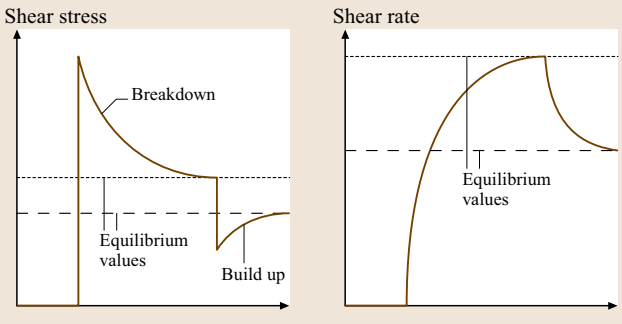

Fig. 9.57 Two kinds of step experiment and their effect on thixotropic liquids

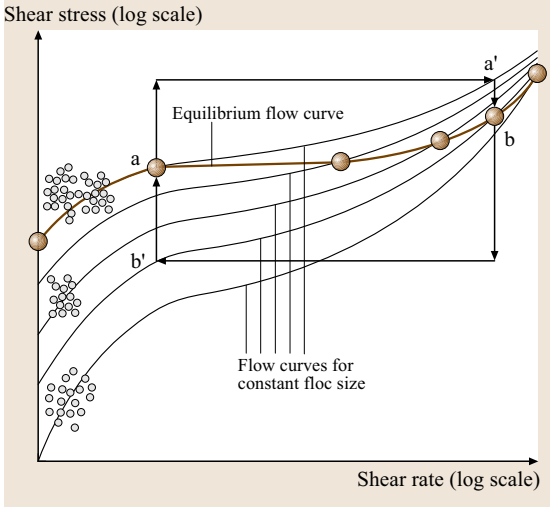

Fig. 9.58 The relationship between microstructure and (thixotropic) flow properties, illustrated for a flocculated suspension

The true steady-state behavior of a thixotropic liquid is seen both after an infinite shear time at any shear rate and shear stress of interest or infinite rest time. Of course, as all true equilibrium states are approached asymptotically, one comes close to this state after a long time rather than an infinite time, but even then, breakdown times of hours and days might be necessary to describe a very thixotropic system fully.

In a flocculated system, breakdown is towards an equilibrium situation that is governed by the balance of hydrodynamic shear stresses pulling structures apart by erosion, and of Brownian and shear forces building the structure up by collision and accretion of particles that agglomerate into flocs. The forces holding the structure together are colloidal in nature, acting over short distances ($\sim 10\,\mathrm{nm}$) within the composite particle (floc). At rest, only the Brownian rebuilding forces are present, and these are quite small compared to the shearing, with energies of of the order of $k_\mathrm{B}T$, where k_B is the Boltzmann constant and T is temperature. This means that the rebuilding time can be very long, since this small, random force takes a long time to rearrange large particles that, as flocs, are getting larger as they move into a more favorable structure, which is then manifested as a higher viscosity.

The typical response to a stepwise change from one steady-state condition to another in terms of the viscosity is often characterized by the so-called 'stretched-exponential' model:

$$\eta = \eta_{\mathrm{e},\infty} + (\eta_{\mathrm{e},0} - \eta_{\mathrm{e},\infty})\left(1 - \mathrm{e}^{-\left(\frac{t}{\tau}\right)}\right)^r , \qquad (9.192)$$

where $\eta_{\mathrm{e},0}$ is the viscosity at the commencement of shearing, $\eta_{\mathrm{e},\infty}$ is the viscosity after an infinite time, τ is a time constant and r is a dimensionless constant (which in the simplest case is unity). This equation can cope with build-up and breakdown in steps up or steps down with the values of τ and r depending on both the level and the direction, i. e., going from 0.1 to $1\,\mathrm{s}^{-1}$ will not have the same value of r found as going from 1 to $10\,\mathrm{s}^{-1}$. The values of r vary with the conditions of the test, as well as the particular system being tested and they decrease linearly with the log of the shear rate, typically from 0.7–0.9 at $10^{-2}\,\mathrm{s}^{-1}$ to 0.3 at $1\,\mathrm{s}^{-1}$ in *Mewis*'s experiments [9.108]. He also showed that, for a typical flocculated system (fumed silica in paraffin oil), τ is a decreasing function of $\eta_{\mathrm{e},0}\dot{\gamma}/\eta_{\mathrm{cont}}$, where η_{cont} is the viscosity of the continuous phase, which when taken into account properly describes the effect of temperature. (Mewis also reports optical, dielectric, and conductivity results on these systems.)

Mewis's approach was also used to describe the thixotropy of hydrophobically modified hydroxyethyl cellulose and nonassociative cellulose water solutions, see *Maestro* et al. [9.109]. The Mewis model fitted structure rebuilding experiments with an exponent r of around 2.

Heymann et al. [9.110] investigated the build-up after shearing of the yield stress of newsprint inks, with a formulation containing carbon black (Sect. 9.3). A period of pre-shearing was carried out at 1500 Pa, and then the flow curves were measured as a function of time. For inks, judged to have a yield stress, an equation similar to that above was used to describe the rebuilding of the shear stress

$$\sigma_\mathrm{y}(t) = \sigma_{\mathrm{y},0} + [\sigma_{\mathrm{y},\infty} - \sigma_{\mathrm{y},0}](1 - \mathrm{e}^{-\frac{t}{\tau}}) . \qquad (9.193)$$

For these materials so described, the values of τ were found to be well over 100 s. Because of this it was judged that the recovery behavior had no relevance to the printing process, because process times are of the order of a few seconds at most.

Not only can shear break down or build up flocs, but it can also change their internal morphology. For instance, the work of *Mills* et al. [9.111] showed that shearing freshly prepared flocculated suspensions can densify individual flocs, causing reorganization within the flocs. This shows how important it is to *condition* such systems before shearing them in experiments to elucidate their thixotropic behavior. They found that, following prolonged shearing, loosely packed flocs became tightly packed and more monodisperse. This can be interpreted as a loss of structure – rheomalaxis or rheodestruction.

The experiments of *Woithers* et al. [9.112] showed how important thixotropy can be in typical flocculated systems. They examined the behavior of a depletion-flocculated polymer latex suspension and showed that the shear stress dropped significantly with time, and the effect was still present after one hour. The values of the initial and final viscosities they found were at least an order of magnitude different. They also found that the unsheared samples contained more open flocs, while shearing flocs made fresh flocs that were denser.

Viscoelasticity and Thixotropy

Viscoelastic systems sheared in their linear region show time dependency because the microstructure takes time to respond to the flow/stress (Sect. 9.1). At short times (high frequencies) structures cannot respond quickly, and we see an elastic response, while at low frequencies, the system can adjust itself continuously, i. e., it can flow,

showing viscous effects (Sects. 9.1 and 9.1.1). Thus, when observed over all time (and frequency) scales, the system is viscoelastic.

For nonlinear viscoelastic – or simply inelastic but shear-thinning systems – not only does the microstructure take time to respond to the flow, but it is also changed by the flow and this change will itself take time. This is the essential difference between linear viscoelasticity and thixotropy – that while both are time effects, the former is in the linear region, where the structure responds but remains unchanged and the latter takes place in the nonlinear region where the structure is broken down by deformation as well as responding to it.

Shear thinning can occur for many reasons, e.g.,

- alignment of rod-like particles in the flow direction
- loss of entanglements in polymer solutions
- rearrangement of microstructure in suspension and emulsion flow
- breakdown of flocs

Since changes in any of these states take some time to come about (either from rest or from some other configuration), thixotropy is always (in principle) to be expected from a thinning mechanism. However thixotropy becomes significant when its time scale becomes significantly longer than the response times of instruments used to test rheology or longer than some flow time in a process, e.g., the average time for a liquid to flow through a pipe. Thixotropic time scales can be longer than viscoelastic time scales and practically important when these time scales become minutes and longer for breakdown. This will inevitably mean many more minutes or even hours for the recovery of the structural nature of most microstructural features that produce thixotropic effects (see above). It is obvious that, at conditions near the fully structured rest state, viscoelastic effects will also be seen. The typical response to a start-up experiment from a rest state shows this. Only a few theories have sought to account for this effect, which shows concurrently the breakdown/rebuilding of both viscous and elastic responses.

The picture presented becomes even more complicated when we consider the linear viscoelastic response of a rebuilding structure, where the typical storage and loss moduli – G' and G'' (Sect. 9.1) – evolve with time. This can be used as a measure of the rebuilding mode since the test is conducted at low-enough stresses/deformations that the evolving structure is unaffected by deformation. The growth of G' particularly is very sensitive to structure rebuilding. *Barut* et al. [9.113] studied an acrylic polymer solution in a mixture of solvents, with titanium dioxide (TiO_2) or a mixture TiO_2 and aluminosilicate particles. These were pre-sheared in a controlled-stress rheometer at 200 Pa for 2 min and after this ceased, the linear oscillatory properties were monitored for 10 min at strains of less than 0.1 over a frequency range of 0.03–62.8 rad s^{-1}. The form of the rebuilding curve of the storage modulus was also of a stretched-exponential form:

$$G' = G'_\infty - (G'_\infty - G'_0)\exp(-kt^p)\,, \qquad (9.194)$$

where G'_0 is the storage modulus at the commencement of oscillations, G'_∞ is the storage modulus after an infinite time, and k and p are material parameters.

Williams and *Ren* [9.114] used an oscillatory rheometer operating over the range 250–800 Hz to examine the rebuilding of 0.045 g/ml aqueous Laponite RD dispersions (synthetic-type clay, circular discs 300 × 10 Å), again measured by G' but now derived from the phase velocity. At these high frequencies, G' is a particularly sensitive measure of the structural solid-like response of the clay. They showed that restructuring was significant over the first 10 minutes or so, but was still going on after 20 minutes. Viewed on a log scale there is a rise from an initial value at small times and a fast build up through a power-law region, eventually (as it must) flattening out at times greater than 20 minutes.

Bouda and *Mikešová* [9.115] simultaneously monitored the AC conductivity and the storage modulus G' to establish the build-up of a carbon-black network in a polyethylene melt. After an initial period where the conductivity was constant, it then increased rapidly. The time a sample with 7.4% by weight took to show the rapid increase was nearly 200 min. Similar behavior was also observed for G'. They explained the observations as resulting from the setting up of a continuous network, and used percolation theory to show that the observed behavior was explainable on the basis of diffusion-limited aggregation of small clusters of primary carbon-black particles under the action of Brownian motion. As the flocs collide and stick together they eventually form an interconnecting network as the percolation threshold is reached, at which point the electrical conductivity and the storage modulus G' rose rapidly; see also [9.116].

On the other hand, *Greener* and *Connelly* [9.117] point out how easy it is to misinterpret thixotropy loops, particularly if there is viscoelasticity present in

the sample being tested. They compared the supposed thixotropic behavior of an aqueous poly-acrylamide solution with the behavior of the Wagner model (cf. Sect. 1.3) and show that all the effects are accounted for by the viscoelastic behavior alone, and not by true thixotropy.

9.2.3 Typical Thixotropic Experiments

Thixotropic/Hysteresis Loops

One of the favorite ways of measuring thixotropy is to perform a loop test; that is to say, to linearly increase the shear rate (or sometimes shear stress) from zero to a maximum value, and then to return at the same rate to zero. This test can then be repeated, until eventually an invariable loop behavior is seen; see Fig. 9.59. The area between the up and down curve is automatically measured in some computer-based rheometers as a measure of thixotropy.

However, this kind of test is to be depreciated, for although useful as a quick, qualitative test, the procedure has a number of disadvantages. First, the loop test is often carried out too quickly, and inertial effects due to the measuring head are introduced but not always recognized. (However, inertia effects can now be accounted for by some rheometer software packages.) Secondly, both shear rate and time are changed simultaneously, in a material where the flow properties are a function of both shear rate and time – as thixotropy obviously is. This is bad experimentation because the response cannot then be resolved into the separate effects from both variables from the one experiment. However the problem in interpreting the loop is even more difficult when we realize that the first part of the behavior on start-up is essentially elastic (cf. the overshoot in Fig. 9.13). As the strain becomes large this moves to nonlinear elastic response. If the behavior were just linear elasticity, then the strain in a simple loop test would increase parabolically, and the curve would be concave to start with, but soon turns over. At the same time the viscous behavior can become apparent, giving a tendency to flatten out. The viscous behavior then itself becomes nonlinear as the microstructure begins to break down at large strains. As the strain rate increases further, the liquid would like to shear-thin, but this takes time since the structure cannot adjust itself fast enough to the increasing shear rate. When the time is long enough and the structure has broken down, the down curve which will be under the up curve. Rebuilding will then begin to take place slowly. Even with an apparatus that responds perfectly to the stress and strain, interpreting the data to obtain the parameters corresponding to a model is very difficult, if not impossible.

A simpler and more-sensible test for a thixotropic liquid is performing and deriving results from stepwise experiments where the shear rate or stress is changed from one condition to another with a carefully controlled prehistory. Even so, it is impossible to eliminate the elastic response and instrument inertia.

Start-Up Experiments

Any experiment that starts from rest is another kind of thixotropic test. The typical behavior of strain- or stress-controlled experiments is shown in Fig. 9.60.

Most, if not all, thixotropic materials that have been at rest for some time show viscoelastic behavior, so the immediate response of such tests is elastic, then depending on the conditions, a thixotropic response will be seen

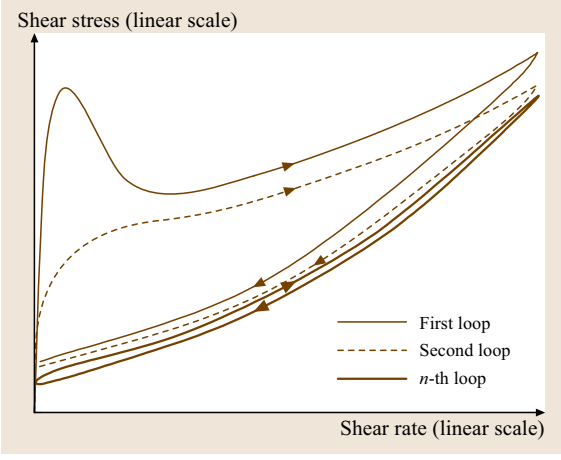

Fig. 9.59 A typical thixotropic loop test

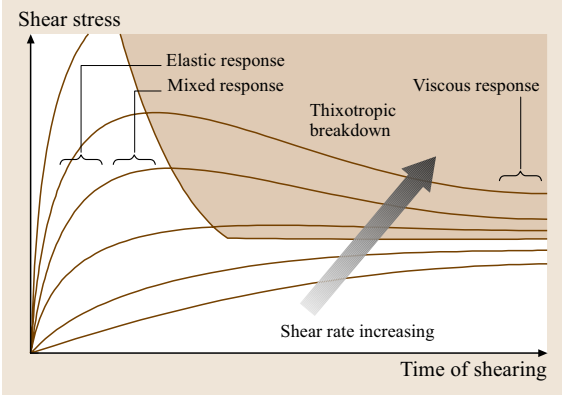

Fig. 9.60 Various regions of start-up flow

as an overshoot in the stress in strain-controlled experiments or an increase in the strain–time curve in creep tests (Sect. 9.1). This sometimes happens after a critical strain has been achieved. This initial elastic response giving way to a thixotropic viscous response makes the behavior quite complicated.

Artefacts Involved in Measuring Thixotropy

The greatest difficulty in understanding and modeling thixotropic materials is in knowing the effect of the – often unknown – deformation prehistory on the liquid of interest. This is particularly true in situations where a thixotropic liquid is subject to mixing and pumping, or even the seemingly simple task of filling a viscometer or rheometer. In both cases it would be interesting to be able to predict the subsequent flow even if only the initial response was known, say the initial torque on a viscometer operating at a certain shear rate, or the torque on a mixing vessel prior to the liquid being pumped out.

A number of methods have been devised to establish a consistent initial condition: fixed rest time after sample loading; pre-shear at a prescribed shear rate for a prescribed time followed by period; pre-shearing to equilibrium at a low shear rate followed by testing at a higher shear rate, etc. These eliminate the problem in characterization, but they can never completely eliminate the problem in practice, since the effects of prehistory on a previously untested sample are always unknown.

The mechanical inertia of the rotating members in viscometers and rheometers (Sect. 9.1.1) means that, in experiments where the shear rate or stress is changed quickly or instantaneously, the instrument response is delayed, and this is often mistaken for thixotropy, and even if thixotropy is present, this can complicate its measurement. Sometimes the presence of a low-compliance spring complicates the measurement because the output of the experiment relates to this spring response.

For isotropic materials, as we have seen, a typical source of thixotropy phenomenon is the breakdown of large flocs. However this also leads to the appearance of apparent slip at the wall, e.g., depletion giving large effects, see *Barnes* [9.118]. This is a case where observing the pressure gradient alone in a pressure-driven rheometer (Sect. 9.1.1) will not differentiate between or account for both effects. A detailed investigation of the flow profile will alone show what is happening. As well as pipe flows, there are many apparently simple flows where the shear rate or shear stress is not constant spatially, for instance, concentric cylinders and parallel plates (Sect. 9.1.1). These geometries are often used in the rheological characterization of thixotropic liquids, and unwittingly many workers are unaware of the complications.

9.2.4 Semi-Empirical Phenomenological Theories Used to Fit Experimental Data

Requirements of Useful Models

The ideal model to describe thixotropic behavior would start from the fact that some rheology-determining physical entity takes time to change when the flow field around it is changed or is changing. As we have already said, this might be, for example, the size of a floc, the orientation angle of an alienable particle, or the density of transient entanglements. In the simplest models, all such fundamental parameters change instantly with shear, shear rate, or shear stress. First we have to know at what rate these changes take place, and then if we know how the microstructure relates to the stress, we can predict the overall behavior. Most workers in this field have used theories to describe viscous thixotropic phenomena while only a few have attempted to describe viscoelastic effects. Representative classes of theories are described below and others in that field are noted.

Viscous Theories

Current theories for thixotropy fall into three groups: first those that use a very good description of microstructure described by a numerical value of a scalar parameter, typically λ and then use $d\lambda/dt$ as the working parameter; second those who attempt some description of the temporal change of the microstructure as for instance the number of bonds, or attempt to describe real floc architecture using fractal analysis, and third those that use time data itself on which to base a theory.

Indirect Microstructural Theories

Most workers in this area have developed mathematical theories of thixotropy. Based on some numerical scalar measure of structure, often designated by λ and using this simplistic concept, the completely built structure is represented by $\lambda = 1$ and completely broken down by $\lambda = 0$. In the simplest case of a typical, inelastic, non-Newtonian liquid with upper and lower Newtonian viscosity plateaux, $\lambda = 1$ corresponds to the zero-shear viscosity η_0 and $\lambda = 0$ corresponds to the lower asymptotic viscosity at an *infinite* shear rate η_∞, with λ taking intermediate values between.

Thixotropy is then usually introduced via the time derivative of the structure parameter $d\lambda/dt$, which is given by the sum of the build-up and breakdown terms, which in the simplest theories are only controlled by the shear rate and the current level of the structure λ. The general description of the rate of breakdown due to shearing is given by the product of the current level of structure and the shear rate raised to some power. The driving force to build up is controlled by the distance the structure is from its maximum value, raised to another power. Thus

$$\frac{d\lambda}{dt} = g(\dot{\gamma}, \lambda) = a(1-\lambda)^b - c\lambda\dot{\gamma}^d \,, \tag{9.195}$$

where a, b, c, and d are constants for any one system. The value of the function $g(\dot{\gamma}, \lambda)$ is negative if the system is breaking down towards equilibrium; if it is positive, it is building up to equilibrium. At equilibrium, for every value of shear rate there is a particular value of λ, which in the equation is found by setting $d\lambda/dt$ to zero.

Godfrey [9.86] summarized the development of these two-process models beginning with

- *Goodeve* and *Whitfield* in 1938 [9.119], which led to an earlier version of the above equation
- to *Moore* [9.120] with both b and d as unity,
- progressing through *Cheng* and *Evans* [9.121] with b unity, but d being non-unitary,
- through to the very general *structural kinetic* model of Mewis, with both powers taking non-unitary values, the formulation used by Lapasin's group [9.122].

The next step in this kind of approach is to relate the λ – as calculated using the equations above – to the stress σ or viscosity η in some suitable equation. As we shall see this has been done in a variety of ways which range from the Bingham equation

$$\sigma = \sigma_y + k\dot{\gamma} \tag{9.196}$$

through the Cross model to a Cross-like model containing a yield stress. Most of the differences between the theories in this area are accounted for in combinations of these structure change and structure–viscosity formulations.

Baravian et al. [9.123] proposed a modification of the Cheng and Evans approach. Their study is worth looking at in detail for two reasons. First it follows the traditional route to describe thixotropy, and second, it shows how long and seemingly involved the procedure to describe thixotropy becomes.

They postulate that the relationship between viscosity and structure is given by

$$\eta(\sigma, t) = \eta(\lambda) = \frac{\eta_\infty}{(1-K\lambda)^2}, \; K = 1 - \left(\frac{\eta_\infty}{\eta_0}\right)^{-\frac{1}{2}} . \tag{9.197}$$

This assumes that the effect of stress on the viscosity is also accounted for by the current value of the structural parameter λ, which can be written

$$\lambda = \left[1 - \left(\frac{\eta_\infty}{\eta}\right)^{\frac{1}{2}}\right] / K \,, \tag{9.198}$$

where η is the current value of viscosity. Then for any system one has to find the values of η_0 and η_∞ (and thus, K), and from these, all values of η can be converted into values of λ. They assume that the relationship between the equilibrium value of the structural parameter λ and the shear stress σ is given by

$$\lambda_{\text{equil}}(\sigma) = \left[1 + \left(\frac{\sigma}{\sigma_c}\right)^p\right]^{-1} \,, \tag{9.199}$$

where σ is the shear stress and σ_c is its critical value.

From any one particular equilibrium position of stress, 1 Pa jumps were made up and down, and plots of $d\lambda/dt$ versus λ were made. These were of the form

$$\lambda = \frac{1}{t_a}\left(1 - \frac{\lambda}{\lambda_{\text{equil}}}\right) . \tag{9.200}$$

This kind of curve was obtained for many values of equilibrium stress. The values of the constants were then described by the equation:

$$\lambda(t) = \lambda_{\text{equil}} + (\lambda_{\text{ini}} - \lambda_{\text{equil}}) \exp\left(-\frac{t}{t_a}\right) \,, \tag{9.201}$$

where λ_{ini} is the initial value of λ.

Thus, for all values of stress, they could now define λ_{ini}, λ_{equil}, and t_a. Using the stress-up as well as stress-down data, the values of t_a were the same. This theory was used to describe a loop test very well, once instrument inertia had been accounted for.

Other variations on this theme include that of *De Kee* et al. [9.124] (following *Tiu* and *Boger* [9.125]) who described the breakdown behavior of various food systems by

$$\frac{d\lambda}{dt} = -c\dot{\gamma}^d(\lambda - \lambda_{\text{equil}})^n \,, \tag{9.202}$$

where c is a constant parameter.

The stress was then described by a multiple exponential-type flow law given by

$$\sigma(\dot{\gamma}) = \lambda \left[\sigma_0 + \dot{\gamma} \sum_i \eta_i \exp(-t_i \dot{\gamma}) \right] , \qquad (9.203)$$

where η_i and t_i are the model parameters. The theory was used to characterize viscosity decay curves for yoghurt and mayonnaise.

Direct Structure Theories

Denny and *Brodkey* applied reaction kinetics to thixotropy via a simple scheme that described the distribution of broken and unbroken bonds [9.126]. The number of these bonds was later related to the viscosity. The forward and reverse rate constants, k_1 and k_2, represented the breakdown characteristics in flow, and the build-up kinetics, see for instance *van den Tempel* [9.127] who related the flocculated system of fat globules. Denny and Brodkey wrote the rate of structure breakdown as (cf. *Ruckenstein* and *Mewis* [9.128]):

$$-\frac{\mathrm{d(unbroken)}}{\mathrm{d}t} = k_1(\mathrm{unbroken})^n - k_2(\mathrm{broken})^m , \qquad (9.204)$$

and solved to give the viscosity by assuming that it is linearly proportional to the unbroken structure, with a maximum value (η_0) when completely structured and a minimum value (η_∞) when completely destructured. The rate constant k_2 is assumed to be independent of shear rate, being merely a description of Brownian collisions leading to restructuring and the rate of breakdown constant is related to shear rate by a power-law expression.

The way the well-known Cross model was derived is instructive [9.129]. Assuming that the structured liquid was made up of flocs of randomly linked chains of particles, Cross described a rate equation of the form:

$$\frac{\mathrm{d}N}{\mathrm{d}t} = k_2 P - (k_0 + k_1 \dot{\gamma}^m) N , \qquad (9.205)$$

where N is the average number of links per chain, k_2 is a rate constant describing Brownian collision, k_0 and k_1 are rate constants for the Brownian and shear contribution to break down, P is the number of single particles per unit volume, and m is a constant less than unity. At equilibrium $\mathrm{d}N/\mathrm{d}t$ is zero, so

$$N_\mathrm{e} = \frac{k_2 P}{k_0(1 + \frac{k_1}{k_0}\dot{\gamma}^m)} . \qquad (9.206)$$

Then, assuming that the viscosity was given by a constant η_∞ plus a viscous contribution proportional to the number of bonds N_e, he derived his well-known relationship

$$\frac{\eta - \eta_\infty}{\eta_0 - \eta_\infty} = \frac{1}{1 + \frac{k_1}{k_0}\dot{\gamma}^m} , \qquad (9.207)$$

where η_e is the equilibrium value of viscosity at long time of shearing (cf. (9.247) in Sect. 9.3).

Cross could have used the nonequilibrium data to derive a thixotropic model, which others did later using his model.

Lapasin et al. [9.130] used a fractal approach to describe flocculated suspensions. They argued that

$$\frac{\mathrm{d}N_\mathrm{max}}{\mathrm{d}t} = a(N - N_\mathrm{max}) - b\sigma^q(N_\mathrm{max} - N_\mathrm{max,\infty}) , \qquad (9.208)$$

where N_max is the number of primary particles in a floc, $N_\mathrm{max,\infty}$ is the lower limit to which N_max tends as the shear stress σ becomes infinite, and a and q are material constants. This can be solved for $N \gg N_\mathrm{max}$ to give

$$N_\mathrm{max} = N_\mathrm{max,\infty} + \frac{aN}{b}\sigma^{-q} , \qquad (9.209)$$

which yields

$$\left(\frac{\eta}{\eta_\mathrm{s}}\right)^{-\frac{1}{2}} = 1 - \frac{\phi}{\phi_\mathrm{max}} \frac{B + A\left(N_\mathrm{max,\infty} + \left(\frac{\sigma}{\sigma_\mathrm{c}}\right)^{-q}\right)^{\beta+1} - 1}{B + N_\mathrm{max,\infty} + \left(\frac{\sigma}{\sigma_\mathrm{c}}\right)^{-q} - 1} , \qquad (9.210)$$

where ϕ is the volume fraction of flocs, and A and B are constants, whereas $\beta = 3/D - 1$, where D is the fractal dimension of the floc.

This equation describes the breakdown of flocs under flow, and predicts a yield stress and a high-shear-rate viscosity. It described very well the behavior of both titanium dioxide (TiO_2) and mica dispersions in steady state. (A much more-complicated theory of this kind had been proposed much earlier by *Eyring* [9.131].)

Simple Viscosity Theories

Frederickson [9.132] formulated an expression for the rate of change of fluidity Θ (the inverse of viscosity) of a non-Newtonian system as

$$\frac{\mathrm{d}\Theta}{\mathrm{d}t} = k_1\dot{\gamma}^2\left(\frac{\Theta_\infty - \Theta}{\Theta}\right) - k_2(\Theta - \Theta_0) . \qquad (9.211)$$

He used this expression for steady-state flow ($d\Theta/dt = 0$), recovery at rest (i. e., zero shear rate), the sudden application of a step stress, and a loop test. Like the Cross model, this model also has higher and lower Newtonian plateaux at equilibrium, and if the quadratic dependence on shear rate is replaced a power-law relationship, they become similar.

Mewis and *Schryvers* [9.133] devised a theory that also circumvents the use of any parameter such as λ, and instead used the viscosity as a direct measure of structure. They proposed that the rate of change of viscosity rather than rate of change of structure be the viscosity difference between the steady state and current values of viscosity (not the structure difference), viz.

$$\frac{d\eta}{dt} = K[\eta_s(\dot{\gamma}) - \eta]^n \,, \tag{9.212}$$

where η_s is the steady-state viscosity.

This integrates to give

$$\eta = \eta_{e,\infty} - (\eta_{e,\infty} - \eta_{e,0}) \times \{[(\eta - 1)Kt(\eta_{e,\infty} - \eta_{e,0})^{n-1} + 1]^{n-1} + 1\}^{1/(1-n)} \,. \tag{9.213}$$

In the notation $\eta_{e,0}$ and $\eta_{e,\infty}$ the initial subscript refers to the fact that the viscosities referred to are at equilibrium, while the second refers to the shear rate.

Mewis and Schryvers then made the (Newtonian) assumption that $\eta_{e,0} = \eta_{e,\infty} = \mu$, which makes the equation simpler since it is much easier to measure the eventual viscosity of the initial steady-state condition. This assumes that the viscosity at the end of the initial steady-state period as that at the beginning of the new shear-rate test, i. e., that the system is essentially between those conditions. This is reasonable under some conditions but, as Mewis's work has shown, it is only strictly true for most systems at higher shear rates. Using a value of n of 5/3, they fitted experimental data very well for carbon black in mineral oil.

Kristen et al. [9.134] modeled the thixotropic breakdown behavior of maize starch pastes using the equation:

$$(\eta - \eta_\infty)^{1-m} = [(m-1)kt + 1](\eta_0 - \eta_\infty)^{1-m} \,, \tag{9.214}$$

where η_0 and η_∞ are the asymptotic values of viscosity η (representing the fully structured and fully destructured states, respectively) measured at time t for any particular shear rate $\dot{\gamma}$, and k and m are material constants. This approach had been used with previous minerals and industrial suspensions [9.135]. For the starch paste they studied the data was satisfactorily described by $m = 3$. Over the shear rate range tested, the steady-state flow curves could be described by a power-law model.

Viscoelastic Theories

Almost any viscoelastic theory can have thixotropy introduced if the particles that give the viscous and elastic responses are made to change in the way we have described for purely viscous behavior. Probably a model due to *Acierno* et al. [9.136] gives the best example of this approach. They considered a model based on a series of Maxwell elements (Sect. 9.1). The number of elements in their model was such that they could be represented by a continuous spectrum. Simplifying the model to a discrete series, it is possible to write the behavior as

$$\sigma = \sum\nolimits_i \sigma_i \,, \quad \frac{\sigma_i}{G_i} + \theta_i \frac{d}{dt}\left(\frac{\sigma_i}{G_i}\right) = \theta_i \dot{\gamma} \,, \tag{9.215}$$

where σ_i is the stress, G_i the modulus, and θ the relaxation time ($= \eta_i/G_i$) of the i-th element in the discrete spectrum.

Thixotropy is introduced via the well-used structure parameter λ (labeled x_i in their paper):

$$G_i = G_{0,i}\lambda_i \,, \quad \theta_i = \theta_{0,i}\lambda_i^{1,4} \,. \tag{9.216}$$

The rate equation is then given by

$$\frac{d\lambda_i}{dt} = \frac{1-\lambda_i}{\theta_i} - \frac{a\lambda_i}{\theta_i}\left(\frac{E_i}{G_i}\right)^{\frac{1}{2}} \,, \tag{9.217}$$

where E_i is the instantaneous elastic energy in the i-th element. This is the same as the Moore linear model [9.84], except that the shear rate is now replaced by the generalized expression $(E_i/G_i)^{1/2}/\theta_i$ that accounts for the elasticity as well as the viscosity. The theory gives an excellent description of most of the rheological behavior of a low-density polyethylene melt in shear and extensional transient and steady-state flow. The model is equivalent to the Moore model if reduced to the viscous case. *Shoong* and *Shen* [9.137] introduced a power-law dependence in the breakdown term, which then compares with the Cheng and Evans' inelastic model.

Quemada [9.138] developed a thixotropic model based on an explicit viscosity–structure relationship, $\eta(S)$, between the viscosity and a structural variable S. Under unsteady conditions, characterized by a reduced shear rate, $\gamma(t)$, shear-induced structural change obeys a kinetic equation (through shear-dependent relaxation times). The general solution of this equation is a time-dependent function, $S(t) = S[t, \gamma(t)]$. Thixotropy was modeled by introducing $S[t, \gamma(t)]$ into $\eta(S)$, which

led directly to $\eta(t) = \eta[t, \gamma(t)]$ without the need for any additional assumptions in the model. Moreover, whilst observation of linear elasticity requires small enough deformation, i. e., no change in the structure, larger deformations cause structural buildup/breakdown, i. e., the presence of thixotropy, and hence leads to a special case of nonlinear viscoelasticity that can be called *thixoelasticity*. Predictions of a modified Maxwell equation, obtained by using the above-defined $\eta(S)$ and assuming $G = G(0)S$ (where $G(0)$ is the shear modulus in the resting state defined by $S = 1$) were discussed in the case of start-up and relaxation tests. Similarly modified Maxwell–Jeffreys and Burger equations (Sect. 9.1) are used to predict creep tests and hysteresis loops. Discussion of model predictions mainly concerned both the effects of varying the model variables or/and the applied shear-rate conditions and comparisons with some experimental data.

9.2.5 The Breakdown and Build-Up of Isolated Flocs

Two key mechanisms of thixotropy for typical systems are floc erosion and Brownian collisions. Work has been published on these topics for diluted flocs and it is instructive to relate these studies to thixotropic build-up and breakdown of suspensions of flocs.

The diffusion rate of isolated flocs decreases significantly as their size grows. *Reynolds* and *Goodwin* [9.139] measured the diffusion coefficients of isolated flocs and found a rapid decrease of diffusion rate with floc size, with the particular value depending on the floc geometry, which they studied as linear or clustered flocs. As these are quite moderate floc sizes, it is obvious that flocs of hundreds or thousands of primary particles will move very sluggishly. The effect of primary particle size on translational diffusion coefficient was worked out by Einstein as a simple inverse dependence on size (cf. (3.203) in Sect. 3.7). However the rotational diffusion of particles scales as the inverse cube of particle size [9.140]. This behavior explains why exponential expressions for rebuilding contain a driving force such as $(1 - \lambda)$ because rebuilding starts as the floc size grows and the diffusion coefficient decreases. This means that collisions become less frequent, and as rebuilding progresses it gets slower and slower, but theoretically never stops.

The breakdown of isolated flocs in imposed shear fields has been studied by a number of workers. *Sonntag* [9.141] summarized the results as $d_f = C\dot{\gamma}^s$ where s has been measured as 0.2 or 0.5. The surface shear force experienced by an isolated floc is given by the product $d_f d\eta\dot{\gamma}$, where d_f is the floc size, d is the size of the primary particles, η is the viscosity of the continuous phase, and $\dot{\gamma}$ is the shear rate. It is this force which produces surface erosion of primary particles if it is greater than some bond shear strength between the primary particles, see *Mûhle* [9.142]. This expression shows that breakdown in a given shear field is fastest for the largest sized flocs, i. e., at the shortest times as being proportional to the shear rate raised to a power. These facts are reflected in the structure breakdown criteria normally used, $d\lambda/dt \propto -\lambda\dot{\gamma}^n$.

9.2.6 Examples of Systems and Studies from the Literature

Previous Work

There are a very large number of systems that have been found to be thixotropic; previous reviews have listed many examples (see *Bauer* and *Collins* [9.83], *Mewis* [9.84], *Cheng* [9.85], and *Godfrey* [9.86]). Here a set of largely new examples is given, with special emphasis on hitherto unreported eastern European and oriental studies.

The present author (*Barnes* [9.87]) has produced extensive tabulations of work on specific thixotropic systems in the following areas:

- Thixotropic paints, inks and coatings: when coatings are applied to vertical or inclined surfaces, the time taken for rebuilding to occur can cause the material to drain. This is obviously undesirable. The thixotropic breakdown of paints is important when such paints are being put onto the brush or brushed out. The desirable properties of nondrip paint might appear quite quickly, but the paint has to be worked to make it thin enough to apply evenly.
- Thixotropic detergent systems: thixotropy in commercial detergent liquids can give rise to problems when they have to be poured from containers or poured into machines. Then dispersion can be a problem. If rebuilding is very slow, physical instability can result due to sedimentation or creaming.
- Thixotropic clay systems: clays are probably the best known examples of thixotropy, because of the extreme changes brought about by shear. A clay suspension can be shaken in a bottle, and the sound generated is almost water-like, but on standing the clay becomes completely gelled and manifests a ringing sound if tapped in a glass container. Clays such as the natural bentonites and the manufactured

and modified Laponites, because of the extensive nature of the very thin sheets from which they are made up, give a very good thickening effect without giving the unwanted viscoelastic effects found in some kinds of polymeric thickeners. However, because of the size of these clay sheets, the rate of structuring is very slow and also the difference between the fully formed structure at rest and the flowing dispersion is large.

- Thixotropic oils and lubricants: greases are thixotropic because of the flocculation of the dispersed material suspended in an oil phase. This is very important in lubricating situations where the grease has to break on shearing so that no unwanted extra drag is experienced in bearings.
- Thixotropic coal suspensions: coal–oil and coal–water suspensions show considerable thixotropy, and problems with start up of pumps and after stopping the flow can be quite severe. The pump duties required for flow of sheared suspensions are very different from start up of a rested suspension. This can result in pump failure, since start-up torques can be very high.
- Thixotropic metal slushes: if metals are sheared just below their melting point, they take on the appearance of a shear-thinning liquid. However, they have been described as thixotropic. While they might possess some thixotropy, the title is probably a misnomer because shear thinning is perhaps more important than thixotropy. In fact, as stated above, thixotropy is probably a nuisance, because what is needed is a fast-responding, very shear-thinning, liquid-like material for casting.
- Thixotropic rubber solutions: the manufacture of black rubber tyres, etc., uses carbon black. When dispersed, carbon-black particles are attracted to one another, and form a network throughout the rubber solution. The latter itself is shear thinning, and the carbon-black network also renders a degree of shear thinning, but is also thixotropic.
- Thixotropic food and biological systems: many food and biological systems are well known examples of thixotropy. For instance, flow makes them thinner, but leaving them to rest thereafter thickens them again. Thixotropy in food thickeners such as xanthan gums can cause problems in that the suspending properties given to liquids may take time to appear after shearing and this could cause some initial sedimentation or creaming of suspended material.
- Thixotropy in creams and pharmaceuticals products: creams and other personal-product and pharmaceutical materials are given *body* by using so-called thixotropes that happen to be thixotropic. Here the original meaning of thixotropy of conferring gel-like properties is still very often the controlling idea. The time effects seen using these materials are therefore again only of nuisance value.

Published Work on the Engineering Consequences of Thixotropy

Flow in Mixers. *Edwards* et al. [9.143] found that the behavior of a range of thixotropic materials in a series of mixers was quite easy to characterize if one assumed that the mixer behaved as a viscometer running at the same shear rate as the average shear rate in the mixer. An average shear rate for the flow in a cylindrical vessel with anchor, helical ribbon or helical screw impellers is given by the impeller rotational speed N (rev s^{-1}) times a constant depending on the impeller geometry, k, where values of k ranges from about 12 for the helical screw, to around 20 for the anchor, or 30 for the helical ribbon. They compared the torque produced by the mixer with the signal from a viscometer running at the same shear rate, both of which could halve over the course of the experiment. For salad cream, tomato ketchup, yoghurt, paint and 3 and 4% aqueous Laponite dispersions, they found that the average viscosity as a function of time in the mixer at a given impeller speed compared well with that in a viscometer running at the same shear rate. For the salad cream, tomato ketchup, and paint, the viscosities agreed to within 10%. The predicted values for 3 and 4% Laponite agreed reasonably well for the anchor and helical ribbon, but were 20–40% too low for the helical screws. This latter fact was probably due to the strongly non-Newtonian behavior and nature of the Laponite dispersions.

Flow in Pipes. When a thixotropic liquid enters a long pipe from a large vessel where it has been at rest, the development of the velocity and pressure fields in the pipe is very complicated. The large pressure involved in the start-up of flow of a thixotropic liquid can cause problems in terms of the necessary pump performance. Often cavitation can be the cause, since even though the pump could cope with sheared material, it might be unable to initiate flow of the material that has been at rest for some time. Cavitation in the liquid within the pipe can also occur.

Once flow has started, the liquid near the pipe wall is subjected to the highest shear rate and the lowest velocity; hence it is subjected to the shear for longer than the fluid flowing in the middle of the pipe. This re-

sults in a very fast and prolonged breakdown near the wall, giving a low-viscosity layer that effectively lubricates the inner, more-viscous layers (the phenomenon quite similar to the one expected for a purely Bingham fluid possessing a yield stress). If the pipe is long enough, the flow profile will evolve such that eventually the steady state profile is established. However, for short pipes the flow can be quite complicated, with a nonlinear pressure profile being a distinct possibility. Distinguishing thixotropy from a developing slip layer caused by particle depletion can be very complicated (*Barnes* [9.114]).

Schmitt et al. [9.144] derived an equation for the prediction of the mean value of the friction factor during the flow of a thixotropic fluid in a horizontal rectilinear cylindrical pipe. According to their equation, the pressure drop is a function of three dimensionless numbers: the generalized Reynolds number Re standing for the ratio of inertial to viscous forces for an Ostwaldian fluid, a modified memory effects number, the Deborah number $\mathrm{De} = \theta/t_{\mathrm{ch}}$, where θ is the characteristic memory time, and t_{ch} the characteristic flow time, and a *structural* number Se, which is correlated to the maximum breakdown of structure of the fluid. This equation is only valid for laminar flows and is based on several hypotheses described in [9.144]. The rheological model used in [9.144] is based on a structural approach, featuring a rheological state equation describing shear stress, and a structural decay equation. The fluid was stirred yoghurt and its structural parameter λ follows a second-order kinetic equation. Experimental validation of the friction factor formula showed good agreement.

Recent Publications on the Subject of Thixotropy

Much work has been presented since the present author originally reviewed the thixotropy literature in 1997 [9.87].

Chinese workers seem to be leading the field recently in studying thixotropic systems and their work deserves separate mention. First *Hou* et al. [9.145] showed a novel type of thixotropic or, as they called it, complex behavior. Similarly *Li* et al. [9.146] looked at the effect of pH on the thixotropy of ferric aluminium magnesium hydroxide/montmorillonite suspensions. They found that for relatively low ratios of Fe-Al-Mg-mixed metal hydroxide, MMH, to sodium montmorillonite (MT, 0, 0.012 and 0.051 by weight), when the pH was slowly increased, the suspension behavior changed from negative, anti-thixotropy (rheopexy), to typical thixotropy; when the ratio of MMH to MT was relatively high (0.091), rising gradually, the suspension behavior changed from 'complex' thixotropy to negative thixotropy (rheopexy) with increasing pH. In another series of similar experiments reported by *Li* et al.[9.147], thixotropy and negative thixotropy (rheopexy) were reported. This showed the complex effects of time and shear rate in influencing the microstructure. The experiments were carried out by first shearing the suspension at high shear rate to destroy the microstructure of the suspension, then monitoring the change of the viscosity or stress with time at a low shear, i. e., to study the process of structure recovery. The shear history and the shear rate strongly influenced the recovery process for MMH/MT suspensions. The system with a weight ratio (R) of MMH/MT of 0.0 and with $R = 0.013$ both show typical thixotropy in the shear-rate range 10–1022 s^{-1}, i. e., shear rate does not change the thixotropic type behavior of the suspensions. The suspension with $R = 0.051$ showed complex thixotropy under lower shear-rate values (10 and 170 s^{-1}), but showed negative thixotropy (rheopexy) under higher shear-rate values (511 and 1022 s^{-1}). The system with $R = 0.091$ showed negative thixotropy (rheopexy) at lower shear-rate values (10 and 170 s^{-1}), but shows complex thixotropy at higher shear-rate values (511 and 1022 s^{-1}). With increasing shear rate, the viscosity of these suspensions decreases gradually, and the degree of change in viscosity similarly slows down, i. e., the thixotropic behavior becomes weaker.

Li et al. [9.148] have also reported on the influence of measuring conditions on the thixotropy of hydrotalcite-like/montmorillonite (HTlc/MT) suspensions. Three kinds of these suspensions were studied, their mass ratios of HTlc to MT, R, were 0.013, 0.051, 0.091, respectively. The HTlc/MT suspension with $R = 0.013$ showed normal thixotropy at zero time of shearing, $t(s) = 0$, but it changed to rheopexy with increasing $t(s)$. The suspension with $R = 0.051$ transformed from complex thixotropy at low shear rate or positive thixotropy at high shear rate into negative thixotropy (rheopexy) with increasing $t(s)$. The suspension with $R = 0.091$ showed complex thixotropy when the shear rate was 1022 s^{-1}, and showed negative thixotropy (rheopexy) at 10 s^{-1}. However, the suspension changed from negative thixotropy to the weak complex one with increasing $t(s)$ when the shear rate was 170 or 341 s^{-1}. For all the systems, the equilibrium viscosity decreased gradually with $t(s)$ at the low shear rate, but the equilibrium viscosity increased with $t(s)$ at high shear rate because of the memory effect.

Last of all for these systems, we quote the work of *Li* et al. [9.149] on the influence of electrolytes

on the thixotropic behavior of ferric aluminum magnesium hydroxide-montmorillonite suspensions [Fe-Al-Mg-MMH and Na-montmorillonite (MT)]. When sodium or magnesium chloride were added to the suspension, the thixotropy of the suspension changed from positive and complex into negative thixotropy (rheopexy), but the electrolytes did not change the thixotropic type of a rheopexic suspension. When aluminium chloride was added to positive thixotropic systems, they were transformed to a complex one, whereas a complex and negative thixotropic suspension remains unchanged, for additions less than 0.01 mol/L; when the level of added aluminium chloride was increased, all types of thixotropic systems are changed to non-thixotropic! In addition, both sodium and magnesium chloride controlled the initial viscosity, measured after cessation of intensive shearing increase, but the value of the viscosity decreased rapidly with time. The equilibrium viscosity of the suspension decreased gradually with increasing concentrations of chlorides in the suspension. With increasing concentration of aluminium chloride, the equilibrium viscosities of the positive thixotropic suspension and the complex thixotropic suspension increase at first, but later decreased, and the equilibrium viscosity of negative thixotropic (rheopexic) suspensions decreased gradually.

The thixotropic properties of mixed suspensions containing oppositely charged colloidal particles were studied by *Guo* et al. [9.150]. In particular, the rheological properties of single-component clay dispersions and clay/MMH mixed dispersions containing oppositely charged colloidal particles were investigated. As the clay concentration is increased, the clay suspensions develop from Newtonian to *yield-stress* behavior. Adding sodium chloride to clay/MMH mixed suspensions caused a decrease in the yield values and apparent viscosities. In the structural recovery measurements, the time dependence of viscoelastic properties of clay/MMH mixed dispersions showed only very small variations of the storage moduli over three hours, in contrast to unusual thixotropic properties of aqueous single-component dispersions of Laponite or MMH. The results were explained using attractive electrostatic interactions between clay and MMH particles due to their opposite charges, similar to the edge(+)/face(-) interactions in single-component clay dispersions at low pH values.

Sun et al. [9.151] investigated the rheological properties of aqueous dispersions of the aluminium–magnesium mixed-metal hydroxide (MMH), which forms solid-like structures. Special emphasis was placed on thixotropy, with structural recovery at rest after steady shear, was characterized by steady shear and small-amplitude oscillatory shear measurements. With increasing MMH concentration, the behavior changed from predominately viscous to a solid-like response. The magnitude of the storage modulus, G', increased strongly and became less dependent on frequency with increasing MMH concentration. After cessation of steady shear, the complex viscosity increased monotonically with time and even after three hours no equilibrium viscosity value was seen, while shear stress under steady rate of $10\,s^{-1}$ approached the equilibrium value only after about 10 min. The recovery of the MMH suspension after cessation of steady shear was strongly affected by pre-shear history and rebuilding time, so that the greater the intensity of pre-shearing, the lower the values of the elastic moduli after pre-shearing had ceased. Conversely, the longer the rebuilding time, the larger the values of the elastic moduli. These results were similar to those obtained for clay dispersions of different ionic strength and clay concentration. Similarities in particle size and shape, though oppositely charged, and rheology between the two systems provided indirect evidence of similar rebuilding mechanism, so it was assumed that, for positively charged MMH suspension, long-range electrostatic double layers forces led to the formation of a solid-like structure.

The rheological properties of calcium-carbonate-filled polypropylene were examined by *Wang* and *Yu* [9.152] using a Rheometrics dynamic analyzer. The study included steady-shear tests, transient stress growth tests with sequential deformation history, and two-step dynamic oscillatory shear flow. Thixotropic behavior was observed in transient tests for highly filled compounds at volume loading exceeding a critical value at about 20%. The material responses of these viscoelastic thixotropic materials depended on the duration of shear as well as on the rate of shear. The effects of filler on the rheological behavior of highly filled compounds were dominant at low strain rates; however, the effects of activity of the filler were almost negligible at high strain rates because of complete breakdown of the filler network. The time scales for structural changes in filled systems often lengthened compared with the viscoelastic time constants of the unfilled melt. The magnitudes of rheological properties and the degree of hysteresis appeared to increase with increasing volume loading of filler particles. Conversely, surface treatment of fillers, which presumably reduced the interaction between the filler particles and the extent of agglomeration, resulted in major reductions of both the rheological properties

and the degree of hysteresis. The diverse experimental observations were interpreted in terms of a system forming a filler network due to weak interparticle forces. The thixotropy resulting from breakdown and recovery of the filler network was dependent on the characteristic time of the individual test.

An experimental investigation was carried out by *Assaad* et al. [9.153] to determine the influence of thixotropy on the use of concrete. Five *self-consolidating* concrete (SCC) mixtures prepared with different combinations of cementitious materials and two flowable mixtures of different stability levels were assessed. The thixotropy of the fresh concretes was evaluated using the variations in apparent yield stress with time and the evolution of the structural breakdown curves. Changes to the impeller of a modified Tattersall concrete rheometer were proposed for the protocol used to assess thixotropy. Instead of the H-shaped impeller that rotates in a planetary motion, a four-bladed vane impeller rotating coaxially around the main shaft was used. This resulted in less slip in the flow of the fresh concrete and an increase in the sheared surface during rotation. Test results showed that thixotropy was not an inherent property of a typical SCC. However, the concrete exhibited a high degree of thixotropy when mixed with ternary cement containing 6% silica fume and 22% fly ash compared with similar concrete made with 4% silica fume and no fly ash. The incorporation of set-accelerating and set-retarding agents resulted in greater and lower degrees of thixotropy, respectively. In the case of one particular very flowable concrete, the addition of a viscosity-modifying additive was shown to increase thixotropy significantly compared with similar concrete made without any viscosity-modifying admixture.

Kinlock et al. [9.154] carried out a rheological study of concentrated aqueous nanotube dispersions, at concentrations at which the nanotubes interacted with each other. The dispersed nanotubes represented a high-aspect-ratio system. The dispersions were thixotropic and hence recovered their structure, and hence their viscosity, on standing.

An experimental study of the viscosity of a macroscopic suspension, i. e., a suspension for which Brownian motion can be neglected, under steady shear was published by *Voltz* et al. [9.155]. Their suspension was made up to a high packing fraction and density matched with the Newtonian continuous phase. The thixotropic behavior was characterized by a long relaxation time that was a unique function of shear. The relaxation times showed a systematic decrease with increasing shear rate. These relaxation times were larger when decreasing the shear rates, compared to those observed after increasing the shear.

Mujumdar et al. [9.156] developed a nonlinear rheological model to account for the time-dependent elastic, viscous and yielding phenomena of thixotropic materials that exhibit an apparent yield stress. A key feature of their formulation was a smooth transition from an elastically dominated response to a viscous response without a discontinuity in the stress–strain curve. The model was phenomenological and based on the kinetic processes responsible for structural changes within the thixotropic material. As such, it could predict thixotropic effects, such as stress overshoot during start-up of a steady shear flow and stress relaxation after cessation of flow. An analysis and comparison to experimental data involving oscillatory shear flow were provided to evaluate the accuracy of the model and to estimate the model parameters in a series of concentrated suspensions of silicon particles and silicon carbide whiskers in polyethylene. The data obtained with this experimental system indicated much better agreement between the theory and experiments than that obtained in earlier work by the authors.

A simple model consisting of the upper-convected Maxwell constitutive equation (cf. Sect. 1.3) and a kinetic equation for destruction and construction of structure, first proposed by Fredrickson in 1970, was used by *Bautista* et al. [9.157] to reproduce the complex rheological behavior of viscoelastic systems that also exhibited both thixotropy and rheopexy under shear flow. The model required five parameters that have a physical significance and could be estimated from rheological measurements. Several steady and unsteady flow situations were analyzed with the model. The model predicted creep behavior, stress relaxation, and the presence of thixotropic loops when the sample is subjected to transient stress cycles. The same kind of behavior has been observed with surfactant-based solutions and dispersions.

To account for thixotropic effects of typical gelled suspensions in the the paint, foodstuffs and pulp and paper areas, *Yziquel* et al. [9.158] proposed a structural network model based on a modified upper-convected Jeffreys model with a single relaxation time and a kinetic equation to describe the flow-induced microstructure evolution. Three distinct kinetic equations were tested for this purpose. The proposed model described yield and thixotropic phenomena, nonlinear viscoelastic behavior and output signal distortions observed for relatively small strain amplitude during oscillatory measurements, and overshoots observed in stress growth

Table 9.8 Details of various studies of thixotropic systems

System	Worker(s)	Description
Vesicular lava	*Bagdassarov*, *Pinkerton* [9.160]	Effect of delayed bubble deformation and recovery
Aqueous fluid gels, based on mixtures of xanthan and gellan	*Martinez-Padilla* et al. [9.161]	Effect of electrolyte addition on thixotropy
Semi-solid dairy desserts	*Tarrega* et al. [9.162]	Effect of test temperature
Aqueous pseudo-bohemite suspensions	*Li* et al. [9.163]	Effect of source of bohemite and electrolyte
Aqueous smectite suspensions	*Malfoy* et al. [9.164]	Effects of the nature of the exchangeable cation and clay concentration
Aqueous solutions of an amphoteric guar gum	*Zhou* et al. [9.165]	Effects of concentration, salts, and temperature
Ayran, a Turkish yoghurt drink	*Koksoy* and *Kilic* [9.166]	Effects of water and salt level
Semi-solid metal alloys	*Koke* and *Modigell* [9.167]	Effects of shear rate and cooling rate on microstructure
Roll coating of paints	*Lopez* and *Rosen* [9.168]	Thixotropy of paints correlated with levelling performance
Some cosmetic products	*Moise* and *Aruxandei* [9.169]	Development of equations to describe thixotropy
Concentrated yoghurt (labneh)	*Abu-Jdayil* and *Mohameed* [9.170]	The effect of storage time, 1–14 days

experiments. A comparison of model predictions and experimental data for fumed silica and coating colors was also presented. However, different model parameters had to be used to correctly predict the different flow properties indicating that a more-versatile or generalized kinetic equation needed to be developed. *Goodwin* and *Reynolds* [9.159] noted that the rheology of such flocculated dispersions is dependent on the suspension microstructure and its time evolution as well as the type and magnitude of the interparticle forces. Much current work focuses on this microstructure as recent developments in experimental techniques have made this type of information more accessible. They noted that computer simulation continued to add breadth to the understanding of the behavior of flocculated suspensions.

Last, we consider in detail two studies that used direct measurement of the flow fields in thixotropic fluids. *Corvisier* et al. [9.171] studied the velocity profile of a thixotropic fluid flow in a pipe. The axial velocity distribution was determined using a particle image velocimetry (PIV) technique (cf. Sect. 5.3.2) and ultrasonic velocity profile measurement. At the entrance section, the fluid was assumed to be in a homogeneous structural state corresponding to a high shear rate. The experimental results showed a progressive flattening of the velocity profiles as the fluid restructured as it moved down the pipe. *Raynaud* et al. [9.172] used a magnetic resonance imaging system to investigate the flow field in a concentric cylinder flow, using thixotropic and very shear-thinning colloidal suspensions. The velocity profiles between the coaxial cylinders were found to be made up of two parts: first, close to the inner cylinder the fluid is sheared at a rate larger than a critical, finite value (in contrast with the behavior of an ideal yield stress fluid), while second, where the fluid is not sheared at all close to the outer cylinder. They monitored the displacement of the critical radius in time after sudden changes of the imposed rotation velocity. They established that the apparent thixotropy of these fluids could be followed by the displacement of the interface between the sheared and unsheared regions.

We conclude our review of recent work with a general list of some other interesting thixotropic systems published by workers from a wide range of countries, together with a brief description of the work, see Table 9.8.

9.2.7 Overall Conclusions

Thixotropy comes about first because of the finite time taken for any shear-induced change in microstructure to take place. The microstructure is brought to a new equilibrium by competition between the processes of tearing apart by stress and flow-induced collision, in a time that can be minutes. Then, when the flow ceases, Brownian motion is able to move the elements of the microstructure around slowly to more-favorable positions and thus rebuild the structure. This can take many hours to complete. The whole process is completely reversible. The manifestation of the effect of the microstructural changes on the flow properties result in the various manifestations of thixotropy described in the present chapter.

9.3 Rheology of Suspensions and Emulsions

Suspensions and emulsions or more generally dispersions are disperse materials containing at least two phases of immiscible constituents. Due to their complicated physical and chemical nature, the rheological behavior of suspensions and emulsions is very complex. Nonlinear flow behavior, normal stress differences, viscoelasticity, and yield stresses are some examples of the effects that can occur in the flow processes of these materials. In this Section some essential basics of the rheological behavior of both material classes, suspensions and emulsions, are described. A classification of disperse materials is given. Common properties of suspensions and emulsions obtained in rheological measurements are discussed and some important sources of errors that may occur in rheological measurements are explained. The physical fundamentals of suspension rheology concerning the properties of the disperse and continuous phases are summarized. The mechanisms of particle–particle interactions and their consequences regarding the stability are shown. A classification of models describing the viscosity as a function of solid volume concentration and shear rate is given. Typical experimental results of the rheological behavior of suspensions both in shear and elongational flows as well as in complex flow situations are summarized. Emulsions as liquid–liquid systems show a similar flow behavior under certain circumstances. A survey of the deviating rheological behavior compared to suspensions is given. Methods of fabrication of emulsions are described. Common ground between the rheology of suspensions and emulsions complete the chapter.

Table 9.9 Most important properties for characterizing dispersions (modified after *Chander* [9.173])

Properties of the disperse phase
Particle size and size distribution
Particle shape and shape distribution
Surface properties
Density viscosity, viscoelasticity (emulsions)
Surface energy
Particle volume concentration
Properties of the continuous phase
Viscosity, viscoelasticity
Aqueous, nonaqueous
Dissolved substances
Properties of the interface
Electric double layer
ζ potential
Adsorption density
Thickness of the adsorbed layer
Structure of the adsorbed layer

9.3.1 Preliminaries

Basics and Definitions

This chapter deals with the large class of two- or multiphase materials that occur in many fields of natural and engineering sciences, industry, and daily life. The chapter is structured as follows. In the first part, we introduce the classification of disperse systems and explain some general assumptions for proper rheological measurements of such multiphase materials. In the second part, the theoretical fundamentals, which are necessary to understand the rheology of suspensions, are summarized and, based on these fundamentals, representative experimental results of the flow behavior of solid–liquid systems are illustrated and discussed. The third part deals with theoretical basics and experimental results of liquid–liquid systems, whereby we only refer to phenomena occurring additionally compared to solid–liquid systems.

Suspensions and emulsions or, more generally, dispersions are ubiquitous materials. Their appearance ranges from biological materials such as blood or cell suspensions over pharmaceutical or food products of the daily life to inorganic materials such as concrete, drilling mud, printing inks or multicomponent metal melts to name a few.

These examples show that dispersions are highly complex systems. Hence, the rheological behavior of dispersions depends on the composition of the system. The most important parameters are summarized in Table 9.9.

Knowledge of the rheological properties of disperse systems is a prerequisite for the increase of effectiveness of production and processing operations, but also for the handling of disperse products by the customer. Disperse systems consist of at least one solid or liquid phase (the disperse phase), which is dispersed in a liquid continuous phase or matrix liquid. Both phases are immiscible. In the context of this chapter only

solid–liquid and liquid–liquid dispersions will be considered. Dispersions with a dispersed fluid-like phase in a solid continuous phase (porous bodies, solid foams) and a solid or liquid phase dispersed in a gaseous continuous phase (dusts, smoke, aerosols, foams) are outside of the scope of this chapter.

Based on the state of aggregation of the disperse phase these materials are distinguished in the following way. Suspensions are materials that contain a granular solid material dispersed in a Newtonian or non-Newtonian matrix liquid. Emulsions consist of a liquid phase dispersed in a second liquid. In some cases, both a liquid and a solid phase may be dispersed in more than one liquid continuous phase.

Dispersions may be regarded as the generic term for materials consisting of discontinuities of any kind dispersed in a continuous phase of different composition or state [9.174]. Regardless of its size or shape, such a discontinuity or discrete element is called a particle, which stands both for solid, slightly deformable, or liquid discontinuities.

According to the International Union of Pure and Applied Chemistry (IUPAC) recommendations [9.175], a colloidal) dispersion is a system, in which particles of (colloidal) size of any nature (gas, liquid, solid) are dispersed in a continuous phase. This definition includes both suspensions and emulsions. The term *colloidal* is used for particles having at least one dimension in the size range 1 nm to 1 μm. Particles with mean size above 1 μm are called *noncolloidal*.

In the literature, another nomenclature can often be found. The term *dispersion* is used for a material consisting of fine insoluble or only slightly soluble solid particles with sizes larger than 1 μm distributed throughout a continuous medium [9.176], whereas emulsions are cited separately without any reference to the particle size. In this context, a suspension with colloidal solid particles is a colloidal dispersion [9.177]. The problem with this notation is that information on the particle size is necessary.

Due to the uncertainties and ambiguities of this second nomenclature, the first classification with the term *dispersion* as generic term describing multiphase materials should be preferred.

At the level of the particles, dispersions can generally be classified concerning their size, size distribution, and the shape or shape distribution of the constituents of the disperse phase. Based on the particle size, dispersions can be classified as shown in Fig. 9.61.

According to the particle size distribution (PSD), a dispersion is termed *monodisperse* if all particles are (nearly) of the same size. If more than one discrete size distribution mode occurs, the dispersion is referred to as *heterodisperse*. If only a few discrete size modes occur the dispersion is *paucidisperse*, e.g. bimodal, trimodal [9.175]. A dispersion consisting of particles of many sizes is called *polydisperse*, if less than 90% of the size distribution lies within ±5% of the average diameter $\bar{d}$, i. e.,

$$\frac{1.645\sigma_{\mathrm{SD}}}{\bar{d}} > 0.05\,, \tag{9.218}$$

where σ_{SD} is the standard deviation [9.174]. This classification is valid for single particles and not for aggregates. Due to agglomeration or coalescence, the number and size of particles can change.

A second possibility to quantify the polydispersity of a dispersion is to calculate the (weighted) polydispersity index PDI as the ratio of the volume average diameter $\bar{d}_{\mathrm{V}}$ and the number-average diameter $\bar{d}_{\mathrm{N}}$

$$\bar{d}_{\mathrm{V}} = \frac{\sum_i n_i d_i^4}{\sum_i n_i d_i^3}\,, \quad \bar{d}_{\mathrm{N}} = \frac{\sum_i n_i d_i}{\sum_i n_i}\,, \quad \mathrm{PDI} = \frac{\bar{d}_{\mathrm{V}}}{\bar{d}_{\mathrm{N}}} \tag{9.219}$$

with n_i as the number of particles with diameter d_i. A dispersion is called polydisperse if the relation PDI > 1.05 holds.

A third possibility to characterize the polydispersity of a dispersion is given by the so-called grade of dispersity ξ [9.178] according to

$$\xi = \frac{d_{\mathrm{V},84} - d_{\mathrm{V},16}}{2d_{\mathrm{V},50}} \tag{9.220}$$

with $d_{\mathrm{V},i}$ as the volume-average diameter (9.219) below which 1% of the particles lie. A dispersion can then be classified as

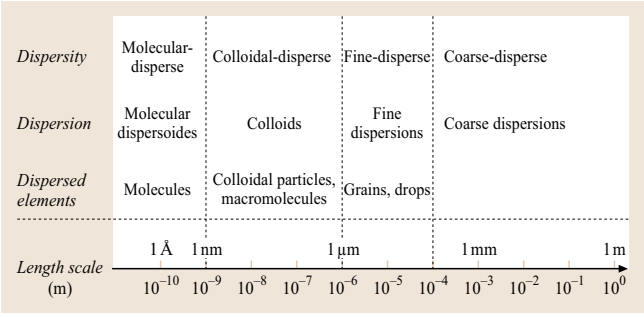

Fig. 9.61 Classification of disperse systems with respect to particle size

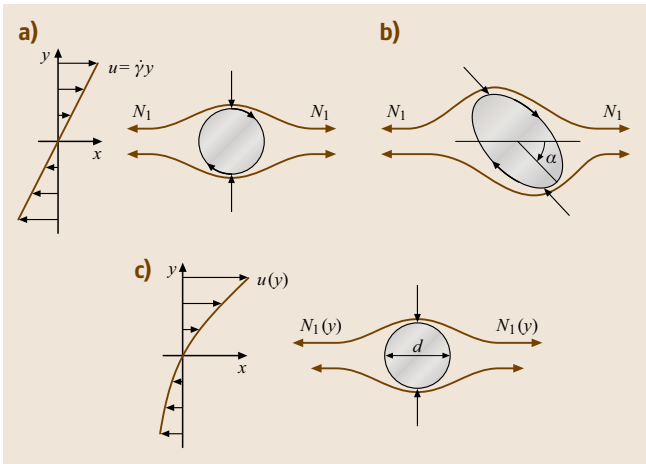

Fig. 9.62a–c Hydrodynamic forces acting on a spherical **(a)** and nonspherical particle **(b)** in a steady homogeneous shear flow and **(c)** on a spherical particle in a nonhomogeneous shear flow (After [9.179], with permission by B. G. Teubner)

- monodisperse if $\xi < 0.14$,
- quasi-monodisperse if $0.14 \leq \xi \leq 0.41$,
- polydisperse if $\xi > 0.41$.

In this chapter we use the grade of dispersity to characterize the polydispersity of a dispersion.

A formal specification of the size of particles with shapes deviating from a sphere is difficult. For this reason, some methods are developed to specify the size of nonspherical particles. In most cases, it is sufficient to reduce the size of a nonspherical particle to the diameter of an equivalent sphere concerning the mass, volume, surface or settling velocity. The sphericity has been proposed as a measure of the deviation of the particle shape from that of a sphere. Different definitions of sphericity are in use. One of the most important definition suggested by *Wadell* [9.180] relates the squared volume-equivalent diameter d_V (diameter of a sphere with the same volume as the particle) to the squared surface-equivalent diameter d_S (diameter of a sphere with the same surface as the particle) of a particle [9.176]. Various other equivalent circle diameters or shape factors can be determined from the projected area of a particle [9.176, 181–185].

It is unusual and also impossible to classify dispersions with regard to all possible particle shapes. If the particle shapes strongly deviate from a spherical shape, the flow behavior of the dispersion will be modified compared with that of hard-sphere suspensions under the same conditions. Hence, a shape factor or shape factor distribution function is necessary. Additionally, the particle size and shape distribution functions affect the applicability of the measuring geometry of the rheological measurements.

Basic Assumptions for Correct Measurement of the Macroscopic Rheological Properties of Dispersions

There are some essential and necessary requirements to be fulfilled in order to characterize dispersions rheologically in the right manner concerning the representative sampling, stability of the sample (settling, aging), migration, the stability of the flow, thermal effects, and the validity of the continuum hypothesis.

These requirements apply independently of the type of the rheological experiment (steady, transient, oscillatory) and the measuring geometry used (coaxial cylinder, cone-and-plate, torsional plate–plate, capillary, and others; Sect. 9.1.1).

In static experiments gravity forces are in competition with the Brownian forces. To estimate the *sedimentation* of samples of suspensions (of spherical particles), the ratio between gravity (settling) and Brownian forces

$$\frac{\text{gravity (settling) force}}{\text{Brownian (thermal) force}} = \frac{(\rho_d - \rho_c) g a^3}{k_B T / a} \quad (9.221)$$

should be provided, where ρ_d and ρ_c are the densities of the disperse and continuous phase, g is the acceleration of gravity, a is the particle radius, k_B is the Boltzmann's constant, and T is the absolute temperature. If this ratio is greater than unity, sedimentation may occur. As shown by *Larson* [9.186], sedimentation takes place for $\Delta\rho = \rho_d - \rho_c \approx 10^3\,\mathrm{kg/m^3}$ and particles or aggregates larger than 1 µm in radius. Prior to rheometric experiments, the tendency to sedimentation should be checked and if necessary, the experimental flow conditions should be adjusted so that during the experimental time the sedimentation does not play an important role. On the other hand, under shearing flow conditions sedimentation is always retarded.

Beyond sedimentation, particle migration under flow conditions can also falsify measurements due to the resulting gradient in solid volume concentration inside the dispersion. Normal force defects acting on particles can cause particle migration. *Böhme* [9.179] sketched the phenomenon of particle migration by illustrating the normal forces acting on a single solid particle in a non-Newtonian shear flow. In Fig. 9.62a the normal forces are equal in magnitude and of opposite sign due to the symmetry. Hence, no particle migration occurs. This is

also true for a nonspherical particle (Fig. 9.62b). The spherical and nonspherical particles only rotate due to the shear force and torque. In case of a nonspherical particle, the particle rotation increases the effective hydrodynamic diameter. Magnus forces due to the rotation of particles in a potential flow do not play any role here and hence do not contribute to migration.

If the shear flow is nonhomogeneous (Fig. 9.62c), the normal stresses at the upper and lower side of the sphere can be quite different. The resulting force acts in the direction of decreasing shear rates and migration occurs. The migration can also occur in Newtonian fluids if the shear flow is nonhomogeneous [9.187]. Hence in any case nonhomogeneous shear flows should be avoided for correct measurement of viscosity, e.g., in coaxial cylinder rheometers (Sects. 9.1.1 and 9.1.2).

Particle inertia can also influence the results of transient or oscillatory experiments. If the shear viscosity of the continuous phase is too small or if the particles are too heavy or too large, they cannot follow the unsteady external flow field. With the particle Reynolds number

$$\mathrm{Re_P} = \frac{\rho_\mathrm{c}\dot{\gamma}a^2}{\eta_\mathrm{c}} \qquad (9.222)$$

an estimation of the inertial effects is possible. In this equation, $\dot{\gamma}$ and η_c are the shear rate and the viscosity of the continuous phase, respectively. Values of $\mathrm{Re_P}$ approximately greater than 10^{-1} indicate that particle inertia may be of relevance [9.188].

One of the most essential assumptions of rheometry is the existence of a hydrodynamically stable flow. During experiments, flow instabilities (e.g., secondary flows in cone-and-plate geometries or Taylor vortices in coaxial cylinder geometries) can falsify the results. Details on stability of rheometric flows can be found in the monographs of *Walters* [9.189] and *Macosko* [9.188].

An important problem may arise if temperature effects come into play. Temperature gradients in the gap of the measurement geometry, or viscous dissipation lead to density differences. This may firstly result in convective flows superimposed on the main flow in a rheometer. Secondly, temperature gradients affect the rheological properties of the continuous phase. Hence, it is important to avoid local temperature differences by tempering the measurement system. If this is not possible or the tempering is not sufficient, it is necessary to correct the data numerically (further information on this problem can be found in the monograph of *Macosko* [9.188]).

Finally, for all rheological measurements, it is necessary to ensure that the material can be regarded as a continuum. In other words, the continuum hypothesis must be fulfilled [9.190]. The macroscopic physical behavior of a fluid under rheometric considerations must be the same if it is perfectly continuous and uniform in structure. The physical quantities associated with the fluid (e.g., density, viscosity) contained within a given volume will be regarded as being spread uniformly over the whole volume. *Jeffrey* and *Acrivos* [9.191] pointed out, that it is possible to regard the dispersion as a continuum *when the length scales describing the motion of the suspension as a whole are much larger than the average size or average separation of the particles*. An essential consequence of the continuum hypothesis is that the size of the largest particle in the dispersion should be substantially smaller than the gap size of the measurement geometry. In rheology, it is a common rule that the maximum particle size must be at least one order of magnitude smaller than the smallest dimension of the measuring geometry. *Barnes* [9.192] showed that this ratio increases with increasing volume concentration of the disperse phase. Independent of the continuum hypothesis, the behavior of single particles or particle collectives in both shear and elongational flows may be of interest as shown by several publications concerning these issues in shear flows.

Aggregation, agglomeration (occurring in suspensions), or coalescence, Ostwald ripening, and creaming (occurring in emulsions) during rheological measurements influence the particle distribution function and should be prevented by implementation of appropriate actions.

If all the criteria mentioned above are fulfilled, it is possible to measure the material function of interest using the methods and devices described in Sect. 9.1.1 (shear flows), Sect. 9.1.3 (elongational flows) and Sect. 9.2 (thixotropy, rheopexy and yield stress).

The rheological nomenclature used in this chapter is based on the recommendation of the Executive Committee of the Society of Rheology [9.193].

9.3.2 Suspensions

The rheological behavior of suspensions is influenced by a very large number of parameters. Due to the fact that suspensions are multiphase materials one has to take into consideration both the properties of continuous and disperse phases, as well as the interactions within and between both phases.

This section gives a survey of the rheology of suspensions. It starts with a short general description of the properties of the components of a suspension. The sta-

bilizing mechanisms are explained. Then a dimensional analysis is applied to show the influencing factors on the viscosity. Subsequently, the basics in measurements and possible sources of errors will be given and representative results of rheological measurements in shear and extensional flow are illustrated and discussed. For more details, we refer to the textbooks of *Larson* [9.186], *Russel* et al. [9.194], and *Morrison* and *Ross* [9.195].

Properties of the Continuous Phase

The continuous phases and their properties can be classified from different points of view – physicochemically or rheologically.

The continuous phase, consisting of water (aqueous suspension) or organic solvent (nonaqueous suspension), can be characterized by its chemical composition, dielectric constant, refractive index, or surface tension (cf. Sects. 3.7.2 and 6.1, and 3.2, respectively). An important property of the continuous phase is the polarizability. A liquid is polarizable if dissociation of the species is possible under special circumstances or if the molecules are dipole-like. By addition of surfactants, dispersants, or electrolytes, it can show strongly different properties compared to the pure liquid. The polarizability affects the type of specific interactions between the continuous and disperse phases when charged species (particles, polymers, polyelectrolytes) are added. If the continuous phase is nonaqueous, the charge properties of the particles are not so important since other mechanisms of interaction between the phases such as hydrodynamic interactions are more dominant [9.195].

The rheological properties of the continuous phase may have an essential influence on the overall rheological properties of the suspensions. If a suspension consists of particles dispersed in a Newtonian liquid, all deviations from the Newtonian behavior (nonlinearity, viscoelasticity) stem from the presence of the disperse phase.

Non-Newtonian continuous phases such as polymer melts or aqueous solvents containing surfactants or other additives modify the interparticle interactions in suspensions and emulsions. In the non-Newtonian case the problem of a locally inflated shear rate due to the particle movement becomes relevant. Due to the shear dependence a viscosity distribution may occur inside of the continuous phase. Thus, the movement of the particles during flow may be modified compared with the case of a Newtonian continuous phase. If the continuous phase is highly elastic, normal stress differences due to local shear rates (Sect. 9.1.2) can fragmentize weak aggregates into smaller species.

Properties of the Disperse Phase

The disperse phase may consist of particles, which have a variety of sizes, size distributions, shapes, densities, and surface morphologies. The surface of the particles can be chemically treated or untreated. The treatment of the particle surface influences the interparticle interactions and, hence, the rheological properties of the suspension.

In the simplest case of a dispersion, the particles are spherical, rigid, and monodisperse. In the case of deviations from the spherical shape, the aspect ratio, i. e., the ratio of the main axes of the particle, must be taken into account. If the aspect ratio is high enough, e.g., for rods, the particles align during the flow which results in a corresponding viscosity. Polydispersity of the particles may decrease the viscosity under certain circumstances (cf. Subsect. “Influence od solid volume concentration” in this section).

An additional difficulty arises if the particles are porous or if the particles aggregate. In these cases some amount of the continuous phase may be immobilized in the pores of the particles or in the interspaces between the aggregated. Thus, the amount of continuous phase around the particles decreases. Hence, the apparent solid volume concentration as well as the dispersion viscosity is then higher than expected for nonporous particles or nonaggregating dispersions.

Polymer blends consisting of immiscible components with a distinct lower viscosity of the dispersed phase show that the particles deform under flow. The steric or electrostatic layer surrounding particles can be deformable under flow (soft spheres). These effects modify the overall flow behavior of the suspension.

Brownian Motion

If the particles suspended in a low viscous continuous phase are sufficiently small (less than 1 μm), they perform a stochastic thermal movement, called Brownian motion. Nonspherical particles (rods, ellipsoids) additionally show a rotational Brownian motion.

The mechanism of translational Brownian motion can be described by a translational diffusion coefficient. For an isolated particle (or droplet) the diffusion coefficient is the ratio of the thermal energy of the particle and the (Stokes–Einstein) friction force acting at the particle which is suspended in a Newtonian continuous phase of the viscosity η_c

$$D_t = \frac{k_B T}{f_t} , \qquad (9.223)$$

where $f_t = 6\pi\eta_c a_H$ is the translational friction coefficient with a_H being the hydrodynamic radius of the

particle. For a spherical particle a_H is equal to its radius a (cf. [9.196] for a survey on the hydrodynamic radii for nonspherical particles). It is seen that the diffusion coefficient is inversely proportional to the viscosity of the continuous phase and the particle size. Under the assumption that the observation time t is long enough with respect to the viscous relaxation time τ_v, i. e., $t \gg \tau_v$ with $\tau_v = \rho_c a_H^2/\eta_c$, the mean squared displacement of the particle is [9.194]

$$\left\langle s^2(t)\right\rangle = 2D_t t \,. \tag{9.224}$$

In the case of rotational Brownian motion, the mean displacement and the translational friction coefficient must be replaced by the mean squared change of the orientation angle $\left\langle \phi^2(t)\right\rangle$ and the rotational friction coefficient f_r, respectively. Hence, a rotational diffusion coefficient $D_r = k_B T/f_r$ comes into play [9.198, 199]. Details concerning the Brownian motion can be found in the textbooks of *Russel* et al. [9.194], *van de Ven* [9.198], *Takeo* [9.196], and *Doi* and *Edwards* [9.199].

Interparticle Interactions and Stabilization

If particles in a suspension approach each other, various types of interactions occur (Fig. 9.63). These interparticle interactions are determined by the solid volume concentration. Beyond the hydrodynamic interaction, there are several other interactions. An extensive review on surface forces can be found in the monograph by *Israelachvili* [9.200]. For hydrodynamic interactions we refer to the monograph by *van de Ven* [9.198]. In the following sections we consider the influence of the hydrodynamic interaction on the suspension and emulsion viscosity not in detail but implicitly through the solid volume concentration and additionally by the Péclet number indicating the nonlinear flow behavior at higher solid volume concentrations (cf. Subsect. "Dimensional Analysis" in this section).

Hard- and Soft-Sphere Interaction. The simplest case of a suspension is that the particles behave like hard spheres. The relevant influence parameters are then viscous forces, Brownian motion, and the excluded volume of the particles. The interaction potential V_{hs}, which generally characterizes the kind and the range of interparticle forces, has the form

$$V_{hs}(r) = \begin{cases} \infty & r \le a \\ 0 & r > a \end{cases} , \tag{9.225}$$

in the case of rigid repulsion. Here, r is the radial coordinate starting from the midpoint of the particle. An

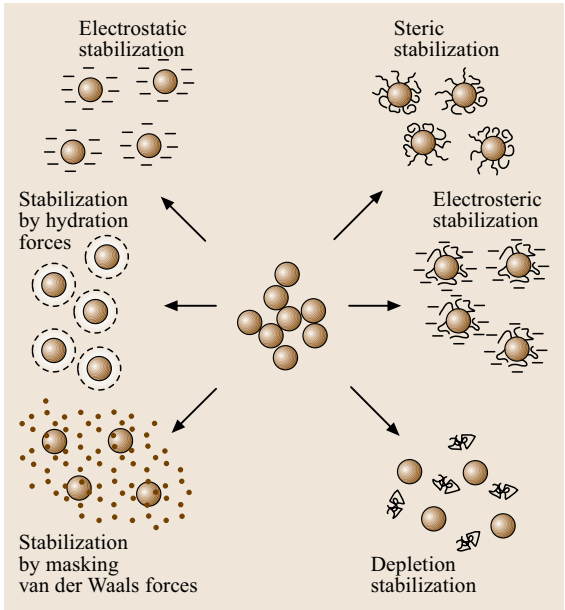

Fig. 9.63 Stabilization methods for dispersions (after [9.197], with permission by Marcel Dekker)

interacting particle causes short- and long-range effects in its neighborhood. Hence, it is (geometrically or virtually) surrounded by a layer (electric double layer, steric molecules). The effective diameter of the particle is then larger than its geometric diameter. If the particles cannot approach each other more than a certain distance, say 2δ or below, due to repulsive forces, the particle radius a must be replaced by an effective particle radius $a_{eff} = a(1 + \delta/a)$ with δ as the thickness of the surrounding layer. If the surrounding layer is deformable and the particles can approach each other less than the distance 2δ, these interactions are called soft-sphere interactions. In the following, an overview of the interparticle forces is given.

Van der Waals Forces. Van der Waals forces are a combination of dispersion interaction (London), dipole–dipole interaction (Keesom) and dipole-induced dipole interaction (Debye) [9.201]. These forces are caused by a temporal asymmetry of the charge distribution around a neutral atom or molecule due to the motion of its electrons. The interaction energies between two single atoms or molecules decay as the inverse sixth power of the atom distance. The nature of the van der Waals interaction is determined by the material-specific Hamaker constant, which characterizes the relative strength of the van der Waals

force between two surfaces. We consider now only two spheres 1 and 2 with given radii a_1 and a_2 (or a ratio of radii $y = a_2/a_1 \leq 1$) and with different properties, surrounded by a continuous phase 0. Hamaker [9.202] obtained for the van der Waals interaction energy V_A the relation [9.203]

$$V_A(x) = -\frac{A_{eff}}{12}\left(\frac{y}{x^2+xy+x} + \frac{y}{x^2+xy+x+y} + 2\ln\frac{x^2+xy+y}{x^2+xy+x+y}\right) \quad (9.226)$$

with $x = h_0/2a_1$ as the dimensionless surface distance (h_0 is the minimum separation between the surfaces of the spheres). The parameter A_{eff} is the effective Hamaker constant, which is calculated according as

$$A_{eff} = A_{00} - A_{01} - A_{02} + A_{12}\,, \quad (9.227)$$

where A_{ij} are the Hamaker constants of the disperse phase ($i = j = 0$), of the sphere 1–sphere 2 interaction ($i = 1$, $j = 2$), of the continuous phase–sphere 1 interaction ($i = 0$, $j = 1$), and of the continuous phase–sphere 2 interaction ($i = 0$, $j = 2$), respectively.

From (9.226) follows that the van der Waals interaction potential depends both on the diameter ratio of the spheres and on the interparticle distance. For $x \ll 1$ the interaction potential is inversely proportional to the interparticle distance. If the components 1 and 2 are identical, the Hamaker constant is positive and, hence, the van der Waals interaction is always attractive. In contrast, when the continuous phase 0 has a Hamaker constant between those of the components 1 and 2, the van der Waals interaction may be repulsive [9.203]. Hamaker constants for some inorganic materials have been calculated by *Bergström* [9.204]. A characteristic value for dimensional-analytical estimates can be given by $V_A = A_{eff}$, which is of the order 10^{-20}–10^{-19} J for the most materials.

Due to the fact that the van der Waals interaction (in the majority of cases) is attractive, it decreases the stability of suspensions by promoting the formation of aggregates.

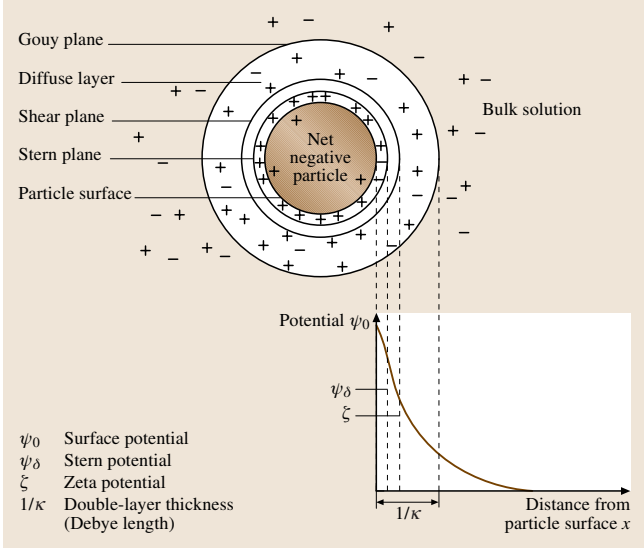

Fig. 9.64 Electrical potential and double layer surrounding a charged particle in a polar liquid (after Birdi [9.203], with permission by CRC)

Electrostatic Forces. There are three main mechanisms that cause the formation of charged phase interfaces in aqueous dispersions: the transition of ions from the disperse to the continuous phase, the specific adsorption of ions from the continuous phase at the surface of the particles, and the adsorption of polar surfactants at the phase interface.

These mechanisms lead to a (partial) charge separation between the particle surface and the surrounding liquid volume. Along with the thermal motion a diffused electrical double layer is generated which consists of the charged surface, neutralizing counterion, and, farther from the surface, co-ions distributed in a diffusive manner [9.203]. Stern proposed a model that assumes that, near the particle surface, some of the counterions are adsorbed (Stern plane) whereas the remaining counterions are distributed diffusively in a double layer (Gouy plane) due to thermal motion. The dependence of the electrical potential or repulsive interaction energy, respectively, on the distance from the particle surface and the electric double layer are shown in Fig. 9.64. Furthermore, the potential at a certain distance, the shear plane, is denoted ζ. *Russel* et al. [9.194] defined the shear plane as the *envelope where shear appears in the fluid adjacent to a rigid body when fluid and solid are in relative motion*.

In the simplest case the repulsive interaction energy between two identical charged spheres of the same radius a with a surface potential ψ_0 is given by [9.205]

$$V_e(x) = 2\pi\varepsilon_r\varepsilon_0\psi_0^2 a \begin{cases} \ln\left(1+e^{-\kappa x}\right) & \kappa a > 10\,, \\ e^{-\kappa x} & \kappa a < 5\,, \end{cases} \quad (9.228)$$

where x denotes the distance of the particle surfaces, ε_r and ε_0 are the relative permittivity of the material and the permittivity of the vacuum, and κ^{-1} is the Debye length which can be regarded as the thickness of the double layer (Fig. 9.64). It can be shown that for small distances, i. e., within the Stern plane the repulsive interaction energy decreases linearly with increasing particle distance. A characteristic value for dimensional-analytical estimates can be given by $V_e = \varepsilon_r \varepsilon_0 \psi_S^2 a$ with ψ_S^2 as the potential at a characteristic distance from the particle surface, e.g., the zeta potential.

The electrostatic forces have a stabilizing effect on the suspensions by preventing the particles from agglomeration (electrostatic stabilization).

DLVO Theory. *Derjaguin* and *Landau* [9.206] as well as *Verwey* and *Overbeek* [9.207] developed independently the first quantitative theory of interactions in dispersions – the Derjaguin–Landau-Verwey–Overbeek (DLVO) theory. The total interaction force between two particles is supposed to be a superposition of the attractive van der Waals forces and the repulsive electrostatic forces. A typical curve of the total interaction energy versus interparticle distance shown in Fig. 9.65 exhibits a maximum representing an energy barrier against agglomeration and two minima, i. e., a primary and a secondary minimum. The primary minimum stems from strong short-range repulsive forces. If the particles are small, the secondary minimum is not very distinctive. Between the primary and the secondary minimum a local maximum, i. e., a so-called electrostatic barrier may appear. If this barrier is high enough, agglomeration does not take place. For larger particles, the secondary minimum may be deep enough to cause weakly flocculated agglomerates due to the slight dominance of attractive forces. A schematic illustration of the potential energy and the corresponding structure of the suspension are depicted in Fig. 9.66. Dominant attractive forces cause aggregation or flocculation of particles and, hence, a destabilization of the suspension, whereas strong repulsive forces stabilize the suspension.

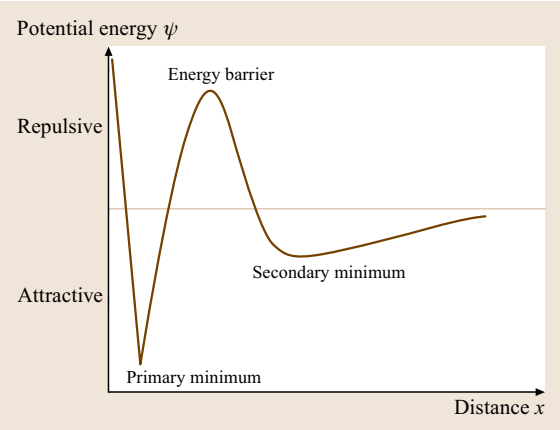

Fig. 9.65 Diagram of the potential energy between two particles in dependence on the surface distance: DLVO theory

Steric Forces. An alternative to stabilize suspensions is steric stabilization. In contrast to the electrostatic stabilization, this method can be used in aqueous and nonaqueous systems. The mechanism of steric repulsion can be realized by the adsorption of organic molecules at the particle surface [9.205]. The adsorbed molecules act like a *brush*, where the strength of this polymer bridge depends strongly on the molecular weight (chain length). If the adsorbed layer has a sufficient thickness and density, the attractive forces can be reduced in a manner that aggregation or bridging flocculation is prevented.

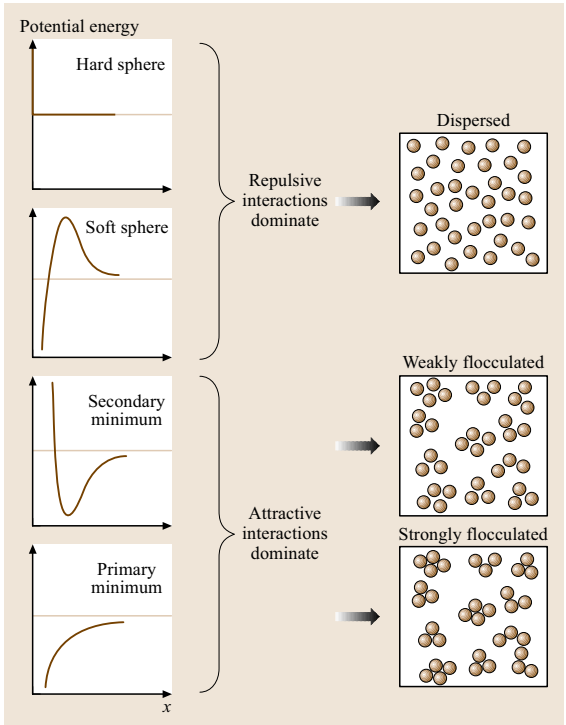

Fig. 9.66 Schematic illustration of the relationship between the total interparticle potential energy and suspension structure (after Lewis [9.205], with permission by the American Ceramic Society)

Table 9.10 Some relevant physical quantities and corresponding dimensionless groups in suspension rheology

Property	Dimensional expression	Dimensionless group
Viscosity	η	$\eta_r = \eta/\eta_c$ (relative viscosity)
Viscosity of the continuous phase	η_c	$\rho_r = \rho_d/\rho_c$ (density ratio)
Density of the disperse phase	ρ_d	$Re_P = \rho_c \dot{\gamma} a^2/\eta_c$ (particle Reynolds number)
Density of the continuous phase	ρ_c	ξ (polydispersity measure)
Polydispersity	ξ (dimensionless)	$\varphi = n(4\pi/3)a^3$ (volume concentration)
Number density	n	$Pe = \eta_c \dot{\gamma} a^3/k_B T$ (Péclet number)
Particle radius	a	δ/a (relative surface layer thickness)
Gap width of the rheometer	h	a/h (continuum parameter)
Adsorption layer thickness	δ	$t_r = t/\left(\eta_c a^3 k_B T\right)$ (relative startup time)
Time	t	$Ga = \frac{(\rho_d - \rho_c) g a}{\eta_c \dot{\gamma}}$ (settling parameter)
Acceleration of gravity	g	
Thermal energy	$k_B T$	
Dispersion (van der Waals) energy	A_{eff}	$\frac{A_{eff}}{\varepsilon_r \varepsilon_0 \psi_S^2 a}$
Electrostatic energy	$\varepsilon_r \varepsilon_0 \psi_S^2 a$	

If two sterically stabilized particles with the adsorption layer thickness δ approach each other, two main domains can be distinguished: a domain, where $\delta < x < 2\delta$, i. e., where the two steric layer interpenetrate, and a domain, where $x < \delta$ with an additional compression of the layers. Hence, the interparticle forces depend on both the distance x and the strength of the steric layers.

The long segments of the polymer or surfactant protruding into the continuous phase can adsorb onto the surface of neighboring particles and form a polymer bridge between the particles [9.176].

Electrosteric Forces. Polyelectrolytes as stabilizers for aqueous suspensions combine steric and electrostatic interactions (electrosteric stabilization). They have at least one type of functional groups (e.g., carboxyl or sulfonic acid groups) that can be ionized. This functional group is responsible for the electrostatic interactions. The chain of the polyelectrolyte causes steric interactions. The adsorption of polyelectrolytes is influenced by the electrochemical and physical properties of the particle surface and the continuous phase. It is interesting to note that small amounts of polyelectrolytes can neutralize the surface charge of the particle and, consequently, weak flocculation may occur. At higher amounts, the polyelectrolytes stabilize the suspension due to the long-range repulsive forces caused by the electrosteric forces.

The thickness of the polyelectrolyte layer is mainly influenced by the concentration of the electrolyte in the aqueous continuous phase, i. e., the pH value, and the ion strength (a measure of electrolyte concentration) [9.208].

Depletion Forces. Depletion forces are a result of the interactions between large colloidal particles suspended in a continuous phase that contains non-adsorbing, smaller constituents – so-called depletants (polymers, polyelectrolytes, smaller particles). Due to depletion, stabilization occurs because the particle aggregation is inhibited by unadsorbed polymer in the continuous phase. That is, depletion characterizes a situation where the concentration of depletants increases with increasing distance from the particle surface up to an equilibrium value obtained in the continuous phase. This distance, called the depletion layer thickness, has an order of two depletant diameters. The shape of the depletant molecules influences the depletion force. It is known that rod-like macromolecules, compared to spheres, increase the depletion force. In the case where the depletants are removed from the interparticle gap due to an osmotic pressure difference (exclusion of the free polymer from the interparticle regions) flocculation may occur. With increasing depletant concentration, restabilization is possible.

Dimensional Analysis

By application of dimensional analysis (Chap. 2.2) we can identify the parameters that influence the rheological behavior of the suspensions. It results in a number of dimensionless groups (dimensionless ratios of various influence parameters) which characterizes the ratio

of the various influence parameters which allow the estimation of the physical relevance or irrelevance of influence parameters. In Table 9.10 the relevant physical parameters for suspensions are summarized.

From dimensional analysis it can be deduced that the following general relation holds for the dependence of the relative viscosity η_r on the dimensionless influence parameters (Table 9.10):

$$\eta_r = f\left(\varphi, \frac{\delta}{a}, \frac{a}{h}, \xi, \rho_r, t_r, \mathrm{Ga}, \mathrm{Pe}, \mathrm{Re_P}, \frac{A_{\mathrm{eff}}}{\varepsilon_r \varepsilon_0 \psi_S^2 a}\right) . \tag{9.229}$$

In the following, we consider buoyant ($\rho_r \to 1$) suspensions with negligibly small particle Reynolds numbers ($\mathrm{Re_P} \ll 1$). For suspensions that are not highly concentrated one can also neglect the influence of the interparticle forces. Hence, the functional relation for the relative viscosity of suspensions within the continuum hypothesis ($a \ll h$) reduces to

$$\eta_r = f\left(\varphi, \frac{\delta}{a}, \xi, t_r, \mathrm{Pe}\right) . \tag{9.230}$$

The continuum parameter a/h, used in this context, is similar to the Knudsen number Kn as the ratio of the molecular mean free path and the characteristic body length. Kn is applied in the field of rarefied gas dynamics or flows in microchannels. For convenience we do not change the functional symbol f. For suspensions with monodisperse unvarying particle size, (9.230) takes the form

$$\eta_r = f(\varphi, \mathrm{Pe}) . \tag{9.231}$$

in the steady state and for thin surface layers $\delta \ll a$. The Péclet number gives the ratio between the shear force and the Brownian force, or in other words, the ratio between order due to shearing and disorder due to Brownian movement. The presence of particles changes the flow behavior from linear flow behavior (Newtonian) to nonlinear flow behavior (non-Newtonian) due to the hydrodynamic interactions between the particles. Hence, with increasing concentration the nonlinear flow behavior increases, which shows the coupling between φ as a measure for hydrodynamic interaction and Pe representing the nonlinear flow behavior.

Only for highly diluted suspensions does the relative viscosity depend solely on the solid volume concentration yielding a Newtonian behavior if the continuous phase is Newtonian

$$\eta_r = f(\varphi) . \tag{9.232}$$

In the literature one can often find another definition of the Péclet number:

$$\mathrm{Pe_{eff}} = \frac{\sigma a^3}{k_B T} = \frac{\eta \dot{\gamma} a^3}{k_B T} . \tag{9.233}$$

In contrast to the Péclet number given in Table 9.10, this *effective* Péclet number is based on the macroscopic shear stress $\sigma = \eta\dot{\gamma}$ or the effective viscosity of the dispersion η, respectively.

Influence of Solid Volume Concentration

The solid volume concentration is defined as the ratio of the volume of the disperse phase V_d to the total volume

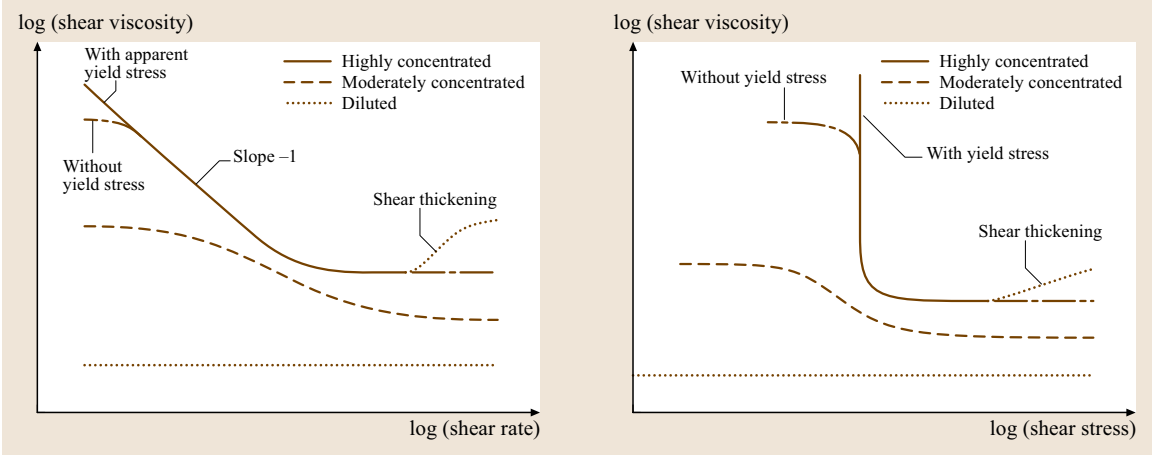

Fig. 9.67 Scheme of the shear viscosity as a function of shear rate and shear stress, respectively. The curve parameter is the solid volume concentration

$V_c + V_d$, where V_c is the volume of the continuous phase:

$$\varphi = \frac{V_d}{V_c + V_d} \,. \tag{9.234}$$

This equation holds, strictly speaking, in the case of nonporous hard spheres. In the case that the particle is surrounded by a layer, the relative layer thickness δ/a can be combined with the solid volume concentration φ to form an effective solid volume concentration

$$\varphi_{\text{eff}} = \varphi \left(1 + \frac{\delta}{a}\right)^3 \,, \tag{9.235}$$

resulting in a modified form of (9.231):

$$\eta_r = f\,(\varphi_{\text{eff}}, \text{Pe}) \,. \tag{9.236}$$

Dependent on the solid volume concentration, suspensions can be classified into three main groups: diluted, concentrated, and highly concentrated or solid suspensions [9.173, 209]. Generally, the flow behavior depends on either the shear rate or shear stress, respectively, the solid volume concentration, and the properties of the continuous phase. A sketch of the possible observations is depicted in Fig. 9.67.

Diluted suspensions of identical spherical particles, i. e., suspensions with very low solid volume concentrations, show a Newtonian behavior. In this case the distances between the particles are large enough, so that the Brownian (thermal) motion of the particles predominates over the effect of the interparticle interactions for colloidal suspensions [9.209]. *Einstein* [9.210, 211] was the first who investigated the hydrodynamic forces resulting from the motion of the continuous phase with respect to noninteracting rigid spherical particles. He derived the equation

$$\eta_r = \frac{\eta}{\eta_c} = 1 + k_1\varphi + \mathrm{O}(\varphi^2) \tag{9.237}$$

for the viscosity of highly diluted suspensions obtained in pure shear flow, where η_c is the viscosity of the continuous phase and $k_1 = 5/2 = 2.5$ is the Einstein coefficient. The order of approximation is denoted by the symbol O(.). A generalization of the Einstein coefficient is the intrinsic viscosity, which is defined as

$$[\eta] = \lim_{\varphi\to 0} \frac{\eta_r - 1}{\varphi} = \lim_{\varphi\to 0} \frac{\eta_{sp}}{\varphi} \,, \tag{9.238}$$

with η_{sp} as the specific viscosity. For other particle shapes the intrinsic viscosity varies (cubes: 3.1; uniaxially oriented fibres parallel to the tensile stress component: $2l/d$ with l and d as fibre length and diameter, respectively) [9.212]. Equation (9.237) shows a linear increase of the suspension viscosity with increasing solid volume concentration, however the behavior remains Newtonian. It is applicable to suspensions of spherical particles with solid volume concentrations up to 10^{-2}.

A further increase of the solid volume concentration, i. e., the transition to concentrated suspensions, causes increasing interactions of the *hydrodynamic fields* between spheres or aggregates. The interaction between two particles was described by *Batchelor* and *Green* [9.213] as well as by *Batchelor* [9.214] to extend Einstein's equation to higher solid volume concentrations:

$$\eta_r = 1 + k_1\varphi + k_2\varphi^2 + \mathrm{O}(\varphi^3) \,. \tag{9.239}$$

In this equation, the coefficient k_2 describes the deviation from the very dilute limit of the suspension. The equation holds for solid volume concentrations up to 2×10^{-1}. This type of power series, a pseudovirial approximant, can be summarized in a general equation for the dependence of the relative viscosity on the solid volume concentration with k_i as concentration-independent expansion coefficients:

$$\eta_r = \sum_{i=0}^{N} k_i \varphi^i \,. \tag{9.240}$$

The relative viscosity in (9.240) represents both shear and elongational viscosities. Table 9.11 gives examples for the coefficients of some useful models for suspensions of monomodal spherical particles (hard spheres) based on power series expansion up to the order of 3. For details refer to the book of *Russel* et al.[9.194].

It should be mentioned that the coefficient $k_2 = 7.6$ obtained by *Batchelor* and *Green* [9.213] for the extensional flow of equal-sized spheres, is uniquely determined. However, in the case of a simple shear flow, the coefficient k_2 cannot be uniquely determined due to the occurrence of closed orbits around a reference particle. This difficulty can be overcome by introduction of some additional physical process, such as three-sphere encounters or Brownian motion, or by the assumption of some particular initial state. By allowing a superimposed Brownian motion *Batchelor* [9.214] calculated the value of the coefficient $k_2 = 6.2$. For non-Brownian suspensions *Batchelor* and *Green* [9.213] found, with some assumptions about the particular initial state, $k_2 = 5.2$.

To extend the application range to higher solid volume concentrations up to $\varphi < 0.60$, *Thomas* [9.215] proposed $k_2 = 10.05$ and replaced the third-order term

Table 9.11 Some models describing the dependence of the viscosity on the solid volume concentration for moderately concentrated suspensions

Source	N	k_0	k_1	k_2	k_3	Comment
[9.210, 211, 216]	1	1	2.5	-	-	$\varphi < 0.01$
[9.213]	2	1	2.5	7.6 (elongation) 5.2 (shear)	-	$\varphi < 0.2$
[9.214]				6.2 (shear)		
[9.217]	3	1	2.5	4.94	8.78	
[9.218]	3	1	2.5	6.25	15.7	$\varphi < 0.3$
[9.219]						
Low-shear limit	3	1	2.5	4 ± 2	42 ± 10	$\varphi < 0.35$
High-shear limit	3	1	2.5	4 ± 2	25 ± 7	

empirically by an exponential term

$$k_3\varphi^3 \to 2.73 \times 10^{-3}\, e^{16.6\varphi}\,, \qquad (9.241)$$

contrary to asymptotic power-series expansion. Many other models of this type with other coefficients are available for special suspensions.

For higher solid volume concentrations, where hydrodynamic and surface force interactions as well as many-body interactions become relevant, the power-series expansion fails since the viscosity tends to infinity at solid volume concentrations in the vicinity of the maximum possible packing fraction. Furthermore, the models given above (with the exception of the de Kruif model [9.219]) are applicable only for a Newtonian behavior or in the low shear or elongation range. Hence, another type of models has been developed taking into account the fact that the viscosity reaches a maximum value at concentrations near the maximum packing fraction. The maximum packing fraction is a characteristic scalar value that mainly depends on the particle size distribution, particle shape (distribution), type of the interactions between the disperse and continuous phases and the shear intensity. For idealized regular packing fractions of monodisperse hard spheres the values given in Table 9.12 hold.

Barnes et al. [9.82] summarized the results described in the literature for nonspherical particles. Table 9.13 reveals that the product $[\eta]\varphi_{max}$ varies only in the range 1.31–3.77, depending on the kind of particles.

Mewis et al. [9.220] found from experimental data a maximum packing fraction of $\varphi_{max} = 0.96$ for soft spheres, which approaches in case of infinite polydispersity $\varphi_{max} \to 1$.

Based on experimental data *Kitano* et al. [9.221] presented the following simple equation (9.242) to calculate the maximum packing fraction for short fibres with an average length-to-diameter ($\overline{l/d}$) ratio of 6–27:

$$\varphi_{max} = 0.54 - 0.0125\,\overline{l/d}\,. \qquad (9.242)$$

If the particle size distribution becomes broader, higher values of the maximum packing fraction occur because smaller particles can fill the gaps between larger particles. Under specific conditions this effect is often coupled with a decrease of the relative viscosity. Examples for bi- and trimodal suspensions are given by *Barnes* et al. [9.82].

In Fig. 9.68 the dependence of the relative viscosity on the amount of smaller particles in a bimodal suspension of various solid volume concentrations is shown. Similar results are described elsewhere [9.222–225].

Table 9.12 Maximum packing fractions for regular arrangements of monodisperse spherical particles

Type of packing	Maximum packing fraction φ_{max} (theoretically from geometry)
Face-centered cubic (fcc)	$\sqrt{2}\pi/6 = 0.7405$
Body-centered cubic (bcc)	$\sqrt{3}\pi/8 = 0.6802$
Random closed	0.6370
Hexagonal	$\sqrt{3}\pi/9 = 0.6046$
Simple cubic	$\pi/6 = 0.5236$
Diamond	$\sqrt{3}\pi/16 = 0.3401$

Table 9.13 Intrinsic viscosities and maximum packing fractions for suspensions with asymmetric particles (in extracts from [9.82] with permission from Elsevier)

System	$[\eta]$	φ_{max}	$[\eta]\varphi_{max}$
Glass fibres ($l/d = 21$)	6.00	0.233	1.398
Glass fibres ($l/d = 14$)	5.03	0.260	1.308
Glass rods (30×700 µm)	9.25	0.268	2.479
Laterite	9.00	0.350	3.150
Quartz grains (53–76 µm)	5.80	0.371	2.152
Glass fibres ($l/d = 7$)	3.80	0.374	1.421
Glass plates (100×400 µm)	9.87	0.382	3.770
Titanium dioxide	5.00	0.550	2.750
Ground gypsum	3.25	0.690	2.243

From Fig. 9.68 one can recognize that an addition of smaller particles under perpetuation of the solid volume concentration reduces the relative viscosity, especially in the range of $\varphi = 0.6$ (amount of large particles) where the relative viscosity has a minimum. This phenomenon is known as the Farris effect. The path P → Q indicates the 50-fold reduction in the relative viscosity of a suspension with $\varphi = 0.6$ if the monodispersity is changed to a bidispersity (50%/50%). The path P → S illustrates

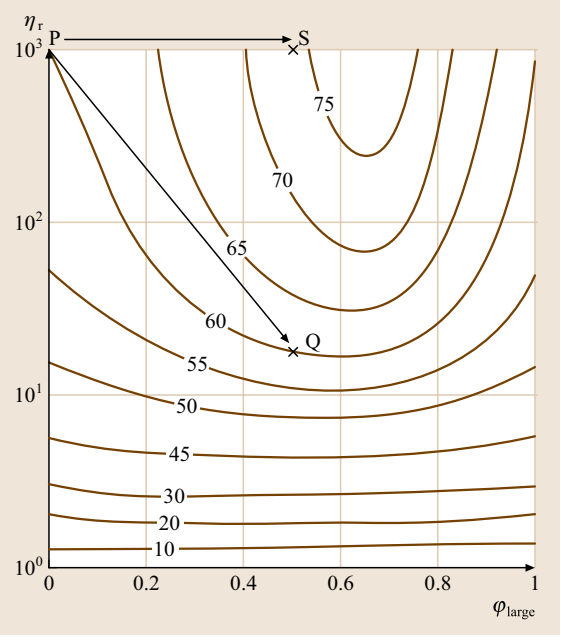

Fig. 9.68 Effect of binary particle-size fraction on the relative viscosity with total percentage solid volume concentration as parameter (particle-size ratio of 1:5) (after Barnes et al. [9.82] with permission by Elsevier)

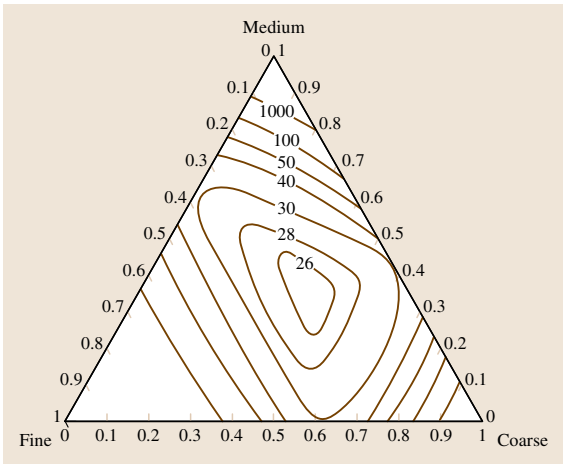

Fig. 9.69 Influence of the particle-size distribution on the relative viscosity of a trimodal suspension of spheres. Contours show values of the relative viscosity at 65% total solids (after Barnes et al. [9.82] with permission by Elsevier)

that a 15% increase of the solid volume concentration by the addition of smaller particles without a change of the relative viscosity is possible.

In Fig. 9.69 a triangular plot of the relative viscosity of a trimodal suspension with a total solid volume concentration of 60% is shown. A relative viscosity minimum of 25 is reached at a given optimum ratio of the solid volume concentration of the components whereas the binary mixture shows a relative viscosity of 30 [9.82].

These effects give rise to the possibility to influence the viscosity of a suspension by an optimum mixing of various fractions of the disperse phase.

In the case of nonspherical particles (ellipsoids, cubes, rods, fibres) the maximum packing fraction decreases. At the same solid volume concentration, the viscosity increases compared to that of a hard-sphere suspension.

The maximum packing fraction is often obtained by fitting of equations of the type shown in Table 9.14 [e.g., (9.244)]. These models describe the dependence of the reduced viscosity on the solid volume fraction. The applicability is not restricted to suspensions with spherical particles because the parameter φ_{max} or k can be regarded as a fitting parameter.

Equations (9.243–9.245) can be formally expanded in a power series according to (9.240), where the coefficients now depend on the solid volume concentration. For small solid volume concentrations the Einstein limit (see eq. (9.237)) is reached.

Table 9.14 Viscosity–concentration models for higher solid volume concentrations

[9.228]	$\ln \eta_r = 2.5\varphi$	9.243
[9.229] $[p = 2,\ f(\varphi) = 1]$ [9.230] $(p = [\eta]\varphi_{max},\ f(\varphi) = 1)$	$\eta_r = f(\varphi)\left(1 - \frac{\varphi}{\varphi_{max}}\right)^{-p(\varphi)}$	9.244
[9.231] $k = 1.35$ (face centered cubic) $k = 1.91$ (simple cubic)	$\eta_r = \exp\left(\frac{2.5\varphi}{1-k\varphi}\right)$	9.245
[9.232, 233] generalized differential form with $k = 1/\varphi_{max},\ [\eta] = 2.5$ $\alpha = 0$: Arrhenius $\alpha = 1$: Krieger/Dougherty $\alpha = 2$: Mooney	$d\eta_r = \eta_r[\eta]\,(1 - k\varphi)^{-\alpha}\,d\varphi$	9.246

Extensive review articles on viscosity models for suspensions (including models for suspensions of non-spherical particles) are given by *Rutgers* [9.226] and *Jinescu* [9.227].

Under shear the arrangement of the particles in the fluid is modified, so that the maximum packing fraction depends on the shear rate or shear stress applied (Fig. 9.70). Thus, the (shear-dependent) maximum packing fraction has been introduced in the models (e.g., [9.219, 234, 235]).

Wildemuth and *Williams* [9.234] developed a simple model to describe the shear-dependent maximum packing fraction. They found the relation

$$\frac{1}{\varphi_{max}(\sigma)} = \frac{1}{\varphi_{max,0}} - \left(\frac{1}{\varphi_{max,0}} - \frac{1}{\varphi_{max,\infty}}\right) S(\sigma)\,, \tag{9.247}$$

which describes the dependence of the maximum packing fraction on the shear stress. The values $\varphi_{max,0}$ and $\varphi_{max,\infty}$ are the maximum packing fractions in the low- and high-shear-rate limit. In analogy to some kinetic models to describe the time-dependent viscous (thixotropic) behavior of suspensions using parameter $\lambda(t)$ (Sect. 9.2), the function $S(\sigma)$ can be interpreted as a scalar structural parameter with values between 0 and 1 depending on the given shear stress σ. For the structural parameter the relation

$$S(\sigma) = \frac{1}{1 + K\sigma^{-m}} \tag{9.248}$$

has been proposed. The parameters K and m must be evaluated by fitting the experimental data. With (9.244), (9.247), and (9.248) the non-Newtonian behavior of concentrated suspensions can be modeled. A similar relation has been proposed by *Zhou* et al. [9.235].

Moderately concentrated suspensions often possess a monotonously decreasing viscosity with plateaus in the low (η_0) and high (η_∞) shear rate limit and a power-law region in between. In Table 9.15 some useful models to describe the time-independent viscous behavior of suspensions without yield stress in steady shear flows with a minimum of parameters are summarized.

If the solid volume concentration approaches the maximum packing fraction, a transition from liquid- to solid-like behavior occurs. The interactions between the particles become very intensive and a true or apparent yield stress may occur. This results in a viscosity that tends to infinity at very low shear rates or shear stresses (Fig. 9.67). The main reason for this behavior is that the free movement of particles is hindered by particles

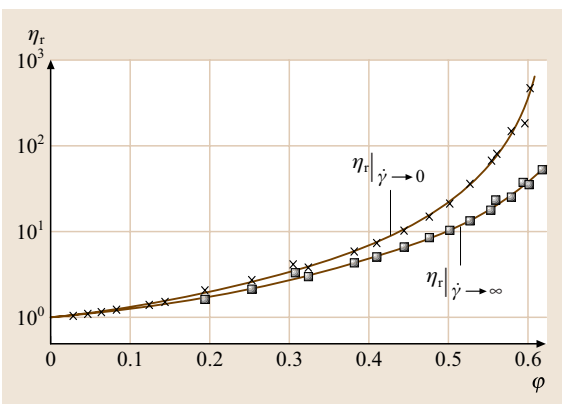

Fig. 9.70 Low- and high-shear limit of the relative viscosity in dependence on the solid volume concentration for monodisperse lattices (after *Barnes* et al. [9.82] with permission by Elsevier)

Table 9.15 Viscosity models (time independent) for suspensions without yield stress

[9.236]	$\frac{\eta(\varphi)-\eta_\infty(\varphi)}{\eta_0(\varphi)-\eta_\infty(\varphi)} = \frac{1}{1+(\sigma/\sigma_{cr}(\varphi))^{m(\varphi)}}$ $1 \le m(\varphi) \le 2$ σ_{cr} ... critical shear stress	9.249
[9.129]	$\frac{\eta(\varphi)-\eta_\infty(\varphi)}{\eta_0(\varphi)-\eta_\infty(\varphi)} = \frac{1}{1+k(\varphi)\dot{\gamma}^{n(\varphi)}}$	9.250
[9.237] special case: Carreau ($m = 2$)	$\frac{\eta(\varphi)-\eta_\infty(\varphi)}{\eta_0(\varphi)-\eta_\infty(\varphi)} = \left(1+(\tau(\varphi)\dot{\gamma})^{m(\varphi)}\right)^{\frac{n(\varphi)-1}{m(\varphi)}}$ (cf. with (9.207) in Sect. 9.2) $\tau(\varphi)$ characteristic material time $n(\varphi)-1$ slope in the power-law region $m(\varphi)$ affects the shape of the transition between zero-shear viscosity and power-law region	9.251

in their direct neighborhood. From a physical point of view, the yield stress is not a single scalar value, but it should be considered a region that characterizes the solid–liquid transition. It is influenced by the solid volume concentration and the interparticle interactions, but also by the intensity of the mechanical load and the type of the flow. The most appropriate method to measure the yield stress is to apply a shear stress ramp. Starting from a very low value, the shear stress is slowly increased and the shear strain or shear rate, respectively, is measured. To resolve the low-shear-stress range accurately, the shear stress should be given as a logarithmic ramp. Assuming a solid-like behavior below the yield stress, a sharp increase of the slope of the $\gamma(\sigma)$ curve occurs if the given shear stress approaches the yield stress. The intersection point of the asymptotes of the solid-like range and the initial liquid-like ranges characterizes the yield stress. It is important to note that the steepness of the shear stress ramp influences the solid–liquid transition. Hence, preliminary investigations are necessary to determine the critical shear stress ramp where the yield stress is independent of the ramp steepness.

Some useful models have been presented to describe the flow behavior of the so-called viscoplastic suspensions (Bingham, Herschel-Bulkley, Casson (see [9.188]). However, it should be noted that the yield stress obtained by fitting the model parameter to the experimental data is neither a unique nor a single material property. It depends on the shear rate range and even on the model used. Detailed information on the measurement and estimation of the yield stress can be found in the review articles by *Nguyen* and *Boger* [9.238] and *Barnes* [9.239].

At higher shear rates, highly concentrated suspensions with solid volume concentration of 50% and higher may show shear thickening, i. e., the viscosity increases with increasing shear rate or shear stress (Fig. 9.71). This effect is caused by a more or less sudden change in the microstructure of the suspension which could be investigated by means of scattering methods (e.g., [9.240–242]). As *Barnes* [9.243] pointed out, this shear-thickening region ranges over more than one decade of shear rate. Most of the parameters shown in Table 9.9 may control the shear-thickening behavior. Usually, the shear-thickening effect is reversible since the viscosity decreases again if the shear rate or stress decreases. Schematically, the phenomenon of shear-thickening is shown in Fig. 9.71. At higher solid volume concentrations a shear-thinning region can be observed which passes into a region with increasing viscosity at a critical shear rate $\dot{\gamma}_{cr}$. The critical shear rate increases and the onset of shear thickening is less severe with a broadening of the particle size distribution. Furthermore, a local viscosity maximum is reached at

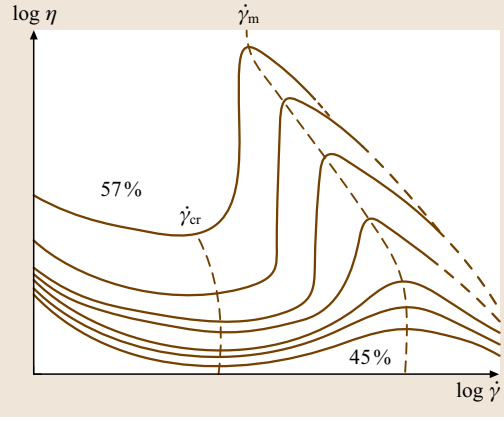

Fig. 9.71 Schematic representation of the viscosity function for shear-thickening suspensions as a function of the solid volume concentration (see text for explanation, after *Barnes* [9.82] with permission by the Society of Rheology)

a shear rate $\dot{\gamma}_m$. Both characteristic shear rates shift to lower values with increasing solid volume concentrations. It is interesting to note that the critical shear rate tends to zero if the maximum packing fraction is reached.

It should be mentioned that a correlation between the particle size and the critical shear rate exists. Based on the data in many publications, *Barnes* [9.243] gave an empirical evidence of an inverse quadratic dependence

$$\dot{\gamma}_{cr}(a) = Ka^{-2} \tag{9.252}$$

with a value of $K \approx 4\,\mu m^2/s$ obtained from a rough fit to the available data.

Furthermore, the critical shear rate depends on the solvability of the continuous phase with regard to a stabilizer (nonaqueous suspensions) or pH value (aqueous suspensions). *Frith* et al. [9.244] indicated for sterically stabilized nonaqueous suspensions that the onset of shear thickening scales with the viscosity of the continuous phase due to the hydrodynamic effects. The critical shear rate was found to decrease with decreasing stabilizer layer thickness, i. e., if the continuous phase is a better solvent for the stabilizer. *Franks* et al. [9.245] demonstrated that the critical shear rate increases if the pH value is adjusted farther from the isoelectric point (IEP). At the (material-specific) IEP, the ζ potential is zero. This effect has been explained by an increase of the repulsive forces between the particles, which delay the onset of shear thickening. If the pH value deviates from the IEP, the addition of salt decreases the repulsive forces and, hence, decreases the critical shear rate. From these observations it can be concluded that shear thickening is not only a hydrodynamic effect but depends on the surface forces as well.

The effect of shear thickening does not only occur in steady shear experiments. *Raghavan* and *Khan* [9.246] observed so-called strain thickening in oscillatory shear flows. Strain thickening in this case means that a critical combination of a shear strain and an angular frequency exists where the complex viscosity sharply increases. Two different cases are possible: high critical strains at low frequencies and high critical frequencies at low strains. In the first case, a correlation with the results obtained in steady shear flow is possible using a modified Cox–Merz rule (the Rutgers–Delaware rule, *Doraiswamy* et al. [9.247])

$$\left|\eta^*(\hat{\gamma}\omega)\right| = \eta(\dot{\gamma})\big|_{\omega=\dot{\gamma}} \ . \tag{9.253}$$

Compared to the original empiric Cox–Merz rule ((9.102) in Sect. 9.1.1), the angular frequency ω has been scaled with the shear strain amplitude $\hat{\gamma}$, which now describes the maximum dynamic shear rate in oscillatory shear experiments. *Gleissle* and *Hochstein* [9.248] extended the range of applicability of the Cox–Merz rule using the concept of the shear stress equivalent inner shear rate. The modified Cox–Merz rule has been applied to the high-shear region where hydrodynamic interactions dominate.

A simple rheological model in a closed form, which describes the complete viscous behavior in simple shear in a broad range of shear rates including the shear thinning and the shear thickening region, is not yet available. Here, the regions should be described separately by the models given in Table 9.15.

Rheological Measurements

Before performing the rheological measurement the following points should be clarified: a suitable measurement geometry, and the dosage and rheological preconditioning of the sample.

In Sect. 9.1.1 various measurement geometries have been described. In the following only the properties of the measurement geometries relevant to the investigation of dispersions will be explained. Details can be found in the monograph by *Walters* [9.189] or the contributions by *Powell* [9.249] on rotational rheometry, and *Mackley* and *Rutgers* [9.250] on capillary rheometry.

Choice of the Measurement Geometry – Settling, Particle Migration, and Wall Slip. The choice of the measurement geometry depends on the expected rheological properties of the suspension. Because the rheological properties are a priori unknown, preliminary measurements are absolutely necessary. However, it is possible to choose a suitable geometry based on the following information:

1. the shear rate or shear stress range of interest – stability of flow in the range of interest
2. the existence of a possible yield stress, as well as the order of magnitude of the viscosity and/or normal stress differences
3. the possibility, to prevent wall slip or, if this is not possible, to detect and correct for wall slip

The stability of flow is an important criterion for the choice of the geometry. The cone-and-plate (CP) system (cf. Fig. 9.32) is suitable for low and medium shear rates. Especially at higher concentration, the flow in CP systems becomes unstable, e.g., due to shear fracture. Starting from the free surface at the edge, the sample contracts with increasing time and shear rate, which results in a decreasing shear plane. In

controlled-shear-rate (CSR) experiments, the slope of the flow curve is reduced dramatically and, hence, the viscosity decreases apparently. This results in strong shear-thinning behavior starting at a critical shear rate. In controlled-shear-stress (CSS) experiments, shear fracture is manifested as a sharp increase of the measured shear rate. Independent of the problems of sample stability, the CP system with small cone angles ($\leq 4°$) is the most preferable geometry for the investigation of suspensions because the shear rate and the shear stress are approximately constant over the whole sample [cf. (9.139) and (9.143) in Sect. 9.1.2]. Especially when investigating the yield stress in suspensions, the CP geometry is the most suitable system. Furthermore, the CP geometry allows the determination of the first normal stress difference from the axial force [cf. (9.148) in Sect. 9.1.2] which can easily be measured by modern rotational rheometers.

Similar sample instabilities can be observed in torsional plate–plate (PP) geometries (cf. Fig. 9.31). Although the main advantage lies in the simple adjustment of the shear rate by varying the gap height, the PP system is unsuitable for the rheological measurements of non-Newtonian suspensions due to the strong inhomogeneous shear field in the gap [cf. (9.136) in Sect. 9.1.2]. However, the torsional PP geometry is a necessary tool for measurements of the difference between the first and second normal stress difference [cf. (9.138) in Sect. 9.1.2], i. e., for the estimation of the second normal stress difference if the first normal stress difference is already known.

Because of the small gap height and the direction of gravity perpendicular to the gap, sedimentation or demixing effects influence the experimental results obtained in CP and PP geometries to a major degree.

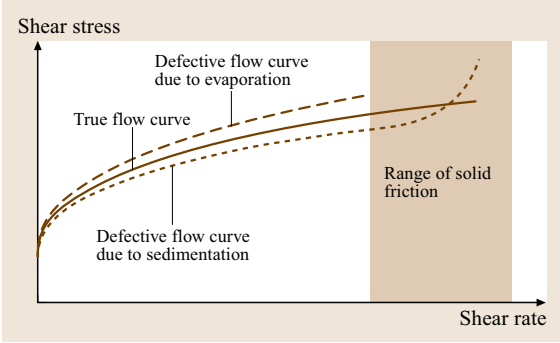

Fig. 9.72 Erroneous flow curves of a shear-thinning suspension in a coaxial cylinder system due to evaporation, sedimentation, or friction between bob and sediment

Here, demixing effects manifest themselves as an untypical time-dependent decrease of the viscosity, which in the case of a Newtonian continuous phase, tends towards the viscosity of the continuous phase. This effect could be misinterpreted as shear thinning or thixotropy (Sect. 9.2).

It is possible to estimate the influence of settling on the rheological measurements. Based on the balance between the Stokes force (cf. Sect. 3.4.5), the gravitational force, and the buoyant force an equation can be derived to estimate the time required for a single sphere to migrate over a length l

$$t_{\mathrm{exp}} = \frac{9}{2}\frac{\eta_{\mathrm{c}} l}{\Delta\rho g a^2} \tag{9.254}$$

with $\Delta\rho = |\rho_{\mathrm{d}} - \rho_{\mathrm{c}}|$ and t_{exp} as experimental time (cf. Sect. 3.4.5: falling-sphere viscometer). For spheres of 10 µm diameter in water and a migration length of 1/10 of a typical gap h of 1 mm (e.g., in a PP geometry), the particle density must be within 0.2% of that of water to prevent settling during typical measurement times of 1000 s [9.188]. As seen from (9.254), the density difference is inversely proportional to the square of the particle size under unchanged conditions, i. e., if smaller particles are used, the possible density difference between particles and liquid increases quadratically. The settling time increases if the solid volume concentration is high enough that hindered settling occurs or if a superposed shear flow during measurements is realized. Generally, the relation

$$\frac{2}{9}\frac{t_{\mathrm{exp}}\Delta\rho g a^2}{\eta_{\mathrm{c}} h} \ll 1 \tag{9.255}$$

must be fulfilled to neglect the influence of settling.

The problems discussed with CP and PP geometries can be at least partially avoided if coaxial cylinders (cf. Fig. 9.29) are used since the gravity acts parallel to the cylinder gap. Due to the length of the gap between the two cylinders, the influence of sedimentation is not as dramatic as has been described for the CP and PP geometries. However, sedimentation leads to depletion of particles in the shear gap and hence to an initial decrease of the viscosity. If the solid volume concentration is high enough, a compact layer of solid is generated at the bottom of the outer cylinder. If this layer reaches the lower edge of the inner cylinder, an additional torque occurs due to solid friction between the inner cylinder and the sediment. This observation, schematically shown in Fig. 9.72, can be misinterpreted as shear thickening or rheopexy (Sect. 9.2). Further problems may appear due to Taylor vortices obtained in coaxial cylinder systems

where the inner cylinder rotates (Searle systems) and/or edge effects. An estimation of the critical shear rates or shear stresses is possible with common methods.

Another general problem is partial evaporation of the continuous phase during the measurements. Evaporation, i. e., the loss of continuous phase, leads to an increase of the solid volume concentration, which causes an increase of the relative viscosity due to the strong influence of the solid volume concentration. This effect can be minimized by carrying out the measurements in a saturated atmosphere of the continuous phase. If this is not possible, a small amount of an immiscible nonevaporating liquid can be applied to the air–sample surface to prevent evaporation.

One of the most well-known problems arising in experimental investigations of suspensions is wall slip, i. e., the violation of the no-slip condition at the walls of the measurement geometry. There are two different types of wall slip.

The first type, true wall slip, has been found with unfilled polymers [9.252]. At higher shear stresses, a relative velocity between the fluid at the wall and the wall velocity itself sets in. This effect is generally associated with the flow instabilities, e.g., during the extrusion process (stick–slip phenomenon). However, the true wall slip is only of relevance when dealing with polymers.

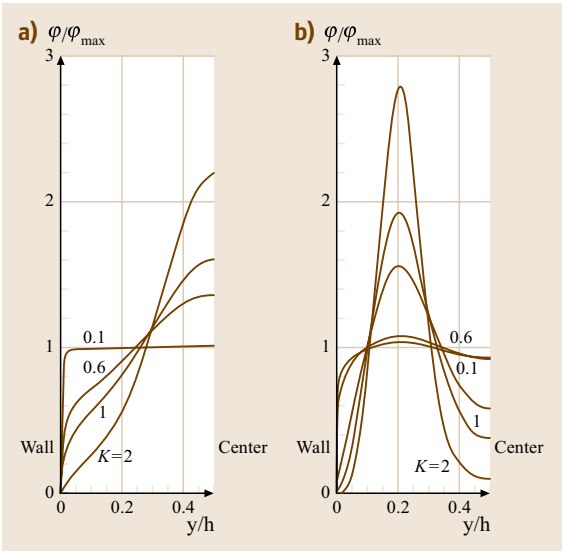

Fig. 9.73a,b Concentration distribution over the shear gap: **(a)** Couette flow, **(b)** plane Poiseuille flow. K is given by (9.256) (after *Ho* and *Leal* [9.251] with permission by Cambridge University Press)

With moderately and highly concentrated suspensions, the second type, an apparent wall slip effect, can occur which is caused by particle migration. An initially homogeneously distributed suspension, which is subjected to non-homogeneous shear field, can demix during the experiment. This demixing effect is caused by additional forces acting at the particles, even in the case where neither inertial nor interparticle forces are relevant. The physical depletion of particles near the solid walls occurring even without flow results from a distortion of the local microstructure. Furthermore, the local isotropy caused by the Brownian motion (of colloidal particles) may be destroyed. The flow-induced forces cause a movement of the particles from regions of higher (near the walls) to regions of lower shear rates or vice versa. This effect, called particle migration, results in a solid volume concentration distribution over the sample. *Ho* and *Leal* [9.251] analyzed the problem of particle migration both in drag (Couette, see Fig. 9.27) and pressure-driven (plane Poiseuille, see Fig. 9.41) slit flow theoretically. The solid volume concentration distributions are shown in Fig. 9.73. Ho and Leal found a criterion for neglecting migration effects that compares the inertial effects and Brownian motion

$$K = \frac{\rho_c \bar{u}^2 a^4}{h k_B T} \begin{cases} < 0.1 & \text{Couette flow} , \\ < 0.01 & \text{plane Poiseuille flow} , \end{cases} \tag{9.256}$$

where $\bar{u}$ is the mean velocity in the gap (Couette flow: $\bar{u} = \frac{1}{2} u_{max}$, plane Poiseuille flow: $\bar{u} = \frac{2}{3} u_{max}$) and h is the gap width. Figure 9.73 makes clear that, in the Couette device where the outer cylinder rotates, the particles (spheres) move towards the centerline. In contrast, in plane Poiseuille flow a maximum solid volume concentration occurs at the distances of about $0.2h$ from the walls. The intensity of migration depends, among other things, on the mean velocity (or shear rate), particle size and the thermal energy of the particle. The danger of migration strongly increases with the particle size, since the influence of the thermal forces decreases with increasing particle size.

An extensive numerical study of particle migration in various geometries has been carried out by *Graham* et al. [9.253]. They used a modified shear-induced migration model based on the model of *Leighton* and *Acrivos* [9.254]. By using the momentum equation, mass conservation equation, and a kinetic equation for the change of the solid volume concentration, they calculated the steady-state spatial concentration profiles and the resulting integral values of pressure drop or torque.

For geometries with inhomogeneous shear fields, they found particle concentrations varying from low values at higher shear rates to higher values at lower shear rates. The surprising result of the numerical study is that, even in the case of a CP system with a practically homogeneous shear field, radial and azimuthal concentration profiles establish. As a result, the driving torque increases significantly due to the outward migration of the particles, which can be misinterpreted as a dilatancy effect. It has been shown that the particle migration results from the curvature of the CP geometry.

Allende and *Kalyon* [9.256] studied pressure-driven flows of suspensions of neutrally buoyant, noncolloidal and unimodal spheres dispersed in a Newtonian continuous phase. On the basis of the model of *Phillips* et al. [9.257] they found that the shear-induced particle migration is typically negligible for length-to-diameter (or gap) ratios of 0–50 provided that the ratios of particle-to-tube (or channel gap) radii are 5×10^{-3} and smaller. Under these conditions, the wall concentration is within 2% of the initial concentration of the suspension in the solid volume concentration range $0.1 \le \varphi \le 0.5$.

Experimentally, the effect of particle migration has been shown by the use of noninvasive methods. *Hartman Kok* et al. [9.258] used the total-reflection Fourier-transform infrared spectroscopy to determine the thickness of the wall slip layer in dependence of the shear rate in a PP geometry. From rheological measurements the thickness of the slip layer δ_S could be estimated [9.259] by

$$\delta_S = \frac{u_S \eta_S}{\sigma} \qquad (9.257)$$

with u_S as the slip velocity (obtained from a plot of the apparent shear rate at the rim of the PP geometry as a function of the inverse gap height). They found a reasonable agreement between both methods where the thickness of the slip layer was of the order of 1 μm and nearly independent of the Péclet number (or dimensionless shear rate).

Other noninvasive methods such as nuclear magnetic resonance (NMR, *Abbott* et al. [9.260] for PP geometry, *Han* et al. [9.261] for tube flow) or laser doppler anemometry (LDA, *Jana* et al. [9.262]; Chap. 5.3.1) have been used to investigate the distribution of the solid volume concentration in various measurement geometries. *Abbott* et al. [9.260] found a particle-depleted zone near the inner cylinder of a wide gap coaxial cylinder (CC) geometry where the particle concentration at the outer wall reached the maximum packing fraction. This may lead to unsheared regions in the cylinder gap and hence to erroneous measurements. The reason for this observation is again the inhomogeneity of the shear field. The effect has been found to be irreversible and independent of the shear rate and the viscosity of the continuous phase. An essential conclusion is that wider cylinder gaps amplify the occurrence of particle migration.

To avoid wall slip caused by particle migration, it is necessary to disrupt the slip layer. This can be achieved by serrated or at least roughened measurement systems. The roughness must be larger than the slip layer thickness, so that the peaks of the surface disrupt the slip layer. On the other hand, to avoid secondary flows in the valleys of the rough surface, the roughness should not be too large.

The influence of the surface roughness on the rheological measurements of concentrated suspensions has been investigated extensively and systematically by *Aral* and *Kalyon* [9.255] for various PP geometries. The suspension used was a poly(butadiene-acrylonitrile-acrylic acid) terpolymer (PBAN) filled with glass beads of 85.4 ± 35.3 μm diameter. Various materials with surfaces of different asperities have been investigated. The authors found that wall slip generally occurs with stainless-steel plates, but could be avoided with plates made of aluminium oxide. A significant influence of the surface roughness could be found for plates of the same material. In Fig. 9.75, the influence of the surface topology on the transient shear stress obtained

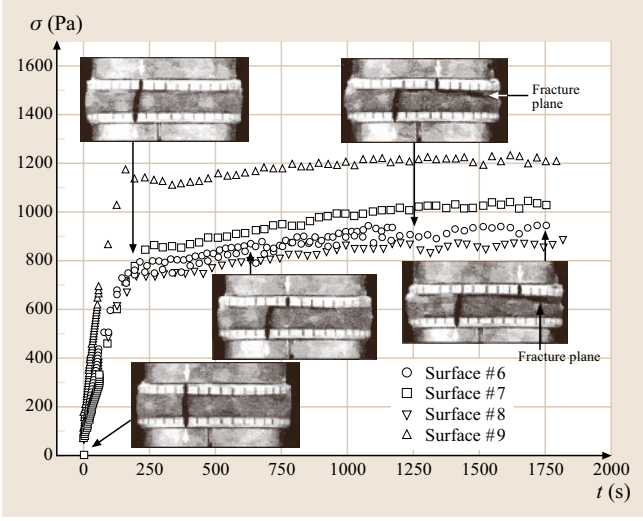

Fig. 9.74 Sample fracture: shear stress as a function of time, including photos of the sample under shear, at an apparent shear rate of $2\times10^{-3}\ s^{-1}$ (after *Aral* and *Kalyon* [9.255] with permission by the Society of Rheology)

in a start-up flow with a given shear rate is shown. The number of the surface #6 to #9 corresponds to the ratio of mean surface roughness to the diameter of the plates (0.005, 0.006, 0.008, and 0.02). Obviously, the corresponding shear stress values increase with increasing surface roughness. Furthermore, some photographs are shown that depict the mechanism of wall slip and shear fracture. At short times or low shear strains ($\gamma = \dot{\gamma} t$), respectively, a homogeneous deformation of the sample occurs (see the marker lines in Fig. 9.75), whereas at higher strains an increasing shear fracture occurs. Shear fracture is caused by internal slip within the sample. This leads to a discontinuity in the velocity field occurring between two neighboring sample layers. It is interesting to note that, in most cases described by *Aral* and *Kalyon* [9.255], the absence of wall slip was coupled with the appearance of shear fracture, i. e., the formation of a fracture plane.

Both effects, i. e., wall and internal slip have also been found by *Persello* et al. [9.263] for colloidal silica dispersions using a marker technology. A result of their experiments is that the plane of shear fracture, which occurred at larger shear rates, typically moved from the upper plate at the start of the experiment to the middle of the gap if wall slip had been suppressed. The internal slip layers occurred due to a partially demixing of the dispersion, i. e., the formation of a layer of the matrix liquid acting as lubricant between the solid layers. Homogeneous deformation without wall slip and shear fracture has been found at low shear stresses. In Fig. 9.74 the effects of homogeneous sample deformation, wall slip, and shear fracture are shown schematically.

It is not surprising that flow instabilities such as wall slip can lead to unusable results. *Walls* et al. [9.264] investigated the influence of various surfaces of the test geometry on the rheological properties of silica gels. They found distinct differences of the viscosity and storage modulus curves obtained with smooth and serrated plates as shown in Fig. 9.76. From their results

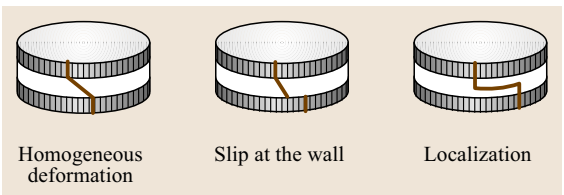

Fig. 9.75 Homogeneous deformation, wall slip, and shear fracture (in modified form after *Persello* et al. [9.263] with permission by the society of Rheology)

it can be concluded that wall slip occurs at a critical shear stress or critical shear stress amplitude. At higher stresses, it seems that wall slip disappears and both curves coincide.

Generally, it is possible to correct the effect of wall slip if a Couette device with two different inner (radii $R_{i,1}$ and $R_{i,2}$) cylinders and outer cylinders ($R_{o,1}$ and $R_{o,2}$) is used. The radii ratio $\beta = R_{o,1}/R_{i,1} = R_{o,2}/R_{i,2}$ is the same for the two geometries, whereas the gap width varies. The wall slip velocity can be calculated by using the formula of *Yoshimura* and *Prud'homme* [9.265] for the Couette device with $\beta - 1 \ll 1$ (small gaps)

$$u_S(\sigma_i) = \frac{\beta}{\beta+1}\left(\frac{\Omega_1 - \Omega_2}{R_{i,1}^{-1} - R_{i,2}^{-1}}\right) , \tag{9.258}$$

where σ_i is the same shear stress at the inner cylinder for the two independent measurements with angular speeds Ω_1 and Ω_2 and the two cylinder systems 1 and 2. The true shear rate at the wall can then be obtained from

$$\dot{\gamma}_{i,a} = \dot{\gamma}_i(\sigma_i) + \frac{2u_S(\sigma_i)}{R_i} . \tag{9.259}$$

A plot of the apparent shear rate versus the inverse inner radius for a given shear stress results in a straight line. The true shear rate can be obtained from the intersection of the straight line with the ordinate. The slope of the straight line corresponds to the twofold increase of the slip velocity.

For torsional plate–plate geometries, *Yoshimura* and *Prud'homme* [9.265] proposed

$$u_S(\sigma_R) = \frac{\dot{\gamma}_{aR,1}(\sigma_R) - \dot{\gamma}_{aR,2}(\sigma_R)}{2\left(h_1^{-1} - h_2^{-1}\right)} \tag{9.260}$$

to calculate the slip velocity from two independent experiments carried out with two different gap heights h_1 and h_2 and apparent shear rates $\dot{\gamma}_{aR,1}$ and $\dot{\gamma}_{aR,2}$ at the outer edge of the plates for the same shear stress σ_R at the outer edge R. The true shear rate at the walls can then be calculated according to

$$\dot{\gamma}_{aR} = \dot{\gamma}_R(\sigma_R) + \frac{2u_S(\sigma_R)}{h} . \tag{9.261}$$

The same procedure can also be used for tube flows.

For further details on wall slip and its prevention in rheometers we refer to the review article by

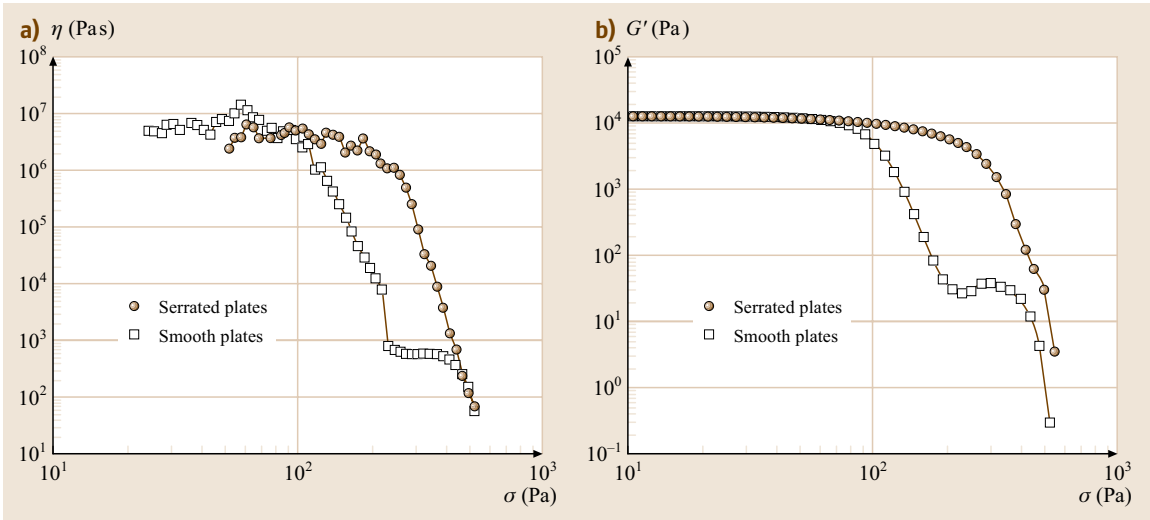

Fig. 9.76a,b Influence of the surface topology **(a)** on the viscosity function and **(b)** the storage modulus (cf. (9.5) in Sect. 9.1.1, adapted from *Walls* et al. [9.264] with permission from the Society of Rheology)

Barnes [9.266] who formulated some conditions which usually lead to significant wall slip effects, such as:

- large particles in the disperse phase (including flocs or aggregates)
- a strong dependence of viscosity on the solid volume concentration of the disperse phase
- smooth walls (sandblasted walls or profiled cones, plates or cylinders can prevent wall slip, but can lead to shear fracture)
- small flow dimensions
- usually low speeds/flow rates
- walls and particles with electrostatic charges while the continuous phase is electrically conductive.

Dosage and Rheological Preconditioning of the Sample. Preconditioning of the rheological sample is an important factor to get correct (and especially reproducible) results. If rotational rheometers are used, the suspension structure at rest can be destroyed by the filling process. Moreover, the lowering of the upper part of the measurement geometry leads to a squeeze flow of the sample. This flow process causes an intensive shear and elongation of the sample and hence a modification and an induced direction of the inner structure. Furthermore, normal or shear stresses that cannot relax even at long times occur, if the samples are highly concentrated and show a yield stress. To avoid such problems, a simple method has been developed by *Heymann* et al. [9.267] to dose and preform a pasty suspension reproducibly. They used a template with a circular opening in the middle. The diameter of the opening corresponded approximately to the diameter of the cone or plate, the thickness was nearly 90% of the maximum gap height in CP systems. The sample is put into the circular opening by a process similar to screen printing with a doctor blade. After forming the circular sample disk, the template was removed and the geometry was closed. The main advantage of this handling is a preformed sample of the thickness of the order of the gap height.

After filling, it is indispensable to use a pre-shear phase to ensure reproducible results. The influence of pre-shear on the results of rheological measurements has been studied intensively. *Heymann* et al. [9.267] analyzed the influence of steady and oscillatory pre-shear on the subsequent oscillatory experiments with suspensions of polymethylmethacrylate (PMMA) spheres dispersed in a Newtonian low-molecular-weight polydimethylsiloxane (PDMS). They found distinct differences between the storage and loss moduli obtained in shear stress controlled (CSS) amplitude sweeps after steady and oscillatory pre-shear. At low shear-stress amplitudes, the moduli were higher after oscillatory pre-shear. At higher shear-stress amplitudes, where the hydrodynamic interactions dominate, no significant differences between steady and oscillatory pre-shear could be obtained. Furthermore, the normal force, induced by the closing of the test geometry, could be reduced and the reproducibility could be enhanced by oscillatory pre-shear. A problem arises if the suspension shows yield behav-

ior. In both cases (stationary and oscillatory pre-shear), the shear stress induced by pre-shear cannot relax completely and the subsequent measurements do not start with a stress-free initial state of the suspensions. In particular, the oscillatory option is problematic because the oscillation cannot be stopped in a well-defined way. This problem can be avoided by a suitable choice of an event control algorithm of the rheometer to set the shear stress to zero.

A dramatic influence of the pre-experimental sample preparation has also been demonstrated by *Carreau* et al. [9.269]. They analyzed the influence of the homogenization procedure prior to the rheological experiments on low-concentrated aqueous colloidal suspensions of fumed silica particles with a mean diameter of 12 nm. After manual mixing, the viscosity showed slightly shear-thinning behavior. In contrast to this observation, the influence of ultrasonic dispersion was dramatic because the viscosity was strongly shear thinning at a clearly higher level. This has been explained by the interaction between water and the silica particles based on hydrogen bridges. At rest, large aggregates are formed, which can be destroyed by shear only slightly. After the ultrasonic dispersion, the suspension consist of single particles that cause a higher viscosity level and can be structured by shear. Furthermore, they observed in controlled-shear-stress (CSS) experiments with suspensions of fumed silica particles in polypropylene glycol that the low-shear viscosity, the onset, and the importance of shear thickening decrease with increasing pre-shear stresses. This effect has been explained by a break-up of aggregates due to pre-shear.

Schmidt and *Münstedt* [9.270] investigated the rheological behavior of concentrated monodisperse suspensions. They detected a significant influence of the pre-shear time at a given shear stress on both the low-shear viscosity and the dynamic moduli. The low-shear viscosity was found to increase with increasing pre-shear time, caused by structuring effects. In contrast to the loss modulus, which has not been influenced significantly by pre-shear, the storage modulus increased markedly with increasing pre-shear times at low angular frequencies. This was interpreted as a transition from a liquid- to a solid-like viscoelastic structure of the particle network.

Summarizing all the results concerning the influence of pre-shear it is indispensable to insert a phase of rheological sample preparation before any rheological measurements are carried out with rotational rheometers (Sect. 9.1.2). Furthermore, the pre-experimental history influences the rheological behavior of suspensions markedly.

If capillary viscometers (Sect. 9.1.2) are used, the influence of various mechanical histories is not as dramatic as in the case of rotational rheometers since the sample flows from a reservoir with a larger diameter into the capillary with a distinctly smaller diameter, driven by a pressure. Due to the convergent flow field, elongational effects modify the structure of the suspension and orientation phenomena disappear.

Viscometric Flows. In this chapter, the most relevant experimental results and phenomena obtained in viscometric flows are presented and explained.

A typical example of the influence of the solid volume concentration on the shear-stress-dependent viscosity shown in Fig. 9.77 has been given by *Laun* [9.268] for an aqueous suspension of charged polystyrene-ethylacrylate copolymer spheres of 250 nm diameter. The viscosity at low solid volume concentrations $\varphi < 0.18$ remains Newtonian. Increasing the solid volume concentration, non-Newtonian shear-thinning behavior can be observed with a subsequent shear thickening region at higher solid volume concentrations. At very high solid volume concentrations a striking increase of the viscosity at lower shear stresses can be obtained, which could be an indication of an apparent, or possibly true, yield stress.

These observations could be attributed to the particle structure changes by applying rheooptical methods during the shear experiments. *Lyon* et al. [9.271] studied

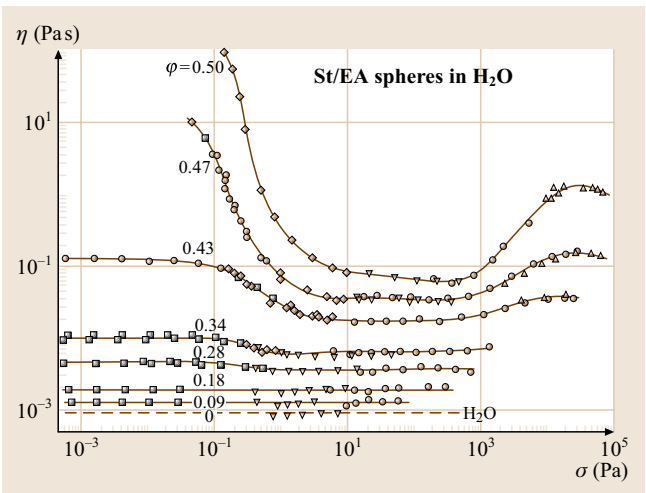

Fig. 9.77 Shear viscosity versus shear stress of a colloidal latex suspension with 250 nm particles at different solid volume concentrations at nearly the same pH values (after *Laun* [9.268] with permission by Hüthig & Wepf Verlag)

the structure formation of suspensions in a simple shear flow and found a transition from a disordered state at the beginning of the experiment to an ordered state induced by a given shear strain or time of shear. The noncolloidal monodisperse particles order in shear bands and, locally, in a hexagonal pattern due to particle migration across the streamlines of the flow.

By a combination of optical and rheological measurements, similar effects in the dependence of viscosity on the microstructure of the suspensions could be obtained by *Gondret* and *Petit* [9.272] for oscillatory shear (Fig. 9.78) as well as by *Völtz* et al. [9.274] for steady shear. They found a time-dependent decrease of the viscosity during shear, as shown for a moderately concentrated suspension of noncolloidal spheres. The decrease of the viscosity was coupled with a transition from a disordered to a periodic band-like [9.272] or hexagonal structure [9.274] of the suspension. The range of the characteristic structuring times can be some milliseconds up to hours. Furthermore, it can be stated that structural modifications from a disordered state via a band-like and hexagonal to disordered structures are the reason for the complex behavior of the suspensions. These effects, dependent on the interparticle interactions and solid volume concentration, occur in both colloidal and noncolloidal suspensions.

Silbert et al. [9.275] studied concentrated, aggregated colloidal suspensions of spherical particles by numerical simulations. Among other things, they claimed, that the microstructure strongly depends on the solid volume concentration under the same shearing conditions, i. e., the same Péclet number. Starting from a semiordered phase with a coexistence of particle strings and disordered regions at $\varphi = 0.47$ they found a transition to a hexagonally packed string phase at $\varphi = 0.50$, an intermediate string/layer phase at $\varphi = 0.55$, and finally to a truly ordered layered phase at $\varphi = 0.57$.

As shown in Table 9.10, the viscosity of a suspension depends strongly on the interparticle interactions and, hence, on the kind of stabilization (hard spheres, electrostatic stabilization, steric or electrosteric stabilization). In the following, some illustrative experimental results will be given for hard spheres, charged spheres, and sterically stabilized spheres.

Shear Viscosity. In the absence of interparticle surface forces the shear viscosity of hard-sphere suspensions depends only on the solid volume concentration and the dimensionless shear rate or Péclet number (9.231). *Krieger* [9.273] investigated some model colloidal hard-sphere suspensions of polystyrene spheres in water or benzyl alcohol and metacresol. He proved that the relative viscosity data form a master curve independent of the continuous phase, as portrayed in Fig. 9.79.

A viscosity function of this type can be best described by (9.249) with $m = 1$. The critical shear stress σ_{cr}, which characterizes the shear thinning region, has been found to be dependent on the solid volume concentration. As demonstrated by *de Kruif* et al. [9.219] the critical shear stress increases initially with increasing solid volume concentration up to a value of $\varphi \approx 0.5$.

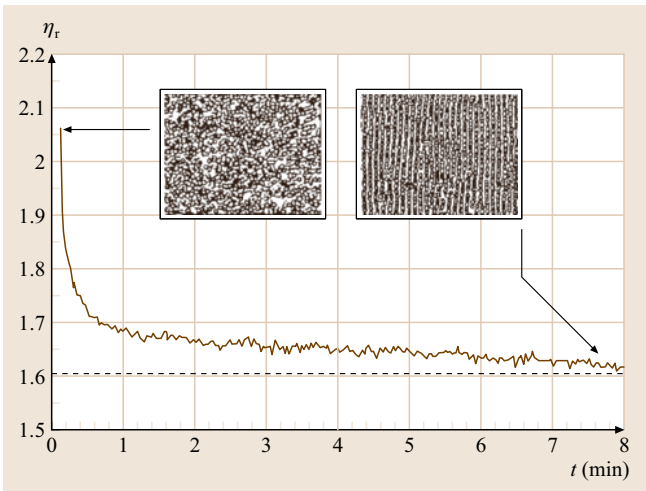

Fig. 9.78 Structuring of a suspension of noncolloidal particles in a Newtonian continuous phase with a solid volume concentration of 0.2 in an oscillatory shear flow (after *Gondret* and *Petit* [9.272] with permission by the AIP)

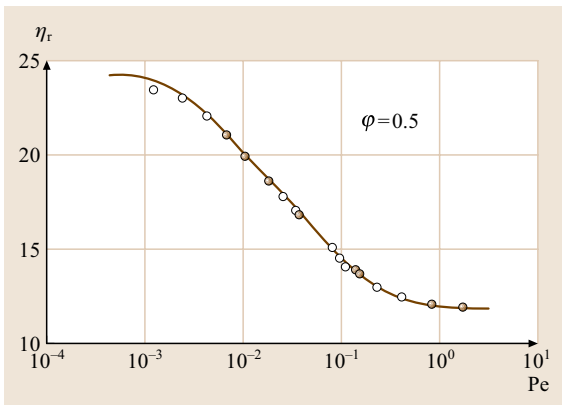

Fig. 9.79 Dimensionless viscosity function of hard sphere suspensions (after *Krieger* [9.273] with permission by Elsevier). Continuous phase: water (*line*), benzyl alcohol (*open circles*), metacresol (*filled circles*)

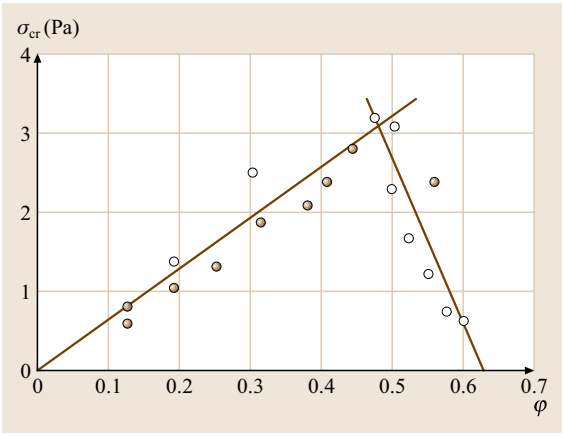

Fig. 9.80 Critical shear stress as a function of solid volume concentration for colloidal hard-sphere suspensions (after *de Kruif* et al. [9.219] with permission by the AIP)

After reaching this maximum, it decreases and reaches zero for a solid volume concentration in the vicinity of the maximum packing fraction, where the viscosity diverges. The maximum of the critical shear stress at $\varphi \approx 0.5$ is an indicator that a hard-sphere disorder–order transition is rheologically relevant [9.194]. The dependence of the critical shear stress on the solid volume concentration is shown in Fig. 9.80.

So et al. [9.277] indicated that it is possible to suppress shear-thickening effects for highly concentrated suspensions of smaller stabilized hard spheres in contrast to suspensions with nonstabilized larger particles at the same solid volume concentration. In the latter case, weak interparticle forces, i. e., attractive forces, lead to a formation of clusters and hence to a modification of the microstructure, which deviates from that of a face-centered cubic or hexagonally close packing at solid volume concentration above $\varphi = 0.5$.

Heymann et al. [9.276] studied noncolloidal suspensions of PMMA spheres dispersed in a Newtonian silicone oil. They measured the flow curves and shear stress–shear strain curves of the suspensions of various solid volume concentration in the controlled-shear-stress (CSS) mode with different logarithmic ramp times t_R. An open question in rheology of highly concentrated hard-sphere suspensions (or suspensions generally) is how the transition from the solid-like behavior at low shear strains or shear rates to the liquid-like behavior at higher mechanical loading takes place.

An example is given in Fig. 9.81. At higher shear stresses and shear rates all flow curves (Fig. 9.81a) coincide and no dependence on the ramp time is found. The shear rate depends only on the actual shear stress. Hence, the suspension shows typical liquid-like behavior at high shear stresses with terminal Newtonian behavior. At small shear stresses scattering of the data occurs. However, the same data presented in the shear strain–shear stress curves (Fig. 9.81b) unveils the problem. At low shear stresses, the curves coincide, independent of the ramp time. This indicates a unique relation between the shear stress and the shear strain. Hence, the suspension behaves like a solid at low shear stresses. Experiments with increasing and subsequently decreasing shear stresses reveal strain hysteresis in the solid-like regime, which depends on the solid volume concentra-

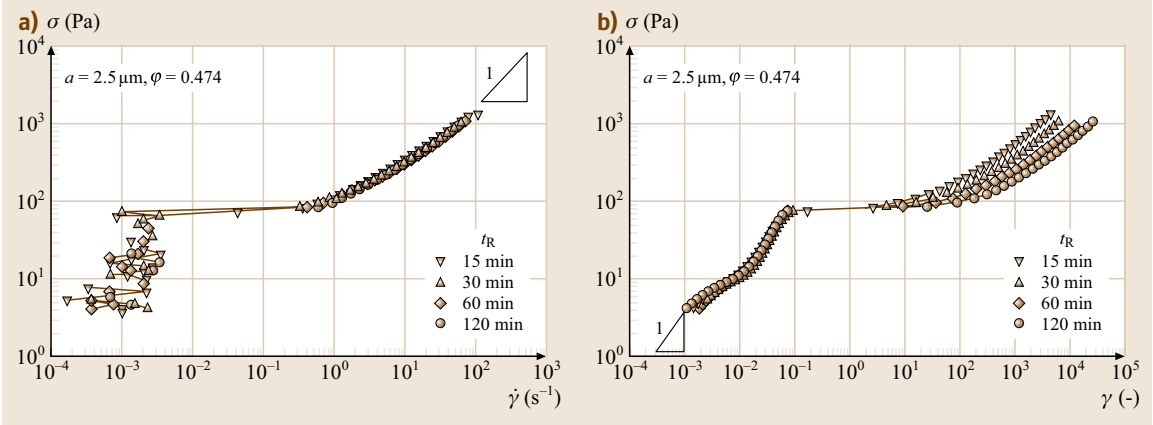

Fig. 9.81a,b Flow and deformation behavior of a suspension with $\varphi = 0.474$ and a mean particle radius a of 2.5 µm: **(a)** flow curve, **(b)** shear stress versus shear strain (after *Heymann* et al. [9.276] with permission by the Society of Rheology)

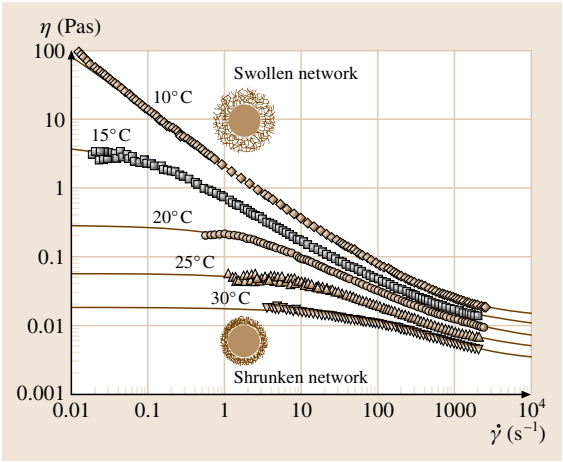

Fig. 9.82 Viscosity change due to reversible swelling of the surface layer as a function of shear rate at various temperatures (after *Senff* et al. [9.278] with permission by the American Chemical Society)

tion and the ramp time of the shear stress variation. At very low shear stresses, Hookean behavior can be speculated. By further increasing the solid volume concentration one leaves the region of suspension rheology and arrives in the region of bulk materials.

Senff et al. [9.278] analyzed the rheological behavior of sterically stabilized, temperature-sensitive core–shell lattices. The polymer layer affixed at the particle surface undergoes a volume transition as a function of the temperature. Due to the volume change the effective size of the particles and, hence, the solid volume concentration changes. By small-angle X-ray and small-angle neutron scattering it could be shown that the spheres behave as hard spheres in both cases of shrunk and swollen surface layers. The volume change was inversely proportional to the temperature, i. e., the effective particle size increased with decreasing temperature. The modification of the solid volume concentration with the temperature can be clearly recognized from the viscosity functions. The viscosity increase over some orders of magnitudes with decreasing temperature, shown in Fig. 9.83, is solely caused by the increase of the effective solid volume concentration due to swelling of the particle surface layer.

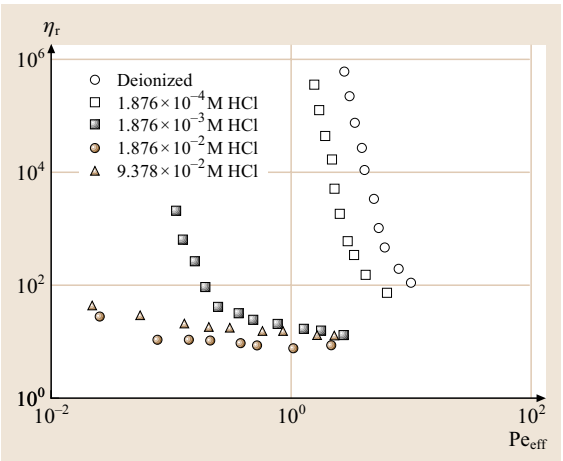

Fig. 9.83 Steady shear viscosity for aqueous polystyrene latex suspensions for $\varphi = 0.4$ at different ion strengths (after *Krieger* and *Eguiluz* [9.279] with permission by the Society of Rheology)

Additionally to the influence parameters for neutral hard spheres, the charge properties of the particles and the continuous phase ($\varepsilon_r \varepsilon_0 \psi_S^2$) and the ratio of the particle radius to the Debye length (a/κ^{-1}) must be taken into account in the case of electrostatically and electrosterically stabilized suspensions.

Krieger and *Eguiluz* [9.279] examined the rheological behavior of colloidal electrostatically stabilized polystyrene lattices consisting of spherical particles with a diameter of 110 nm in water as a function of the ion strength, characterized by the concentration of hydrochloric acid. As seen in Fig. 9.84, the ion strength (or the acid concentration) strongly influences the viscosity. With decreasing ion strength, the viscosity increases dramatically and a transition from liquid-like behavior at higher ion strengths to a more solid-like behavior at lower ion strength, comparable to that of deionized water, occurs. The viscosity lies some orders of magnitude above that for uncharged hard spheres. This effect is caused by the increasing attractive forces and the formation of aggregates. Similar results were obtained for the viscosity as a function of electrosterically stabilized silica-particle suspensions by *So* et al. [9.280].

By steric stabilization or surface modification of the particles it is possible to modify the flow behavior of the suspensions. In Fig. 9.85 the flow curves of suspensions of noncolloidal untreated and surface-modified (treated) silica spheres with a mean diameter of 4.6 μm dispersed in a Newtonian silicone oil (NM1-200) are shown. The flow curves were measured with increasing (open symbols) and a subsequent decreasing shear stresses (filled symbols). The surface of the treated particles has been modified with octadecyl groups. It can be recognized that surface modification leads to a decrease of the shear rates at comparable shear stresses and solid volume concentrations. This indicates the occurrence of a yield stress

due to the surface modification. Furthermore, it can be stated that at low shear stresses hysteresis between the up and down curves of the treated suspensions occurs, which is caused by the brush-like structure of the surface modification. At higher shear rates no differences between the behavior of untreated and treated suspensions can be observed due to the dominance of the hydrodynamic over the interparticle effects. The pure continuous phase shows a Newtonian behavior.

Normal Stress Differences. Experimental results concerning the first and second normal stress difference of true hard-sphere suspensions with a Newtonian continuous phase are very rare in literature due to their small magnitude and the prevalence of many troublesome artefacts.

Experimental results concerning the first and second normal stress difference in charged or sterically stabilized non-hard-sphere suspensions are also rare in the literature. Most of the results have been obtained by numerical simulation. For higher shear rates, a general relation between the first normal stress coefficient Ψ_1 (Sect. 9.1.2) and the shear rate

$$\Psi_1(\dot{\gamma}) \sim |\dot{\gamma}|^{-n} \qquad (9.262)$$

is valid. *Brady* and *Bossis* [9.282] investigated the shear flow behavior of interacting charged spherical particles dispersed in a Newtonian continuous phase. From numerical results, based on the Stokesian dynamics, they found an inverse proportionality ($\Psi_1(\dot{\gamma}) \sim |\dot{\gamma}^*|^{-1}$) between the first normal stress coefficient and the dimensionless shear rate $\dot{\gamma}^* = 3\pi\eta a^2\dot{\gamma}/\varepsilon_r\varepsilon_0\psi_S^2$ for $|\dot{\gamma}^*| \to \infty$, which corresponds to the experimental results of *Gadala-Maria* [9.283]. Here, ψ_S is the surface potential for infinite separation between the particle surfaces. An initially constant first normal stress coefficient for low shear rates could not be obtained. *Schoukens* and *Mewis* [9.284] observed, for suspensions of carbon-black particles in mineral oil, which form weak particulate structures, the proportionality $\Psi_1 \sim |\dot{\gamma}|^{-3/2}$. Again, no indication for a constant first normal stress coefficient at $|\dot{\gamma}| \to 0$ could be found. Indeed, the exponent $-3/2$ shows that the anisotropic structure of the particle network is weaker and can be destroyed by shear.

In contrast to these observations, *Moan* et al. [9.285] observed a qualitatively different behavior for aqueous, highly concentrated suspensions of oblate particles, which interact through excluded volume and electrostatic potential. For the first normal stress difference N_1 and the difference between the normal stress differences

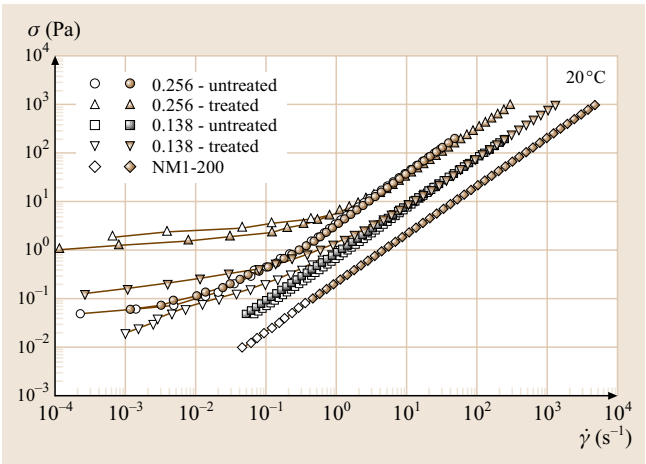

Fig. 9.84 Influence of the surface treatment on the rheological behavior of suspensions. *Open symbols*: up curve. *Filled symbols*: down curve (*Heymann* and *Aksel* [9.281]). The numbers in the legend indicate the solid volume concentration

$N_1 - N_2$, they found negative values. At low shear rates both functions decreased to a minimum and increased subsequently again. It is interesting that the second normal stress difference was negative at low shear rates and increased to positive values at higher shear rates contrary to the familiar behavior of polymers with a positive first and a smaller but negative second normal difference.

Lin-Gibson et al. [9.286] detected in nanotube suspensions a first normal stress difference which becomes negative during shear over a time period of 1000 min. By rheooptical investigations it could be shown that the development of a negative first normal stress difference is coupled with the formation of cylindrical aggregates orientated perpendicular to the flow and shear gradient direction. Similar effects were observed in emulsions too (Sect. 9.3.3).

Zarraga et al. [9.287] measured in noncolloidal suspensions of spheres in a Newtonian fluid negative values for both the first and second normal stress differences with $|N_1| < |N_2|$. The normal stress differences were proportional to the shear stress and the difference between the first and second normal stress difference, as well as the first normal stress difference were proportional to the solid volume concentration with $N_1 - N_2 \sim \varphi^3 e^{2.34\varphi}$ and $N_1 \sim \varphi^3 e^{2.34\varphi}$, respectively, in the range $\varphi = 0.35$–0.5. For noncolloidal suspensions of spheres in an elastic fluid with constant viscosity (Boger fluid), *Zarraga* et al. [9.288] measured positive first and negative second normal stress differences, as known for polymers. The normal stress differences increased with

the solid volume concentration, but the ratio $|N_1/N_2|$ decreased as the solid volume concentration increased. The magnitude of N_2 at high solid volume concentrations approached the magnitude measured for the suspensions with a Newtonian continuous phase [9.287], while the magnitude of N_1 could be attributed to the viscoelasticity of the continuous phase.

A familiar normal stress behavior, known from polymers, could be observed by *Mall-Gleissle* et al. [9.290]. They investigated suspensions of glass spheres dispersed in a constant-viscosity but viscoelastic continuous phase (Boger fluid). The first normal stress difference was positive and decreased in magnitude with increasing solid volume concentration, whereas the second normal stress difference was negative, with a magnitude that increased with increasing solid volume concentration. The variation of both normal stress differences with the shear stress followed a power-law behavior.

A new method to measure normal stresses of non-Brownian suspensions at low to moderate solid volume concentration has been developed by *Singh* and *Nott* [9.291]. Due to the low normal forces at moderate solid volume concentrations the force signal was found to be very noisy. Therefore, they used pressure holes (cf. Fig. 9.35) to measure the radial component of the normal stresses in a Couette device or the axial component in a torsional PP device. They found that both the first and second normal stress coefficients are negative and $|N_1| < |N_2|$ with a strong dependence on the solid volume concentration at higher concentrations.

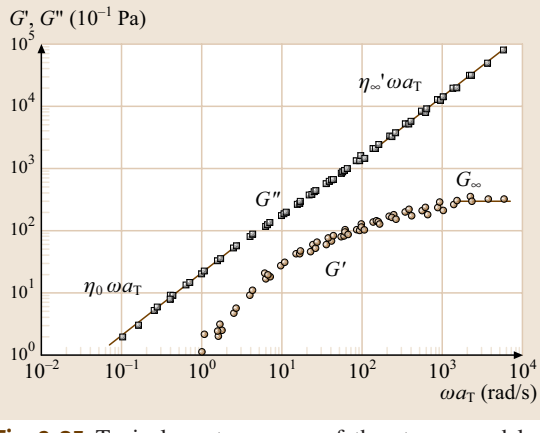

Fig. 9.85 Typical master curves of the storage and loss moduli as a function of the angular frequency for a hard-sphere suspension with $\varphi = 0.37$ (after *Shikata* and *Pearson* [9.289] with permission by the Society of Rheology)

Summarizing the results concerning the normal stress differences, it can be stated that suspensions behave in a more-complex manner than polymer melts or solutions. It is not a priori clear how the magnitudes and the sign of the normal stress differences depend on the physicochemical properties of the suspensions. A crucial assumption for an exact measurement of the normal stress differences is an absolutely stress-free state of the sample at the beginning of the experiment. Residual stresses, induced by the closing procedure of the measurement geometry, have an essential influence of the results. One should be aware of the fact that normal stress measurements are very sensitive to errors since normal stress differences are of second order. Consequently, the sample preparation must be carried out in a much more exact way as it is necessary for the measurements of the viscosity.

Storage and Loss Modulus, Fourier-Transform Rheology. *Shikata* and *Pearson* [9.289] investigated the linear viscoelastic behavior of concentrated suspensions of submicron silica spheres in a continuous phase consisting of ethylene glycol and glycerol. Typical master curves of the storage and loss modulus for this hard-sphere suspension with a solid volume concentration of $\varphi = 0.37$ are illustrated in Fig. 9.86. The data were obtained using the time–temperature superposition [9.292]) where a temperature-dependent shift factor a_T is used to shift the curves horizontally to produce a master curve. (cf. *Shikata* and *Pearson* [9.289] for details; definitions of all the parameters shown in Fig. 9.87 are given in Sect. 9.1.1). The viscous properties dominate over the frequency range investigated. Furthermore, the loss modulus shows Newtonian regions at low and high frequencies, whereas the storage modulus reaches a plateau at high frequencies.

So et al. [9.280] analyzed the storage and loss moduli of colloidal, electrosterically stabilized silica particle suspensions in dependence on the solid volume concentration and ion strength. At a given low ion strength they found a transition from a viscously dominated behavior via a gel-like to an elastically dominated behavior with increasing solid volume concentration as shown in Fig. 9.87a. It is noteworthy that the moduli vary over more than four orders of magnitude. Furthermore, a solid-like behavior arises with increasing solid volume concentration indicated by the plateau of the loss modulus. Figure 9.87b shows the influence of the salt concentration, i. e., the ion strength. At higher salt concentrations, the suspensions show liquid-like behavior which passes to a gel-like behavior if the salt con-

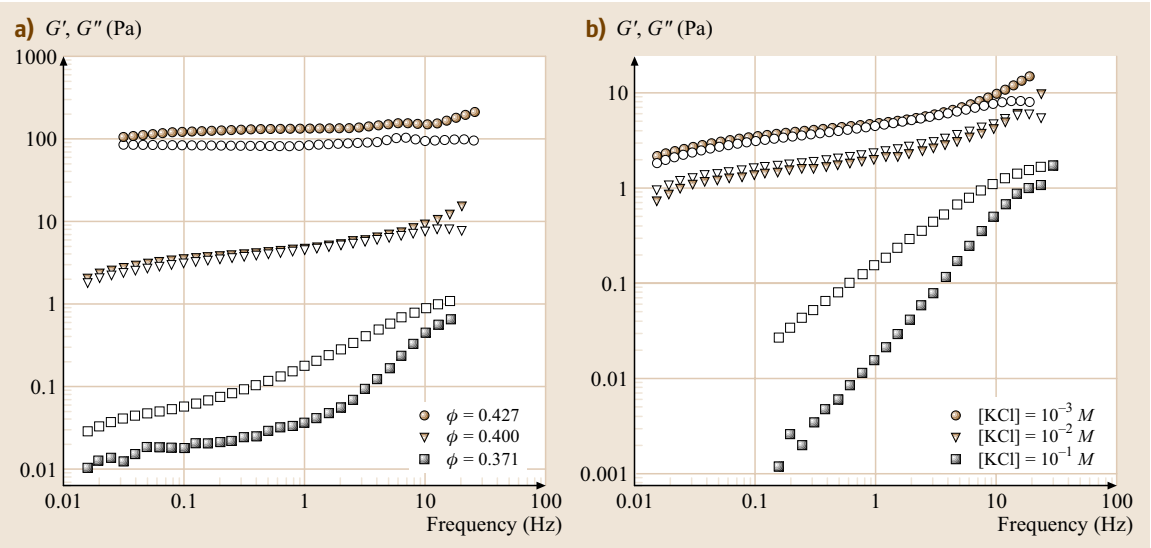

Fig. 9.86a,b Storage (G', *filled symbols*) and loss (G'', *open symbols*) moduli of an electrosterically stabilized silica particle suspension as a function of frequency (after *So* et al. [9.277] with permission by Elsevier): **(a)** dependence on the solid volume concentration at an ion strength [KCl] = 10^{-3} M, **(b)** dependence on the ion strength at a solid volume concentration of $\varphi = 0.4$

centration decreases and the influence of the attractive interparticle forces increases.

A crucial problem in determining the storage and loss modulus is to meet the necessary condition of linearity between input (strain or stress) and output (stress or strain) signal. Due to the strong interactions in highly concentrated suspensions the critical shear strain or shear stress amplitudes are very small in contrast to polymers. Exceeding the critical values (intentionally in large-amplitude oscillatory shear (LAOS) or unintentionally) can lead to nonharmonic output signals and the equations for the calculation of the storage and loss moduli are no longer applicable (Sect. 9.1.1). The only way out is the analysis of the output signal concerning the occurrence of higher harmonic components (overtones) by use of the method of Fourier-transform rheology (FTR) as developed by the group of *Wilhelm* [9.293–295]. *Heymann* et al. [9.267] used this method to analyze the rheological behavior of highly concentrated suspensions. As depicted in Fig. 9.88 for a hard-sphere suspension with a solid volume concentration of $\varphi = 0.474$, the fifth harmonic in the shear stress signal occurs in the vicinity of the yield stress ($\sigma_y = 7.9$ Pa), i. e., in the range of transition from solid- to liquid-like behavior. However, the behavior of the suspension becomes already nonlinear at a shear stress amplitudes below the yield stress which is indicated by the first occurrence of the third harmonic.

Kallus et al. [9.296] studied polymer dispersions with the FTR method. An essential result of their experi-

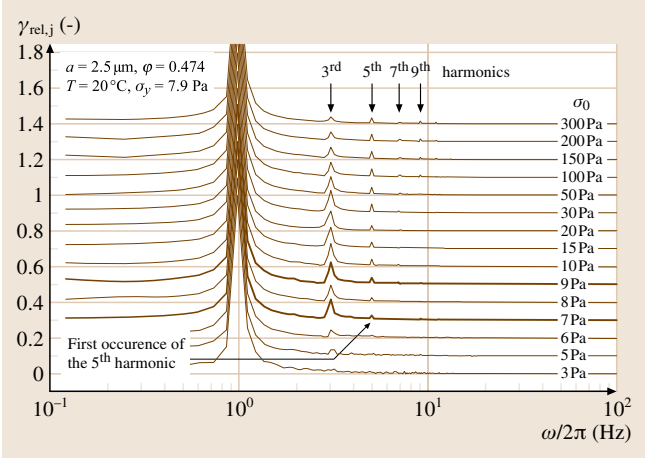

Fig. 9.87 Example of relative strain amplitude spectra obtained in oscillatory shear flow for various shear stress amplitudes of a hard-sphere suspension (for details see legend) (after *Heymann* et al. [9.267] with permission by the Society of Rheology). The curves are shifted vertically to avoid overlap. The amplitude of the shear stress σ_0 is defined in Fig. 9.3 in Sect. 9.1.1

ments is that the particle surface characteristics influence the nonlinear response significantly. The intensity of the overtones was found to be higher for dispersions of particles with a *hairy* swollen surface layer compared to a system of smooth particles at the same steady shear viscosity.

A general classification of the rheological behavior of complex fluids such as dispersions in LAOS has been given by *Hyun* et al. [9.297]. They found four main types of the fluid behavior in LAOS amplitude sweeps and pointed out that it is possible to relate the results of LAOS experiments to the microstructure of the materials. However, it must be emphasized again that the calculation of the storage and loss moduli on the basis of the linear theory is no longer valid, if overtones in the output signal occur.

In the case of flocculated colloidal suspensions *Otsubo* [9.298] proposed a rule similar to the Cox–Merz rule ((9.102) in Sect. 9.1.1), which relates the storage modulus to the first normal stress difference at low frequencies and shear rates, respectively

$$G'(\omega) = \frac{1}{2} N_1(\dot{\gamma})\Big|_{\omega=\dot{\gamma}} \,. \tag{9.263}$$

Transient Experiments – Shear Creep and Start-Up Flow. Studies on the transient behavior of suspensions were carried out, e.g., by *Heymann* et al. [9.276] and *Schmidt* and *Münstedt* [9.299]. *Heymann* et al. [9.276] investigated the creep and start-up flow behavior of non-

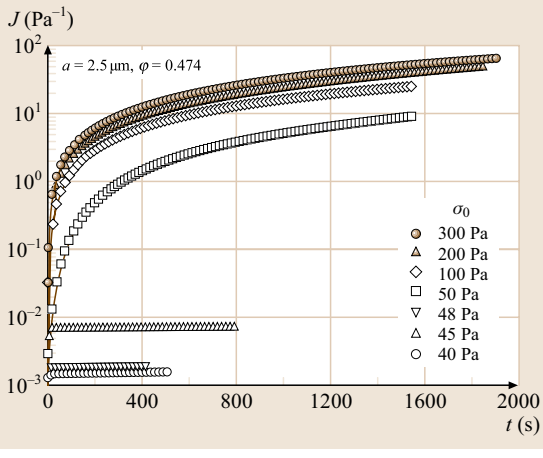

Fig. 9.88 Shear creep behavior of a suspension of PMMA spheres in a Newtonian continuous phase for various shear stresses (after *Heymann* et al. [9.276] with permission by Springer)

colloidal suspensions of monodisperse PMMA spheres (*Heymann* et al. [9.267] for details) dispersed in silicone oil. They pointed out a qualitatively different behavior of the suspensions below and above the yield stress in creep flow. Below the yield stress a typical elastic behavior has been found characterized by a time-independent creep compliance at a given shear stress. Above the apparent yield stress, a typical liquid-like behavior could be observed. The results of the creep experiment could be correlated to the start-up flow experiment. At low shear rates a linear viscoelastic behavior was found, followed by a nonlinear viscoelastic behavior with an overshoot in the shear stress output. A further increase of the shear rate led to a liquid-like behavior characterized by an instantaneous increase of the shear stress without any delay.

In Fig. 9.89, the shear compliance $J(t)$ of suspensions of (PMMA) hard spheres in a Newtonian continuous phase is shown. One can distinguish between two ranges. At shear stresses below the yield stress (in this case $\sigma_y = 48.5\,\text{Pa}$) no creep could be observed. Exceeding the yield stress leads to a significant creep. It should be noted that this transition from solid- (elastic) to liquid-like behavior occurs in a small range of $48\,\text{Pa} < \sigma_0 < 50\,\text{Pa}$.

Schmidt and *Münstedt* [9.299] presented similar results for suspensions of monodisperse hydrophilic glass spheres in a Newtonian continuous phase. At low shear stresses a viscoelastic behavior has been observed in creep, whereas at high shear stresses the suspensions showed liquid-like behavior. Due to the problems described in the part dealing with the normal stress differences, transient experiments seem to be a suitable tool to investigate the viscoelastic properties of suspensions.

Most of the authors cited above investigated suspensions of spheres in various continuous phases. If the particles are nonspherical (e.g., ellipsoids, rods), additionally to the aforementioned influence parameters, the axis ratio must be taken into account to understand the flow behavior of such suspensions. For details on this subject it is referred to the monographs of *Macosko* [9.188] or *Larson* [9.186], to the contributions of *Utracki* [9.300], and to the review article of *Petrie* [9.301] on the rheology of fibre suspensions.

Elongational flows. The kinematics of elongational flows (cf. Sect. 9.1.3) is quite different from the kinematics of viscometric flows (cf. Sect. 9.1.1). Due to the exponential path–time relation, the distance between neighboring particles increases more rapidly than in viscometric flows. Hence, the collision probability between

the particles is lower than in shear flows. Furthermore, particle migration, as described for shear flows, does not occur due to the kinematics.

However, experimental results obtained for suspensions in elongational flows are very rare in literature. A review of elongational rheometers applicable to special disperse and other materials has been given by *Greener* and *Evans* [9.303].

The main problem of elongational measurements with filament stretching rheometers is that the preparation of a stable sample for measurements is very difficult. Often, rods with cylindrical or rectangular cross-sectional area are used, which must be stable under gravity or in a buoyancy-neutral environment. Other devices (four-roller apparatus, opposite nozzle device) have been used for suspensions with viscosities lower than that of filled polymer melts.

Greener and *Evans* [9.302] investigated suspensions of aluminium powder dispersed in a polyisobutylene (PIB) matrix. Using a fibre filament stretching device they measured the elongational viscosity at constant strain rates. Qualitatively, they observed a similar behavior of the elongational viscosity in dependence of the extensional rate and the solid volume concentration as found for the shear properties. The Trouton ratio (the ratio of the elongational to shear viscosity at the same elongational and shear rates), was found to be approximately 3 in the low shear and strain rate range as is exactly the case for incompressible Newtonian liquids. It is interesting to note that this observation is true up to solid volume concentrations of $\varphi = 0.42$. The uniaxial elongational viscosity η_e as a function of the strain rate $\dot{\varepsilon}$ and the relative uniaxial elongational viscosity $\eta_{r,e} = \eta_e/\eta_{e,c}$ as a function of the solid volume concentration are shown in Fig. 9.90. The behavior differs from that obtained for unfilled or filled polymers. Contrary to polymers where the elongational viscosity rises from a plateau at low strain rates through a pronounced maximum and then decreases at higher strain rates, the elongational viscosity of the suspension shown here decreases monotonously with increasing strain rates.

In a more-quantitative manner, *Le Meins* et al. [9.304] observed for suspensions of colloidal polystyrene spheres in polyisobuthylene (PIB) a deviation of the relative elongational viscosity from the behavior, which can be described by the Krieger–Dougherty equation (9.244). For larger particles and at low solid volume concentrations good agreement has been found, whereas for smaller particles and at higher solid volume concentrations deviations occurred. The deviations were smaller for the relative elongational viscosity than for the relative shear viscosity. These observations have been explained by dominating hydrodynamic effects occurring with larger particles, whereas with colloidal particles the interparticle interactions become relevant.

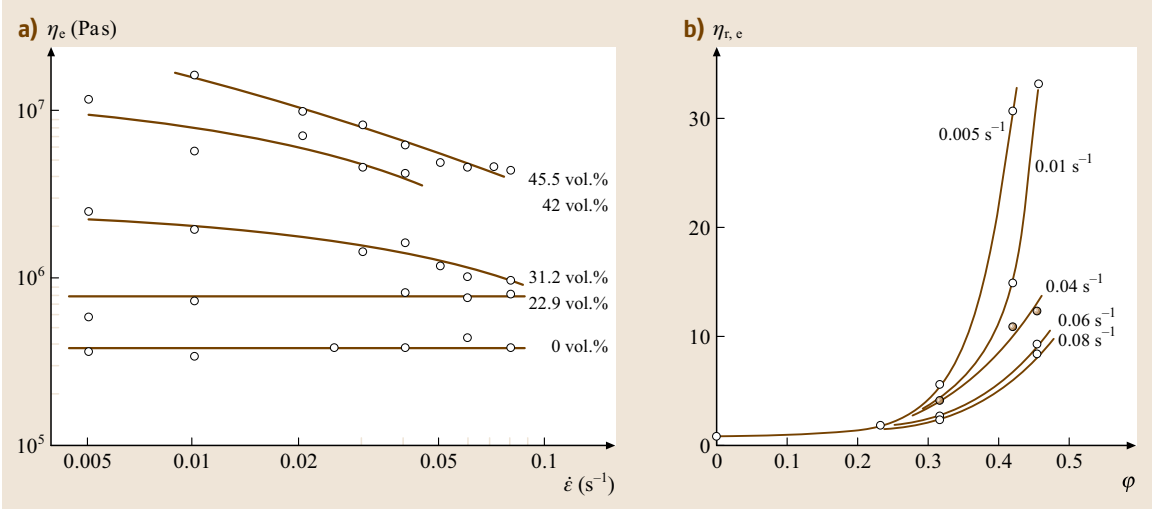

Fig. 9.89a,b Elongational behavior of suspensions of Al powder in PIB, **(a)** dependence of the uniaxial elongational viscosity η_e on the extensional strain rate $\dot{\varepsilon}$ at various solid volume concentrations, **(b)** dependence of the relative extensional viscosity on the solid volume concentration at various extensional strain rates (after *Greener* and *Evans* [9.302] with permission from the Society of Rheology)

Furthermore, a reduction in strain hardening could be observed for various elongational rates if rigid spherical polystyrene particles are added to the viscoelastic polymer matrix. The particles cannot follow the externally applied elongational field and, hence, a partial conversion form elongational to shear flow within the polymer matrix occurs.

O'Brien and *Mackay* [9.306] obtained for suspensions of kaolin suspensions elongational viscosities with elongation thinning and elongation thickening ranges depending on the particles size. Additionally, they observed particle-size-dependent Trouton ratios of the order of 50–100.

Husband et al. [9.305] measured the tensile creep behavior of suspensions containing noncolloidal limestone ($CaCO_3$) particles dispersed in a polyisobuthylene (PIB) matrix over long time periods. At low stresses they obtained a solid-like behavior indicated by an equilibrium tensile strain. At higher stresses a flow process, i. e., a liquid-like behavior, has been observed characterized by continuously increasing strain rates. The results of the tensile creep experiments are portrayed in Fig. 9.91. The tensile creep coefficient is defined as

$$\eta^{+}_{\mathrm{E,c}}[t, \sigma_{\mathrm{E}}(t)] = \frac{\sigma_{\mathrm{E}}(t)}{\dot{\varepsilon}^{-}[t, \sigma_{\mathrm{E}}(t)]} \qquad (9.264)$$

where $\dot{\varepsilon}^{-}[t, \sigma_{\mathrm{E}}(t)]$ is the tensile creep rate decay function, $\sigma_{\mathrm{E}}(t) = F/A(t)$ is the tensile stress, F is the force, and $A(t)$ is the time-dependent cross-sectional area of the sample. For tensile stresses $\sigma_{\mathrm{E}} < 540$ Pa constant tensile strains, i. e., vanishing tensile strain rates, are reached. The tensile strains depend on the tensile stress. The vanishing tensile strain rates correspond to an increase of the tensile creep rate coefficient. This is attributed to a viscoelastic solid-like behavior. For higher tensile stresses a tensile creep rate coefficient independent of both the tensile strain and the tensile stress has been found as a characteristic of a viscoelastic liquid-like behavior. The critical tensile stress, indicating the transition between both ranges, can be interpreted as a static yield stress. The observations concerning the yield transition obtained by *Husband* et al. [9.305] in elongational flow correspond qualitatively to the results obtained by *Heymann* et al. [9.276] in viscometric flows.

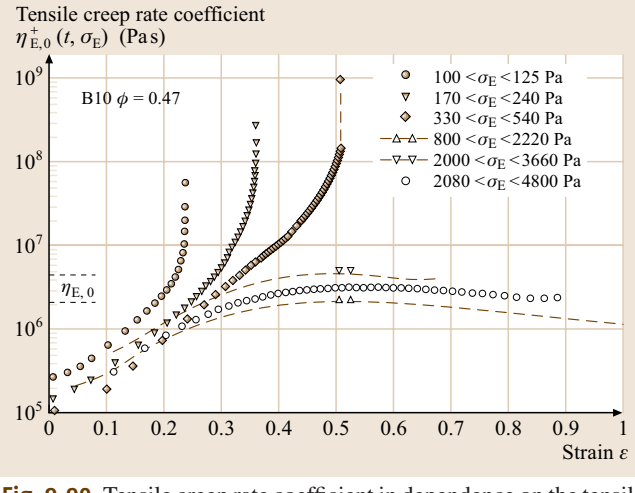

Fig. 9.90 Tensile creep rate coefficient in dependence on the tensile strain ε for a suspension with $\varphi = 0.47$; the *dashed lines* near the ordinate indicate the range of the limiting viscosity $\eta_{E,0}$ at zero extension rate (after *Husband* et al. [9.305] with permission by the Society of Rheology)

Complex Flows. Due to the tensorial character of the constitutive equations (Sect. 1.5 and Sect. 1.8) the shear and elongational experiments are not sufficient to describe the material completely in every flow situation.

One of the most popular complex flow situations is squeeze flow, which combines shear and elongational flow kinematics. A defined volume of the sample is placed in a gap between two (usually circular) parallel plates. One of the plates is kept fixed and the other plate moves towards the fixed one either at a given velocity or driven by a given force. Depending on the experimental mode, the normal force, velocity, or the separation between the plates is measured. Two modes are possible: the constant-area and constant-volume techniques. Details of the modeling of the squeeze flow process have been described by *Gibson* et al. [9.307] and *Macosko* [9.188].

The kinematics of the flow field is highly complex because of two velocity components, one in radial direction ($u(r, z)$) and the other in axial direction ($w(r, z)$), where r and z are the radial and axial coordinates. In contrast to viscometric flows, where only one velocity gradient occurs, in the squeeze flow up to four velocity gradients ($\partial u/\partial z$, $\partial u/\partial r$, $\partial w/\partial z$, $\partial w/\partial r$) complicate the situation, especially for non-Newtonian materials where the rheological behavior of the material is a priori unknown. Therefore, it is impossible to obtain rheologically exactly defined material functions for non-Newtonian liquids from squeeze flow experiments.

Beyond the aforementioned difficulties, the boundary conditions have an essential influence on the kinematics of squeeze flow. If the no-slip condition at the walls holds, the flow is dominated by shear effects. The existence of wall slip leads to the dominance of

elongational effects. If it is not clear whether or not the material slips at the walls, it is not possible to obtain reliable results from the measurements.

Despite these disadvantages, squeeze flow of disperse materials is subject of many investigations. The determination of the squeeze force as a function of the gap height and estimation of the yield stress is mainly the aim of these studies.

An important problem in the investigation of suspensions in squeeze flows is demixing of the sample, i. e., filtration of the continuous phase through the *particle skeleton*. *Delhaye* et al. [9.308] found for a highly concentrated suspension of spheres in a Newtonian fluid a significant change of the radial concentration distribution in an initially homogeneously distributed sample during the experiment. Similar effects of binder migration were shown by *Poitou* and *Racineux* [9.309]. Due to the inhomogeneity of the sample, the measured squeeze force is not representative for the experiment. Other authors (e.g., *Chan* and *Baird* [9.310], *Sherwood* and *Durban* [9.311]) calculated the squeeze force as a function of the gap width for various viscoplastic models (Herschel-Bulkley, Bingham) whose parameters were obtained from definite viscometric flows. They found a reasonable agreement between the numerical simulation and the experimental data. Some contributions, dealing only with the analytical or numerical simulation of the squeeze process, are available, which consider wall slip and various models for the flow behavior [9.312–314]. However, a relation to experiments has not been established and no relevant material parameters (viscosity, yield stress) have been given. Summarizing the results available in the literature, it must be stated that the squeeze flow is not the first choice as an experiment for the measurement of rheologically relevant material functions.

9.3.3 Emulsions

Emulsions are disperse systems containing one liquid dispersed in another liquid. Both liquids are immiscible or, at least, partially immiscible. Usually, drop sizes are in a range between 10 nm and 10 µm. Emulsions with drop sizes between 10 nm and 100 nm are called microemulsions. Emulsions with drop sizes between 100 nm and 1 µm are known as miniemulsions [9.196]. Some fundamental principles of emulsion rheology have been summarized by *Sherman* [9.315], *Barnes* [9.316], *Tadros* [9.317], and *Pal* [9.318].

Generally, two fundamental types of emulsions can be distinguished: water in oil (W/O) and oil in water (O/W) emulsions. The classification depends on the kind of the dispersed (liquid 1) and continuous (liquid 2) phase. In the case of a nonaqueous continuous phase this classification is not very clear. But, in a more-general manner, an O/W emulsion is characterized by a viscosity of the disperse phase higher than that of the continuous phase, or vice versa for W/O emulsions. A further addition of a liquid 1, dispersed in a liquid 2, up to a critical volume concentration $\varphi_{1,PI}$ leads to a change of the type of emulsion, called phase inversion. In Fig. 9.91 the influence of the disperse phase 1 on the relative viscosity of emulsions is depicted. Similar to suspensions, the relative viscosity increases with increasing volume concentration of the disperse phase 1 until the maximum packing fraction is reached. At this point, a phase inversion takes place, leading to a decrease of the viscosity with increasing volume concentration of the, from now on, continuous phase 1. The continuous phase 2 below $\varphi_{1,PI}$ is now the disperse phase. Phase inversion is a typical phenomenon in emulsions that does not appear in suspensions.

In the previous sections, the rheological behavior of suspensions has been extensively described. Most of the basics described for suspensions hold also for emulsions. However, compared to suspensions, differences occur because the disperse phase consist of a second liquid with a finite viscosity and surface tension. The drops of the disperse phase can be deformed or broken-up due to shear or elongational flow. The interfacial tension influences the interactions between the two phases. Furthermore, the drop size distribution may change due to coalescence, Ostwald ripening, creaming, flocculation,

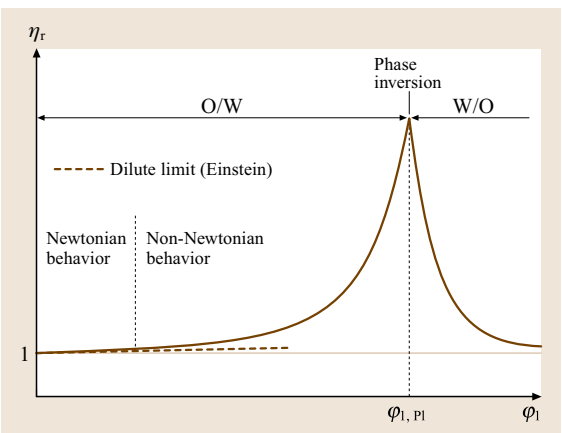

Fig. 9.91 Influence of volume concentration of phase 1 on the relative viscosity of emulsions prior and after phase inversion

or drop break-up. Additionally, the continuous phase contains surface-active agents (surfactants) that may cause increased viscosity and even non-Newtonian behavior of the continuous phase and influence the overall rheology of the emulsion.

In the following, only properties of emulsions that deviate from those of suspensions will be illustrated.

Dimensional Analysis. In addition to the dimensionless groups in suspension rheology (Sect. 9.3.1), emulsions involve the capillary number

$$\mathrm{Ca} = \frac{\eta_c \dot{\gamma} a_0}{\sigma_I} \qquad (9.265)$$

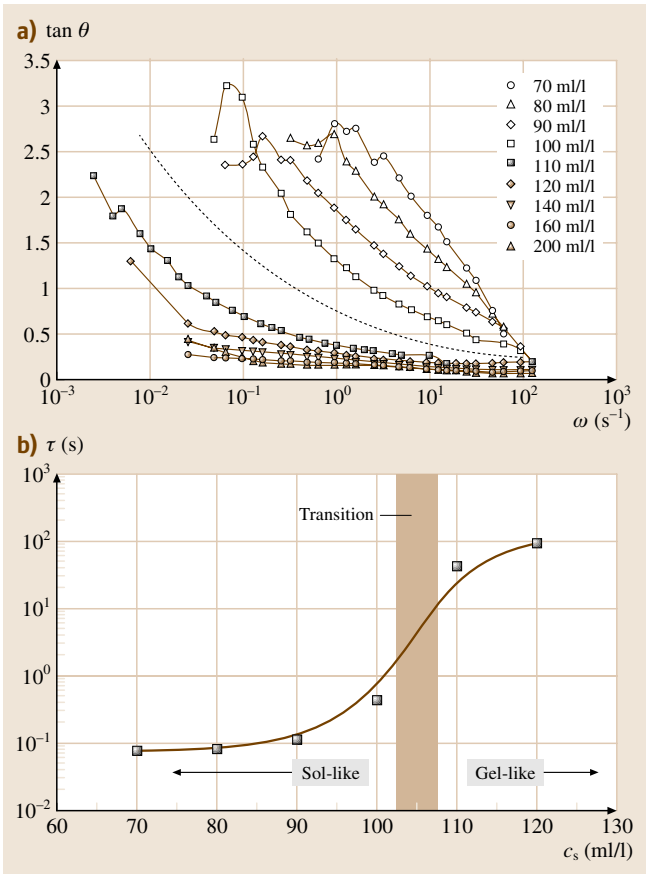

Fig. 9.92a,b Aqueous solution of Tween 85®at a temperature of 20 °C: **(a)** Loss tangent as a function of angular frequency and volume concentration (after *Teipel* et al. [9.319] with permission by Elsevier), **(b)** characteristic relaxation times τ as a function of the volume concentration of surfactant. The lines are drawn to guide the eye. The surfactant concentration is denoted by c_s

as the ratio of viscous to capillary forces (σ_I is the interfacial tension) and the viscosity ratio

$$V_r = \frac{\eta_d}{\eta_c} \,. \qquad (9.266)$$

As the characteristic droplet length in (9.265) the initial droplet radius a_0 is given. In contrast to suspensions, the initial droplet radius can change at higher shear or elongational rates. Larger droplets with a weak surfactant layer can deform during shear, which is often coupled with an orientation of the droplets in the flow direction as shown in Fig. 9.94. Droplet deformation and/or break-up lead to the formation of new interfacial areas. For non-Newtonian continuous phases the definition of the capillary number according to (9.265) is not unique because the viscosity η_c is itself a function of the shear rate.

If one neglects van der Waals, electrostatic, electrosteric, and steric interactions and assumes a gap width large enough compared to the initial droplet size, the relative viscosity of emulsions can then be formulated as [9.320, 321] (cf. Table 9.10)

$$\eta_r = f\left(\varphi, V_r, \xi, \rho_r, t_r, \frac{\delta}{a_0}, \mathrm{Ga}, \mathrm{Ca}, \mathrm{Pe}, \mathrm{Re_P}\right) \,. \qquad (9.267)$$

The relation can be further simplified for emulsions containing a nonvarying monodisperse phase ($\xi = \text{const.}$) of buoyant droplets ($\rho_r \to 1$) with thin surface layer thickness ($\delta/a_0 \ll 1$) and with vanishingly small droplet Reynolds number ($\mathrm{Re_p} \to 0$) under steady-state conditions ($t_r \to \infty$) to give the relation

$$\eta_r = f\,(\varphi, V_r, \mathrm{Ca}, \mathrm{Pe}) \,. \qquad (9.268)$$

The deviations in (9.268) from the analogous relation for suspensions (9.231) stems from the appearance of the viscosity ratio V_r and the capillary number Ca, which occur only in emulsions.

For high viscosity ratios ($V_r \gg 1$) and high interfacial tensions ($\mathrm{Ca} \to 0$), emulsions with small droplets behave like suspensions (Sect. 9.3.2) as demonstrated by *Teipel* and *Aksel* [9.321]. On the other hand, for highly dilute emulsions with high interfacial tensions G. I. Taylor derived a relation for $\eta_r = f(\varphi, V_r)$ which for $\varphi \to 0$ tends to the Einstein result (9.237).

Properties of the Continuous Phase, Micellar Rheology. The continuous phase of emulsions often consists of low-molecular-weight liquids showing a Newtonian behavior. To stabilize the emulsions emulsifying agents (emulsifiers or surfactants) must be added, which lead

to a modification of the rheological properties of the continuous phase. Surfactants are low-molecular-weight materials with amphiphilic properties (Chap. 3.2). Due to their amphiphilic character the surfactants can adsorb at interfaces, which results in a decrease of the interfacial or surface tension. Above a certain surfactant concentration the surfactant molecules undergo reversible aggregation to form micelles (Chap. 3.2).

A typical example has been given by *Teipel* et al. [9.319] who systematically investigated aqueous solutions of a nonionic surfactant polyoxyethylene sorbitan trioleate (Tween 85®) at various volume concentrations of surfactant. They demonstrated that with increasing surfactant concentration an increasing shear thinning effect in the viscosity function could be observed. This concentration-dependent non-Newtonian viscosity behavior is coupled with an increase of the elasticity of the micellar solutions. The oscillatory data show that, in the range of surfactant concentrations of 100–110 ml/l, a transition from a weakly elastic (sol-like) to a highly elastic (gel-like) response occurs. This transition, shown in Fig. 9.92a, is characterized by crossing the value of the loss tangent $\tan\theta = 1$ (Sect. 9.1.1). Correspondingly, the transition from sol- to gel-like behavior can also be seen in Fig. 9.92b by the characteristic relaxation time obtained from the inverse angular frequency at $\tan\theta = 1$, which increases dramatically over more than two orders of magnitude. The grade of elasticity indirectly shows the change of the internal structure of the micelles in the solution.

The rheological properties of the micellar solutions strongly depend on the conditions of preparation. In Fig. 9.93 the viscosity functions obtained under various fabrication (ϑ_F) and measurement (ϑ_M) temperatures are depicted.

Obviously, both the fabrication temperature and the measurement temperature influence the viscosity function. The low-shear viscosity increases over approximately one day if measured at a temperature than the fabrication temperature. In the high-shear-rate region the influence of the temperature preloading vanishes due to the dominance of hydrodynamic forces. These effects are caused by a structure formation process both during and after the fabrication process.

Other important properties of the continuous phase are the polarity and pH value. Both affect the charge of the droplets and the repulsive forces. Further information on the physicochemical properties of micellar solutions can be found, e.g., in the textbooks of *Larson* [9.186] or *Morrison* and *Ross* [9.195].

Properties of the Disperse Phase. In contrast to suspensions, the droplets of the disperse phase of emulsions have a finite viscosity. Hence, the viscosity ratio (9.266) must be taken into consideration. During shear (or elongation) the droplets can be deformed and/or broken up, as shown in Fig. 9.94. *Rumscheidt* and *Mason* [9.323] analyzed the droplet deformation and break-up mechanism, varying the viscosity ratio and shear rate. At low viscosity ratios Fig. 9.94a and for shear rates above a critical value, formation of a sigmoidal droplet shape and creation of small satellite droplets has been observed. At viscosity ratios of the order of 1 two identical droplets with smaller satellite droplets could be found, resulting from an elongation and an increasing contraction of the initial droplet (Fig. 9.94b). Alternatively, a droplet is stretched due to shear and a subsequent droplet break-up occurred (Fig. 9.94c). At higher viscosity ratios only droplet deformation and orientation without break-up have been observed (Fig. 9.94d). Generally, a droplet orientation was found at higher shear rates. However, it should be noted that the results described above have been found for single droplets without the influence of neighboring droplets.

The deformability of the droplets depends both on the viscosity ratio and the capillary number. *Taylor* [9.324] derived a theoretical function

$$f_1(V_r) = \frac{1 + 19V_r/16}{1 + V_r} \qquad (9.269)$$

in simple shear, taking into account the viscosity ratio according to (9.266). The function $f_1(V_r)$ can vary in the

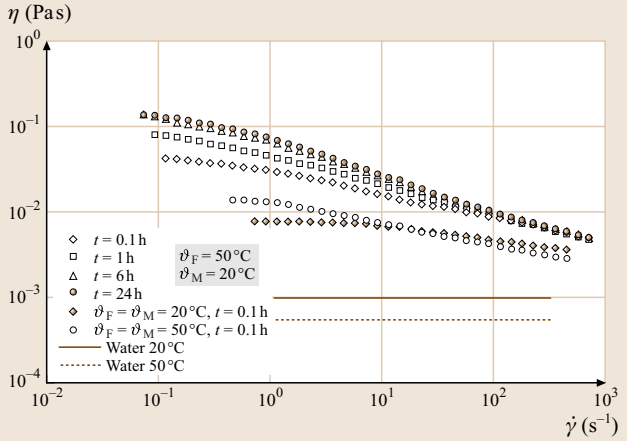

Fig. 9.93 Time dependence of the micellar solutions (Tween 85®in water) at different fabrication (ϑ_F) and measurement (ϑ_M) temperatures (after *Teipel* et al. [9.322] with permission by Elsevier)

range 1–1.88. The droplet deformation D, dependent on the viscosity ratio, is then given by

$$D = \frac{A_r - 1}{A_r + 1} = f_1(V_r)\mathrm{Ca} \qquad (9.270)$$

where A_r is the main axis ratio of ellipsoidal drops (major to minor axis length).

The effect of droplet break-up is then characterized by a critical capillary number $\mathrm{Ca_{cr}}$. Droplet break-up occurs if the capillary number exceeds a critical value, i. e., $\mathrm{Ca} > \mathrm{Ca_{cr}}$. *Grace* [9.325] reported some experimental findings of critical capillary numbers as a function of the viscosity ratio of the two phases for Newtonian liquids. The interpolating curve in Fig. 9.95 separates the region below where droplet break-up occurs from the region above where no droplet break-up takes place. The horizontal part of the curve represents tip-streaming break-up where small droplets are shed off from the tips of a larger sigmoidally shaped *mother drop*, as shown in Fig. 9.94a. It should be noted that *Grace* [9.325] used the dynamic surface tension to calculate the capillary number.

For a planar elongational flow, *Grace* [9.325] found that the critical capillary numbers were even smaller compared to those for shear flows at the same viscosity ratio. Furthermore, he found that it is possible to induce droplet break-up in elongational flows for viscosity ratios up to 1000. Hence, the elongational flow mechanism is more efficient for the fabrication of emulsions, even at higher viscosity ratios where shear flows fail.

Some reports have been published in the literature dealing with the problem of single droplet deformation and break-up in shear and elongational flows. *Tsakalos* et al. [9.326] investigated experimentally the deformation and break-up mechanism of a Newtonian droplet in a viscoelastic continuous phase in steady shear flow. The initially spherical droplets deform to threads during shear. They found for large capillary numbers that the deformation of threads, above a certain strain larger than 20, follows a pseudoaffine deformation for $\mathrm{Ca}/\mathrm{Ca_{crit}} > 2.5$. Another mechanism of droplet break-up is end pinching (the ends of a stretched drop pinch off from the central filament due to drop relaxation after an abrupt change of the flow conditions). Capillary instabilities only develop when the thread diameter reaches a critical value. *Cristini* et al. [9.327] investigated the break-up phenomenon in impulsively started shear flow. They stated that the mechanism of break-up of Newtonian droplets in a Newtonian continuous phase (formation of threads with capillary break-up or end pinching) depends only on the average initial particle size. The mechanism of end pinching of Newtonian droplets in a Newtonian continuous phase during large oscillatory shear could be confirmed by *Wannaborworn* and *Mackley* [9.328] both experimentally and by numerical simulation. Furthermore, the critical capillary number was found to be higher for oscillatory shear than for steady shear, i. e., the droplets are more stable in oscillatory shear flows. At low strains, i. e., in the case of small-amplitude oscillatory

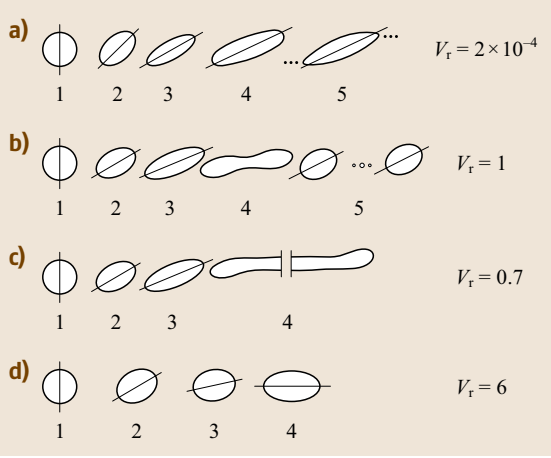

Fig. 9.94a–d Deformation and orientation of a single droplet in shear flow for increasing shear rates, indicated by the increasing numbers, at various viscosity ratios (after *Rumscheidt* and *Mason* [9.323] with permission by Elsevier)

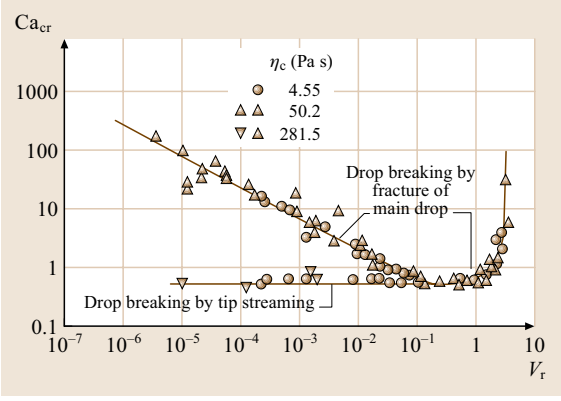

Fig. 9.95 Influence of the viscosity ratio on the critical capillary number obtained in shear flows (after *Grace* [9.325] with permission by Taylor & Francis)

shear (SAOS), *Cavallo* et al. [9.329] found a harmonic time behavior of the axis of the deformed droplets at lower strains, i. e., the response of the drop was sinusoidal, but shifted in phase with respect to the applied stress. At higher strains overtones with multiple frequencies of the basic frequency occurred. End-pinching effects have not been found in LAOS experiments. *Mighri* et al. [9.330] investigated emulsions with both phases consisting of constant-viscosity elastic (Boger) liquids in uniaxial elongational flow. They found that, for a given continuous phase, the drop deformation decreases as its elasticity increases, whereas for a given drop liquid, the drop deformation increases with increasing elasticity of the continuous phase. An overview on the dynamics of drop deformation and break-up has been given by *Stone* [9.331].

Loewenberg and *Hinch* [9.332] studied numerically the collision behavior of two deformable drops in shear flow. Their calculations indicate that drop interactions do not induce significantly subcritical capillary number break-up. In dilute emulsions, the critical Capillary number is a weak function of volume fraction because deformable drops can easily squeeze past each other.

As mentioned above, the continuous phase contains surfactants as stabilizers for the emulsion. The surfactants form a surfactant layer around the droplets. The formation of this interfacial layer modifying the droplet–droplet interactions is a kinetic process depending on the temperature, concentration of surfactants, the diffusion and adsorption properties of the surfactants. The adsorption kinetics of nonionic surfactants has been investigated by *Teipel* and *Aksel* [9.333].

If the surfactant layer is only weakly elastic it can transmit flow-induced shear stresses into the droplets and the liquid inside of the droplet can rotate, similar to the movement of a crawler. Additionally, droplet deformation occurs as shown in Fig. 9.94. With decreasing droplet radius and perfect surfactant coverage the emulsions show suspension-like behavior.

As in the case of suspensions, the viscosity of an emulsion increases with decreasing droplet size at a fixed volume concentration.

Interfacial Rheology. The mechanical properties of the interface between the continuous and disperse phases influence both the rheological properties and the stability of the emulsions. The surfactants added to facilitate the fabrication of emulsions and to stabilize them adsorb at the interface between the two phases, forming a thin film of surfactant molecules. At higher surfactant concentrations, the surfactant surface forms a compact interface with rheological properties that can differ greatly from those of the bulk phases. This can lead to viscoelastic or viscoplastic properties of the interface even though the bulk phases are Newtonian. To investigate the rheological properties of surfactant layers or films adsorbed at the interface, special rheological devices are needed. Reviews on some basic principles of interfacial rheology have been given by *Tadros* [9.317] and *Warburton* [9.334].

Generally, interfaces between two liquid phases contain monolayers of adsorbed surfactants. These layers show resistance of the surface against change of shape in shear, change of area in dilatation, and change of curvature in bending [9.334].

One of the most important mechanical properties of interfaces is the interfacial shear viscosity η_I. In contrast to the bulk viscosity η, the interfacial shear viscosity η_I has units of Pas · m (surface Pas). Hence, it represents not the viscosity in the volume, but the viscosity in a plane, namely in the interface. The measurement of the interfacial shear viscosity requires special devices such as torsional pendulum or rotational viscometers with special measurement geometries. Three examples are shown in Fig. 9.96a–c. The theory of the measurements of the interfacial shear viscosity with a torsional pendulum viscometer has been given by *Criddle* [9.335].

The shear device is suspended by a torsional wire and positioned at the interface. If the pendulum oscillates, the damping of the oscillation and the period due to the viscous drag of the interface is measured. A main disadvantage of the torsional pendulum viscometer is that

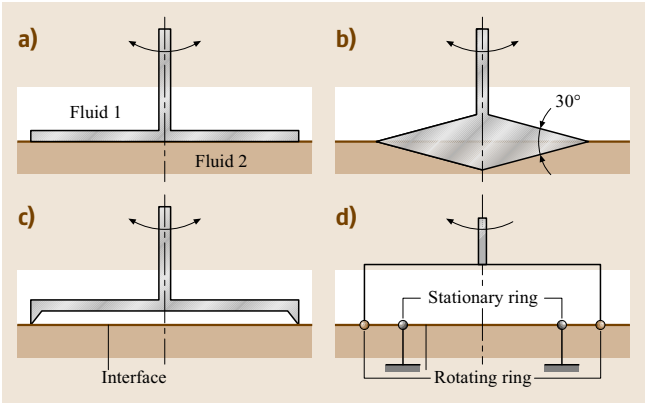

Fig. 9.96a–d Geometries used for the measurement of interfacial shear viscosity: **(a)** disk viscometer, **(b)** knife-edge disk viscometer, **(c)** ring viscometer, **(d)** concentric ring viscometer

the shear rate varies in the course of one period, which makes the measurement of non-Newtonian properties of the interface impossible. In this case, the concentric-ring viscometer, schematically shown in Fig. 9.96d, should be preferred. One ring rotates at a given angular velocity and the torsional momentum is measured at the other stationary ring. If the distance between the rings is small, the shear rate is approximately constant as in the case of the concentric cylinder viscometer (Sect. 9.1.2). In this case the non-Newtonian properties of the interface layer can be measured with more confidence.

There are other methods such as the deep-channel surface viscometer [9.317] where small particles are used as tracers to measure the surface velocities. *Petkov* et al. [9.336] developed a method to calculate the interfacial shear viscosity from the drag coefficient of a small sphere moving through an interfacial film.

To measure the dilatational surface properties three methods are used [9.317]: application of surface waves to the interface; rotation, translation or deformation of bubbles and droplets; and the maximum bubble pressure method. From these methods some information on the mechanical properties of the interface, but also on the kinetics of the surfactant adsorption at the interface, can be obtained.

Influence of Drop Volume Concentration. The deformation of the droplet surface and hence the transmission of surface tractions, causes internal circulations in the droplet, which results in a modification of the Einstein's viscosity relation (9.237)

$$\eta_r = 1 + (5/2)\, f_2(V_r)\varphi\,. \tag{9.271}$$

The *correction factor* $f_2(V_r)$ has been derived by *Taylor* [9.324] as

$$f_2(V_r) = \frac{\eta_d + (2/5)\eta_c}{\eta_d + \eta_c} = \frac{V_r + (2/5)}{V_r + 1} \tag{9.272}$$

for the case of infinitely diluted emulsions of two immiscible Newtonian liquids. The droplets of the dispersed phase are assumed to be perfectly spherical due to their smallness and the surface-tension effect. In the limit $V_r \to \infty$ (solid particles in a Newtonian liquid) with $f_2(V_r) = 1$, Einstein's equation for suspensions is obtained. The other limit $V_r \to 0$ describes the case of bubbles in a Newtonian liquid, leading to $f_2(V_r) = 2/5$. For finite viscosity ratios the viscosity of a comparable emulsion according to (9.271) and (9.272) is smaller than that of a suspension at the same volume concentration.

As in the case of suspensions, equations of the power-series type fail for higher volume concentrations. For this, the models summarized in Table 9.14 for suspensions of arbitrary particle shapes and shape distributions should be used because their applicability is not restricted to solid spherical particles of uniform size. *Pal* [9.337] combined Taylor's approach with the equations of *Mooney* [9.231] and *Krieger* and *Dougherty* [9.230]. Thus, he obtained two viscosity equations for volume concentrations up to 0.635:

Model 1 (Mooney type):

$$\eta_r \left(\frac{2\eta_r + 5V_r}{2 + 5V_r}\right)^{\frac{3}{2}} = \exp\left(\frac{2.5\varphi}{1 - \varphi/\varphi_{max}}\right)\,, \tag{9.273}$$

Model 2 (Krieger/Dougherty type):

$$\eta_r \left(\frac{2\eta_r + 5V_r}{2 + 5V_r}\right)^{\frac{3}{2}} = \left(1 - \frac{\varphi}{\varphi_{max}}\right)^{-2.5\varphi_{max}}\,. \tag{9.274}$$

Pal [9.337] fitted both models on the basis of several experimental data and found good agreement. As shown for suspensions, the maximum packing fraction φ_{max} is a fit parameter that depends (in this case) additionally on the type of model.

An empirical equation for the viscosity–volume concentration relation of non-Newtonian emulsions with volume concentration below a maximum packing fraction has been derived by *Pal* and *Rhodes* [9.338]

$$\eta_r(\dot\gamma) = (1 - K_0 K_F(\dot\gamma)\varphi)^{-A} \tag{9.275}$$

with

$$A = 6(\eta_d - \eta_c)/[10(\eta_d + \eta_c)] + (19\eta_d + 16\eta_c)/[10(\eta_d + \eta_c)] \tag{9.276}$$

as shown by *Lee* et al. [9.339]. For $V_r \gg 1$ the value $A = 2.5$ is valid. The factor K_0 accounts for the effect of hydration, i. e., the association of significant amounts of the continuous-phase liquid with the droplets, which is constant for a given emulsion. Due to the immobilization of the continuous phase, the effective dispersed-phase volume concentration increases compared to the true concentration. Furthermore, a shear-rate-dependent flocculation factor $K_F(\dot\gamma)$, describing the morphology of the emulsion, has been introduced. The product of both factors can be interpreted as the inverse of a shear-dependent maximum packing fraction, resulting in an equation similar to the Maron/Pierce equation (9.244), however with an exponent of 2.5.

Due to the deformability of the particles the maximum packing fraction can reach values greater than those for corresponding monodisperse spherical rigid particles and the viscosity increases significantly compared to suspensions. At this stage, the occurrence of yield stresses is possible. The dependence of the viscosity on the shear rate can then be described with the models discussed in Sect. 9.3.2. A further addition of disperse-phase liquid leads to a sudden decrease of the viscosity due to the phase inversion process (Fig. 9.91).

Beyond nonlinearity, emulsions show also viscoelastic flow behavior. For this reason, models for the complex modulus G^* and complex viscosity (Sect. 9.1), respectively, have been developed. For moderately concentrated emulsions of monodisperse deformable droplets in a viscoelastic continuous phase with constant interfacial tension, *Palierne* [9.340] has shown that the complex modulus in the linear viscoelastic region is given by

$$G^* = G_c^* \left(\frac{1 + 3\varphi H/2}{1 - \varphi H} \right) , \tag{9.277}$$

where

$$H = \frac{2\left[\left(G_d^* - G_c^*\right)\left(19G_d^* - 16G_c^*\right) + \left(4\sigma_I/a\right)\left(5G_d^* + 2G_c^*\right)\right]}{\left(2G_d^* - 3G_c^*\right)\left(19G_d^* - 16G_c^*\right) + \left(40\sigma_I/a\right)\left(G_d^* + G_c^*\right)} . \tag{9.278}$$

The Palierne model underpredicts the shear modulus at higher volume concentrations of the disperse phase. It fails at volume concentrations in the vicinity of the maximum packing fraction. For vanishing interfacial tension, the model of *Kerner* [9.341] can be obtained from (9.278), which is restricted to high frequencies where the influence of the interfacial tension can be neglected. *Bousmina* [9.342] extended the Kerner model to the low-frequency range by considering the interfacial tension. For the complex modulus of the emulsions he obtained

$$G^* = G_c^* \frac{2(G_d^* + \sigma_I/a) + 3G_c^* + 3\varphi(G_d^* + \sigma_I/a - G_c^*)}{2(G_d^* + \sigma_I/a) + 3G_c^* - 2\varphi(G_d^* + \sigma_I/a - G_c^*)} . \tag{9.279}$$

The prediction of the Bousmina model deviates only slightly from that of the Palierne model.

Based on the Palierne model for the shear modulus of emulsions and the models of *Mooney* [9.231] (9.245) and *Krieger* and *Dougherty* [9.230] (9.244), *Pal* [9.343] developed models for the shear modulus of emulsions of two immiscible viscoelastic liquids taking into account that the shear modulus diverges at $\varphi \to \varphi_{max}$ in a similar way as done for the viscosity. *Pal* [9.343] found a reasonable agreement between the model predictions and experimental data.

Preparation and Stability of Samples. An overview of various methods commonly used to prepare emulsions has been given by *Morrison* and *Ross* [9.195]. The most usual mechanical equipment used to fabricate emulsions are high-shear mixers, colloid mills, homogenizers, and ultrasonic and sonic dispersers, which realize intensive steady or oscillating high-shear fields to break-up the droplets or aggregates and mix the phases. Some examples are shown in Fig. 9.97.

Besides the mechanical processes, some physicochemical methods [9.195] exist to produce emulsions by phase inversion, phase inversion temperature (PIT), condensation or electric emulsification.

An important requirement to obtain stable emulsions is that the concentration of the emulsifier is high enough to be adsorbed at the required concentration at the newly developed interfaces in order to avoid, or at least retard, coalescence. If the surfactant at the droplet interface is inhomogeneously distributed due to shear, temperature

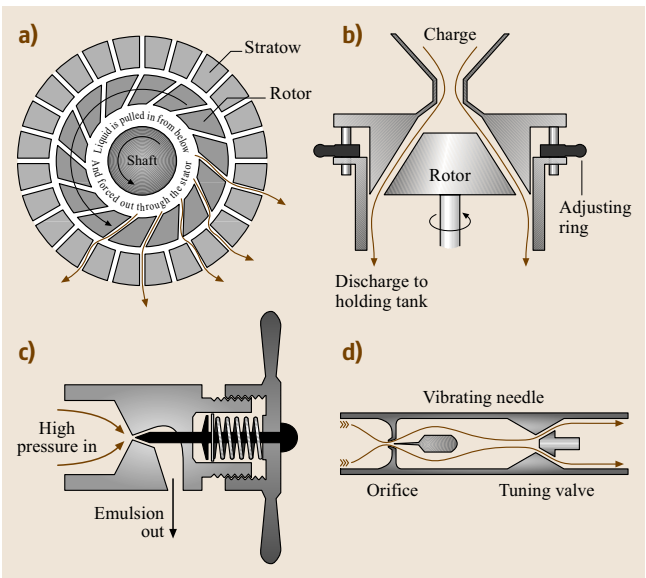

Fig. 9.97a–d Mechanical devices for making emulsions: **(a)** Rotor-stator disperser, **(b)** colloid mill, **(c)** single-stage homogenizer, **(d)** sonolator (after *Morrison* and *Ross* [9.195] with permission by Wiley)

effects or depletion, effects such as coalescence, Ostwald ripening, creaming or flocculation can destabilize the emulsion.

Coalescence is caused by the collision of two or more droplets, leading to depletion of surfactant at the interface. The collisions result in the formation of larger droplets and take place when the volume concentration of the disperse phase is high. Coalescence involves breaking of the interfacial film and is therefore irreversible. Various factors (solubility and concentration of the surfactant, pH value, salt concentration, phase-volume ratio, temperature, and properties of the film) affect the coalescence of emulsions.

Ostwald ripening only occurs in polydisperse emulsions. Collisions between two droplets may lead to one bigger droplet and one smaller droplet. Due to the material transition, small droplets become smaller and, in the extreme case, become solubilized in the continuous medium. Ostwald ripening requires a high solubility of the disperse in the continuous phase.

Due to the density differences between the two phases, a demixing process may occur. This process is called creaming [9.344] and may often be coupled with flocculation and a subsequent coalescence. The rate of creaming can be lowered by reducing the droplet size (with retention of the same interface loading of surfactant), lowering the density difference between the phases, or increasing the viscosity of the medium. In addition, the creaming rate is dependent on the volume fraction of the dispersed phase, and is usually slow in concentrated emulsions. Creaming is dominant at medium volume concentrations of 0.1–0.5 and droplet sizes of 2–5 μm. Complete demixing of the liquid phases caused by a combination of all other processes is called breaking. Further information on emulsion stability can be found in the contribution of *Walstra* [9.345].

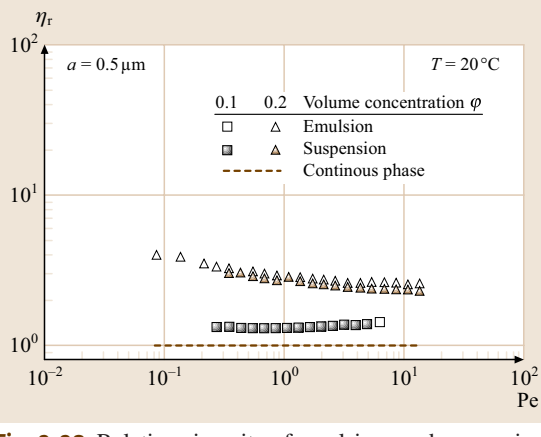

Fig. 9.98 Relative viscosity of emulsions and suspensions of monodisperse spherical particles as a function of the dimensionless shear rate (Péclet number) at identical volume concentrations of the disperse phase (after *Teipel* and *Aksel* [9.321] with permission by Wiley-VCH)

Viscometric Flows.

Shear Viscosity. Emulsions containing small droplets can behave like suspensions. The suspension-like behavior of emulsions in shear flow has been experimentally demonstrated by *Teipel* and *Aksel* [9.321] for O/W emulsions and suspensions with the same volume concentrations of the dispersed phase, the same droplet and particle sizes, and the same viscosity for both continuous phases. The lower points in Fig. 9.98 exhibit Newtonian behavior $\eta_r = f(\varphi)$, while the upper points show slight shear-thinning behavior $\eta_r = f(\varphi, \mathrm{Pe})$. The viscosity functions of suspensions and emulsions are nearly identical in both cases, which shows that the droplets can be regarded as rigid particles under the given shear conditions.

If the influence of droplet deformation and hence the modification of the droplet size distribution due to droplet break-up become relevant, the viscous behavior of emulsions is expected to be quite different. Consequently, the droplet size plays an important role in emulsions. Furthermore, additional viscoelastic effects may occur due to drop-shape relaxation mechanisms.

The influence of the droplet size, droplet deformation, and volume concentration of the dispersed phase on the rheological properties of the emulsions has been investigated by *Teipel* [9.346] and *Teipel* [9.319]. He confirmed the well-known effect that the viscosity of monodisperse emulsions with smaller droplets ($a = 0.5\,\mu m$) is significantly higher than that of emulsions with larger droplets ($a = 10\,\mu m$). At lower volume concentrations (40%) this effect has been observed over the whole shear-rate range investigated. However, at higher volume concentrations (up to 65%) the viscosities of the 0.5–10 μm emulsions coincide surprisingly at higher shear rates. This observation can be explained only by modification of the morphology of the 10 μm emulsion. Due to shear, the larger droplets deform and orientate in the flow direction. The effective hydrodynamic radius of the deformed and orientated droplets decreases and the viscosity tends to that of the 0.5 μm emulsion.

Pal [9.320] found that the relative viscosities of two polydisperse oil-in-water emulsions with $V_r \gg 1$

and mean droplet diameters of 6.5 μm(fine) and 32 μm (coarse), as well as 9.1 μm (fine) and 65 μm (coarse), scale with the particle Reynolds number based on the initial droplet radius. From an estimate of the Capillary numbers, he concluded that the deformation of the droplets due to shear is negligible. Only under this restriction are the results of *Pal* [9.320] applicable.

The influence of the volume concentration of the disperse phase and the viscosity ratio on the relative viscosity has been investigated by *Pal* [9.337]. In Fig. 9.99 some experimental data obtained by several authors for various emulsions ([9.337] for details) are summarized, showing the influence of the viscosity ratio for a given volume concentration. The limiting values of a constant viscosity at very low (bubbly liquid) and very high viscosity ratios (suspensions) are reached. Furthermore, the prediction of Pal's model 2 for the relative viscosity of emulsions (9.276) at a given volume concentration and a maximum packing fraction of 0.63 is depicted, which sufficiently describes the experimental trends.

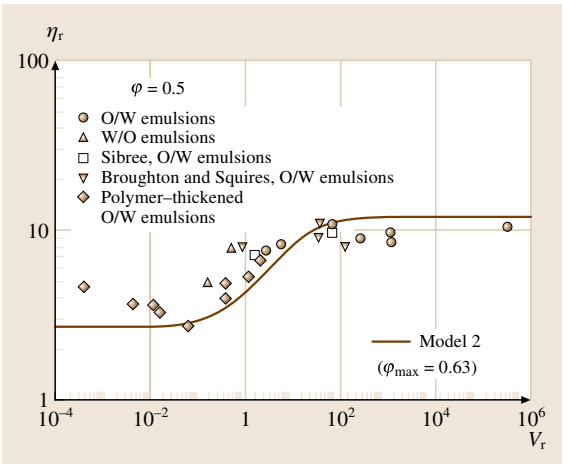

Fig. 9.99 Relative viscosity of emulsions as a function of the viscosity ratio at a given volume concentration (after *Pal* [9.337] with permission by the Society of Rheology)

Li and *Pozrikidis* [9.347] studied numerically the influence of insoluble surfactants on the rheology of dilute emulsions in Stokes flow. For the numerical calculations they assumed a viscosity ratio of $V_r = 1$ and a linear dependence of the interfacial tension on the local surfactant concentration. As an important result they discovered a decrease of the reduced interfacial stress $\sigma_{12}/\eta_c\dot{\gamma}$ with increasing capillary number, i. e., with decreasing interfacial tension. Hence, it can be concluded that, under otherwise identical conditions, the viscosity of emulsions with higher interfacial tensions is higher than for lower interfacial tensions due to the drop deformation, i. e., the emulsions behave like suspensions at higher interfacial tensions. This numerical result confirms the experimental results of *Teipel* and *Aksel* [9.321] for emulsions with $V_r \approx 60$. Details concerning the surface and interfacial tension can be found in Chap. 3.2.

Hollingsworth and *Johns* [9.348] studied the steady-state shear properties of various emulsion systems using the technique of rheo-nuclear magnetic resonance (rheo-NMR) coupled with a torque transducer. From direct measurements of the velocity maps they were able to determine the parameter of the Herschel–Bulkley model. Moreover, with the rheo-NMR technique it is possible to detect wall slip at both walls of the Couette cell used for the experiments.

Normal Stress Differences. Recently, *Montesi* et al. [9.349] investigated the shear behavior of a moderately concentrated, *attractive emulsion* of water droplets dispersed in a lubricating oil ($V_r = 0.01$). They found a sharp transition from a positive to a negative first normal stress difference in a range where the shear viscosity is still constant. This observation has been explained by the formation of dough-rolling aggregates, leading to larger normal stresses in shear gradient direction compared to the normal stress in flow direction. Because this effect has also been found in other complex materials such as nanotube suspensions [9.286] it suggests some underlying rheological principle.

Li and *Pozrikidis* [9.347] calculated an increase of the first normal stress difference with increasing capillary number in shear flows, i. e., an increase of the elastic properties with decreasing interfacial tension or increasing deformation of the droplets. The negative second normal stress difference was found to increase in magnitude, reach a maximum and then start to decline with increasing capillary number. The minimum of the negative second normal stress difference occurred at capillary number $Ca = 0.4$ for all the investigated conditions.

Storage and Loss Moduli. Due to the large number of factors that influence emulsions and hence the range of types of the rheological behavior of emulsions, it is not possible to give generally valid curves for the storage and loss moduli. The behavior at various frequencies depends not only on the rheological properties of both phases, the composition of the emulsion, the droplet sizes, and the size distribution, but also on the properties of the interface between the two phases. Qualitatively, *Barnes* [9.316] pointed out some curves for the typ-

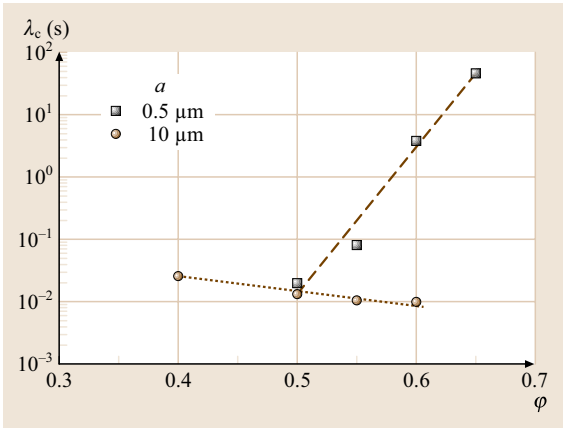

Fig. 9.100 Structural relaxation time as a function of the volume concentration for two monodisperse O/W emulsions with different droplet radii (based on results of *Teipel* [9.346]). The *dotted* and *broken lines* are drawn to guide the eye

ical behavior of emulsions in oscillatory shear flows. For low and medium concentrations the loss tangent as (ratio of the loss and storage modulus) is greater than one, indicating the dominance of the viscous component, whereas at higher concentrations the elastic component dominates. The influence of relevant parameters such as the viscosity ratio, interfacial tension or droplet sizes, and a possible solid–liquid transition have not been considered in the qualitative explanation. The statements given by Barnes have been experimentally confirmed by *Bower* et al. [9.350] for concentrated oil-in-water emulsions or by *Kulicke* et al. [9.351] for hydroxylpropylmethylcellulose-stabilized emulsions.

For flocculated W/O emulsions with a given surfactant concentration, *Pal* [9.352] showed that at low frequencies the elasticity of the emulsion is the dominating effect, whereas at higher frequencies the emulsion behaves as a viscous liquid. The crossover frequency ω_C or the characteristic structural relaxation time $\lambda_C = \omega_C^{-1}$, which characterizes the transition from the elastic to the viscous regime, depends on the volume concentration of the disperse phase at a given surfactant concentration. Contrary to the results of Pal, *Moates* et al. [9.353] observed for weakly flocculated concentrated emulsions dominating viscous properties at low and high frequencies and dominating elastic effects at medium frequencies, which indicates a double crossover in the curves of the storage and loss moduli.

Pal [9.352] found a decrease of the structural relaxation time with increasing volume concentration. In contrast to Pal, *Teipel* [9.346] observed an opposite effect in a monodisperse O/W emulsion with a droplet radius of 0.5 µm, i. e., a significant increase of the relaxation time over three decades with increasing volume concentration ($\varphi = 0.5$–0.65). For an emulsion with droplets of $a = 10$ µm a slight decrease of the relaxation time has been found, confirming the trend observed by Pal. The results are shown in Fig. 9.100.

Elongational Flows. Investigations of the elongational properties of emulsions are very few in the literature. *Anklam* et al. [9.354] used the opposed nozzle configuration to investigate the elongational behavior of W/O emulsions. They showed that for highly diluted emulsions the extensional viscosity decreases with increasing elongational rate similar to the shear behavior whereby the limiting Trouton ratio (for Newtonian liquids) of 3 seems to be reached. For higher volume concentrations an influence of the nozzle diameter and nozzle separation has been observed, which may be caused by the increasing impact of the yield stress. The effect of elongational thinning has also been found by *Plucinski* et al. [9.355] for a food emulsion.

As a final statement, one can conclude that emulsion rheology and partially suspension rheology are not completely understood and that research work in these fields is continuing.

9.4 Entrance Correction and Extrudate Swell

This section is dedicated to two effects that appear during flow in pressure-driven rheometers and also in plastic processing. The first is the entrance effect during flow from the reservoir into the capillary; it results in so-called Bagley plots. The second is so-called extrudate swell or die swell, which occurs as an increase of the diameter of the polymer extrudate with respect to the diameter of the capillary. This phenomenon is due to the elasticity of the polymer melt.

9.4.1 Correction for Entrance Effect: Bagley Correction

In the foregoing we neglected the effect of the entrance of the fluid into the capillary. The flow rate in the capillary

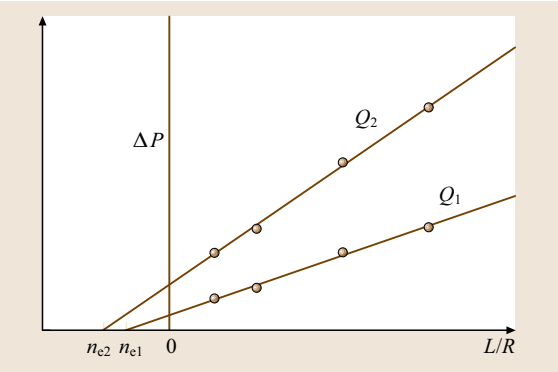

Fig. 9.101 Bagley correction plots for two flow rates: $Q_2 > Q_1$

is much higher than in the reservoir. This causes an increase of the kinetic energy, so that part of the imposed pressure ΔP in the reservoir above the capillary is used to accelerate the flowing mass in the capillary entrance region, so that

$$\Delta P = \Delta P_{\text{capillary}} + \Delta P_{\text{entrance}} \,. \tag{9.280}$$

For the determination of the shear stress at the wall we made use of the assumption of fully developed flow and neglected the entrance effect in $\partial\sigma_{11}/\partial z$ and $\partial\Delta P/\partial z$. The consequence of neglecting the entrance effect is an apparent lengthening of the capillary. For constant-volume flow rate the shear stress at the wall has to be corrected by increasing the length of the capillary by a term $n_e R$, where n_e is dimensionless. The end correction n_e seems to be constant for a given radius of the capillary. The shear stress at the wall is now expressed as

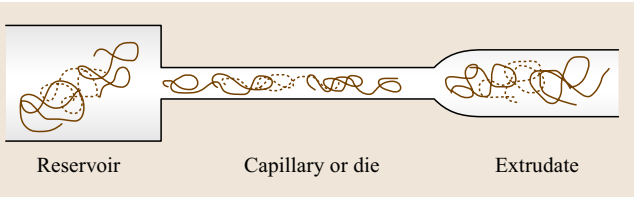

Fig. 9.103 Schematic representation of three macromolecules during flow in a capillary rheometer

$$\sigma_w = -\frac{R\Delta P}{2(L + n_e R)} \tag{9.281}$$

or

$$\Delta P = -2\sigma_w \left(\frac{L}{R} + n_e\right) \,. \tag{9.282}$$

This entrance correction is called the Bagley correction. The value of the end correction n_e may be determined by measuring ΔP at constant-volume flow rate Q as a function of L/R, where preferably R is to be constant. This is shown in Fig. 9.101 for two values of the volumetric flow rate Q.

An example of a Bagley plot is shown in Fig. 9.102 for polyethylene with a melt flow index (MFI) of 2.9 at 190 °C for shear rates of 40–250 s^{-1}, as measured by Bagley himself [9.356]. It clearly shows straight lines and increasing values of n_e with increasing shear rate or increasing volume flow rate.

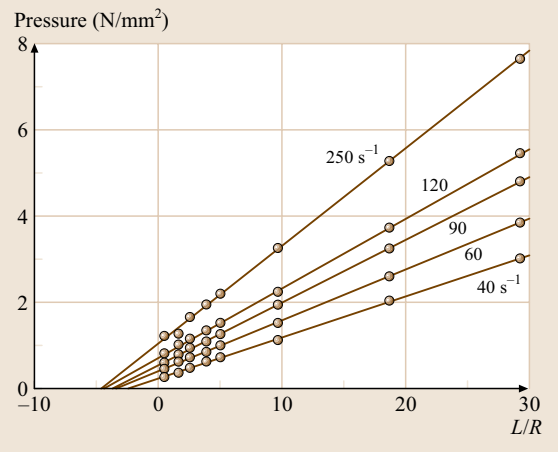

Fig. 9.102 Bagley plot for a polyethylene melt with melt flow index of 2.9 at 190 °C for shear rates of 40–250 s^{-1}, as presented by *Bagley* himself [9.356]

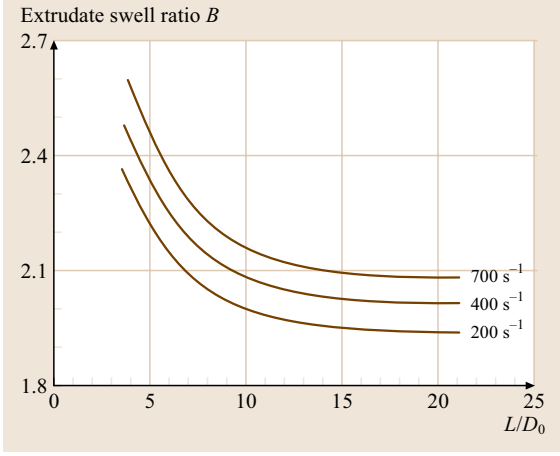

Fig. 9.104 Extrudate swell ratio as a function of L/D_0 for high-density polyethylene at 180 °C for shear rates, as indicated. After [9.357]

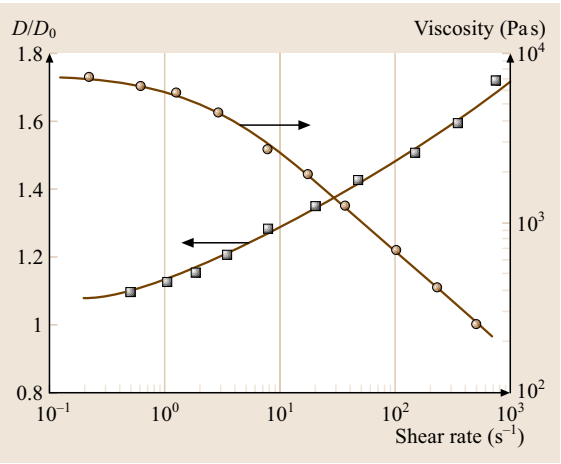

Fig. 9.105 Extrudate swell ratio and viscosity, both as functions of the shear rate for a polystyrene melt of $\overline{M}_w = 2.2\times10^5$ and $\overline{M}_w/\overline{M}_n = 3.1$, where $\overline{M}_w$ and $\overline{M}_n$ are the weight and number-averaged molecular weights, respectively. After [9.3]

9.4.2 Extrudate Swell or Die Swell

When a polymer melt leaves the die of a capillary rheometer (or, e.g., an extruder or injection moulding machine) its diameter increases, as was shown schematically in Fig. 9.36. This swelling behavior is the consequence of the elastic properties of polymer melts. Let us consider a thought experiment in which

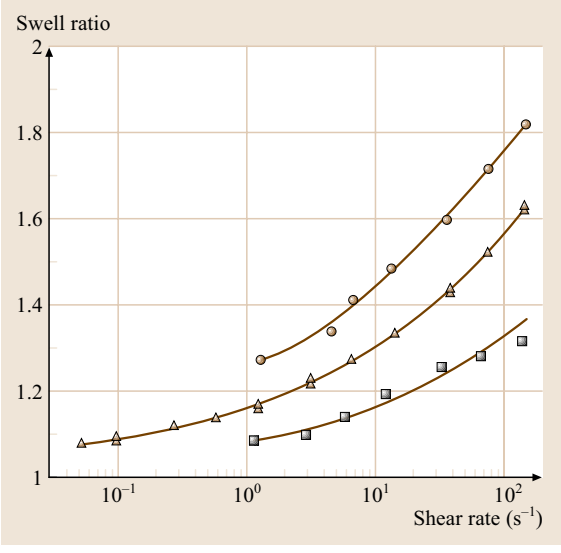

Fig. 9.106 Extrudate swell ratio of the same polystyrene melt as in Fig. 9.105, plotted versus shear rate for temperatures of (*circles*) 160 °C; (*triangles*) 180 °C and (*squares*) 200 °C; L/D_0 ratios varied from 27 to 56. After [9.3]

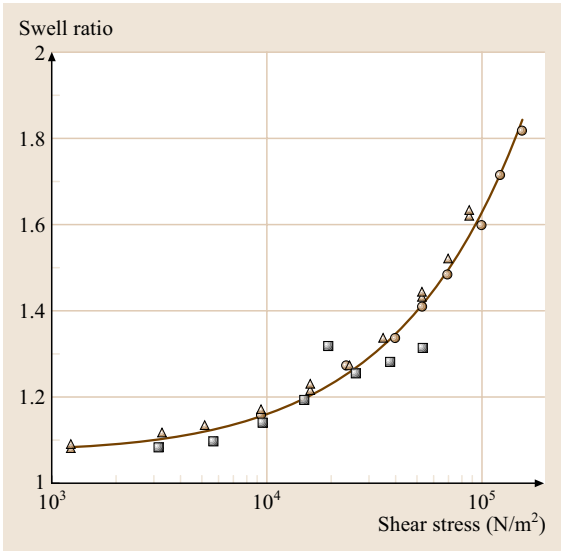

Fig. 9.107 Extrudate swell ratio of the same polystyrene melt as in Fig. 9.105, now plotted versus shear stress for temperatures of (*circles*) 160 °C; (*triangles*) 180 °C and (*squares*) 200 °C; L/D_0 ratios varied from 27 to 56. After [9.3]

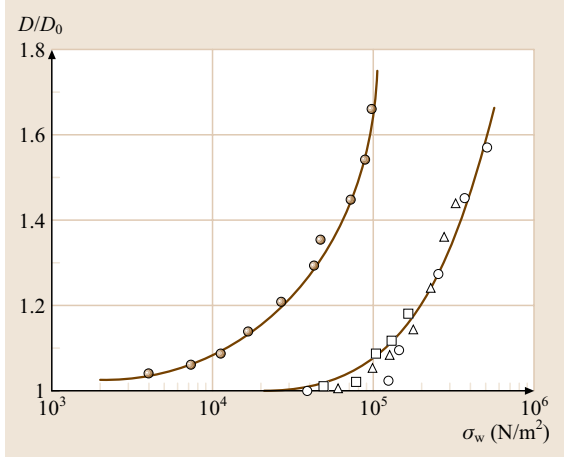

Fig. 9.108 Extrudate swell ratio as a function of shear stress at the wall for various polystyrene melts. *Filled symbols*: broad ($\overline{M}_w/\overline{M}_n = 3.1$) molecular-weight distribution polystyrene mentioned in Figs. 9.105–9.107. *Open symbols*: narrow ($\overline{M}_w/\overline{M}_n < 1.1$) molecular-weight distribution polystyrene, with $\overline{M}_w = 1.6\times10^5$ (After [9.3])

a crosslinked rubber is driven through a capillary. When the rubber leaves the capillary it will swell again, trying to recover its original dimensions due to elasticity. A polymer melt will swell almost like the rubber. However, upon leaving the die the original dimensions of the reservoir will not be reached, because of stress relaxation, primarily due to the coil–stretch–coil transition of macromolecules (see Fig. 9.103) and their reptation (disentanglement and subsequent re-entanglement). Die swell, or the swell ratio B, being a function of many parameters, is defined as ratio of the diameters of the extrudate and the capillary:

$$B \equiv D/D_0 = B(\dot{\gamma}_w, T, t, L/D_0, M, \text{MWD}) , \tag{9.283}$$

where D_0 is the diameter of the capillary with circular cross section, D is the diameter of the extrudate at a relatively large distance from the outlet, T the is temperature, L/D_0 the length-to-diameter ratio of the capillary, M is the molecular weight of the polymer, and MWD its molecular-weight distribution (polydispersity). B can reach values of 2–4.

Many of the effects of the various parameters can be attributed to stress relaxation. In general die swell is larger when the residence time in the capillary t is shorter and when the polymer relaxation times are longer. Several of these effects are demonstrated in Figs. 9.104–9.108. In Fig. 9.104 the extrudate swell ratio is plotted versus L/D_0 for various values of the shear rate [9.357]. This shows that, at larger L/D_0 ratios, there is more time for relaxation and accordingly the swell ratio decreases. The same holds for the shear rate as the parameter: increasing the shear rate means shorter residence times and thus less time for relaxation; accordingly the swell ratio increases with increasing shear rate. In Fig. 9.105 the extrudate swell ratio and viscosity of a polystyrene melt are shown as a function of shear rate. This clearly shows again that die swell increases with shear rate, in this case even in the range where the viscosity decreases, and hence where the long relaxation times that are responsible for high die swell ratios are already felt. One could imagine that die swell ratios would even be higher if the viscosity would not be shear thinning.

In Fig. 9.106 die swell is shown as a function of shear rate for temperatures of 160 °C, 180 °C, and 200 °C for the same polystyrene melt as presented in Fig. 9.105. The L/D_0 ratios are high, so that die swell is almost independent of this ratio. It is not surprising that the die swell ratio decreases with increasing temperature, because the relaxation times are strongly decreasing functions of temperature. If one plots the extrudate swell ratio versus some function of relaxation times one could expect a common curve. This is demonstrated in Fig. 9.107, where the extrudate swell ratio is now shown as a function of the shear stress, which is equal to shear rate × viscosity, and the viscosity is strongly dependent on the relaxation times. The points measured at the three different temperatures follow the same line over more than two decades of shear stress. Apparently, in this case the die swell ratio scales well with viscosity.

Finally in Fig. 9.108 die swell data are shown as a function of shear stress at the wall for various polystyrene melts. The filled and open symbols refer to polystyrenes with broad and narrow molecular-weight distributions, respectively. The *narrow* polymer was measured under different conditions. The *broad* polymer exhibits much higher extrudate swell ratios than the *narrow* polymer. The weight-averaged molecular weight of the *broad* polymer is approximately two times higher than that of the *narrow* polymer, which means that the viscosity is 10 times higher (the viscosity increases as $\overline{M}_w^{3.4}$). Apparently, the viscosity is not the only parameter that is responsible for the die swell phenomenon. Elasticity of the melt, as expressed by G_e or J_e or ψ_1, also seems to be of great importance [9.3].

9.4.3 Conclusions

In this Section measurements relevant to two phenomena that are observed in pressure-driven rheometers (and also in plastic processing such as extrusion or injection moulding) are discussed:

1. Entrance correction, due to accelerating forces during the flow from the reservoir into the capillary. This results in an apparent increase of the length of the capillary, which can be measured with the aid of a Bagley correction plot.
2. Extrudate swell, which occurs when the polymer leaves the capillary, and also due to elasticity of the polymer melt. This phenomenon depends on many parameters and in principle can be qualitatively related to the relaxation times. The exact description is not available yet.

9.5 Birefringence in Non-Newtonian Flows

The optical properties of transparent media, representing the interaction of the electric vector of the electromagnetic wave with electrons in the material are briefly reviewed. A distinction is drawn between optically isotropic and anisotropic media, and the molecular origin of optical anisotropy is discussed. Methods for measurement and imaging birefringence are discussed and compared, including Sénarmont, polarization modulation, and two-color birefringence techniques. Experimental issues discussed include choice of light source, windows, photodetectors, optical components, and the geometry of flow cells. Finally the origin of birefringence for the important class of flexible coil polymers is discussed, with interpretation of birefringence in terms of molecular strain, and in terms of bond polarizability, and micro- and macroform birefringence.

Light propagates through transparent media via a series of interactions with electrons, mediated by the bonds between atoms. Birefringence refers to a physical system that transmits light but is optically anisotropic, i.e., the light propagates differently in different directions; generally (but not always) this manifests itself as a directional variation of the refractive index (Chap. 3.7). In general this is due to the interaction between the electric vector of the light and the bond polarizabilities of the medium.

Many substances are isotropic, that is they have the same physical properties in all directions. This includes most fluids, most amorphous materials, and cubic crystal structures. Of specific importance here is that the bonds that mediate the passage of light either possess such symmetry or such randomness that the light propagates in the same way in all directions. Indeed normal, stress-free, single-phase fluids are intrinsically optically isotropic, even when they contain, as solutions or suspensions, molecules or particles that are themselves anisotropic. This is due to the randomization of the orientational order of the molecules or particles.

The exception, at rest, is the liquid-crystalline fluid, where above a specific concentration of anisotropic molecules, spontaneous order will emerge in the form of the liquid-crystalline phase. This ordering is long-range and cooperative, typically extending over many microns. In nematic phases this corresponds to orientational order, but in smectic liquid crystals it is both orientational and positional, and in cholesteric materials it possesses a longer-length-scale twisting structure, arising generally from the packing constraints of helical molecules. Such systems also include the important classes of surfactant and lipid mesophases, where anisotropic structures have specific biological functions, for instance in cell walls.

Non-Newtonian fluids that are isotropic at rest are of special interest here. In general the non-Newtonian flow characteristics arise from an internal structure which changes with applied flow. This may arise from orientation of suspended particles or colloidal structures (Sect. 9.2), where the particles possess an intrinsic optical anisotropy. Of particular importance is the non-Newtonian flow of flexible polymer melts and solutions (Sect. 9.1). At rest the polymer chains are locally anisotropic (in general most of the covalent bonds lie along the chain direction), but the chains exist as *drunkard's walk* random coils, either interpenetrating in melts and concentrated solutions or isolated in dilute solutions. On the scale of the wavelength of light such coils are physically and optically isotropic.

When such polymeric fluids exhibit non-Newtonian behavior it is due to a flow-induced order being imposed upon the molecules. Typically, beyond some flow-rate characteristic of the system relaxation time, the random coils become orientated preferentially, or, exceptionally, stretched by the flow field. This, coupled with the associated relaxation processes as entropy drives the coil back to its equilibrium conformation, creates the anisotropic stresses and normal forces characteristic of such fluids.

As discussed below, birefringence is a relatively straightforward phenomenon to measure. For 200 years birefringence has been used as a window into molecular processes. It has been used in conjunction with flow since 1873 when Maxwell discovered birefringence in

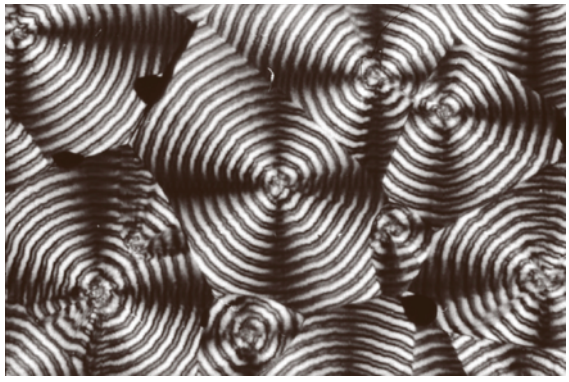

Fig. 9.109 Birefringent spherulites growing from a melt of biological thermoplastic poly(hydroxybutyrate)

flowing Canada balsam resin [9.358]. Many birefringent techniques can give fast, noninvasive information related to the microstructure and origin of non-Newtonian flow stresses. Further, normally a birefringent microscope image is available, giving information on the spatial variation of stresses and orientational order created in the flow field.

There is a problem, however. This is analogous to the phase problem is X-ray scattering: there is not a unique relationship between birefringence and induced microstructure. The same birefringence can arise from more than one molecular or phase structure, so that birefringence analysis needs to contain a model and a conjectured mode of the deformation of that model, so that calculated birefringence can be compared with observed birefringence. Sometimes, then, the correspondence is so compelling that the structure is clearly *right*. This was famously the case with spherulitic growth structures in crystallization of semicrystalline polymers [9.359] (Fig. 9.109). However, sometimes the interpretation can be contentious so that unambiguous, structures can only be assigned through a combination of birefringence studies with other techniques such as light, X-ray, or Neutron scattering.

9.5.1 The Molecular Origin of Birefringence

As discussed above, the essence of an optically anisotropic material is that its electron bonds possess directional variation. Now light propagates through the interaction of the electric $\boldsymbol{E}$ vector with electrons in the bonds, resulting in photon re-emission. The speed of this propagating wave is determined by the difference in the frequency of the wave and the characteristic frequency of the electrons. The nature of this difference determines the speed of propagation and hence the refractive index, n, for the wave (Chap. 3.7). It clearly follows that light with differing orientations of the $\boldsymbol{E}$ vector will exhibit differing refractive indices and propagation delays in the material. Specifically there will generally be an $\boldsymbol{E}$ vector direction exhibiting a maximum refractive index and another a minimum. A material or fluid of this type that displays spontaneous or flow-induced variation of refractive index is said to be *birefringent*. Dependent upon the polarization and direction of the incoming light, components of the light will propagate at different rates, recombining on emergence from the medium to give the phase and chromic effects familiar in microscope birefringent images.

In general there will be one or more directions through such a medium where the bonds (or components of bonds) perpendicular to that direction exhibit the same interaction with the $\boldsymbol{E}$ vector, which is itself perpendicular to the direction of propagation. In this special direction, the refractive index will not be a function of the direction of polarization and the medium will not exhibit birefringence. This is termed the *optic axis*. For a given direction of propagation of light there will be a direction in the fluid in which the refractive index (n_1) is a maximum (the principal axis of the birefringence) and an orthogonal direction in which the refractive index is a minimum (n_2). For this direction the birefringence is $\Delta n = (n_1 - n_2)$. Light polarized in each of these directions will propagate at different speeds (c/n) and emerge out of phase. The *retardation phase shift* (δ) results in interference when the waves recombine.

The birefringence, Δn, and δ are related by

$$\Delta n = \frac{\lambda\delta}{2\pi d} , \tag{9.284}$$

where d is the path length through the birefringent medium, and λ is the incident wavelength.

The birefringence axes are of course related to the internal molecular structure through the intrinsic birefringence of the structural entities (from the sum of bond polarizabilities) and the average orientation of the entities (molecules, etc). The average orientation of the entities is characterized as the *director*. This will often, but not always, coincide with the principal axis of the birefringence. The molecular direction can correspond to the maximum birefringence (positive birefringence) or the minimum (negative birefringence). In a few cases (e.g., polyacrylamide) the bond polarizabilities almost exactly cancel, resulting in a non-birefringent entity.

Here we should formally mention that, if the electromagnetic frequency is comparable to one of the characteristic frequencies of the anisotropic electron vibrations, this radiation will be heavily absorbed, so that one polarization or direction may be suppressed. This phenomenon is called *dichroism*. For many materials and fluids such frequencies are in the infrared and the technique of infrared dichroism spectroscopy can indicate stress and orientational order associated with specific bond types. Beyond this, dichroic materials are the basis for the polarizer filters ubiquitously used in sun glasses and the optical systems described below.

9.5.2 Techniques for Birefringence Measurement

The polarizing microscope is shown schematically in Fig. 9.110a (the lenses have been omitted for clarity). It

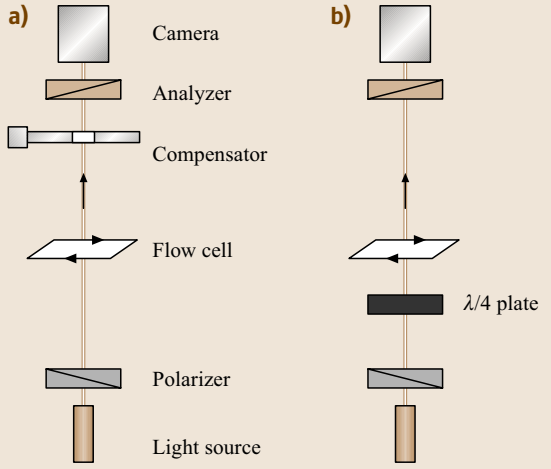

Fig. 9.110a,b The optical trains of **(a)** a polarizing microscope, **(b)** a Senarmont compensator

consists of a source, which can be monochromatic or white light, light from which passes through a polarizer to pick out a unique polarization direction, then through the medium of interest and an optional compensator and finally through an analyzer, generally orientated orthogonal to the polarizer. Such an instrument is generally semiquantitative; optically isotropic media will be seen as dark, since there is no rotation of the polarization direction and the light is stopped by the analyzer. The degree of retardation of the waves determines the perceived brightness when the emerging waves recombine. A full analysis of the propagation of polarized light through anisotropic media can be approached through Jones and Mueller matrix calculations [9.360], the intensity of the transmitted light is

$$I_s = I_0 \sin^2 2\theta \sin^2(\delta/2)\,, \tag{9.285}$$

where I_s is the intensity of transmitted light, I_0 is the intensity of the input beam, and θ is the angle between the incident polarization direction and the direction of the principal axis of the birefringence (maximum refractive index n_1), δ is the average retardation angle.

If θ is set to 45° the transmitted intensity becomes simply [9.361]:

$$I_s = I_0 \sin^2(\delta/2) \quad \text{or for small } \delta: \tag{9.286}$$

$$I_s = \frac{I_0 \delta^2}{4}\,. \tag{9.287}$$

For polychromatic or white light, generally colors are seen due to different interference for different wavelengths; this can be semiquantitatively interpreted through the *Michel-Lévy* chart. The compensator consists of a well-defined adjustable crystal, typically of calcite or quartz. More-precise measurements can be obtained by adjusting the compensator to provide an exactly equal and opposite retardation in the optical train, at which point the birefringence can be read from the compensator calibration.

Equation (9.287) demonstrates that the quadratic dependence of intensity on retardation and problems will arise from subtraction of scattered and stray light at low intensities due to the nonlinear dependence of δ upon I_s. A particular problem with flow birefringence is stray birefringence due to the variable stresses in the windows. These can dominate the signal, especially for solution studies, where the birefringence may be very small. For more-quantitative assessment, higher speed, greater linearity, and greater sensitivity many other techniques have been invented.

Figure 9.110b illustrates the Sénarmont compensator technique [9.362]. Now a quarter-wave plate (introducing up to an additional $\lambda/4$ retardation dependent upon rotation, but normally aligned with its high-refractive-index direction parallel to the low refractive index of the analyzer with the polarizers crossed) is included in the optical train. The analyzer is then uncrossed a little (by an angle ϕ). This can be used to compensate for stray window birefringence or to compensate out the signal birefringence as a way of measuring it.

Without flow birefringence, the transmitted intensity can be written

$$I_s = I_0 \cos^2 \varphi\,, \tag{9.288}$$

where ϕ is the angle between the polarizer and analyzer.

We can see that the same intensity received by the photodiode can be induced either by a flowing solution [that is caused by retardation in the sample, (9.287)] or by uncrossing the polarizers in the absence of the sample (9.288).

Comparing (9.288) and (9.286) we can estimate the value of the retardation in a flow knowing the rotation angle of the analyzer

$$\sin^2(\delta/2) = \cos^2 \varphi\,. \tag{9.289}$$

From (9.289)

$$\delta = \pi - 2\varphi\,. \tag{9.290}$$

This value is used in the calculation of experimental birefringence via equation (9.285)

Substituting (9.290) into (9.284) we finally obtain for Δn:

$$\Delta n = \frac{\lambda \arcsin(\cos\varphi)}{\pi d} \,. \tag{9.291}$$

A more-useful *linear* detection method [9.363], yielding much improved signal-to-noise ratio, can easily be adapted from the Sénarmont compensator. This simply involves uncrossing the polarizers to permit a background intensity to be transmitted. It is then possible to express δ as $\delta = \delta_1 + S$, where δ_1 is the constant background signal introduced by uncrossing the polarizers and S is the retardation introduced by all other optical effects. Hence from equation (9.287) we obtain:

$$I_s = \frac{I_0}{4}(\delta_1^2 + 2\delta_1 S + S^2) = \frac{I_0}{4}\delta_1^2 + \frac{I_0}{2}\delta_1 S + \frac{I_0}{4}S^2 \,. \tag{9.292}$$

If δ_1 is large compared to S, the S^2 term may be neglected, leaving a constant intensity plus a term linear in S. In practice the background intensity signal can be set to around 10 or more times the intrinsic signal, only limited by the stability of the light source.

Such systems work well in cases where the orientational angle θ is known or defined by the flow symmetry (e.g., in extensional flows). They can be impractical where the orientational angle is unknown or variable; this is generally the case in Couette, cone and plate, Poiseuille and other shear flows (Sect. 9.1.1). In simple shear flows, generally the principal axis of the birefringence (the director) will lie at a setting angle to the velocity and the velocity gradient vector. Techniques such as polarization modulation (PM) and two-color flow birefringence (TCFB) are capable of determining simultaneously this orientational angle and the optical retardation and birefringence.

PM [9.364] techniques cause a fast oscillation of the polarization direction, which then samples all refractive indices normal to the direction of propagation, enabling analysis to determine δ and θ simultaneously. This is commonly achieved by mechanically rotating a $\lambda/2$ plate (circular polarizer) in the beam line. There are photoelastic alternatives requiring no moving parts, such as Pockels or Faraday cells. Phase-sensitive detection techniques are employed to monitor the intensity and compare it with the incident beam, enabling correction for variations of the input intensity and an absolute determination of δ, without calibration.

The TCFB technique [9.365] is powerful, sensitive and faster than the PM techniques. The technique employs, typically, the blue (488.8 nm) and green (514.5 nm) lines of an argon-ion laser with the polarization of the two beams rotated by 45° to each other, to provide the two independent measurement required to determine δ and θ separately. However, TCFB cannot determine the sign of the orientation angle or the retardation. *Fuller* [9.366] has presented a comprehensive description of the field of optorheometry.

Light Sources

Any precise determination of birefringence requires the light source to be highly monochromatic. Further, the achievement of maximum sensitivity in possibly tiny volumes, requires high focusability of the source. These conditions point to lasers as the primary source. Most systems have utilized relatively low-powered HeNe lasers, of order 10–20 mW having λ of 632.8 nm. Optical components can be easily and economically obtained with antireflection coatings optimized for HeNe wavelengths, practically eliminating unwanted reflections.

Such lasers are cheap, reliable, and robust. They are not, however, intrinsically stable and the output intensity and power will drift considerably as the laser warms up and with ambient conditions and age of the laser. As discussed above, stability is an important requirement to achieve optimum signal-to-noise ratio and sensitivity. Stabilized HeNe lasers are available, generally operating on the principle of sensing the laser output and closed-loop feedback into a heater circuit to maintain either frequency or intensity stability. The lasers are primarily intended for metrology, so output powers tend to be at the low end of the spectrum, around 1 mW.

Increasingly solid-state lasers are available with power and performance comparable with or exceeding that of HeNe lasers. These are also intrinsically unstable with temperature, but can be feedback stabilized rather more easily than the HeNe with small Peltier heaters and coolers. They can also be an order of magnitude cheaper than similar HeNe devices. A possible drawback is that the effective source size is larger than for HeNe lasers, so that the minimum size to which the beam may be focused is limited, as is the specific achievable intensity. Such lasers can have wavelengths of operation very similar to HeNe lasers, enabling quite effective use of HeNe antireflection optics.

Windows

Clearly high-clarity low-birefringence windows are important in optorheology. But for solution studies, where the birefringent signals are commonly very small (as low as $\delta = 0.01$ nm or $\lambda \times 10^{-5}$), windows are the bane of optorheology birefringence measurements. Even though

the windows may be free of stress and birefringence at rest, during flow they will inevitably contain stresses, arising from the pressure, the shear forces or the normal forces, dependent upon the geometry. These stresses will induce variable birefringence that may swamp the fluid birefringence. Part of the solution is usually to utilize thick windows. The retardation will scale with thickness for a particular stress, but the stress will generally reduce much more rapidly with window thickness. Similarly the area of the window should be kept as small as is feasible.

Photodetectors

Peltier-cooled charge-coupled device (CCD) detectors now provide excellent performance combined with speed and convenience. They can have greater than 1 megapixel resolution. Air cooling down to of the order $-40\,^{\circ}\mathrm{C}$ can reduce thermal (dark-current) noise to the level of 0.01 electrons per second per pixel. Coupled with photon efficiencies of the order of 50%, long integration times can be employed to recover even the weakest signal. Selectable *areas of interest* enable fast frame rates. At the same time 12- or 16-bit cameras can provide a wide dynamic range, which is essential for experiments that require background subtraction.

Polarizers and Waveplates

The performance of any birefringence experiment will be restricted by the performance of the polarizers. Dichroic film polarizers are designed to produce a ratio of intensity of the unwanted polarization to the wanted of order 10^{-5} (the extinction ratio). Higher ratios, up to 10^{-6}, can be obtained from birefringent components such as calcite (Glan–Taylor and Glan–Thompson prisms). These devices have the further advantages of high power throughput without damage and high transparency for the wanted polarization (up to 90%).

Temperature stability of wave plates is of prime importance, and is best achieved by the use of *zeroth-order* plates, which utilize compensating components to give exactly $\lambda/4$, rather than higher-order but much cheaper plates which give $(4n+1)\lambda/4$, with correspondingly worse stability.

Flow Cells

All optorheological experiments, with the exception of thread-line experiments, require the construction of flow cells to define and constrain the flow and provide windows through which the optical effects can be observed. These flows can be defined that which approach idealized flows as closely as possible.

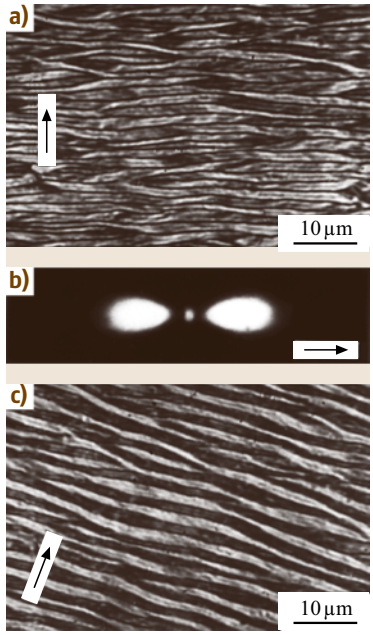

Fig. 9.111a–c Birefringence in a parallel-plate flow cell in relaxation of oriented thermotropic liquid-crystalline material (**(a)** with polars at 45° to flow direction, **(c)**with polars at 90° to flow direction), together with the accompanying light scattering pattern **(b)**. The bands correspond to regions of co-operative disorientation, where the variation in brightness arises from periodic variation of the molecular director. Such banding is ubiquitous in liquid-crystalline systems, but is poorly understood

Simple shear flow will be approached through a parallel-plate or cone-and-plate apparatus (Sect. 9.1.1), usually with the light beam along the velocity gradient direction and the plates forming the windows. An alternate arrangement for simple shear is the Couette or concentric cylinders apparatus. In principle, this permits optical probes along the velocity or velocity gradient direction, but optical trains are difficult to define compared to with parallel-plate cells.

Figure 9.111 shows simple shear birefringence in a thermotropic liquid-crystalline copolymer. The flow cell is a parallel-plate cell, with polarizing optics and simultaneous light scattering. The pronounced banding texture correspond to regions of cooperative disorientation, where the variation in brightness arises from periodic variation of the molecular director. The local director can be assessed by rotation with respect to the crossed polarizer and analyzer; darkness indicates a director parallel to a principal axis. Such banding is

ubiquitous in liquid-crystalline systems, but poorly understood, the banding suggests a zigzag variation in the director with respect to the shear direction, whilst the single peak in the light scattering suggests a sinusoidal variation in director.

Extensional flows can be attained through capillary entrance flows (Sect. 9.1.2), G. I. Taylor four-roll mill experiments or cross-slots (pure shear) and opposed jets. The opposed jets realize a good approximation to ideal extensional flows. If the jets impinge, then the flow will correspond to a uniaxial compression, which is equivalent to a biaxial extension. If the jets are sucking, then the flow is close to ideal uniaxial extension. The four-roll mill and jets devices permit very high strain rates coupled with the incorporation of a stagnation point. The stagnation point has a special significance, since the strain rate is finite, but the residence time is infinite, so that the fluid strain is unlimited and birefringent structures build up to close to equilibrium (maximum extension or orientation). This leads to discrete *strands* of birefringence, localized in space. Such a structure is shown in Fig. 9.112a, where the solution is just 10 ppm concentration of atactic polystyrene; retardations of less than $\lambda/1000$ can be resolved. Figure 9.112b shows the birefringent profile across the strand through the stagnation point.

Fluid mechanics presents a range of *benchmark* problems, such as flow around corners and around cylinders and spheres. Appropriate cells can be constructed to enable an optical probe to analyze birefringent patterns. In conjunction with velocimetry such approaches can visualize the stress distributions and their effects on the flow-field. Figure 9.113 shows the birefringence behind a falling ball, again the birefringence has a strand-like appearance, arising from the stagnation point behind the sphere.

Beyond well-defined flows there are flows of major industrial and commercial interest, such as porous media flow. This is generally modeled by flow through an assembly of glass spheres (ballotini). Multiple scattering makes the use of optical probes problematic, but refractive-index matching of the fluid to the glass has resulted in direct birefringence observations in random porous media [9.367].

9.5.3 Relation Between Birefringence and Molecular Strain

The orientation of the segments of a macromolecule depend on the volume and deformation of the macromolecule as a unit. Therefore birefringence demonstrated by polymer solutions is a function of the geometrical, hydrodynamic and optical properties of the dissolved macromolecules.

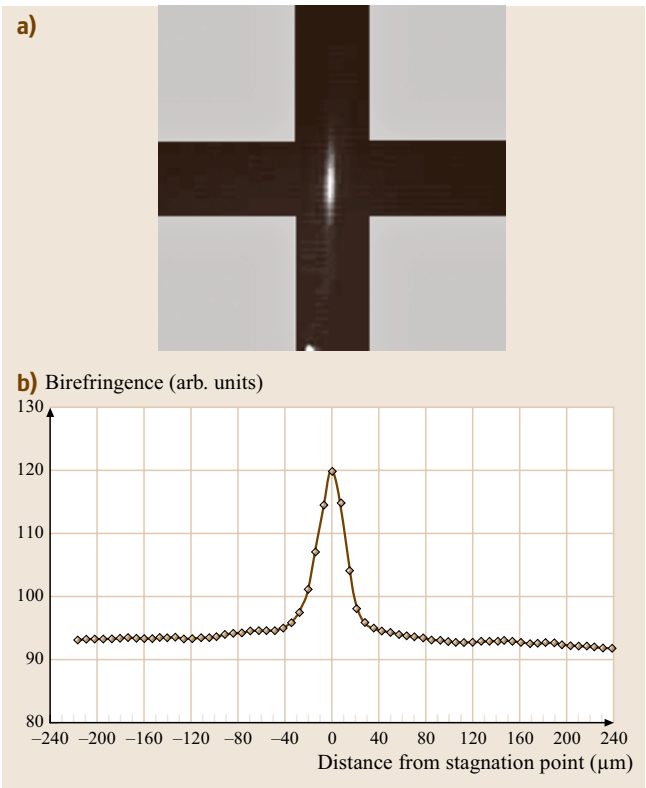

Fig. 9.112 **(a)** Birefringence response from a solution of 10 ppm 10.2×10^6 molecular-weight atactic polystyrene (aPS) in dioctyl phthalate (DOP). The flow corresponds to a pure shear extension along the vertical channel, coupled with a stagnation point at the center. The strain rate is $995\,s^{-1}$. **(b)** A birefringence scan across the birefringent strand through the stagnation point

If the optical polarizability of the segments is anisotropic, their preferential orientation within the coiled molecule will result in an overall optical anisotropy of the chain (intrinsic anisotropy). According to *Peterlin* [9.368, 369] the optical anisotropy of a randomly coiled macromolecule is:

$$\gamma_1 - \gamma_2 = 3/5(\alpha_1 - \alpha_2)_i(h^2/h_0^2)\upsilon(\beta)\,; \qquad (9.293)$$

here: γ_1 and γ_2 are the principal polarizabilities of a macromolecule, α_1 and α_2 are the polarizabilities of a segment parallel and perpendicular to its length with subscript i denoting segmental anisotropy, h^2 is the mean square end-to-end distance of a deformed molecule, h_0^2 is the mean square end-to-end distance of a molecule at

Fig. 9.113 Birefringence behind a 10 mm diameter steel ball bearing falling through a 0.7% solution of 10.2×10^6 molecular weight atactic polystyrene (aPs) in dioctyl phthalate (DOP)

rest (the gyration radius squared), the factor:

$$\upsilon(\beta)=\frac{5}{3\beta}\left(1-\frac{3\beta}{L^{-1}(\beta)}\right)\,, \tag{9.294}$$

where $\beta=h/L$ is the degree of extension of a molecule, L is the contour length of a macromolecule, and $L^{-1}(\beta)$ is the inverse Langevin function.

The intrinsic optical anisotropy of a chain (9.293) has been derived from the average optical polarizability of the ensemble of all conformations compatible with a fixed end-to-end vector $\boldsymbol{h}$ [9.370]. The factor $\upsilon(\beta)$ takes into account the small nonlinearity effect on the optical anisotropy of the macromolecule as a function of the mean square end-to-end distance and varies from 1 at $\beta=0$ to 5/3 at $\beta=1$.

Now one has to relate the polarizability of a molecule and refractive index of an optically anisotropic medium, and also to obtain the dependence of birefringence on the degree of extension of a molecule in a hydrodynamic field. The Lorenz–Lorentz formula relates the average refractive index, n, to the specific polarizability of a medium P

$$\frac{n^2-1}{n^2+2}=\frac{4}{3}\pi P\,. \tag{9.295}$$

Upon differentiating, this gives

$$\frac{6n}{(n^2+2)^2}\,\mathrm{d}n=\frac{4}{3}\pi\,\mathrm{d}P \tag{9.296}$$

and the increment in polarizability can be related to the polarizabilities of the subunits through

$$\mathrm{d}P\approx\Delta P=\frac{MN_\mathrm{A}}{\rho}(\alpha_1-\alpha_2)\,, \tag{9.297}$$

where M is the molecular weight and ρ is the density and N_A is Avogadro's number.

Kuhn and Grün assumed the validity of the above formula in respect of the separate polarizabilities of the subunits (α_1,α_2) and applied the differential equation (9.296) to the finite difference of polarizabilities (9.293), since the absolute values of differences $(\alpha_1-\alpha_2)$ are small. Rearranging equation (9.296) we get

$$\frac{\Delta n}{n}=\frac{2\pi N_\mathrm{A}\rho}{9Mn^2}(\alpha_1-\alpha_2)(n^2+2)^2\,, \tag{9.298}$$

The dependence of birefringence on the degree of extension of macromolecules in flow was obtained by *Peterlin* [9.371]. He considered the problem of the dynamics of macromolecules in flow and used for this purpose two models: the simple dumbbell [9.372] and the more-realistic necklace model [9.373, 374]. The difference between solutions of the diffusion equation obtained by the two models resides more in the values of numerical coefficients than in the functional dependence.

For a dumbbell model in a predominantly extensional flow, where stretching occurs in the x-direction, the specific birefringence of a solution $(\Delta n/nc)$ can be written as:

$$\frac{\Delta n}{nc}=\frac{6\pi}{5h_0^2}\left\{\frac{n^2+2}{3n}\right\}^2(\alpha_1-\alpha_2)\frac{N_A}{M}\upsilon(\beta)\left\langle\beta_x^2-\beta_y^2\right\rangle\,, \tag{9.299}$$

and the corresponding expression for simple shear flow

$$\frac{\Delta n}{nc}=\frac{6\pi}{5h_0^2}\left\{\frac{n^2+2}{3n}\right\}^2(\alpha_1-\alpha_2)\frac{N_A}{M}\times\upsilon(\beta)\sqrt{\left\langle\beta_x^2-\beta_y^2\right\rangle^2+4\left\langle\beta_x^2\beta_y^2\right\rangle^2}\,, \tag{9.300}$$

where β_x and β_y are square projections of vector $\boldsymbol{\beta}=\boldsymbol{h}/L$ on the x- and y-axes,

$$\beta^2=\beta_x^2+\beta_y^2+\beta_z^2 \tag{9.301}$$

with β_z being the projection of β on the third axis z, n is the refractive index of a solution, and c is the concentration, conventionally in $\mathrm{g/cm^3}$. The total polarizability $(\alpha_1-\alpha_2)$ is given by (9.309) below.

The ratio of experimental birefringence (Δn) to the maximum achievable for fully stretched molecules (Δn_0) is

$$\frac{\Delta n}{\Delta n_0}=\frac{3}{5}\upsilon(\beta)\left\langle\beta_x^2-\beta_y^2\right\rangle\,. \tag{9.302}$$

In order to plot the dependence of the dimensionless birefringence (9.302) on the degree of extension we make the following approximations. Taking into account that the deformation occurs mainly in the stretching direction x we obtain

$$\left\langle\beta_y^2\right\rangle=\left\langle\beta_z^2\right\rangle=\frac{1}{3N}\,, \tag{9.303}$$

where N is the number of segments in a molecule, and symmetry of the y- and z-directions is assumed (axisymmetric stretching).

From (9.301) and (9.303) it follows that

$$\left\langle \beta_x^2 - \beta_y^2 \right\rangle = \beta^2 - 1/N \,. \tag{9.304}$$

The function $\upsilon(\beta) = 5/3\beta[1 - 3\beta/L^{-1}(\beta)]$ can be approximated by the dependence [9.375]:

$$\upsilon(\beta) \approx \left(1 + \frac{\beta^2}{3} + \frac{\beta^4}{3}\right) . \tag{9.305}$$

Using (9.302) and the approximation (9.305), we finally obtain for the dependence of dimensionless birefringence on the degree of extension

$$\frac{\Delta n}{\Delta n_0} = \frac{3}{5}\left(1 + \frac{\beta^2}{3} + \frac{\beta^4}{3}\right)\left(\beta^2 - \frac{1}{N}\right) . \tag{9.306}$$

The dependence (9.306) is shown in Fig. 9.114 for $N = 10^4$, which corresponds to a molecule of atactic polystyrene with $M \approx 8 \times 10^6$ (the $1/N$ term is negligible)

An analogous result for the dependence of birefringence on degree of extension has been obtained by Treloar. His model of the uncoiling process, as well as Peterlin's dumbbell, implied that the mean molecular segmental orientation (denoted by the end-to-end separation, h) during each stage of uncoiling in the flow field, is consistent with that of a molecule in a stationary solution whose ends are fixed at a distance h apart.

Other models of uncoiling, for example, the yo-yo model of *Ryskin* [9.376] and the models of *Rallison* and *Hinch* [9.377], *Wiest* et al. [9.378], *Larson* [9.379] and *Hinch* [9.380], who predicted the formation of kinks during uncoiling, would lead to birefringence versus extension curves different from that of Peterlin and Treloar models. The models of [9.376–380] produce lower estimated molecular strain values for the same birefringence during extension in comparison to the Peterlin and Treloar result (9.306), since folded chains give the same birefringence as extended ones.

9.5.4 Optical Properties of Macromolecules in Solution: Effects of Macroform and Microform Birefringence

In the derivation of the intrinsic anisotropy (9.293) the optical influence of the solvent, which modifies the internal field and hence the effective optical properties of the segment as well as those of the whole coil, has been neglected. If the refractive index of the solvent n_s is different from that of the dissolved polymer, n_p, an additional anisotropy of the molecule arises as a result of optical interaction between separate parts of the chain [9.381]. Interaction between chain elements far removed from each other (long-range optical interaction) leads to an anisotropy of the polarizing field within the molecular coil. This anisotropy is positive in sign and is directly dependent on the shape of the molecular coil (macroform anisotropy). The difference between the two principal polarizabilities of the macromolecule (in the direction of vector $\boldsymbol{h}$ and perpendicular to it) corresponds to the macroform effect and is [9.382]:

$$(\alpha_1 - \alpha_2)_f = \left(\frac{n_p^2 - n_s^2}{4\pi n_s \rho N_A}\right)^2 \frac{M^2}{V_s}(L_2 - L_1) \,, \tag{9.307}$$

where ρ is the density of the polymer, $V_s = 0.36\,h^3$ is the volume of the molecular coil in solution (including the solvent in the molecule), and $L_2 - L_1$ is the optical shape factor, which is a function of the axial ratio of the statistical coil. The anisotropy of the polarizing field that occurs as a result of this is therefore a value averaged over the whole volume of a molecule.

The neighboring elements (monomers) in the chain are arranged in a linear order and their interactions cannot be spherically symmetrical. Such asymmetrical short-range interaction causes local anisotropy of the polarizing field, which is analogous to the average field anisotropy due to the geometrical asymmetry of the entire molecule. Thus an additional anisotropy of polarizability arises (microform anisotropy), which is also positive in sign. The principal polarizability difference corresponding to the microform effect can be written

$$(\alpha_1 - \alpha_2)_{fs} = \left(\frac{n_p^2 - n_s^2}{4\pi n_s}\right)^2 \frac{M_0 s}{\rho N_A}(L_2 - L_1)_s \,. \tag{9.308}$$

Here $(L_2 - L_1)_s$ is the segmental spatial asymmetry function, M_0 is the molecular weight of the monomer, and s is the number of monomers per segment.

Therefore the total polarizability difference for the macromolecule in solution $(\gamma_1 - \gamma_2)$ is the sum of three components: the segmental anisotropy, the anisotropy due to the macroscopic shape of the polymer chain (or *macroform*), and the microstructure (or *microform*) anisotropy

$$\alpha_1 - \alpha_2 = (\alpha_1 - \alpha_2)_i + (\alpha_1 - \alpha_2)_f + (\alpha_1 - \alpha_2)_{fs} \,. \tag{9.309}$$

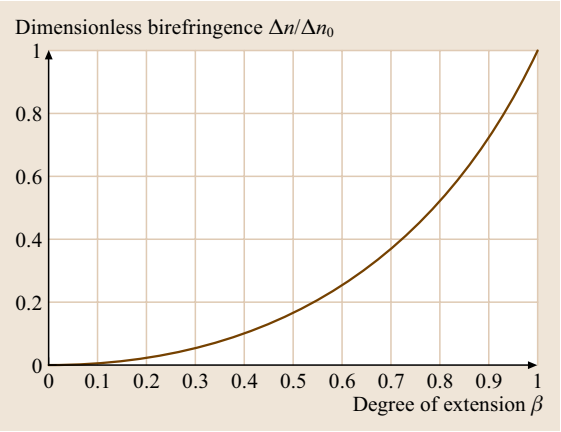

Fig. 9.114 Dependence of birefringence on the degree of extension of a polymer coil

So, the total principal polarizability difference $(\gamma_1 - \gamma_2)$ can be calculated with the help of (9.293), with $(\alpha_1 - \alpha_2)$ replacing $(\alpha_1 - \alpha_2)_i$.

9.5.5 Example Calculation of the Theoretical Birefringence for Stretched Molecules of Atactic Polystyrene

The maximum achievable birefringence calculated under the assumption that all molecules in solution are fully stretched follows from (9.298)

$$\Delta n = \frac{2\pi}{9}\left(\frac{n^2+2}{n}\right)^2 (\alpha_1 - \alpha_2)\frac{N_A c}{M_s}\,, \qquad (9.310)$$

where $(\alpha_1 - \alpha_2)$ is determined by (9.309), and $M_s = M_0 s$ is the molecular weight of the segment. It is easily seen that, as a macromolecular coil extends in the flow and the distances between the peripheral segments increase, so the optical long-range interactions in the chain will become weaker. This means that the relative role of the macroform effect is reduced. According to *Tsvetkov* [9.383], the macroform effect $(\alpha_1 - \alpha_2)_f \to 0$ for fully stretched molecules. So finally we obtain

$$\Delta n_0 = \frac{2\pi}{9}\left(\frac{n^2+2}{n}\right)^2 \frac{N_A c}{M_s} \times [(\alpha_1 - \alpha_2)_i + (\alpha_1 - \alpha_2)_{fs}]\,, \qquad (9.311)$$

where $(\alpha_1 - \alpha_2)_{fs}$ is determined by (9.308).

For atactic polystyrene in tricresylphosphate (TCP) we have [9.384]

$$n_p = 1.6,\, n_s = 1.55,\, (L_2 - L_1) = 5,$$
$$M_s = M_0 s = 822,\, (\alpha_1 - \alpha_2)_i = 145 \times 10^{-25}\ \mathrm{cm}^3\,. \qquad (9.312)$$

The value of intrinsic segmental anisotropy of atactic polystyrene (a-PS) was determined in bromoform, which has a refractive index very close to that of a-PS molecule. Substituting these values into (9.310) and (9.311), we get for maximum achievable for a-PS in TCP: $\Delta n = 0.09\,c$, where c (g/cm^3) is the concentration of the solution. The contribution of the microform effect to the total anisotropy is about 3% for this system.

9.5.6 Conclusions

Birefringence continues to provide a major insight into molecular structure; it is noninvasive, can be used in vivo and is extremely fast. The latter property makes it especially significant in non-Newtonian fluid mechanics. Careful experimentation can yield extraordinary sensitivity. Birefringence relies upon small differences in polarizability, but the *subtraction* is done at the molecular level. On the experimental scale, zero birefringence is the background upon which flow effects are superimposed. However, the relationship between birefringence and structure is ambiguous and models need to be used with caution to interpret results in terms of molecular orientation and conformation.

References

9.1 J.D. Ferry: *Viscoelastic Properties of Polymers*, 3rd edn. (Wiley, New York 1980)

9.2 R. Whorlow: *Rheological Techniques*, 2nd edn. (Ellis Horwood, Chichester 1992)

9.3 W.W. Graessly, S.D. Grasscock, R.L. Crawley: Die Swell in Molten Polymers, Trans.Soc.Rheol. **14**, 519–544 (1970)

9.4 K. te Nijenhuis: Survey of measuring techniques for the determination of the dynamic moduli. In: *Rheology*, Vol. 1, ed. by G. Astarita, G. Marucci, L. Nicolais (Plenum, New York 1980) pp. 263–280

9.5 K. te Nijenhuis, R. van Donselaar: A newly designed coaxial cylinder type dynamic rheometer, Rheol. Acta **24**, 47–57 (1985)

9.6 F.H. Gortemaker, M.G. Hansen, B. de Cindio, H.M. Laun, H. Janeschitz-Kriegl: Flow birefringence of polymer melts: application to the investigation of time dependent rheological properties, Rheol.Acta **15**, 256–267 (1976)

9.7 J. L. den Otter: Dynamic Properties of Some Polymeric Systems, Doctoral Thesis (Leiden, 1967)

9.8 F. Trouton: On the coefficient of viscous traction and its relation to that of viscosity, Proceedings of the Royal Society of London **A77**, 426–440 (1906)

9.9 C.J.S. Petrie: Elongational flows: Aspects of the behavior of model elasticoviscous fluids. In: *Research Notes in Mathematics*, ed. by Pitman (London 1979)

9.10 G.V. Vinogradov, V.D. Fikhman, B.V. Radushkevich, A.Y. Malkin: Viscoelastic and relaxation properties of a polystyrene melt in axial extension, J. Polym. Sci.: Part A-2 **8**, 657–678 (1970)

9.11 G.V. Vinogradov, B.V. Radushkevich, V.D. Fikhman: Extension of elastic fluids: Polyisobutylene, J. Polym. Sci., Part A-2 **8**, 1–17 (1970)

9.12 H. Munstedt, S. Kurzbeck, L. Egersdorfer: Influence of molecular structure on rheological properties of polyethylenes Part II. Elongational behavior, Rheol. Acta **37**, 21–29 (1998)

9.13 H. Munstedt: New universal extensional rheometer for polymer melts. Measurements on a polystyrene sample, J. Rheol. **23**, 421–436 (1979)

9.14 H. Munstedt, H.M. Laun: Elongational behaviour of a low density polyethylene melt II. Transient behavior in constant stretching rate and tensile creep experiments. Comparision with shear data. Temperature dependence of the elongational properties, Rheol. Acta **18**, 492–504 (1979)

9.15 J. Meissner, T. Raible, S.E. Stephenson: Rotary clamp in uniaxial and biaxial extensional rheometry of polymer melts, J. Rheol. **25**, 1–28 (1981)

9.16 S. Spiegelberg, D. Ables, G. McKinley: Role of end-effects on measurements of extensional viscosity in viscoelastic polymer solutions with a filament stretching rheometer, J. Non-Newt. Fluid Mech. **64**(2-3), 229–267 (1996)

9.17 V. Tirtaatmadja, T. Sridhar: Filament Stretching Device for Measurement of Extensional Viscosity, J. Rheol. **36**(3), 277–284 (1993)

9.18 R. Muller, D. Froelich: New extensional rheometer for elongational viscosity and flow birefringence measurements: some results on polystyrene melts, Polymer **26**, 1477–1482 (1985)

9.19 J. Meissner, J. Hostettler: New elongational rheometer for polymer melts and other highly viscoelastic liquids, Rheol. Acta **33**, 1–21 (1994)

9.20 M.L. Sentmanat: Dual windup drum extensional rheometer. Patent 6691569 (2004)

9.21 M.H. Wagner, B. Collignon, J. Verbeke: Rheotens-mastercurves and elongational viscosity of polymer melts, Rheol. Acta **35**, 117–126 (1996)

9.22 M.H. Wagner: Rheotens-mastercurves and drawability of polymer melts, Polym. Eng. Sci. **36**, 925–935 (1996)

9.23 W.H. Talbott, J.D. Goddard: Streaming birefringence in extensional flow of polymer solutions, Rheol. Acta **18**, 505–517 (1979)

9.24 R.C. Chan, R.K. Gupta, T. Sridhar: Fiber spinning of very dilute solutions of polyacrylamide in water, J. Non-Newt. Fluid Mech. **30**(2-3), 267–283 (1988)

9.25 G.H. McKinley, A. Tripathi: How to extract the Newtonian viscosity from capillary breakup measurements in a filament rheometer, J. Rheol. **44**(3), 653–670 (2000)

9.26 A.V. Bazilevskii, V.M. Entov, A.N. Rozhkov: Liquid Filament Microrheometer and Some of its Applications. In: *Proceedings of the 3rd European Rheology Conference* (Elsevier, New York 1990)

9.27 G.J.C. Braithwaite, S.H. Spiegelberg: *Capillary breakup to determine the extensional properties of polymeric fluids. In American Chemical Society North Eastern Regional Meeting* (American Chemical Society, Durham 2001)

9.28 P.N. Dunlap, L.G. Leal: Dilute polystyrene solutions in extensional flows: birefringence and flow modification, J. Non-Newt. Fluid Mech. **23**, 5–48 (1987)

9.29 G.G. Fuller, L.G. Leal: Flow birefringence of concentration polymer solutions in two-dimensional flows, J. Polym. Sci., Polym. Phys. **19**, 557–587 (1981)

9.30 D.M. Binding: Further consideration of axisymmetric contraction flows, J. Non-Newt. Fluid Mech. **41**, 27–42 (1991)

9.31 D.V. Boger: Viscoelastic flows through contractions, Ann. Rev. Fluid Mech. **19**, 157–182 (1987)

9.32 G.G. Fuller, C.A. Cathey, B. Hubbard, B.E. Zebrowski: Extensional viscosity measurements for low-viscosity fluids, J. Rheol. **31**, 235–249 (1987)

9.33 H.M. Laun, H. Schuch: Transient elongational viscosities and drawability of polymer melts, J. Rheol. **33**, 119–175 (1989)

9.34 M. Moan, A. Magueur: Transient extensional viscosity of dilute flexible polymer solutions, J. Non-Newt. Fluid Mech. **30**(2-3), 343–354 (1988)

9.35 A.L. Yarin: *Free liquid jets and films: Hydrodynamics & rheology. Interaction of Mechanics and Mathematics Series* (Wiley, New York 1993)

9.36 H.J. Shore, G. Harrison: The Effect of Added Polymer on the Formation of Drops Ejected from a Nozzle, Phys. Fluids **17**, 033104 (2005)

9.37 R.H. Fernando, L.-L. Xing, J.E. Glass: Rheology Parameters Controlling Spray Atomization and Roll-Misting Behavior of Waterborne Coatings, Prog. in Organic Coatings **42**, 244–248 (2001)

9.38 R.B. Bird, R.C. Armstrong, O. Hassager: *Dynamics of Polymeric Liquids. Volume 1: Fluid Mechanics*, 2nd edn. (Wiley Interscience, New York 1987)

9.39 D.F. James, K. Walters: A critical appraisal of available methods for the measurement of extensional properties of mobile systems. In: *Techniques of Rhe-*

ological Measurements, ed. by A.A. Collyer (Elsevier, New York 1994) pp. 33–53
9.40 C.J.S. Petrie: Extensional flow – A mathematical perspective, Rheol. Acta **34**, 12–26 (1995)
9.41 D.W. Bousfield, R. Keunings, G. Marrucci, M.M. Denn: Nonlinear analysis of the surface-tension driven breakup of viscoelastic fluid filaments, J. Non-Newt. Fluid Mech. **21**, 79–97 (1986)
9.42 H.K. Rasmussen, O. Hassager: The role of surface tension on the elastic decohesion of polymeric filaments, J. Rheol. **45**(2), 527–537 (2001)
9.43 J. Meissner: Experimental aspects in polymer melt elongational rheology, Chem. Eng. Commun. **33**, 159–180 (1985)
9.44 R.K. Gupta, T.E. Sridhar: Elongational Rheometers. In: *Rheological Measurement*, ed. by A.A. Collyer, D.W. Clegg (Elsevier, London 1988) pp. 211–245
9.45 M.L. Sentmanat, B. Wang, G.H. McKinley: Measuring the extensional rheology of polyethylene melts using the SER Universal Testing Platform, J. Rheol. **49**(3), 571–803 (2004)
9.46 A. Bach, H.K. Rasmussen, O. Hassager: Extensional Viscosity for Polymer Melts Measured in the Filament Stretching Rheometer, J. Rheol. **47**(2), 429–441 (2003)
9.47 T.C.B. McLeish, R.G. Larson: Molecular constitutive equations for a class of branched polymers: the Pom-Pom polymer, J. Rheol. **42**, 81–110 (1998)
9.48 H.K. Rasmussen, J.K. Nielsen, A. Bach, O. Hassager: Viscosity Overshoot in the Start-Up of Uniaxial Elongation of Low Density Polyethylene Melts, J. Rheol. **49**(2), 369–381 (2005)
9.49 A.Y. Malkin, C.J.S. Petrie: Some conditions for rupture of polymer liquids in extension, J. Rheol. **41**, 1–25 (1997)
9.50 G.H. McKinley, O. Hassager: The Considere condition and rapid stretching of linear and branched polymer melts, J. Rheol. **43**(5), 1195–1212 (1999)
9.51 Y.M. Joshi, M.M. Denn: Failure and recovery of entangled polymer melts in elongational flow. In: *Rheology Review, British Soc. Rheology*, ed. by D.M. Binding, K. Walters (2004) pp. 1–17
9.52 T. Sridhar: An overview of the project M1, J. Non-Newt. Fluid Mech. **35**, 85–92 (1990)
9.53 J. Matta, R. Tytus: Liquid stretching using a falling cylinder, J. Non-Newt. Fluid Mech. **35**, 215–229 (1990)
9.54 T. Sridhar, V. Tirtaatmadja, D.A. Nguyen, R.K. Gupta: Measurement of extentional viscosity of polymer solutions, J. Non-Newt. Fluid Mech. **40**, 271–280 (1991)
9.55 J. van Nieuwkoop, M.M.O. von Muller Czernicki: Elongation and subsequent relaxation measurements on dilute polyisobutylene solutions, J. Non-Newt. Fluid Mech. **67**, 105–124 (1996)
9.56 M.J. Solomon, S.J. Muller: Transient extensional behavior of polystyrene-based Boger fluids of varying solvent quality and molecular weight, J. Rheol. **40**, 1–19 (1996)
9.57 R.W.G. Shipman, M.M. Denn, R. Keunings: Mechanics of the falling plate extensional rheometer, J. Non-Newt. Fluid Mech. **40**, 281–288 (1991)
9.58 S. Berg, R. Kröger, H. Rath: Measurement of extensional viscosity by stretching large liquid bridges in microgravity, J. Non-Newt. Fluid Mech. **55**, 307–319 (1994)
9.59 M. Yao, G.H. McKinley: Numerical simulation of extensional deformations of viscoelastic liquid bridges in filament stretching devices, J. Non-Newt. Fluid Mech. **74**, 47–88 (1998)
9.60 M.I. Kolte, H.K. Rasmussen, O. Hassager: Transient filament stretching rheometer II: numerical simulation, Rheol. Acta **36**, 285–302 (1997)
9.61 S.L. Anna, C. Rogers, G.H. McKinley: On controlling the kinematics of a filament stretching rheometer using a real-time active control mechanism, J. Non-Newt. Fluid Mech. **87**, 307–335 (1999)
9.62 N.V. Orr, T. Sridhar: Probing the dynamics of polymer solutions in extensional flow using step strain rate experiments, J. Non-Newt. Fluid Mech. **82**, 203–232 (1999)
9.63 J.P. Rothstein, G.H. McKinley: Inhomogeneous transient uniaxial extensional rheometry, J. Rheol. **46**(4), 1419–1443 (2002)
9.64 P.S. Doyle, E.S.G. Shaqfeh, G.H. McKinley, S.H. Spiegelberg: Relaxation of dilute polymer solutions following extensional flow, J. Non-Newt. Fluid Mech. **76**(1-3), 79–110 (1998)
9.65 S.L. Anna, G.H. McKinley: Elasto-capillary thinning and breakup of model elastic liquids, J. Rheol. **45**, 115–138 (2001)
9.66 S.H. Spiegelberg, G.H. McKinley: Stress relaxation and elastic decohesion of viscoelastic polymer solutions in extensional flow, J. Non-Newt. Fluid Mech. **67**, 49–76 (1996)
9.67 A.V. Bazilevskii, V.M. Entov, M.M. Lerner, A.N. Rozhkov: Failure of polymer solution filaments, Polymer Science, Series A **39**(3), 316–324 (1997)
9.68 D. Papageorgiou: On the breakup of viscous liquid threads, Physics of Fluids **7**(7), 1529–1544 (1995)
9.69 A. Tripathi, P. Whittingstall, G.H. McKinley: Using filament stretching rheometry to predict strand formation and processability in adhesives and other non-Newtonian fluids, Rheol. Acta **39**, 321–337 (2000)
9.70 N. Willenbacher: Elongation viscosity of aqueous thickener solutions from capillary breakup elongation rheometry (CaBER). In: Proc. XIVth Int. Cong. Rheol. (2004). Seoul (S. Korea)
9.71 G. Neal, G. Braithwaite: The use of capillary breakup extensional rheology to examine concentration dependence of relaxation time. In: Society of Rheology Annual Meeting. Pittsburgh, PA (2003)
9.72 V.M. Entov, E.J. Hinch: Effect of a spectrum of relaxation times on the capillary thinning of a filament of elastic liquid, J. Non-Newt. Fluid Mech. **72**, 31–53 (1997)

9.73 L.E. Rodd, T.P. Scott, J.J. Cooper-White, and G.H. McKinley: Capillary breakup rheometry of low-viscosity elastic fluids, submitted to Applied Rheology, (2004)
9.74 S. Anna, G.H. McKinley, D.A. Nguyen, T. Sridhar, S.J. Muller, J. Huang, D.F. James: Interlaboratory comparison of measurements from filament-stetching rheometers using common test fluids, J. Rheol. **45**, 83–114 (2001)
9.75 S.L. Anna, S.H. Spiegelberg, G.H. McKinley: Elastic instability in elongating filaments, Phys. Fluids **9**(5), 10 (1997)
9.76 M. Stelter, G. Brenn, A. Yarin, R. Singh, F. Durst: Investigation of the elongational behavior of polymer solutions by means of an elongational rheometer, J. Rheol. **46**(2), 507–528 (2002)
9.77 P. Dontula, M. Pasquali, L.E. Scriven, C.W. Macosko: Can extensional viscosity be measured with opposed nozzle devices, Rheol. Acta **36**, 429–448 (1997)
9.78 D.F. James: Developments in extensional rheology, AMD **191**, 1–3 (1994)
9.79 S.L. Ng, R.P. Mun, D.V. Boger, D.F. James: Extensional viscosity measurements of dilute solutions of various polymers, J. Non-Newt. Fluid Mech. **65**, 291–298 (1996)
9.80 D.F. James: Extensional viscosity, an elusive property of mobile liquids. In: 3rd European Rheology Conference (1990)
9.81 V.M. Entov, A.L. Yarin: Influence of elastic stresses on the capillary breakup of jets of dilute polymer solutions, Fluid Dynamics **19**, 21–29 (1984)
9.82 H.A. Barnes, J.F. Hutton, K. Walters: *An Introduction to Rheology* (Elsevier, Amsterdam 1989)
9.83 W.H. Bauer, E.A. Collins: Chap. 8. In: *Rheology: Theory and Applications*, ed. by F.R. Eirich (Academic, New York 1967)
9.84 J. Mewis: Thixotropy – a general review, J. Non-Newt. Fluid Mech. **6**, 1–20 (1979)
9.85 D.C-H. Cheng: Report Number CR 2367 (MH), Warren Spring Laboratory, UK, October 1 (1982)
9.86 J.C. Godfrey: Ph.D. Thesis, Characterisation of thixotropic fluids (University of Bradford 1983)
9.87 H.A. Barnes: Thixotropy – A review, J. Non-Newt. Fluid Mech. **70**(1/2), 1–33 (1997)
9.88 F. Schalek, A. Szegvari: Ferric oxide jellies, Kolloid Z **32**, 318–319 (1923)
9.89 F. Schalek, A. Szegvari: The slow coagulation of concentrated ferric oxide sols to reversible jellies, Kolloid Z **33**,326–334 (1923)
9.90 T. Peterfi: Arch, Entwicklungsmech. Organ. **112**, 680 (1927)
9.91 T. Peterfi: Uber die thixotropie, Verhanitlungen 3rd. Intern. Zellto Arch. Exp. Zelif. **15**, 373–381 (1934)
9.92 H. Freunlich: *Thixotropie* (Hermann, Paris 1935)
9.93 E.L. McMillen: Thixotropy and Plasticity. 1 – The measurement of thixotropy, J. Rheol. **3**(1), 75–94 (1932)
9.94 G.W. Scott-Blair: *A Survey of General and Applied Rheology* (Pitman, London 1943)
9.95 J. Pryce-Jones: Thixotropy, JOCCA **17**, 305–375 (1934)
9.96 J. Pryce-Jones: JOCCA, Some fundamental aspects of thixotropy **19**, 295–337 (1936)
9.97 J. Pryce-Jones: Experiments on thixotropic and other anomalous fluids with a new rotation viscometer, J. Sci. Instr. **18**, 39–48 (1941)
9.98 J. Thewlis (Ed.): *Oxford Encyclopedia Dictionary of Physics* (Pergamon Press, Oxford 1962)
9.99 T.C. Collocott (Ed.): Chambers Dictionary of Science and Technology (W&R Chambers 1971)
9.100 S.P. Parker (Ed.): *McGraw-Hill Dictionary of Scientific and Technical Termsn*, 4th edn. (McGraw-Hill, New York 1989)
9.101 D.M. Considine (Ed.): *Van Nostrand's Scientific Encyclopedia, 5th end* (Van Nostrand Reinhold Company, New York 1976)
9.102 *Oxford Concise Science Dictionary*, 2nd edn. (Oxford Univ. Press, Oxford 1991)
9.103 *Chambers 20th Century Dictionary* (Chambers, London 1993)
9.104 T. Whelan (Ed.): *Polymer Technology Dictionary* (Chapman Hall, London 1994)
9.105 M.S.M. Alger (Ed.): *Polymer Science Dictionary* (Elsevier, London 1990)
9.106 M. Reiner, G.W. Scott-Blair: *Rheological Terminology in Rheology Theory and Applied* (Academic Press, New York 1967), Chap. 9
9.107 S. Rahimi, B. Natan: Thixotropic effect of inorganic gel fuels, J. Propuls. Power **16**, 1182–1184 (2000)
9.108 Unpublished report, International Fine Particle Research Institute, (1996)
9.109 A. Maestro, C. Gonzalez, J.M. Gutierrez: Shear thinning and thixotropy of HMHEC and HEC water solutions, J. Rheol. **46**(6), 1445–1457 (2002)
9.110 L. Heymann, E. Noack, L. Kampfe, B. Beckmann: Rheology of printing inks - Some new experimental results. In: *Proceedings of the XIIth International Congress on Rheology*, ed. by A. Ait-Kadi, et al. (Laval University, Quebec 1996) pp. 451–452
9.111 P.D.A. Mills, J. Goodwin, B.W. Grover: Shear field modification of strongly flocculated suspensions - aggregate morphology, Colloid. Polym. Sci. **269**(9), 949–963 (1991)
9.112 W. Woithers: Proc. XIIth International Congress on Rheology, ed. by A. Ait-Kadi et al. (Laval University, Quebec 1996) pp. 526–527
9.113 M. Barut, R. Lapasin, A. Zupanic, M. Zumer: Time-dependent rheological behavior of Ti02 suspensions. In: *Proceedings of the XIIth International Congress on Rheology*, ed. by A. Ait-Kadi, et al. (Laval University, Quebec 1996) pp. 578–579
9.114 P.R. Williams, S.R. Ren: Direct determination of the mechanical relaxation spectra of concentrated suspensions in the presence of controlled shear fields. In: *Proceedings of the XIIth International Congress*

on Rheology, ed. by A. Ait-Kadi, et al. (Laval University, Quebec 1996) pp. 458–459
9.115 V. Bouda, J. Mikešová: Vibrational carbon black agglomaration in polythylene melt. In: *Proceedings of the XIIth International Congress on Rheology*, ed. by A. Ait-Kadi et al. (Laval University, Quebec 1996) pp. 27–28
9.116 H.H. Winter: Evolution of rheology during chemical gelation, Progr. Colloid Polym. Sci. **75**, 104–110 (1987)
9.117 J. Greener, R. W.Connelly: The response of viscoelastic liquids to complex strain histories – the thixotropic loop, J. Rheol. **30**(2), 285–300 (1986)
9.118 H.A. Barnes: A review of the slip (wall depletion) of polymer solutions, emulsions and particle suspensions in viscometers: its cause, character and cure, J. Non-Newt. Fluid Mech. **56**, 221–251 (1995)
9.119 C.F. Goodeve, G.W. Whitfield: The measurement of thixotropy in absolute units, Trans. Farad. Soc. **34**, 511–520 (1938)
9.120 F. Moore: The rheology of ceramic slips and bodies, Trans. Brit Ceramics Soc. **58**, 470–494 (1959)
9.121 D.C.-H. Cheng, F. Evans: Phenomenological characterization of rheological behaviour of inelastic reversible thixotropic and antithixotropic fluids, Brit. J. Appl. Phys. **16**(11), 1599–1617 (1965)
9.122 A. Allesandrini, R. Lapasin, F. Sturzi: The kinetics of thixotropic behavior in clay kaolin aqueous suspensions, Chem. Eng. Commun. **17**(1-6), 13–22 (1982)
9.123 C. Baravian, D. Quemada, A. Parker: A new methodology for rheological modelling of thixotropy application to hydrocolloids. In: *Proceedings of the XIIth International Congress on Rheology*, ed. by A. Ait-Kadi, et al. (Laval University, Quebec 1996) pp. 779–780
9.124 D. de Kee, R.K. Code, G. Turcotte: Flow properties of time-dependent foodstuffs, J. Rheol. **27**, 581–604 (1983)
9.125 C. Tiu, D.V. Boger: Complete rheological characterization of time dependent food products, J. Texture Stud. **5**(3), 329–338 (1974)
9.126 D.A. Denny, R.S. Brodkey: Kinetic interpretation of non-Newtonian flow, J. Appl. Phys. **33**(7), 2269–2274 (1962)
9.127 M. van den Tempel: Mechanical properties of plastic-disperse systems at very small deformations, J. Coll. Sci. **16**, 284–296 (1961)
9.128 E. Ruckenstein, J. Mewis: Rheology of non-Newtonian fluids – a new flow equation for pseudoplastic systems, J. Coll. Interface Sci. **44**, 532 (1973)
9.129 M.M. Cross: Rheology of non-Newtonian fluids: a new flow equation for pseudoplastic systems, J. Coll. Sci. **20**, 417–437 (1965)
9.130 R. Lapasin, M. Grassi, S. Pricl: Viscoelastic properties of welan systems. In: *Proceedings of the XIIth International Congress on Rheology*, ed. by A. Ait-Kadi, et al. (Laval University, Quebec 1996) pp. 524–525
9.131 I. Park, T. Ree: Kinetics of Thixotropy of Aqueous Bentonite Suspension J, Korean Chem. Soc. **15**(6), 293–303 (1971)
9.132 A.G. Fredrickson: Model for the thixotropy of suspensions, AIChEJ **16**(3), 436–441 (1970)
9.133 J. Mewis, J. Schryvers: unpublished International Fine Particle Research Institute report (1996)
9.134 P.J. Kristensen, C.T.B. Jensen, Q.D. Nguyen: Rheological characterisation of maize starch pastes. In: *Proceedings of the XIIth International Congress on Rheology*, ed. by A. Ait-Kadi et al. (Laval University, Quebec 1996) pp. 471–472
9.135 Q.D. Nguyen, D.V. Boger: Thixotropic behavior of concentrated bauxite residue suspensions, Rheol. Acta **24**(4), 427–437 (1985)
9.136 D. Acierno, F.P. La Mantia, G. Marrucci, G. Titomanlio: Nonlinear viscoelastic model with structure-dependent relaxation-times .1. basic formulation, J. Non-Newt. Fluid Mech. **1**(2), 125–146 (1976)
9.137 D. Shoong, M. Shen: Kinetic network model for non-linear viscoelastic flow properties of entangled monodisperse polymers, J. Polym. Sci., Lett. Ed. **17**(9), 595–599 (1979)
9.138 D. Quemada: Rheological modelling of complex fluids: IV: Thixotropic and thixoelastic behaviour. Start-up and stress relaxation, creep tests and hysteresis cycles, European Physical J. Appl. Phys. **5**, 191–207 (1999)
9.139 P.A. Reynolds, J.W. Goodwin: Direct measurement of the translational diffusion-coefficients of aggregated polystyrene latex-particles, Colloid Surf. **11**(1-2), 145–154 (1984)
9.140 H.A. Barnes: *Dispersion Rheology, a Survey of Industrial Problems and Academic Progress* (Royal Soc. Chem. Industrial Div., London 1981)
9.141 H. Sonntag: Coagulation Kinetics. In: *Coagulation and Flocculation: Theory and Applications*, ed. by B. Dobias (Dekker, New York 1993), Chap. 3
9.142 K. Mûhle: Floc stability in laminar and turbulent flow. In: *Coagulation and Flocculation: Theory and Applications*, ed. by B. Dobiasc (Dekker, New York 1993)
9.143 M.F. Edwards, J.C. Godfrey, M.M. Kashani: Power requirement for mixing of thixotropic liquids, J. Non-Newt. Fluid Mech. **1**(4), 309–322 (1976)
9.144 L. Schmitt, G. Ghnassia, J.J. Bimbenet, G. Cuvelier: Flow properties of stirred yogurt: Calculation of the pressure drop for a thixotropic fluid, J. Food Engin. **37**, 367–388 (1998)
9.145 W.G. Hou, D.J. Sun, S.H. Han: A novel thixotropic phenomenon – Complex thixotropic behavior, Chem. Res. Chinese Universities **13**, 86–88 (1997)
9.146 S.P. Li, W.G. Hou, X.N. Dai, J.F. Hu, D.Q. Li: The influence of pH on the thixotropy of ferric aluminum

magnesium hydroxide/montmorillonite suspension, Chem. J. Chinese Universities **23**, 1763–1766 (2002)
9.147 S.P. Li, W.G. Hou, J.F. Hu, D.Q. Li: Influence of shear rate on thixotropic suspensions, J. Disp. Sci. Technol. **24**, 709–714 (2003)
9.148 S.P. Li, W.G. Hou, J.C. Xiao, J.F. Hu, D.Q. Li: Influence of measuring conditions on the thixotropy of hydrotalcite-like/montmorillonite suspension, Colloids and Surfaces A-Physicochemical and Engineering Aspects **224**, 149–156 (2003)
9.149 S.P. Li, W.G. Hou, X.N. Dai, P. Jiang: Influence of electrolytes on the thixotropy of ferric aluminum magnesium hydroxide-montmorillonite suspensions, J. Disp. Sci. Techn. **24**, 145–152 (2003)
9.150 P.Z. Guo, D.J. Sun, Z.L. Jin, C.G. Zhang: Rheological properties of mixed suspensions containing oppositely charged colloidal particles, Chem. J. Chinese Universities **24**, 1052–1055 (2003)
9.151 D.J. Sun, W.G. Hou, S.Y. Liu, B.Q. Zhang, C.G. Zhang: Thixotropic properties of aqueous dispersions of positively charged Al/Mg mixed metal hydroxide particles, Acta Chimica Sinica **59**, 163–167 (2001)
9.152 Y. Wang, M.J. Yu: Effect of volume loading and surface treatment on the thixotropic behavior of polypropylene filled with calcium carbonate, Polymer Composites **21**, 1–12 (2000), sec2-Taiwan
9.153 J. Assaad, K.H. Khayat, H. Mesbah: ACI Materials, J. Assessment of thixotropy of flowable and self-consolidating concrete **100**, 99–107 (2003)
9.154 I.A. Kinloch, S.A. Roberts, A.H. Windle: A rheological study of concentrated aqueous nanotube dispersions, Polymer **43**, 7483–7491 (2002)
9.155 C. Voltz, M. Nitschke, L. Heymann, I. Rehberg: Thixotropy in macroscopic suspensions of spheres, Phys. Rev. E **65**(5), 051402 (2002)
9.156 A. Mujumdar, A.N. Beris, A.B. Metzner: Transient phenomena in thixotropic systems, J. Non-Newton. Fluid Mech. **102**, 157–178 (2002), Special Issue SI
9.157 F. Bautista, J.M. de Santos, J.E. Puig, O. Manero: Understanding thixotropic and antithixotropic behavior of viscoelastic micellar solutions and liquid crystalline dispersions. I. The model, J. Non-Newt. Fluid Mech. **80**, 93–113 (1999)
9.158 F. Yziquel, P.J. Carreau, M. Moan, P.A. Tanguy: Rheological modeling of concentrated colloidal suspensions, J. Non-Newt. Fluid Mech. **86**, 133–155 (1999)
9.159 J.W. Goodwin, P.A. Reynolds: The rheology of flocculated suspensions, Current Opinion in Colloid & Interface Science **3**, 401–407 (1998)
9.160 N. Bagdassarov, H. Pinkerton: Transient phenomena in vesicular lava flows based on laboratory experiments with analogue materials, J. Volcanology and Geothermal Research **132**, 115–136 (2004)
9.161 L.P. Martinez-Padilla, F. Lopez-Araiza, A. Tecante: Steady and oscillatory shear behavior of fluid gels formed by binary mixtures of xanthan and gellan, Food Hydrocolloids **18**, 471–481 (2004)
9.162 A. Tarrega, L. Duran, E. Costell: Flow behaviour of semi-solid dairy desserts. Effect of temperature, Int. Dairy J. **14**, 345–353 (2004)
9.163 M.M. Li, J.P. Zhi, G.Y. Zhang, Q.L. Ma: Thixotropy comparison of different peptized pseudo-bohemites, Acta Petrologica Sinica **20**, 35–39 (2004)
9.164 C. Malfoy, A. Pantet, P. Monnet, D. Righi: Effects of the nature of the exchangeable cation and clay concentration on the rheological properties of smectite suspensions, Clays And Clay Minerals **51**, 656–663 (2003)
9.165 J.F. Zhou, L.M. Zhang, P.S. Hui: Rheological characteristics of aqueous solutions of an amphoteric guar gum derivative, Acta Physico-Chimica Sinica **19**, 1081–1084 (2003)
9.166 A. Koksoy, M. Kilic: Effects of water and salt level on rheological properties of ayran, a Turkish yoghurt drink, Int. Dairy J. **13**, 835–839 (2003)
9.167 J. Koke, M. Modigell: Flow behaviour of semi-solid metal alloys, J. Non-Newt. Fluid Mech. **112**, 141–160 (2003)
9.168 F.V. Lopez, M. Rosen: Rheological effects in roll coating of paints, Latin American Applied Research **32**, 247–252 (2002)
9.169 A. Moise, A. Aruxandei: Tire influence of temperature on the viscoplastic compound of some cosmetic products, Revista De Chimie **53**, 222–225 (2002)
9.170 B. Abu-Jdayil, H. Mohameed: Experimental and modelling studies of the flow properties of concentrated yogurt as affected by the storage time, J. Food Engin. **52**, 359–365 (2002)
9.171 P. Corvisier, C. Nouar, R. Devienne, M. Lebouche: Development of a thixotropic fluid flow in a pipe, Exp. Fluids **31**, 579–587 (2001)
9.172 J.S. Raynaud, P. Moucheront, J.C. Baudez, F. Bertrand, J.P. Guilbaud, P. Coussot: Direct determination by nuclear magnetic resonance of the thixotropic and yielding behavior of suspensions, J. Rheol. **46**, 709–732 (2002)
9.173 S. Chander: Challenges in characterization of concentrated suspensions, Colloids and Surfaces A **133**, 143–150 (1998)
9.174 V.A. Hackley, C.F. Ferraris: The Use of Nomenclature in Dispersion Science and Technology, National Institute of Standards and Technology, Technology Administration, U.S. Department of Commerce, Special Publication 960-3, Washington (2001)
9.175 D.H. Everett: Manual of symbols and terminology for physicochemical quantities and units (Appendix II/Part I), Pure. Appl. Chem. **31**, 577–638 (1972)
9.176 E. Kissa: *Dispersions – Characterization, Testing, and Measurement* (Dekker, New York 1999)
9.177 G.D. Parfitt (Ed.): *Dispersions of Powders in Liquids*, 2nd edn. (Wiley, New York 1973)
9.178 VDI-Richtlinie 3491: *Messen von Partikeln, Kennzeichnung von Partikeldispersionen in Gasen, Begriffe*

und Definitionen, VDI-Handbuch: Reinhaltung der Luft, Band 4 (VDI-Verlag, Düsseldorf 1980)
9.179 G. Böhme: *Strömungsmechanik nicht-Newtonscher Fluide*, 2nd edn. (Teubner, Stuttgart 2000), in German
9.180 H. Wadell: Volume shape and roundness of rock particles, J. Geol. **40**, 443–451 (1932)
9.181 A. Jillavenkatesa, S.J. Dapkunas, L.S.H Lum: Particle size characterization, National Institute of Standards and Technology, Technology Administration, U.S. Department of Commerce, Special Publication 960-1, Washington (2001)
9.182 M.H. Pahl, G. Schädel, H. Rumpf: Methods for describing particle shapes (part 1), Aufbereitungstechnik **5**, 257–263 (1973)
9.183 M.H. Pahl, G. Schädel, H. Rumpf: Methods for describing particle shapes (part 2), Aufbereitungstechnik **10**, 672–683 (1973)
9.184 M.H. Pahl, G. Schädel, H. Rumpf: Methods for describing particle shapes (part 3), Aufbereitungstechnik **11**, 759–764 (1973)
9.185 R.M. Turian, T.W. Ma, F.LG. Hsu, D.J. Sung: Characterization, settling, and rheology of concentrated fine particulate mineral slurries, Powder Technol. **93**, 219–233 (1997)
9.186 R.G. Larson: The Structure and Rheology of Complex Fluids (Oxford Univ. Press, New York 1999)
9.187 P.G. Saffmann: The lift on a small sphere in a slow shear flow, J. Fluid. Mech. **22**, 385–400 (1965)
9.188 C.W. Macosko: *Rheology – Principles, Measurements, and Applications* (VCH, New York 1994)
9.189 K. Walters: *Rheometry* (Chapman Hall, London 1975)
9.190 G.K. Batchelor: *An Introduction to Fluid Dynamics* (Cambridge Univ. Press, Cambridge 2000)
9.191 D.J. Jeffrey, A. Acrivos: The rheological properties of suspensions of rigid particles, AIChE J. **22**, 417–432 (1976)
9.192 H.A. Barnes: Measuring the viscosity of large-particle (and flocculated) suspensions – a note on the necessary gap size of rotational viscometers, J. Non-Newt. Fluid Mech. **94**, 213–217 (2000)
9.193 Official nomenclature for material functions describing the response of a viscoelastic fluid to various shearing and extensional deformations, J. Rheol. **39**, 253–265 (1995)
9.194 W.B. Russel, D.A. Saville, W.R. Schowalter: *Colloidal Dispersions* (Cambridge Univ. Press, Cambridge 1989)
9.195 I.D. Morrison, S. Ross: *Colloidal Dispersions – Suspensions, Emulsions, and Foams* (Wiley, New York 2002)
9.196 M. Takeo: *Disperse Systems* (Wiley-VCH, Weinheim 1999)
9.197 R.J. Pugh, L. Bergström: *Surface and Colloid Chemistry in Advanced Ceramic Processing* (Dekker, New York 1994)
9.198 T.G.M. van de Ven: *Colloidal Hydrodynamics* (Academic, London 1989)
9.199 M. Doi, S.F. Edwards: *The Theory of Polymer Dynamics* (Clarendon Press, Oxford 2003)
9.200 J. Israelachvili: *Intermolecular and Surface Forces*, 2nd edn. (Academic, London 1992)
9.201 H.R. Kruyt: *Colloidal Science Vol. I* (Elsevier, Amsterdam 1952)
9.202 H.C. Hamaker: The London-van der Waals attraction between spherical particles, Physica **4**, 1058–1072 (1937)
9.203 K.S. Birdi (Ed.): *Handbook of Surface and Colloid Science* (CRC Press, Boca Raton 1997)
9.204 L. Bergström: Hamaker constants of inorganic materials, Adv. Colloid. Interface Sci. **70**, 125–169 (1997)
9.205 J.A. Lewis: Colloidal Processing of Ceramic, J. Am. Ceram. Soc. **83**, 2341–2358 (2000)
9.206 B.V. Derjaguin, L. Landau: Theory of the stability of strongly charged lyophobic sols and the adhesion of strongly charged particles in solutions of electrolytes, Acta Physicochim URSS **14**, 633–652 (1941)
9.207 E.JW. Verwey, J.TG. Overbeek: *Theory of the Stability o Lyophobic Colloids* (Elsevier, Amsterdam 1948)
9.208 O.J. Rojas, P.M. Claesson, D. Muller, R.D. Neuman: The Effect of Salt Concentration on Adsorption of Low-Charge-Density Polyelectrolytes and Interactions between Polyelectrolyte-Coated Surfaces, J. Colloid. Interface Sci. **205**, 77–78 (1998)
9.209 T.F. Tadros: Correlation of viscoelastic properties of stable and flocculated suspensions with their interparticle interactions, Adv. Colloid. Interface Sci. **68**, 97–200 (1996)
9.210 A. Einstein: Eine neue Bestimmung der Moleküldimensionen, Ann. Phys. **34**, 591–592 (1906)
9.211 A. Einstein: Eine neue Bestimmung der Moleküldimensionen, Ann Phys **19**, 289–306 (1911)
9.212 R.K. Gupta: *Polymer and Composite Rheology* (Dekker, New York 2000)
9.213 G.K. Batchelor, J.T. Green: The determination of the bulk stress in a suspension of spherical particles to order c^2, J. Fluid. Mech. **56**, 401–427 (1972)
9.214 G.K. Batchelor: The effect of Brownian motion on the bulk stress in a suspension of spherical particles, J. Fluid. Mech. **83**, 97–117 (1977)
9.215 D.G. Thomas: Transport characteristics of suspensions: VIII. A note on the viscosity of Newtonian suspensions of uniform spherical particles, J. Colloid. Sci. **20**, 267–277 (1965)
9.216 A. Einstein: Berichtigung zu meiner Arbeit: Eine neue Bestimmung der Moleküldimensionen, Ann Phys **34**, 591–592 (1911)
9.217 H. Eilers: Die Viskositäts-Konzentrationsabhängigkeit kolloider Systeme in organischen Lösungsmitteln, Kolloid.-Z **102**, 154–169 (1943)
9.218 E.H. Harbard: An investigation into the variation of the viscosity of a suspension with its concentration, Chem. Ind. **22**, 491–492 (1956)
9.219 C.G. de Kruif, E.MF. van Iersel, A. Vrij, W.B. Russel: Hard sphere colloidal dispersions: Viscosity as a

function of shear rate and volume fraction, J. Chem. Phys. **83**, 4717–4725 (1985)
9.220 J. Mewis, J.W. Frith, T.A. Strivens, W.B. Russel: Rheology of suspensions containing polymerically stabilized particles, AIChE J. **35**, 415–422 (1989)
9.221 T. Kitano, T. Kataoko, T. Shiraota: An empirical equation of the relative viscosity of polymer melts filled with various inorganic fillers, Rheol. Acta. **20**, 207–209 (1981)
9.222 D. He, N.N. Ekere: Viscosity of concentrated non-colloidal bidisperse suspensions, Rheol. Acta. **40**, 591–598 (2001)
9.223 K. Qin, A.A. Zaman: Viscosity of concentrated colloidal suspensions: comparison of bidisperse models, J. Colloid. Interface Sci. **266**, 461–467 (2003)
9.224 T. Shikata, H. Niwa: Viscoelastic behaviour of bimodal ideal suspensions, Nihon Reorojï Gakkaishi **28**, 127–135 (2000)
9.225 T. Shikata: Viscoelastic behaviour of ideal bimodal suspensions, Chem. Eng. Sci. **56**, 2957–2966 (2001)
9.226 I.R. Rutgers: Relative viscosity and concentration, Rheol. Acta. **2**, 305–348 (1962)
9.227 V.V. Jinescu: The rheology of suspensions, Int. Chem. Eng. **14**, 397–420 (1974)
9.228 S. Arrhenius: The viscosity of solutions, Biochem. J. **11**, 112–133 (1917)
9.229 S.H. Maron, P.E. Pierce: Application of Ree-Eyring generalized flow theory to suspensions of spherical particles, J. Colloid. Sci. **11**, 80–95 (1956)
9.230 I.M. Krieger, I.J. Dougherty: A mechanism for non-Newtonian flow in suspensions of rigid spheres, Trans. Soc. Rheol. **3**, 137–152 (1959)
9.231 M. Mooney: The viscosity of a concentrated suspension of spherical particles, J. Colloid. Sci. **6**, 162–170 (1951)
9.232 R.C. Ball, P. Richmond: Dynamics of colloidal dispersions, Phys. Chem. Liq. **9**, 99–116 (1980)
9.233 R.D. Sudduth: A generalised model to predict the viscosity of solutions with suspended particles I, J Appl Polym Sci **48**, 25–36 (1993)
9.234 C.R. Wildemuth, M.C. Williams: Viscosity of suspensions modeled with a shear-dependent maximum packing fraction, Rheol. Acta. **23**, 627–635 (1984)
9.235 J.Z.Q. Zhou, T. Fang, G. Luo, P.HT. Uhlherr: Yield stress and maximum packing fraction of concentrated suspensions, Rheol. Acta. **34**, 544–561 (1995)
9.236 W.J. Frith, J. Mewis, T.A. Strivens: Rheology of concentrated suspensions: Experimental investigations, Powder Tech. **51**, 27–34 (1987)
9.237 K. Yasuda, R.C. Armstrong, R.E. Cohen: Shear flow properties of concentrated solutions of linear and star branched polystyrenes, Rheol. Acta. **20**, 163–178 (1981)
9.238 Q.D. Nguyen, D.V. Boger: Measuring the flow properties of yield stress fluids, Annu. Rev. Fluid. Mech. **24**, 47–88 (1992)
9.239 H.A. Barnes: The yield stress–a review or $\pi\alpha\nu\tau\alpha\rho\varepsilon\iota$ everything flows?, J. Non-Newt. Fluid Mech. **81**, 133–178 (1999)
9.240 H.M. Laun, R. Bung, S. Hess, W. Loose, O. Hess, K. Hahn, E. Hadicke, R. Hingman, F. Schmidt, P. Lindner: Rheological and small angle neutron scattering investigation of shear-induced particle structures of concentrated polymer dispersions submitted to plane Poiseuille and Couette flow, J. Rheol. **36**, 743–787 (1992)
9.241 P. d'Haene, J. Mewis, G.G. Fuller: Scattering dichroism measurements of flow induced structure of a shear thickening suspension, J. Colloid. Interface Sci. **156**, 350–358 (1993)
9.242 M.K. Chow, V.F. Zukoski: Nonequilibrium behaviour of dense suspensions of uniform particles: Volume fraction and size dependence of rheology and microstructure, J. Rheol. **39**, 33–59 (1995)
9.243 H.A. Barnes: Shear-thickening (Dilatancy) in suspensions of nonaggregating solid particles dispersed in Newtonian liquids, J. Rheol. **33**, 329–366 (1989)
9.244 W.J. Frith, P. d'Haene, R.R. Buscall, J.J. Mewis: Shear thickening in model suspensions of sterically stabilized particles, J. Rheol. **40**, 531–547 (1996)
9.245 G.V. Franks, Z. Zhou, N.J. Duin, D.V. Boger: Effect of interparticle forces on shear thickening of oxide suspensions, J. Rheol. **44**, 759–779 (2000)
9.246 S.R. Raghavan, S.A. Khan: Shear thickening response of fumed silica suspensions under steady and oscillatory shear, J. Colloid. Interface Sci. **185**, 57–67 (1997)
9.247 D. Doraiswamy, A.N. Mujumdar, I. Tsao, A.N. Beris, S.C. Danforth, A.B. Metzner: The Cox-Merz rule extended: a rheological model for concentrated suspensions and other materials with a yield stress, J. Rheol. **35**, 647–685 (1991)
9.248 W. Gleissle, B. Hochstein: Validity of the Cox-Merz rule for concentrated suspensions, J. Rheol. **47**, 897–910 (2003)
9.249 R.L. Powell: Rotational rheometry. In: *Rheological Measurement*, 2nd edn., ed. by A.A. Collyer, D.W. Clegg (Chapman Hall, London 1998), Chap. 9
9.250 M.R. Mackley, R.PG. Rutgers: Capillary rheometry. In: *Rheological Measurement*, 2nd edn., ed. by A.A. Collyer, D.W. Clegg (Chapman Hall, London 1998)
9.251 B.P. Ho, L.G. Leal: Inertial migration of rigid spheres in two-dimensional unidirectional flows, J. Fluid. Mech. **65**, 365–400 (1974)
9.252 H. Gevgilili, D.M. Kalyon: Step strain flow: Wall slip effects and other error sources, J. Rheol. **45**, 467–475 (2001)
9.253 A.L. Graham, A.A. Mammoli, M.B. Busch: Effects of demixing on suspension rheometry, Rheol. Acta. **37**, 139–150 (1998)
9.254 D.T. Leighton, A. Acrivos: The shear-induced migration of particles in concentrated suspensions, J. Fluid. Mech. **181**, 415–439 (1987)

9.255 B.K. Aral, D.M. Kalyon: Effects of temperature and surface roughness on time-dependent development of wall slip in steady torsional flow of concentrated suspensions, J. Rheol. **38**, 957–972 (1994)

9.256 M. Allende, D.M. Kalyon: Assessment of particle-migration effects in pressure-driven viscometric flows, J. Rheol. **44**, 79–90 (1999)

9.257 R.J. Phillips, R.C. Armstrong, R.A. Brown, A.L. Graham, J.R. Abbott: A constitutive equation for concentrated suspensions that accounts for shear-induced particle migration, Phys. Fluids A **4**, 30–40 (1992)

9.258 P.J.A. Hartman Kok, S.G. Kazarian, C.J. Lawrence, B.J. Briscoe: Near-wall particle depletion in a flowing colloidal suspension, J. Rheol. **46**, 481–493 (2002)

9.259 U. Yilmazer, D.M. Kalyon: Slip effects in capillary and parallel disk torsional flows of highly filled suspensions, J. Rheol. **33**, 1197–1212 (1989)

9.260 J.R. Abbott, N. Tetlow, A.L. Graham, S.A. Altobelli, E. Fukushima, L.A. Mondy, T.S. Stephens: Experimental observations of particle migration in concentrated suspensions: Couette flow, J. Rheol. **35**, 773–795 (1991)

9.261 M. Han, C.C. Kim, M.M. Kim, S.S. Lee: Particle migration in tube flow of suspensions, J. Rheol. **43**, 1157–1174 (1999)

9.262 S.C. Jana, B. Kapoor, A. Acrivos: Apparent wall slip velocity coefficients in concentrated suspensions of non-colloidal particles, J. Rheol. **39**, 1123–1132 (1995)

9.263 J. Persello, A. Magnin, J. Chang, J.M. Piau, B. Cabane: Flow of colloidal aqueous silica dispersions, J. Rheol. **38**, 1845–1870 (1994)

9.264 H.J. Walls, S. Brett Caines, A.M. Sanchez, S.A. Khan: Yield stress and wall slip phenomena in colloidal silica gels, J. Rheol. **47**, 847–868 (2003)

9.265 A. Yoshimura, R.K. Prud'homme: Wall slip correction for Couette and parallel disk viscometer, J. Rheol. **32**, 53–67 (1988)

9.266 H.A. Barnes: A review of the slip (wall depletion) of polymer solutions, emulsions and particle suspensions in viscometers: its cause, character, and cure, J. Non-Newt. Fluid Mech. **56**, 221–251 (1995)

9.267 L. Heymann, S. Peukert, N. Aksel: Investigation of the solid-liquid transition of highly concentrated suspensions in oscillatory amplitude sweeps, J. Rheol. **46**, 93–112 (2002)

9.268 H.M. Laun: Rheological properties of aqueous polymer dispersions, Angew. Makromol. Chem. **123**, 335–359 (1984)

9.269 P.J. Carreau, P.A. Lavoie, F. Yziquel: Rheological properties of concentrated suspensions. In: *Advances in the Flow and Rheology of Non-Newtonian Fluids. Rheology Series 8*, ed. by D.A. Siginer, D. De Kee, R.P. Chhabra (Elsevier, Amsterdam 1999)

9.270 M. Schmidt, H. Münstedt: Rheological behaviour of concentrated monodisperse suspensions as a function of preshear conditions and temperature: an experimental study, Rheol. Acta. **41**, 193–204 (2002)

9.271 M.K. Lyon, D.W. Mead, R.E. Elliott, L.G. Leal: Structure formation in moderately concentrated viscoelastic suspensions in simple shear flow, J. Rheol. **45**, 881–890 (2001)

9.272 P. Gondret, L. Petit: Viscosity of periodic suspensions, Phys. Fluids **8**, 2284–2290 (1996)

9.273 I.M. Krieger: Rheology of monodisperse lattices, Adv. Colloid. Interface Sci. **3**, 111–136 (1972)

9.274 C. Völtz, M. Nitschke, L. Heymann, I. Rehberg: Thixotropy in macroscopic suspensions of spheres, Phys. Rev. E **65**, 051402 (2002)

9.275 L.E. Silbert, J.R. Melrose, R.C. Ball: The rheology and microstructure of concentrated, aggregated colloids, J. Rheol. **43**, 673–700 (1999)

9.276 L. Heymann, S. Peukert, N. Aksel: On the solid-liquid transition of concentrated suspensions in transient shear flow, Rheol. Acta. **41**, 307–315 (2002)

9.277 J.H. So, S.M. Yang, J.C. Hyun: Microstructure evolution and rheological responses of hard sphere suspensions, Chem. Eng. Sci. **56**, 2967–2977 (2001)

9.278 H. Senff, W. Richtering, C. Norhausen, A. Weiss, M. Ballauf: Rheology of temperature sensitive core-shell latex, Langmuir **15**, 102–106 (1999)

9.279 I.M. Krieger, M. Eguiluz: The second electroviscous effect in polymer lattices, Trans Soc Rheol **20**, 29–45 (1976)

9.280 J.H. So, S.M. Yang, C. Kim, J.C. Hyun: Microstructure and rheological behaviour of electrosterically stabilized silica particle suspensions, Coll. Surf. A **190**, 89–98 (2001)

9.281 L. Heymann, N. Aksel: Progress and trends in rheology V. In: *Proc. 5th Europ. Conf. Rheol* (Steinkopff Verlag, Darmstadt 1998)

9.282 J.F. Brady, G. Bossis: The rheology of concentrated suspensions of spheres in simple shear flow by numerical simulation, J. Fluid. Mech. **155**, 105–129 (1985)

9.283 F. Gadala-Maria: The rheology of concentrated suspensions, Ph. D. Dissertation, Stanford University (1979)

9.284 G. Schoukens, J. Mewis: Nonlinear rheological behaviour and shear-dependent structure in colloidal dispersions, J. Rheol. **22**, 381–394 (1978)

9.285 M. Moan, T. Aubry, F. Bossard: Nonlinear behaviour of very concentrated suspensions of plate-like kaolin particles in shear flow, J. Rheol. **47**, 1493–1504 (2003)

9.286 S. Lin-Gibson, J.A. Pathak, E.A. Grulke, H. Wang, E.K. Hobbie: Elastic flow instability in nanotube suspensions, Phys Rev Lett **92**, 048302; Erratum: Phys. Rev. Lett. **92**, 239901 (2004)

9.287 I.E. Zarraga, D.A. Hill, D.T. Leighton Jr: The characterization of the total stress on concentrated suspensions of noncolloidal spheres in Newtonian fluids, J. Rheol. **44**, 185–220 (2000)

9.288 I.E. Zarraga, D.A. Hill, D.T. Leighton Jr: Normal stresses and free surface deformation in concentrated suspensions of noncolloidal spheres in a viscoelastic fluid, J. Rheol. **45**, 1065–1084 (2001)

9.289 T. Shikata, D.S. Pearson: Viscoelastic behaviour of concentrated spherical suspensions, J. Rheol. **38**, 601–616 (1994)

9.290 S.E. Mall-Gleissle, W. Gleissle, G.H. McKinley, H. Buggisch: The normal stress behaviour of suspensions with viscoelastic matrix fluids, Rheol. Acta. **41**, 61–76 (2002)

9.291 A. Singh, P.R. Nott: Experimental measurements of the normal stress in sheared Stokesian suspensions, J. Fluid. Mech. **490**, 293–320 (2003)

9.292 J.D. Ferry: *Viscoelastic properties of polymers* (Wiley, New York 1980)

9.293 M. Wilhelm: Fourier-transform rheology, Macromol. Mater. Eng. **287**, 83–105 (2002)

9.294 M. Wilhelm, D. Maring, H.W. Spiess: Fourier-transform rheology, Rheol. Acta. **37**, 399–405 (1998)

9.295 M. Wilhelm, P. Reinheimer, M. Ortseifer: High sensitivity Fourier-transform rheology, Rheol. Acta. **38**, 349–356 (1999)

9.296 S. Kallus, N. Willenbacher, S. Kirsch, D. Distler, T. Neidhöfer, M. Wilhelm, H.W. Spiess: Characterization of polymer dispersions by Fourier transform rheology, Rheol. Acta. **40**, 552–559 (2001)

9.297 K. Hyun, S.H. Kim, K.H. Ahn, S.J. Lee: Large amplitude oscillatory shear as a way to classify the complex fluids, J. Non-Newt. Fluid Mech. **107**, 51–65 (2002)

9.298 Y. Otsubo: Rheology of colloidal suspensions flocculated by reversible bridging, Chem. Eng. Sci. **56**, 2939–2946 (2001)

9.299 M. Schmidt, H. Münstedt: On the elastic properties of model suspensions as investigated by creep revovery measurements in shear, Rheol. Acta. **41**, 205–210 (2002)

9.300 L.A. Utracki: The rheology of two-phase flows. In: *Rheological Measurement*, ed. by A.A. Collyer, D.W. Clegg (Elsevier, Barking 1988), Chap. 15

9.301 C.J.S. Petrie: The rheology of fibre suspensions, J. Non-Newt. Fluid Mech. **87**, 369–402 (1999)

9.302 J. Greener, J.RG. Evans: Uniaxial elongational flow of particle-filled polymer melts, J. Rheol. **42**, 697–709 (1998)

9.303 J. Greener, J.RG. Evans: Review – Measurements of elongational flows in ceramic processing, J. Europ. Ceram. Soc. **17**, 1173–1183 (1997)

9.304 J.F. Le Meins, P. Moldenaers, J. Mewis: Suspensions of monodisperse spheres in polymer melts: particle size effects in extensional flows, Rheol. Acta. **42**, 184–190 (2003)

9.305 D.M. Husband, N. Aksel, W. Gleissle: The existence of static yield stresses in suspensions containing noncolloidal particles, J. Rheol. **37**, 215–235 (1993)

9.306 V.T. O'Brien, M.E. Mackay: Shear and elongation flow properties of kaolin suspensions, J. Rheol. **46**, 557–572 (2002)

9.307 A.G. Gibson, G. Kotsikos, J.H. Bland, S. Toll: Squeeze flow. In: Rheological measurement, ed. by A.A Collyer, Clegg DW (Elsevier, Barking 1988) Chap. 18

9.308 N. Delhaye, A. Poitou, M. Chaouche: Squeeze flow of highly concentrated suspensions of spheres, J. Non-Newt. Fluid Mech. **94**, 67–74 (2000)

9.309 A. Poitou, G. Racineux: A squeezing experiment showing binder migration in concentrated suspensions, J. Rheol. **45**, 609–625 (2001)

9.310 T.W. Chan, D.G. Baird: An evaluation of a squeeze flow rheometer for the rheological characterization of a filled polymer melt with a yield stress, Rheol. Acta. **41**, 245–256 (2002)

9.311 J.D. Sherwood, D. Durban: Squeeze flow of a power-law viscoplastic solid, J. Non-Newt. Fluid Mech. **62**, 35–54 (1996)

9.312 H.M. Laun, M. Rady, O. Hassager: Analytical solutions for squeeze flow with partial wall slip, J. Non-Newt. Fluid Mech. **81**, 1–15 (1999)

9.313 D.N. Smyrnaios, J.A. Tsamopoulos: Squeeze flow of Bingham plastics, J. Non-Newt. Fluid Mech. **100**, 165–190 (2001)

9.314 A. Matsoukas, E. Mitsoulis: Geometry effects in squeeze flow of Bingham plastics, J. Non-Newt. Fluid Mech. **109**, 231–240 (2003)

9.315 P. Sherman: *Rheological properties of emulsions. In: Encyclopedia of Emulsion Technology*, Vol. 1 (Dekker, New York 1983), Chap. 7

9.316 H.A. Barnes: Rheology of emulsions – a review, Coll. Surf. A **91**, 89–95 (1994)

9.317 T.F. Tadros: Fundamental principles of emulsion rheology and their applications, Coll Surf A **91**, 39–55 (1994)

9.318 R. Pal: Rheology of emulsions containing polymeric liquids. In: *Encyclopedia of Emulsion Technology*, Vol. 4, ed. by P. Becher (Dekker, New York 1996), Chap. 3

9.319 U. Teipel: Einfluss der Tropfengröße auf das rheologische Verhalten von Emulsionen (Influence of droplet size on the rheological behaviour of emulsions), Chemie-Ingenieur-Technik **73**, 1006–1012 (2001), in German

9.320 R. Pal: Scaling of relative viscosity of emulsions, J. Rheol. **41**, 141–150 (1997)

9.321 U. Teipel, N. Aksel: Rheologically identical behaviour of emulsions and suspensions in steady shear flow: Dimensional analysis and experimental evidence, Chem. Eng. Technol. **26**, 947–951 (2003)

9.322 U. Teipel, L. Heymann, N. Aksel: Indirect detection of structural changes in micellar solutions by rheological measurements, Coll. Surf. A **193**, 35–49 (2001)

9.323 F.D. Rumscheidt, S.G. Mason: Particle motions in sheared suspensions, XII. Deformation and burst of

drops in shear and hyperbolic flow, J. Colloid. Sci. **16**, 238–261 (1961)
9.324 G.I. Taylor: The formation of emulsions in definable fields of flow, Proc. Roy. Soc. **A146**, 501–523 (1934)
9.325 H.P. Grace: Dispersion phenomena in high viscosity immiscible fluid systems and application of static mixers as dispersion devices in such systems, Chem. Eng. Comm. **14**, 225–277 (1982)
9.326 V.T. Tsakalos, P. Narvard, E. Peuvrel-Disdier: Deformation and breakup mechanism of single drops during shear, J. Rheol. **42**, 1403–1417 (1998)
9.327 V. Cristini, S. Guido, A. Alfani, J. Blawzdziewicz, M. Loewenberg: Drop breakup and fragment size distribution in shear flow, J. Rheol. **47**, 1283–1298 (2003)
9.328 S. Wannaborworn, M.R. Mackley: Experimental observation and matching numerical simulation for the deformation and breakup of immiscible drops in oscillatory shear, J. Rheol. **46**, 1279–1293 (2002)
9.329 R. Cavallo, S. Guido, M. Simeone: Drop deformation under small-amplitude oscillatory shear flow, Rheol. Acta. **42**, 1–9 (2003)
9.330 F. Mighri, A. Ajji, P.J. Carreau: Influence of elastic properties on drop deformation in elongational flow, J. Rheol. **41**, 1183–1201 (1997)
9.331 H.A. Stone: Dynamics of drop deformation and breakup in viscous fluids, Annu. Rev. Fluid Mech. **26**, 65–102 (1994)
9.332 M. Loewenberg, E.J. Hinch: Collision of two deformable drops in shear flow, J. Fluid. Mech. **338**, 299–315 (1997)
9.333 U. Teipel, N. Aksel: Studies on the adsorption of nonionic surfactants and the dripping behaviour of their solutions by the drop volume and maximum bubble pressure technique, Tenside Surf. Det. **37**, 297–309 (2000)
9.334 B. Warburton: Interfacial rheology. In: *Rheological Measurement*, 2nd edn., ed. by A.A. Collyer, D.W. Clegg (Chapman Hall, London 1998), Chap. 22
9.335 D.W. Criddle: The viscosity and elasticity of interfaces. In: *Rheology – Theory and Applications*, Vol. 3, ed. by F.R. Eirich (Academic, New York 1960)
9.336 J.T. Petkov, K.D. Danov, N.D. Denkov, R. Aust, F. Durst: Precise method for Measuring the surface shear viscosity of surfactant monolayers, Langmuir **12**, 2650–2653 (1996)
9.337 R. Pal: Novel viscosity equations for emulsions of two immiscible liquids, J. Rheol. **45**, 509–520 (2001)
9.338 R. Pal, E. Rhodes: Viscosity/concentration relationship for emulsions, J. Rheol. **33**, 1021–1045 (1989)
9.339 H.M. Lee, J.W. Lee, O.O. Park: Rheology and dynamics of water-in-oil emulsions under steady and dynamic shear flow, J. Colloid. Interface Sci. **185**, 297–305 (1997)
9.340 J.F. Palierne: Linear rheology of viscoelastic emulsions with interfacial tension, Rheol. Acta. **29**, 204–214 (1990), Erratum Rheol. Acta. **30**, 497 (1991)
9.341 E.H. Kerner: The elastic and thermoelastic properties of composite media, Proc. Phys. Soc. A **69**, 808–813 (1956)
9.342 M. Bousmina: Rheology of polymer blends: linear model for viscoelastic emulsions, Rheol. Acta. **38**, 73–83 (1999)
9.343 R. Pal: Novel shear modulus equations for concentrated emulsions of two immiscible elastic liquids with interfacial tension, J. Non-Newt. Fluid Mech. **105**, 21–33 (2002)
9.344 M.M. Robins: Emulsions – creaming phenomena, Curr. Opinion Coll. Interface Sci. **5**, 265–272 (2000)
9.345 P. Walstra: Emulsion stability. In: *Encyclopedia of Emulsion Technology*, Vol. 4, ed. by P. Becher (Dekker, New York 1996), Chap. 1
9.346 U. Teipel: Rheologisches Verhalten von Emulsionen und Tensidlösungen (Rheological behaviour of emulsions and surfactant solutions), Ph.D. Thesis, University of Bayreuth, published in: Wissenschaftliche Schriftenreihe des Fraunhofer-Institutes für Chemische Technologie, Pfinztal (Germany), in German (1999)
9.347 X. Li, C. Pozrikidis: The effect of surfactants on drop deformation and on the rheology of dilute emulsions in Stokes flow, J. Fluid. Mech. **341**, 165–194 (1997)
9.348 K.G. Hollingsworth, M.L. Johns: Rheo-nuclear magnetic resonance of emulsion systems, J. Rheol. **48**, 787–803 (2004)
9.349 A. Montesi, A.A. Peña, M. Pasquali: Vorticity alignment and negative normal stresses in sheared attractive emulsions, Phys. Rev. Lett. **92**, 058303 (2004)
9.350 C. Bower, C. Gallegos, M.R. Mackley, J.M. Madiedo: The rheological and microstructural characterisation of the non-linear flow behaviour of concentrated oil-in-water emulsions, Rheol. Acta. **38**, 145–159 (1999)
9.351 W.M. Kulicke, O. Arendt, M. Berger: Characterization of hydroxylpropylmethylcellulose-stabilized emulsions. Part II: The flow behaviour, Rheol. Acta. **276**, 1024–1031 (1998)
9.352 R. Pal: Dynamics of flocculated emulsions, Chem. Eng. Sci. **52**, 1177–1187 (1997)
9.353 G.K. Moates, A.D. Watson, M.M. Robins: Creaming and oscillation rheology of weakly flocculated concentrated emulsions, Coll. Surf. A **190**, 167–178 (2001)
9.354 M.R. Anklam, G.G. Warr, R.K. Prud'homme: The use of opposed nozzles configuration in the measurement of the extensional rheological properties of emulsions, J. Rheol. **38**, 797–810 (1994)
9.355 J. Plucinski, R.K. Gupta, S. Chakrabarti: Wall slip of mayonnaises in viscometers, Rheol. Acta. **37**, 256–269 (1998)
9.356 E.B. Bagley: End Corrections in the Capillary Flow of Polyethylene, J.Appl. Phys. **28**, 624–627 (1957)

9.357 C.D. Han, M. Charles, W. Philippoff: Rheological Implications of the Exit Pressure and Die Swell in Steady Capillary Flow of Polymer Melts. I. The Primary Normal Stress Difference and the Effect of L/D Ratio on Elastic Properties, Trans. Soc. Rheol. **14**, 393–408 (1970)

9.358 J.C. Maxwell: On double refraction of a viscous fluid in motion Proc. R. Soc. London, Ser. A **22**, 46–47 (1873)

9.359 J.K. Hobbs, D.R. Binger, A. Keller, P.J. Barham: Spiralling optical morphologies in spherulites of poly(hydroxybutyrate) J.Polym. Sci. Part B **38**, 1575–1583 (2000)

9.360 R.M.A. Azzam, N.M. Bashara: *Ellipsometry and Polarized Light* (North Holland, Amsterdam 1977)

9.361 N.H. Hartshorne, A. Stuart: *Crystals and the Polarizing Microscope* (Edward Arnold, London 1960)

9.362 E. Fredericq, C. Houssier: *Electric Dichroism and Electric Birefringence* (Clarendon Press, Oxford 1973)

9.363 C.L. Riddiford, H.G. Jerrard: Relaxation times by the Kerr effect, J. Phys. D.: Appl. Phys. **3**, 1314–1321 (1970)

9.364 G.G. Fuller, K.J. Mikkelsen: Optical rheometry using a rotary polarization modulator, J.Rheol **33**, 761–769 (1989)

9.365 A.W. Chow, G.G. Fuller: Xanthan gum two color flow birefringence, J. Rheol. **28**, 23–43 (1984)

9.366 G.G. Fuller: Optical Rheology, Annu. Rev. Fluid Mech. **22**, 387–417 (1990)

9.367 M. Muller, J. Vorwerk, P.O. Brunn: Optical studies of local flow behaviour of a non-Newtonian fluid inside a porous medium, Rheol. Acta **37**, 189–194 (1998)

9.368 A. Peterlin: Streaming birefringence of soft, linear macromolecules with finite chain length, Polymer **2**, 257–264 (1961)

9.369 A. Peterlin: Hydrodynamics of macromolecules in a velocity field with longitudinal gradient, J.Polym. Sci. Poly. Lett. **4**, 287–291 (1966)

9.370 W. Kuhn, F. Grün: Beziehungen zwischen elastischen Konstanten und Dehnungsdoppelbrechung hochelastischer Stoffe, Kolloidzscr. **101**, 248–271 (1942)

9.371 A. Peterlin: Streaming birefringence and hydrodynamic interaction, Pure and Appl. Chem. **12**, 563–586 (1966)

9.372 W. Kuhn: Über die Gestalt für den förminger Moleküle in Lösungen, Kolloidzscr. **68**, 2–15 (1934)

9.373 P.E. Rouse: A theory of the linear viscoelastic properties of dilute solutions of coiling polymers, J. Chem. Phys. **21**, 1272–1280 (1953)

9.374 B.H. Zimm, : Dynamics of polymer molecules in dilute solution: viscoelasticity flow birefringence, J. Chem. Phys. **24**, 269–278 (1956)

9.375 L.K.G. Treloar: *The Physics of Rubber Elasticity, 3rd edn.* (Clarendon Press, Oxford 1975)

9.376 G. Ryskin: Calculation of the effect of polymer additive in a converging flow, J. Fluid Mech. **178**, 423–440 (1987)

9.377 J.M. Rallison, E.J. Hinch: Do we understand the physics in the constitutive equation?, J. Non-Newt. Fluid Mech. **29**, 37–55 (1988)

9.378 J.M. Wiest, L.E. Wedgewood, R.B. Bird: On coil-stretch transitions in dilute polymer solutions, J. Chem. Phys. **90**, 587–594 (1989)

9.379 R.G. Larson: The unraveling of a polymer chain in a strong extensional flow, Rheol. Acta **29**, 371–390 (1990)

9.380 E.J. Hinch: Uncoiling a polymer molecule in a strong extensional flow Non-Newton, Fluid Mech. **54**, 209–230 (1994)

9.381 (Nauka, Moscow 1964). Translated by C. Crane-Robinson, National lending Library for Science and Technology Boston Spa. (1971)

9.382 V.N. Tsvetkov: Dynamic flow birefringence, optical anisotropy, and shape of macromolecules in solutions, J. Polym. Sci. **23**, 151–166 (1957)

9.383 V.N. Tsvetkov: The effects of shape in streaming birefringence of polymer solutions, J. Polym. Sci. **30**, 297–314 (1958)

9.384 J. Brandrup, E.H. Immergut: *Polymer Handbook*, 3rd edn. (Wiley, New York 1989)